Thermomechanics of Nano-Filled Elastomers

by

Shawna M. Liff
Master of Science in Mechanical Engineering
Massachusetts Institute of Technology, 2005
Bachelor of Science in Mechanical Engineering
Northeastern University, 2003

SUBMITTED TO THE DEPARTMENT OF MECHANICAL ENGINEERING IN PARTIAL FULFILLMENT OF THE REQUIREMENTS FOR THE DEGREE OF

DOCTOR OF PHILOSOPHY IN MECHANICAL ENGINEERING
AT THE
MASSACHUSETTS INSTITUTE OF TECHNOLOGY

AUGUST 2008
[September]

Signature of Author ______________________________
Department of Mechanical Engineering
August 13, 2008

Certified by ______________________________
Gareth H. McKinley
Professor of Mechanical Engineering
Thesis Supervisor

Accepted by ______________________________
Lallit Anand
Professor of Mechanical Engineering
Chair, Committee on Graduate Students

Thermomechanics of Nano-Filled Elastomers

by

Shawna M. Liff

Submitted to the Department of Mechanical Engineering
on August 13, 2008 in partial fulfillment of the
requirements for the Degree of
Doctor of Philosophy in Mechanical Engineering

Abstract

The incorporation of nanoparticles into engineering thermoplastic elastomers affords engineers an opportunity to formulate flexible, tough and multifunctional polymer nanocomposites that potentially rival the most advanced materials in nature. Development of these materials is difficult since thermodynamic and kinetic barriers inhibit the dispersal of inorganic, hydrophilic nanoparticles into inherently hydrophobic polymer matrices. Thermoplastic polyurethanes (TPUs) are particularly attractive nanocomposite matrix materials due to their vast range of potential applications (e.g. in artificial organs, coatings, foams, and active wear), their mechanical versatility, and tunable block-polymeric structure. In this thesis we explore methods for systematically nanoreinforcing such materials by exploiting the microphase structure, differential polarities and multiple thermomechanical phase transitions of the macromolecular blocks that constitute the elastomeric matrix.

Using a solvent exchange technique we show that it is possible to preferentially nanoreinforce the hard micro-domains of thermoplastic elastomers with smectic clay nanofillers that have characteristic dimensions similar to the hard segment. The adhesion between the clay and the hard micro-domains coupled with the formation of a percolative network not only stiffens and toughens, but increases the heat distortion temperature (HDT) of the material. The discotic clay platelets induce morphological ordering over a range of length scales that results in significant thermomechanical enhancement and expands high temperature applications. This thesis seeks to further enhance the understanding and utility of thermoplastic polyurethane nanocomposites by answering two questions: (1) what thermo-physical interactions between nano-clay and elastomeric thermoplastic polyurethane are taking place? and (2) how can these thermo-physical interactions be exploited?

To answer these questions the nano-reinforced-hard micro-domain morphology was monitored during deformation using in-situ wide angle x-ray scattering and combined with the results of extensive quasi-static mechanical testing which enabled the identification two characteristic relaxation times. A one-dimensional constitutive model to account for such morphological changes augmenting the previous model for unfilled polyurethanes developed by Qi and Boyce (2005) is discussed. Finally, the thermo-mechanical influence of nano-clay fillers on the shape memory effects exhibited by polyurethane nanocomposites is examined and multi-responsive shape memory polyurethane fibrous mats are developed via electrospinning.

Quantifying and controlling the thermo-physical interactions between a block-copolymer with polar segments (e.g. thermoplastic polyurethane) and inorganic nanoparticles (e.g. nano-clay) is important for future nanocomposite processing strategies: the efficacy of nanoreinforcement hinges upon the close matching of characteristic length scale and the adhesion of the nanoparticles to the targeted polymer phase morphology. Exploiting the different polarity of the blocks in conjunction with solvent exchange approach developed in this thesis and solution processing techniques such as electro-spinning, offers an avenue toward the development of high performance, hierarchically-ordered materials that rival natural materials.

Thesis Advisor: Gareth H. McKinley
Title: Professor of Mechanical Engineering

Acknowledgements

This research was supported by the US Army through the Institute for Soldier Nanotechnologies, under Contract DAAD-19-02-D-0002 with the US Army Research Office. The content does not necessarily reflect the position of the Government, and no official endorsement should be inferred. I also want to thank the National Science Foundation for the financial support it provided in the form of a graduate research fellowship.

I would like to thank Professor Gareth H. McKinley, my advisor, and the rest of my committee, Professors Mary C. Boyce, Robert E. Cohen, and Paula T. Hammond for sharing their expertise, for asking thought-provoking questions and for offering support and guidance. Gareth, thank you for broadening my knowledge of polymer science and non-Newtonian fluids, teaching me to prepare for and think about the tough questions I think you or someone else will ask, and then always asking a question I did not consider. Professor Boyce thank you for allowing me to work with you as a teaching assistant for the undergraduate Mechanics and Materials II course (2.002), for adopting me as a group member, and continuing to tutor me in polymer mechanics. I am grateful to have worked with you both. I am also grateful for the friendship and mentorship Dr. Nitin Kumar and Dr. LaShanda James-Korley afforded me my first two years at MIT. Their support and knowledge was invaluable. I also want to thank my lab-mates at the Institute for Soldier Nanotechnologies and at the Non-Newtonian Fluids Laboratory for sharing their expertise. I am particularly thankful for the help Merideth Silberstein provided with the ELF, the useful wide angle x-ray diffraction analysis advice Ryan Waletzko offered, the TEM preparation Dr. Steve Kooi completed with the FIB, the TEM imaging completed by Dr. Mark Johnson, Dr. Yong Zhang, and Daniel Alcazar, and the Mercury Porosimetry tests completed by Joseph Lowery. I also want to thank Wonjae Choi, Shreerang Chattre, and Dr. Anish Tuteja for their assistance with the goniometer and preparation and supply of the oleophobic coating used on the electrospun mats, as well as Dr. Brian Pate, Emily Chen and Cate Morgan for their data collection at CHESS, and Patrick Boisvert for his ESEM and SQUID assistance.

Finally, and most importantly I would also like to wholeheartedly acknowledge and thank my family for their continuing support, patience, and love. Mom, Dad, and Harmony, thank you for always answering the phone and talking with me no matter if I were ecstatic or a just a stressed out mess, for supporting me always, and loving me no matter what. Mom for five years I always looked forward to our phone conversations, especially on Saturday morning when I was in the lab and even when I wanted to crush the DMA with a sledgehammer. Shannon, you are my lighthouse. You stand resolute no matter what the conditions and I rely heavily on you to keep me grounded and to guide me home. I may have been able to do this without you, but I certainly would not have smiled as big as when I came home at the end of each day. Thanks for your patience when I set the alarm every two hours through the night so that I could tend to experiments, for altering our plans last-minute so that I could meet deadlines, and for always being supportive and positive. Most importantly, thank you for sharing your love and life with me.

Contents

List of Figures 9
List of Tables 15
1. Introduction 17
  1.1 References 22
2. Background 24
  2.1 Inspiration 24
  2.2 Introduction to Polyurethanes 27
  2.3 Importance of Polymer-Clay Nanocomposites 29
  2.4 Brief Synopsis of Previous Polyurethane Nanocomposite Research 33
  2.5 Summary 49
  2.6 References 50
3. Nanoparticle Dispersal Via Solvent Exchange 55
  3.1 Introduction 55
  3.2 Previous Dispersal Techniques Utilized 55
    3.2.1 Dispersion Via Melt and Mixing 56
    3.2.2 In Situ Polymerization 57
    3.2.3 Common Solvent Process 57
  3.3 Solvent Exchange Approach 58
    3.2.1 Method to Disperse Laponite in Thermoplastic Polyurethane 60
  3.4 Proof of Exfoliation 63
    3.4.1 Materials 63
    3.4.2 Dispersal Characterization 64
      3.4.2.1 Transmission Electron Microscopy 64
      3.4.2.2 Atomic Force Microscopy 64
      3.4.2.3 Wide Angle X-ray Diffraction 64
    3.4.3 Results and Dicussion 64
  3.5 Influence of Processing Parameters 67
    3.5.1 Influence of Segment Polarity 67
      3.5.1.1 Materials 67
      3.5.1.2 Evidence of Exfoliation 68
      3.5.1.3 Evidence of Preferential Reinforcement 71
    3.5.2 Influence of Processing Time 74
  3.6 Conclusion 75

3.7 References 76
4. High Performance Elastomeric Nanocomposites via Solvent Exchange Processing 79
  4.1 Introduction 79
  4.2 Materials and Characterization Methods 80
    4.2.1 Materials 80
    4.2.2 Atomic Force Microscopy 81
    4.2.3 Mechanical Characterization 81
    4.2.4 Thermal Characterization 81
  4.3 Results and Discussion 81
  4.4 Conclusion 95
  4.5 References 95
5. Influence of Nano-Clay on Morphology and Mechanics of High Performace Elastomeric Nanocomposites 99
  5.1 Introduction 99
  5.2 Mechanical and Morphological Characterization Techniques 101
    5.2.1 Mechanical Test Descriptions 101
      5.2.1.1 Hysteresis 102
      5.2.1.2 Softening 102
      5.2.1.3 Rate Dependence 102
      5.2.1.4 Time Dependence 102
      5.2.1.5 Relaxed Response and Equilibrium Paths 102
    5.2.2 Morphological Characterization Techniques 103
      5.2.2.1 Wide Angle X-Ray Scattering 103
      5.2.2.2 Attenuated Total Reflectence Fourier Transform Infrared Spectroscopy 104
      5.2.2.3 Cross-Polarized Microscopy 105
  5.3 Results and Discussion 105
    5.3.1 Hysteresis 105
    5.3.2 Softening 107
    5.3.3 Rate Dependence 109
    5.3.4 Time Dependence 111
    5.3.5 Relaxed Response and Equilibrium Paths 120
    5.3.6 X-Ray Scattering 122
    5.3.7 Attenuated Total Reflectence Fourier Transform Infrared Spectroscopy 125
    5.3.8 Cross-Polarized Microscopy 128
  5.4 Conclusions 129
  5.5 References 130

6. Influence of Laponite on the Shape Memory Behavior of Polyurethane 133

6.1 Introduction 133

6.2 Materials and Experimental Methods 136

6.2.1 Materials 136
6.2.2 Composite Preparation 136
6.2.3 Characterization Methods 136
6.2.3.1 Laponite Dispersal 136
6.2.3.2 Thermal Transitions 137
6.2.3.3 Thermal Expansion Coefficient 137
6.2.3.4 Stress-Strain Behavior Above and Below the Transition Temperature 137
6.2.3.5 Free Strain Recovery 140
6.2.3.6 Constrained Strain, Stress Recovery 142

6.3 Results and Discussion 142

6.3.1 Laponite Dispersal 142
6.3.2 Thermal Transitions 143
6.3.3 Thermal Expansion Coefficient 147
6.3.4 Stress-Strain Behavior Above and Below the Transition Temperature 148
6.3.5 Free Strain Recovery 154
6.3.6 Constrained Strain, Stress Recovery 160

6.4 Conclusion 163

6.5 References 164

7. Development of Multi-Responsive Electrospun Fabric 166

7.1 Introduction 166

7.2 Materials and Experimental Methods 169

7.2.1 Materials 169
7.2.2 Solution Preparation 169
7.2.3 Electrospinning Parameters and Mat Preparation 170
7.2.4 Characterization Methods 171
7.2.4.1 Interrogation of Solution Conductivity 171
7.2.4.2 Interrogation of Fiber Morphology 171
7.2.4.3 Interrogation of Non-Woven Mat 171
7.2.4.4 Interrogation of Pore Size 172

7.3 Results and Discussion 173

7.3.1 Fibrous Morphology 173
7.3.2 Results of Thermal and Aqueous Actuation 176
7.3.4 Evidence of Reversible Surface Energy 182

7.4 Conclusions 185

7.5 References 186

8. Concluding Remarks 190

8.1 Summary of Accomplishments 190

8.2 Future Work 192

8.2.1 Scale-Up of Time Efficient, Environmentally-Friendly, Solvent Exchange Approach 192

8.2.2 Deformation Induced Orientation and Damage by Nano-Clay 194

8.2.3 Utility of Magnetite in Shape Memory Polyurethane Composites 196

8.3 References 200

Appendices 201

A-1 Movie Demonstrating the Mechanical Enhancement of Elasthane at High Temperature by the Addition of Laponite 201

A-2 Elasthane/Laponite Composite Moduli Measured with a Video Extensometer 202

A-3 Discussion of Appropriate Constitutive Model 206

A-4 2-D WAXS Spectra Collected at Each Specimen Stretch for Pure Elasthane and that Reinforced with 8 wt% Laponite 213

A-5 Movies of Electrospun Mat Lateral Shrink 219

List of Figures

Figure 1-1: The aspect ratio of various shaped nano-filer is the ratio of the longest dimension, *l*, to the shortest dimension, *d*....17
Figure 1-2: Schematic visually describing how the surface area to volume ratio of a discotic platelet increases when thinner, higher aspect ratio platelets are utilized....18
Figure 1-3: Prediction of nanoparticle, nanocomposite formulation and nanocomposite component market size by the chemical company BASF for the year 2015 taken from [4]....19
Figure 2-1: Engineering stress-strain curves of dragline and viscid silk as displayed [2]....25
Figure 2-2: A Urethane Linkage....27
Figure 2-3: Thermomechanical behavior of various polyurethanes....28
Figure 2-4: Schematic illustrations of various polymer-clay nanocomposites with different extents of clay dispersal....32
Figure 2-5: Comparison of the Montmorillonite and Laponite crystal structure as shown in [27]....32
Figure 2-6: Tensile properties of the polyurethane-clay nanocomposites prepared with the longest onium ion Montmorillonite-modification at various clay loadings as reported in [28]: (A) tensile strength, (B) tensile modulus, and (C) strain-at-break....33
Figure 2-7: Dispersal of 1 wt% Montmorillonite modified with most reactive swelling agent in the PU containing 39 wt% hard segment as shown in [34]....35
Figure 2-8: Representative force-extension curves of the polyurethane urea nanocomposites in [36]....36
Figure 2-9: Storage moduli (left) and stress-strain plots (right) of the polyurethane containing 0 (a), 4 (b), 20 (c), and 40 (d) wt% clay from [38]....37
Figure 2-10: Transmission Electron Micrographs of the solvent cast (left) and melt compounded (right) soft polyurethane nanocomposites containing 3 wt% Montmorillonite depicted in [42]....39
Figure 2-11: Stress-strain response of a polyurethane filled with the same concentration of synthetic fluoromica (3 wt%) but of different aspect ratio [43]....40
Figure 2-12: Hysteresis exhibited by a polyurethane filled with the same concentration of synthetic fluoromica (3 wt%) but of different aspect ratio [43]....40
Figure 2-13: Storage modulus versus strain amplitude curves of the polyethylene-polyurethane (PEPU) nanocomposites containing 0, 2.5, and 5 wt% clay depicted in [46]....41
Figure 2-14: The recovery stress of the shape memory polyurethane with 0, 1, 3 and 5 wt% clay at a fixed strain of 100% while a 4°C min^{-1} heating rate is applied [47]....42
Figure 2-15: Evolution of *d*-spacing with respect to a nanocomposite loaded with 5 wt% clay during stretching [53]....44
Figure 2-16: Tapping mode AFM phase images of (a) pure polyurethane containing 36 wt% hard segment and (b) the same polyurethane loaded with 1 wt% clay in [14]. 45
Figure 2-17: Mechanical properties of the waterborne PU filled with various weight concentrations of Saponite as shown in [68]....48
Figure 2-18: Transmission electron micrographs of sepiolite (a) and 3 wt% sepiolite in polyurethane (b) [64]....49

Figure 3-1: Vapor-Liquid equilibrium curve for H_2O and for DMAc (left) and vapor-liquid equilibria of H_2O-DMAc determined via experiment in [33]..........................61
Figure 3-2: Structure of Elasthane 80A based on available non-proprietary information..........63
Figure 3-3: a, b, & c, Transmission electron micrographs (TEM) of nanocomposites containing 4, 10, and 20 wt% Laponite show fully exfoliated, uniformly dispersed and randomly oriented, Laponite platelets..65
Figure 3-4: Laponite dispersal within the polyurethane matrix via WAXD, using a different diffraction instrument and different nanocomposite samples (Dispersal Characterization). 66
Figure 3-5: Structure of PEO-based polyurethane [42]..67
Figure 3-6: Structure of PTMO-based polyurethane [44]..68
Figure 3-7: (a) TEM image of 10 wt % Laponite dispersed in PTMO:HDI-BDO PU; 50 nm scale bar. (b)TEM image of 10 wt % Laponite dispersed in PEO-PPO-PEO:HDI-BDO PU; 50 nm scale bar. (c) TEM image of 10 wt % Laponite dispersed in PEO-PPO-PEO:HDI-BDOPU; 20 nm scale bar..69
Figure 3-8: WAXD spectra of HDI:BDO hard segment, of pure Laponite and of the pure and 10 wt % Laponite-filled polyurethane nanocomposites..................................70
Figure 3-9: Flexural storage modulus, *E*' (a), and loss tangent, tan δ (b), both determined via DMA and DSC thermograms and (c) during initial heating and cooling cycles of the pure (black) and 10 wt % Laponite-filled PUs (red)..................................72
Figure 3-10: Representative engineering stress-strain tensile curves of the pure and 10 wt % Laponite filled polyurethanes are presented, and the corresponding cross-polarized image...73
Figure 4-1: Structure of Elasthane 80A and Laponite dispersal within the polyurethane matrix...82
Figure 4-2: Hard and soft micro-domain distribution in nanocomposites containing 0, 4, 10, and 20 wt % Laponite as observed via AFM phase imaging. 84
Figure 4-3: Impact of Laponite concentration on the mechanical properties of Elasthane. 86
Figure 4-4: Impact of Laponite concentration on the thermomechanical properties of Elasthane.. 89
Figure 4-5: DSC of the nanocomposites containing 0, 4, 10, and 20 wt% Laponite. 91
Figure 4-6: Laponite concentration and impact on thermal degradation. 92
Figure 4-7: Evidence of long range order or crystallization in the nanocomposites is apparent in images obtained with a cross-polarized microscope. 93
Figure 4-8: Polarized optical microscopy images of the ordered, fractal-like domains in various nanocomposite films exhibit birefringence. 94
Figure 5-1: Hysteresis of pure Elasthane and composites filled with 4, 10, and 15 wt% Laponite when thin-film specimens are stretched 80% and 160%.....................................106
Figure 5-2: Comparison of the hysteresis of pure Elasthane and a composite filled with 15 wt% Laponite when thin-film specimens are stretched 80% and unloaded and then to 160%..106
Figure 5-3: Cyclic softening behavior of pure Elasthane and nanocomposites filled with 4, 10, and 15 st% Laponite when the specimens are stretched to nominal strains equal to 0.1, 0.2, 0.4, 0.8, 1.2, 1.6, and 2.0...107

Figure 5-4: Evolution of the maximum stress and plastic strain as 0, 2, 4, 10, and 15 wt% Laponite-filled nanocomposites are cycled 5 times at applied nominal strains equal to 0.1, 0.2, 0.4, 0.8, 1.2, 1.6, and 2.0..108
Figure 5-5: Rate dependence of 0, 4, 10, and 15 wt% Laponite-filled Elasthane when stretched to a nominal strain of 1.0 at three different nominal strain rates....................109
Figure 5-6: The flow stress, or engineering stress as ε=0.3, at the various strain rates is plotted against the Laponite concentration...110
Figure 5-7: Comparison of the engineering stress-strain response of 0, 4, 10, and 15 wt% Laponite-filled Elasthane when stretched to a a nominal strain of 1.0 at three different nominal strain rates..111
Figure 5-8: Applied strain history for stress relaxation tests as well as the engineering stress response vs. time and applied strain for nanocomposites containing 0, 4, 10 and 15 wt% Laponite 112
Figure 5-9: One-dimensional description of the rheological model of the experimental stress relaxation and corresponding fir to the pure Elasthane stress relaxation after the specimen is stretched 10%..113
Figure 5-10: Two characteristic time constants observed in the stress relaxation behavior of the polyurethane nanocomposites...114
Figure 5-11: Schematic of the stretched eight-chain network as depicted in [18]................114
Figure 5-12: Relationship between the orientation parameter as wel as the normalized orientation parameter and the principal stretch of an eight-chain RVE for an incompressible material..116
Figure 5-13: Evolution of the two characteristic time constants observed in the stress relaxation behavior of the polyurethane nanocomposites with orientation.........................116
Figure 5-14: Evolution with tensile stretch of the three moduli that capture the stress relaxation behavior of the polyurethane nanocomposites.......................................117
Figure 5-15: Power-law decay of the polyurethane nanocomosite moduli with orientation...117
Figure 5-16: Comparison of the polyurethane nanocmposite moduli evolution with increased orientation determined from experimental data and that prediced via empirical relations..119
Figure 5-17: Stress relaxation behavior of pure polyurethane and that filled with 4, 10, and 15 wt% Laponite through five load-unload cycles......................................120
Figure 5-18: Equilibrium paths of the 0, 4, 10, and 15 wt% Laponite-filled nanocomposites determined from the stress relaxation behavior during the 1st and 5th cycle...121
Figure 5-19: WAXS spectra of pure and 8 wt% Laponite-filled Elasthane as the material is deformed...123
Figure 5-20: Azimuthal scan of the pure and 8 wt% Laponite-filled polyurethane composite as the deformation increases at *d*-spacing between 0.447 and 0.468 nm...............124
Figure 5-21: Azimuthal scan of the pure and 8 wt% Laponite-filled polyurethane composite as the deformation increases at *d*-spacing between 0.409 and 0.427 nm...............125
Figure 5-22: ATR-FTIR spectrum of pure Elasthane 80A and that filled with 6 wt%, 10 wt%, and 15 wt% Laponite...127
Figure 5-23: Comparison of the long range order exhibited through cross-polarized microscopy of pure Elasthane prior to deformation and after deformation to yield.............128

Figure 5-24: Comparison of the long range order exhibited through cross-polarized microscopy of 10 wt% Laponite-filled Elasthane prior to deformation and after significant stretch and soft-segment reorientation and alignment....................................129
Figure 6-1: Images of a pure MM5510 polyurethane film inside the ELF 3200 as seen with the video extensometer. 139
Figure 6-2: Visual description of the free strain recovery test and the locations with respect to engineering stress, strain and temperature.......... 141
Figure 6-3: Transmission electron micrographs of MM5510 PU nanocomposites containing 4, 10, and 15 wt% Laponite..143
Figure 6-4: First and second heat flow cycles of pure MM5510 polyurethane and composites filled with 4, 10, and 15 wt% Laponite using differential scanning calorimetry...144
Figure 6-5: Dynamic mechanical response of pure MM5510 polyurethane and composites filled with 4, 10, and 15 wt% Laponite soon after preparation (left) and nine months later (right)..146
Figure 6-6: a) Thermal expansion of pure MM5510 polyurethane films and composites filled with 4, 10, and 15 wt% Laponite from -150°C to 125°C while under a 10 kPa tensile load. b) Enlarged view of the thermal expansion behavior within the shape memory operational temperature range interrogated. c & d) The thermal expansion coefficients below and above the transition temperature (55°C), respectively, are elucidated...147
Figure 6-7: True stress-strain response of the MM5510 polyurethane composites at 25°C, a temperature below the transition temperature (55°C), and 70°C, a temperature above the transition temperature when the films are stretched 2.5 times their original length..149
Figure 6-8: Uniaxial tensile response of the various nanocomposites at 70°C, a temperature above the transitition temperature..150
Figure 6-9: Uniaxial tensile response of the various nanocomposites at 70°C and the corresponding response at 25°C after five cycles of deformation at the elevated temperature..151
Figure 6-10: Uniaxial tensile response of the various nanocomposites at 25°C, a temperature below the transition temperature...153
Figure 6-11: Stretch recovery of the nanocomposites after stretching the specimen to 1.1, 1.2, 1.4, 1.7, or 2.0 times its original length at 70°C using the TA Instruments Q800 DMA..154
Figure 6-12: Comparison of the stretch recovery of the nanocomposites after stretching the specimens to 1.1, 1.2, 1.4, 1.7, or 2.0 times their original length at 70°C using the TA Instruments Q800 DMA...155
Figure 6-13: Comparison of the extent of strain recovery, total strain recovery and strain fixity for the polyurethane nanocomposites determined after deformation at elevated temperature..156
Figure 6-14: Comparison of the strain recovery of the nanocomposites after stretching the specimens to 1.4, 1.7, or 2.5 times their original length at 25°C using the ELF 3200..158

Figure 6-15: The strain recovery of the polyurethane nanocomposites containing 0, 4, 10, and 15 wt% nano-clay after stretching the speciments to 1.4, 1.7, or 2.5 times their original length at 25°C using the ELF 3200 159
Figure 6-16: Comparison of the stress recovered when the strain is constrained after stretching the polyurethane nanocomposite specimens to 1.4, 1.7, or 2.5 times their original length at 25°C using the ELF 3200 160
Figure 6-17: The stress recovered when the strain is constrained after stretching each polyurethane nanocomposite specimen to 1.4, 1.7, or 2.0 times their original length at 25°C using the ELF 3200 162
Figure 7-1: Schematic representation of the parallel-plate fiber spinner 170
Figure 7-2: Scanning electron micrographs demonstrate the change in fibrous morphology as theconcentration of polyurethane in solution increases 173
Figure 7-3: Complex plane impedance diagram of the 17 wt% polyurethane solution with (b) and without Laponite (a) from which the solution conductivity is calculated 175
Figure 7-4: Microscopic images of the as spun, pure, non-woven mat prior to and after actuation and of a 4 wt% Laponite-filled mat 175
Figure 7-5: Differential scanning calorimetry of the as spun non-woven mat, the thermally actuated mat, and the water soaked mat prior to drying and after drying 177
Figure 7-6: Evolution of water uptake in the electrospun mat as it is soaked in a DI H_2O bath 178
Figure 7-7: Influence of polyurethane concentration in solution on fiber diameter (a) and the extent of strain recovered after actuation (b & c) 179
Figure 7-8: Flexural storage moduli of the BOAS electrospun mat at various stages of actuation 180
Figure 7-9: Resultant change in pore size distribution within the pure and Laponite composite, 'beads on a string' morphology, non-woven mats prior to and after thermal and aqueous actuation 181
Figure 7-10: Scanning electron micrographs of the pure, non-woven, electrospun mat coated with a 50/50 blend of fluorinated POSS & PMMA in the relaxed, free-standing, as spun configuration, in the thermally actuated and shrunk state, the re-stretched state, and the again shrunk or recovered state and the corresponding static contact angle of a drop of hexadecane 183
Figure 7-11: Comparison of the top and bottom side of an electrospun polyurethane mat filled with 10 wt% magnetite 185
Figure 8-1: Stress-strain curves of poly(etherurethane urea) (PEUU-A) and that filled with 5 wt% vitamin E (PEUU-VE) [2] 193
Figure 8-2: Comparison of the viscosity of Dl-α-tocopherol (Vitamin E) as a function of temperature when constant shear stress or constant shear rate is applied 194
Figure 8-3: Transmission electron micrographs of magnetite nanoparticles dispersed in a commercial thermoplastic polyurethane (MM 5510) after precipitation and compression molding: scale bar 500nm in a and 100 nm in b, c, and d 198
Figure 8-4: Magnetization of commercial thermoplastic polyurethane Diaplex™ MM 5510 filled with 5 wt% magnetite (Fe_3O_4) as a function of applied magnetic field (left) and temperature when no magnetic field is applied (right) 199
Figure A-2-1: Images of 2 wt% Laponite-filled polyurethane film inside the Zwick Z010 as seen with the video extensometer 203

Figure A-2-2: Selection of the sequential images taken with the video extensometer as the Elasthane filled with 2 wt% nano-clay is deformed using the Zwick Z010 mechanical tester at a nominal strain rate of 0.0167 s^{-1}....204
Figure A-2-3: Comparison of the engineering stress-strain response of 2 wt% nano-clay filled Elasthane calculated from the change in length reported by the Zwick mechanical tester crosshead and that measured via the video extensometer at various sections along the length of the specimen gauge length....205
Figure A-3-1: One dimensional rheological model and material parameters summary of the Qi and Boyce thermoplastic polyurethane constitutive model as shown in [1]....207
Figure A-3-2: Cartoon of the soft segment evolution with matrix stretch....208
Figure A-3-3: Eight chain rubber elasticity model developed by Arruda and Boyce....209
Figure A-3-4: The equilibrium or hyperelastic response of the Elasthane/Laponite nanocomposites is the same despite Laponite concentration and can be captured by the constitutive model of Qi and Boyce [1, 5]....210
Figure A-3-5: Comparison of the equivalent shear stress versus shear strain for pure Elasthane in tension to that of the polyurethane evaluated by Qi and Boyce in compression [1]....211
Figure A-4-1: The specimen stretches equal to 1.1, 1.6, 3.0 and 9.0 correspond to the locations shown above in the stress-strain curve due to specimen slip during testing....213
Figure A-4-2: Enlarged scatter patterns at specimen stretches equal to 1.1, 1.6, 3.0 and 9.0 for pure Elasthane....214
Figure A-4-3: Enlarged scatter patterns at specimen stretches equal to 1.1, 1.6, 3.0 and 9.0 for the 8 wt% Laponite-filled Elasthane nanocomposite....215
Figure A-4-4: 1-D SAXS spectra of pure Elasthane and that filled with 8 wt% Laponite....218

List of Tables

Table 1-1: List and comparision of the various clays investigated for polyurethane reinforcement [7-11]........19
Table 2-1: Comparison of the mechanical properties of silk to other high-performance materials [2]........25
Table 2-2: The molecular weight, tensile strength, elongation, and water absorption of the pure polyurethane and polyurethane-Montmorillonite nanocomposites prepared in [32]........34
Table 2-3: List and comparison of the various clays investigated for polyurethane reinforcement [19, 61-64]........47
Table 3-1: Polyurethane soft segment polarity expressed in terms of the solubility parameter which was calculated using the group contribution method and values given in [45]........71
Table 5-1: Parameters describing the power-law decay of the polyurethane nanocomposite moduli with increased orientation........118
Table 5-2: ATR-FTIR spectral assignments for Elasthane determined by Christenson et al in [28]........126
Table 5-3: Ratio of area under the absorbance peaks of the hydrogen-bonded carbonyl bonds and the free carbonyl bonds as well as the ratio of these areas to the total absorbance area constituting carbonyl bonds described by [30]........127
Table 6-1: Analysis of the glass transition temperatures observed between 0°C and 100°C via dynamic mechanical analysis and differential scanning calorimetry upon heating freshly prepared and aged samples........146
Table 6-2: Predicted thermal stress of the various polyurethane nanocomposites when the length is constrained........160
Table 6-3: Comparison of the true stretch achieved in each nanocomposite as seen via the video extensometer during the constrained strain, stress recovery test when the specimen was stretched to 1.4, 1.7, or 2.5 its original length........161
Table 7-1: Electrospinning parameters for each fibrous morphology discussed........170
Table A-3-1: Five parameters needed to describe the hyperelastic or equilibrium response of the Elasthane/Laponite nanocomposites........209

1. Introduction

Stronger, stiffer polymeric materials are attractive to numerous industries due to their light weight, easy manufacturing, low-cost, and recyclability [1]. Reinforcement of polymer matrices with inorganic nanoparticles produces composite materials that exhibit enhanced mechanical, thermomechanical and barrier properties without significantly increasing the weight of the material. Excellent stiffness and strength are achieved while utilizing far less high-density inorganic material than is utilized in conventional composites filled with micron or millimeter size particles. Whether the nano-filler is cylindrical (carbon nanotubes), spherical (carbon black), or a platelet (clay) the efficiency of the inorganic nano-reinforcement depends on three parameters: filler mechanical properties, filler aspect ratio, and adhesion between the matrix and the filler [2]. The filler aspect ratio, α, is given by the ratio of the longest dimension, l, to the shortest dimension, d. The aspect ratio of various shaped nano-filler is visually compared in Figure 1-1.

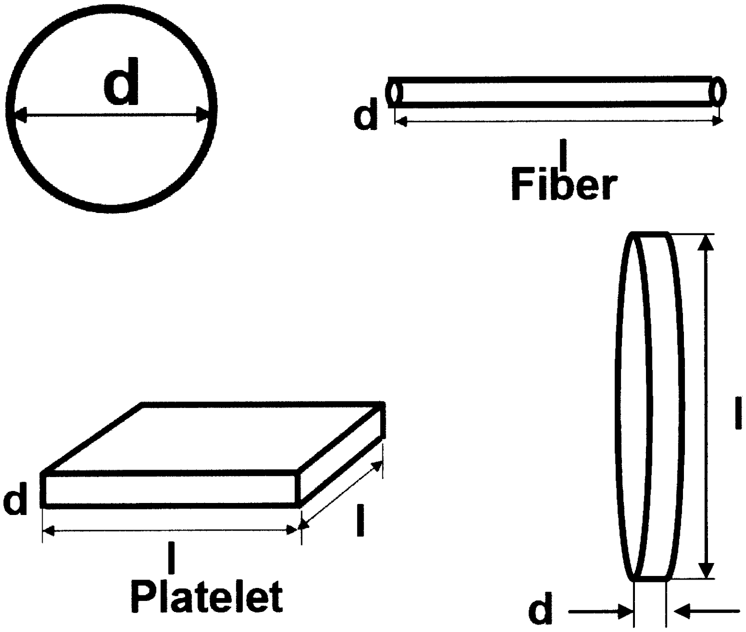

Figure 1-1: The aspect ratio of various shaped nano-filer is the ratio of the longest dimension, *l*, to the shortest dimension, *d*. The aspect ratio of spherical particles like carbon black is equal to 1 while that of the clay platelets can range from 25 to over 200.

The aspect ratio of the nanoparticles is important, because as shown for the discotic platelets of constant diameter l in Figure 1-2, as the aspect ratio increases the surface-area (A_s) to volume (V) ratio increases. Consequently, when the surface area to volume ratio is high, the nanoparticles occupy a small volume and do not significantly increase the weight of the material, but afford the polymer a large, more rigid, area on to which stress can be transferred.

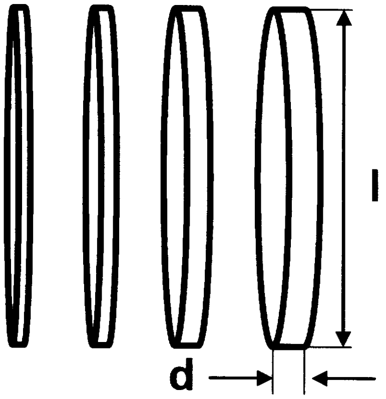

$$\alpha = \frac{l}{d}$$

$$\frac{A_s}{V} = \frac{2}{l}(\alpha + 2)$$

Figure 1-2: Schematic visually describing how the surface area to volume ratio of a discotic platelet increases when thinner, higher aspect ratio platelets are utilized.

The advantages provided by the widespread use of polymer nanocomposites can be significant. For example, if automobile weight was reduced by the judicious use of polymer nanocomposites vehicle manufactures could reduce their gasoline need by 1.5 billion liters and carbon dioxide emissions by 10 billion pounds in just one year's time [3]. The elimination of multi-polymer, multi-layer materials in food and beverage packing and replacement with polymer nanocomposites would significantly increase the recyclability of these materials and further ease the burden placed on the environment. Consequently, the chemical company BASF predicts that nanocomposite formulations and bulk materials will account for 50 billion Euros of the nanotechnology market in 2015 as shown in Figure 1-3. Meanwhile, resulting nanocomposite components will account for an even greater share—over 500 billion Euros of that same market [4].

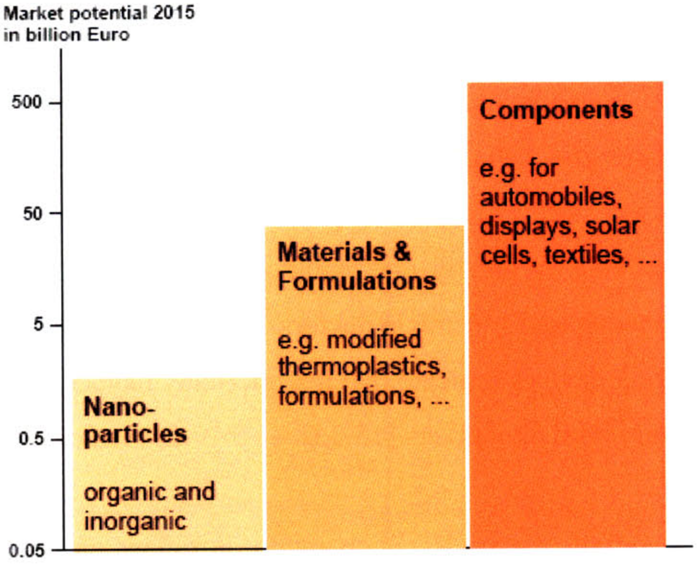

Source: Growth forecast: European Commission, DG Bank, BCC
Consumer Market Data from Sal. Oppenheim, In Realis and Evolution Capital

Figure 1-3: Prediction of nanoparticle, nanocomposite formulation and nanocomposite component market size by the chemical company BASF for the year 2015 taken from [4].

The most often utilized inorganic nanoparticle used for polymer matrix reinforcement is montmorillonite—a natural silicate [3, 5]. Clay platelets like montmorillonite that are 1-2 nm thick are attractive inorganic nanoparticles because they are naturally-occurring, inexpensive, and their aspect ratio ranges from 25 to 600 depending on the type utilized. Table 1-1 lists and compares a series of clays that can be utilized as inorganic nanoreinforcement. Since the development of Nylon-6/Montmorillonite composites in the late 1980s by Toyota Research Labs [6], polymer-clay nanocomposites have attracted much attention. By adding less than 5 wt% clay to nylon, researchers were able to significantly enhance the mechanical properties, heat resistance, and dimensional stability of the nylon and utilize the material in an under-the-hood automotive application, i.e. as a timing belt cover [1].

Clay	Empirical Formula	Lateral dimension, *D* [nm]	Thickness, *t* [nm]	*d*-spacing [nm]
Hectorite	$Na_{0.3}Mg_{2.7}Li_{0.3}Si_4O_{10}(OH)_2$	600	1	1.53
Laponite	$Na^{+0.7}[(Si_8Mg_{5.5}Li_{0.3})O_{20}(OH)_4]^{-0.7}$	25	1	1.28
Montmorillonite	$Na_{0.2}Ca_{0.1}Al_2Si_4O_{10}(OH)_2\cdot 10H_2O$	70-218	1	1.50
Rectorite	$Na_{0.6}Ca_{0.3}K_{0.1}Al_6Si_6O_{20}(OH)_4\cdot 2H_2O$	200-300	1	2.22
Saponite	$Na_{0.1}Ca_{0.1}Mg_{2.25}Fe^{2+}{}_{0.75}Si_3AlO_{10}(OH)_2\cdot 4H_2O$	165	1	1.23
Sepiolite	$(Si_{12}Mg_8O_{30})(OH)_4(OH_2)_4\cdot 8H_2O$	25	20-1500	1.03

Table 1-1: List and comparison of the various clays investigated for polyurethane reinforcement [7-11].

Because well-dispersed clay can significantly increase the strength, heat distortion temperature, barrier properties, flame retardance, and dimensional stability of a polymer at small volume fractions, polymer-clay nanocomposites are desired in numerous applications. Endeavors by the Army to design light-weight vehicles, contamination-protecting and freshness-enhancing packaging for food, and uniforms that better protect soldiers from shrapnel each rely upon polymer nanocomposites [12]. Work by electronics companies like Intel to design low-cost, flexible substrates and packaging for semiconductors, and by energy and biomedical companies to design 'smart,' actuating devices indicate that polymer-clay nanocomposites will comprise an even greater share in future product markets [13-15].

Tough, high energy absorbing materials which retain sufficient elasticity are desired for the closefitting fabric of soldier's uniforms. Fabric materials which can be worn comfortably, yet fit closely for improved chemical and biological protection, are currently of interest to the Army. Traditional polyurethane materials like Lycra/Spandex do not provide satisfactory strength and toughness when compared to Nylon/cotton fiber blends. Consequently, development of higher modulus, light-weight, elastomeric materials that can exhibit enhanced cut, tear and puncture resistance, resistance to fabric wear, in conjunction with breathability are needed. These superior, lightweight, energy absorbing materials would also be useful in helmets and in other gear that protects the soldier's body, especially his or her extremities, from low to moderate strain rate impacts. These impacts could include those received during general field maneuvers, moving across sharp objects, or from falling projectiles. The current, baggie BDU uniform is heavy and suffocating. Through utilization of a more closefitting, lightweight garment with enhanced mechanical properties the soldier gains mobility through enhanced comfort and protection. Adding nanoreinforcement to polyurethane is one way in which to strengthen and toughen polyurethane.

Polyurethanes are attractive nanocomposite matrix materials due to their numerous product markets, mechanical versatility, and tunable block-polymeric structure. Polyurethanes are well-studied multipurpose polymers that comprise about 5% of the polymer market today and are used in a variety of applications, including in chair cushions, bra padding, artificial organs and other biomedical applications, in active wear (spandex/lycra), footwear, roller ski and skate wheels, ski boots, wake boards, and in paints and coatings [16, 17]. The various soft and hard blocks of polyurethane can interact with nanoparticles and organic modifiers depending on the polarity of these segments. In the past eight years numerous research groups [5] have examined various large aspect-ratio (α >100) nano-clays, organic modifiers, and dispersal techniques for clay in polyurethane, most of which have relied upon in situ polymerization. These nanocomposite systems often display thermomechanical enhancement and/or better barrier properties; however, clay intercalation persists and limits the extent of these improvements.

Two challenges exist in the development of polymer/clay nanocomposites. The first challenge is fully dispersing and exfoliating inorganic, hydrophilic clay within organic and often hydrophobic polymer matrices. The second major challenge, as Krishnamoorti and Vaia assert, "is developing nanocomposites for systems ranging from high performance to commodity polymers...[without]...even simple structure-property models" [3]. By using a novel solvent exchange approach and a true nano-clay filler—meaning the longest length scale is on the order of tens of nanometers—elastomeric thermoplastic polyurethane-clay nanocomposites with superior thermomechanical properties have been developed without reducing the extensibility of the matrix elastomer. Consequently this nanocomposite system and other polyurethane nanocomposites containing discotic, Laponite RD, platelets which measure 25 nm in diameter and less than 1 nm in thickness are excellent systems in which to investigate the structure-property relations because the size of the inorganic filler is similar to that of polyurethane hard domains.

This thesis details the development of elastomeric polyurethane/clay nanocomposites that are preferentially reinforced and describes the resulting structure-property relations. Chapter 2 introduces the reader to polyurethanes, clay reinforcement, specifically the nano-clay Laponite, and previous polyurethane-clay nanocomposite research findings. In Chapter 3 our method for the nanoparticle preparation is described and its efficacy compared to other dispersal techniques. Then in Chapter 4 the resultant characterization and thermomechanical properties of the model Elasthane-Laponite nanocomposite are emphasized. The complete thermomechanical response is detailed and morphological evolution examined in Chapter 5. Furthermore, a constitutive model that captures the room-temperature, uniaxial tensile mechanical response of this polyurethane-clay nanocomposite is discussed. The knowledge gained from the thorough analysis of the model nanocomposite system is utilized in conjunction with experimental results to evaluate the influence of Laponite reinforcement on the strain recovery and the resulting actuating stress of a commercial shape memory polyurethane/clay nanocomposite in Chapter 6. Furthermore, discussion of the extension of the solvent exchange approach for polyurethane nanocomposites to an alternate, "fast," processing technique—electrospinning—in order to develop multi-responsive, porous, non-woven, shape-memory fabrics is presented in Chapter 7. Finally, in Chapter 8 a summary of the results is listed with recommendations for future work.

1.1 References

[1] J. DeGaspari, "Prospecting Paydirt," http://www.memagazine.org/backissues/april01/features/prospect/prospect.html, April 2001: Accessed February 17, 2005.

[2] N. Sheng, M. C. Boyce, D. M. Parks, G. C. Rutledge, J. I. Abes, and R. E. Cohen, "Multiscale micromechanical modeling of polymer/clay nanocomposites and the effective clay particle," *Polymer*, vol. 45, pp. 487-506, 2004.

[3] R. Krishnamoorti and R. A. Vaia, "Polymer Nanocomposites: Synthesis, Characterization, and Modeling," in *ACS Symposium Series*, 1st ed. Washington, D.C.: American Chamical Society, 2002.

[4] BASF, "Nanotechnology: We innovate for growth," http://www.corporate.basf.com/en/sustainability/dialog/politik/nanotechnologie/service/praesentationen.htm?getasset=fileabs1&name=BASF_Equity_Story_Nanotechnology_July07.pdf&MTITEL=Charts&suffix=.pdf&id=2mpN9Circbcp-2W, 2008: Accessed August 1, 2008.

[5] S. S. Ray and M. Okamoto, "Polymer/layered silicate nanocomposites: a review from preparation to processing," *Progress in Polymer Science*, vol. 28, pp. 1539-1641, 2003.

[6] T. K. Chen, Y. I. Tien, and K. H. Wei, "Synthesis and characterization of novel segmented polyurethane clay nanocomposite via poly(epsilon-caprolactone)/clay," *Journal of Polymer Science Part a-Polymer Chemistry*, vol. 37, pp. 2225-2233, 1999.

[7] D. Barthelmy, "Mineralogy Database," 2004.

[8] X. Y. Ma, H. J. Lu, G. Z. Liang, and H. X. Yan, "Rectorite/thermoplastic polyurethane nanocomposites: Preparation, characterization, and properties," *Journal Of Applied Polymer Science*, vol. 93, pp. 608-614, 2004.

[9] K. Yano, A. Usuki, and A. Okada, "Synthesis and Properties of Polyimide-Clay Hybrid Films," *Journal of Polymer Science Part A-Polymer Chemistry*, vol. 35, pp. 2289-2294, 1997.

[10] C. Zilg, F. Dietsche, B. Hoffmann, C. Dietrich, and R. Mulhaupt, "Nanofillers based upon organophilic layered silicates," *Macromolecular Symposia*, vol. 169, pp. 65-77, 2001.

[11] H. X. Chen, M. S. Zheng, H. Y. Sun, and Q. M. Jia, "Characterization and properties of sepiolite/polyurethane nanocomposites," *Materials Science And Engineering A-Structural Materials Properties Microstructure And Processing*, vol. 445, pp. 725-730, 2007.

[12] MIT Institute for Soldier Nanotechnologies, "ISN Day: The ISN-Army-Industry Collaboration Conference." Cambridge, MA, May 28th, 2008.

[13] D. Ratna and J. Karger-Kocsis, "Recent advances in shape memory polymers and composites: a review," *Journal Of Materials Science*, vol. 43, pp. 254-269, 2008.

[14] P. P. Kundu, V. Sharma, and Y. G. Shul, "Composites of proton-conducting polymer electrolyte membrane in direct methanol fuel cells," *Critical Reviews In Solid State And Materials Sciences*, vol. 32, pp. 51-66, 2007.

[15] Intel, "Technology Innovation," http://www.intel.com/technology/index.htm?iid=gg_work+home_technology, 2008: Accessed August 1, 2008.

[16] D. Randall and S. Lee, "The Polyurethanes Book," 2nd ed. New York: Huntsman International, 2002, pp. 477.

[17] T. Thomson, *Polyurethanes as Specialty Chemicals: Principles and Applications*. Boca Raton, Florida: CRC Press, 2005.

2. Background

The following sections provide more detailed information regarding the findings of previous researchers, which inspired the development of the thermoplastic polyurethane-Laponite nanocomposites as synthetic, high-energy-absorbency, multi-functional materials. The structural, mechanical, and thermal properties of spider silk and thermoplastic polyurethanes are examined and compared. Furthermore, the efficacy of clay nanoreinforcement in polymers is evidenced and the major challenge facing the development of polymer-clay nanocomposites is discussed as well as the polyurethane-clay research over the past ten years summarized.

2.1 Inspiration

A strong, elastomeric material with excellent toughness would be ideal in numerous products ranging from clothing and food packaging for soldiers, to compression stockings for flight attendants. The material would have a high tolerance to puncture and tear yet would be very flexible and easy to wear. Spider silk is nature's high-performance polymer that best exhibits these qualities.

The orb-web-weaving araneid spider can produce a family of high-performance silk fibers that exhibit superior energy absorbency capabilities in conjunction with various combinations of extensibility, stiffness, and strength. Each fiber in the family has a different function, depending on the mechanical properties of the fiber. These mechanical properties in turn depend upon the protein combinations excreted by the spider. Consequently, a spider is a technologically advanced fiber manufacturer, producing fibers for various functions by manipulating amino acid sequences, water content, and spinning speeds [1].

The orb-web-weaving araneid spiders are most studied because these spiders have seven glands which produce different proteins that each has a specific function [1]. For example, the major ampullate gland produces the dragline or web, frame silk and the flagelliform glands produce the core of the spiraling, fly-catching, viscid silk [1]. These fibers have completely different mechanical functions and behaviors, yet have similar energy absorbency capabilities as shown in Figure 2-1 and Table 2-1.

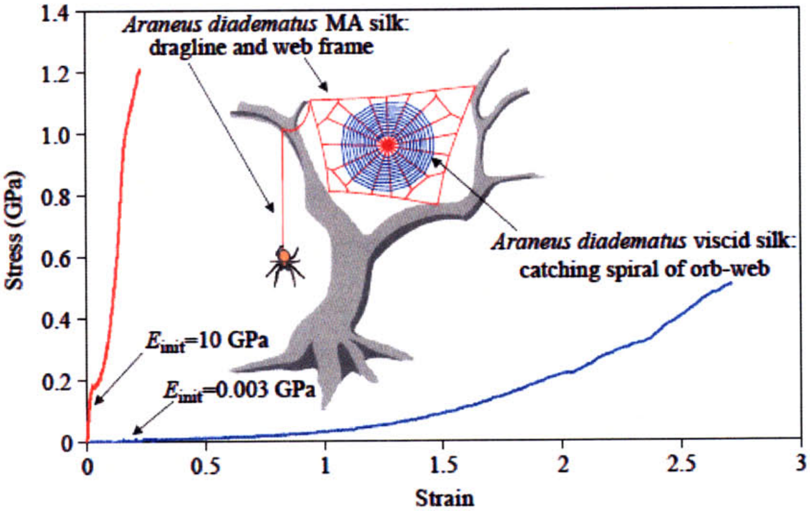

Figure 2-1: Engineering stress-strain curves of dragline and viscid silk as displayed in [2].

The dragline silk, which must hold the weight of the spider and form the frame of the web, exhibits an initial modulus of 10 GPa, an ultimate strength of 1.1 GPa, a 27% extensibility and a toughness of 160 MJ m^{-3} [2]. The viscid silk, which must bend extensively to slow and trap flies that collide with the web, exhibits a similar toughness of 150 MJ m^{-3}, but instead an initial modulus of 3 MPa, a 270% extensibility, and an ultimate strength of 500 MPa [2]. Other natural and synthetic materials may exhibit similar combinations of stiffness, extensibility and strength to silk, but the toughness of native-spider silk is unmatched as is shown in Table 2-1.

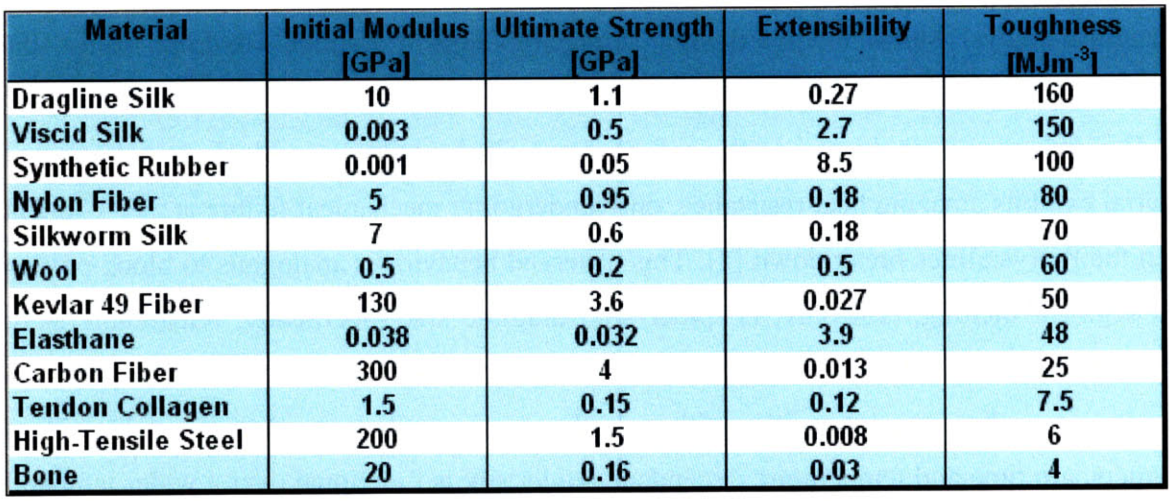

Material	Initial Modulus [GPa]	Ultimate Strength [GPa]	Extensibility	Toughness [MJm^{-3}]
Dragline Silk	10	1.1	0.27	160
Viscid Silk	0.003	0.5	2.7	150
Synthetic Rubber	0.001	0.05	8.5	100
Nylon Fiber	5	0.95	0.18	80
Silkworm Silk	7	0.6	0.18	70
Wool	0.5	0.2	0.5	60
Kevlar 49 Fiber	130	3.6	0.027	50
Elasthane	0.038	0.032	3.9	48
Carbon Fiber	300	4	0.013	25
Tendon Collagen	1.5	0.15	0.12	7.5
High-Tensile Steel	200	1.5	0.008	6
Bone	20	0.16	0.03	4

Table 2-1: Comparison of the mechanical properties of silk to other high-performance materials [2].

Synthetic rubber comes closest to matching the toughness of the weaker, viscid silk, but the ultimate strength exhibited by the viscid silk is unachievable in synthetic or natural rubbers. Consequently, knowledge of the amino acid sequence and morphology of spider silk, and their relation to the mechanical properties is critical for the development of new high-performance materials.

Investigation of the amino acid sequence and structural motif of the various spider silks has shown that dragline spider silk, in particular, is an optimized block copolymer. The silk is based on two proteins, spidroin I and spidroin II, sequenced by Xu and Lewis in 1990 [3]. Like multi-block polymeric systems, the resultant silk consists of hydrophilic, soft glycine-rich blocks and hydrophobic, alanine-rich hard blocks. The alanine-rich blocks hydrogen bond with each other and form small crystalline β-sheets that comprise 12% of the fiber by volume and measure approximately 2 x 5 x 7 nm^3 [4]. These highly oriented β-sheets are coupled to the amorphous glycine-rich soft blocks via the less oriented β-sheets. Consequently during deformation these crystalline sheets are moved and aligned by the soft glycine-rich matrix [5]. The soft blocks give the fiber its elasticity and their structural motif is not easily identified and may consists of a combination of 3_1-helices, β-spirals, and random coils, which are probably highly ordered and hydrogen bonded [6-8]. Furthermore, the soft blocks may change conformation depending on extension and water content, providing a means for the silk to obtain the superior ultimate strength it exhibits prior to failure [7].

Dragline silk also exhibits remarkable thermomechanical behavior. At ~200°C, dynamic mechanical analysis shows that the flexural storage modulus of dragline silk drops from ~10 GPa to ~2 GPa when the intermolecular hydrogen bonds of the non-crystalline domains break down [8]. This behavior is analogous to the soft segment glass transition in block-co-polymers. This material exhibits amazing heat resistance, only undergoing mechanical failure at 371°C the point when the β-crystallites break down [8]. This observed behavior is analogous to block-polymeric hard segment melting. Not only, is spider silk, dragline silk specifically, remarkable at room temperature, but the static mechanical properties between -60°C and 150°C are superior when compared to other properties [8]. Although the mechanical properties of spider silk, like polymers, are time and temperature dependent, spider silk is functional over a wider temperature range.

Spider dragline silk is a highly evolved and optimized protein polymer that has a combination of thermomechanical properties that are unmatched by synthetic materials. The strength, toughness, and heat resistance exhibited by dragline silk fibers are desirable. If these fibers could be replicated on a mass scale the potential applications are vast. At this point synthetic analogs of spider silk, like nylons, rubbers, and polyurethanes are still thermomechanically inferior to native-spider silk.

2.2 Introduction to Polyurethanes

Polyurethanes are well-studied versatile polymers that have been used in a variety of applications, including in chair cushions, bra padding, artificial organs and other biomedical applications, in active wear (spandex/lycra), footwear, roller ski and skate wheels, ski boots, wake boards, and in paints and coatings [9, 10]. Any polymer that contains urethane linkages, depicted in Figure 2-2, is considered a polyurethane.

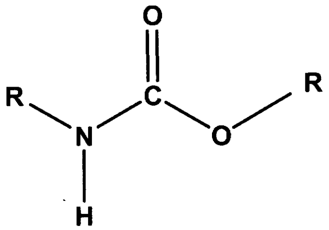

Figure 2-2: A urethane linkage

Polyurethanes or polyurethane ureas are made by reacting diisocyanates with dialcohols or diamines, respectively [11]. The urethane linkages like to hydrogen bond and can form rigid, crystalline aggregates. In numerous applications segmented polyurethanes are desired and polyols, polymeric compounds containing alcoholic hydroxyl groups, of various lengths (M_w ~600-3000 g mol^{-1}) are polymerized with the urethane reactants in either a one-step or two-step reaction [12]. The material properties of the segmented polyurethane can be tuned between that of a hard plastic and a flexible elastomer depending on the polyol added and the resultant chemical or physical crosslinks formed [12].

Thermoplastic polyurethanes are those segmented, elastomeric polyurethanes that contain soft polymeric segments that have a glass transition temperature (T_g) below room temperature [13]. Consequently, at temperatures below the soft segment T_g a thermoplastic polyurethane behaves as a glass, while at temperatures above the T_g the polyurethane behaves as an elastomer. The soft segment imparts good extensibility and the rigid hydrogen bonded crystal aggregates, identified as hard domains, act as physical crosslinks imparting moderate stiffness and strength [9].

The stiffness, strength, extensibility, and thermomechanical behavior of segmented polyurethanes are dependent upon numerous factors. These include the extent of phase separation between the hard and soft segment, the concentration of hard segment to soft segment, the type of polyol added, the molecular weight of the polymer, and the extent of the polymer crystallinity [12].

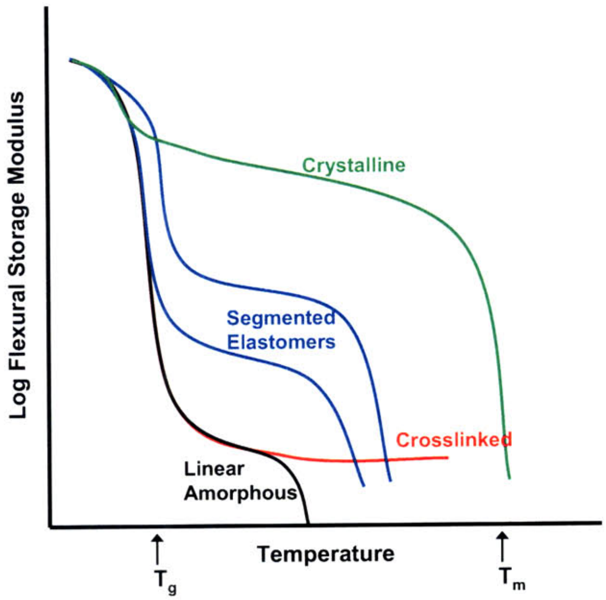

Figure 2-3: Thermomechanical behavior of various polyurethanes.

For example, soft segment crystallinity or hard segment content can be increased in segmented polyurethanes to increase the magnitude of the rubbery plateau modulus, as shown in Figure 2-3. Furthermore, an increase in polyurethane molecular weight can increase the hard segment melting temperature (T_m) or point of liquid flow without influencing the magnitude of the rubbery plateau modulus [12]. Consequently, there are numerous ways in which the thermomechanical properties of polyurethanes can be tailored.

The semi-crystalline, block-polymeric structure of elastomeric polyurethane is similar to spider silk. Each contains crystalline aggregates that act as physical crosslinks. The aggregates or hard domains in polyurethane, which have a lateral dimension measuring 3-32 nm in length depending on the chemistry, are bigger than the β-sheets in spider silk [14-16] and are easily tailored. Unfortunately, the properties of thermoplastic polyurethanes are inferior to spider silk. Because the onset of the urethane dissociation is near 200°C, polyurethanes undergo a three-orders-of-magnitude change in flexural storage modulus between -100°C and 250°C. Comparatively, spider dragline silk undergoes less than an order-of-magnitude change within this temperature range because the dissociation of the β-sheets is well above 200°C [8, 12]. Polyurethane-based materials have the potential to be spider silk analogs if the mechanical properties and thermal stability of the polyurethane can be significantly enhanced.

2.3 Importance of Polymer-Clay Nanocomposites

Nano-clay has proven to be effective polymer filler, enhancing mechanical properties, thermal stability, and decreasing permeability of numerous polymers at small volume fractions. For example, in the late 1980s Toyota Research Labs developed a Nylon 6-Monmorillonite nanocomposite that at only a 4.2 wt% clay loading exhibited a 100% increase in initial modulus, a 50% increase in ultimate strength, and a 80°C increase in heat distortion temperature [17]. This thermomechanical enhancement was greater than that produced by glass or talc at over 30 wt% loading [18]. This finding initiated numerous investigations of other polymer-clay nanocomposites.

Nylon was not the only polymer that exhibited thermomechanical enhancements and improved barrier properties when filled with clay. The inclusion of well-dispersed clay has exhibited enhancements in a handful of other polymer systems as is shown in the list below.

- In 1993, Yano and colleagues from Toyota Research Labs in Japan found that when polyimide was filled with 2 wt% synthetic mica the water vapor permeability coefficient was less than 10% that of the pure polyimide permeability coefficient. Furthermore, the thermal expansion coefficient of the composite was 60% of the pure polyimide coefficient [19].

- In 1994, Lan and Pinnavai found that when rubbery epoxy was filled with exfoliated Montmorillonite at 15 wt%, the composite exhibited more than a 10-fold increase in both tensile strength and modulus when compared to the properties of the pure epoxy [20].
- In 2001, Nam and colleagues reported that a 6 wt% loading of modified Montmorillonite in polypropylene foam resulted in a 44°C increase in heat distortion temperature when compared to the properties of the pure polypropylene [21].
- In 2002, Lepoittevin and colleagues reported that poly(ε-caprolactone) exhibited a higher thermal stability when filled with modified Montmorillonite. Whether the clay was exfoliated or intercalated the degradation temperature at 50% mass loss was at least 25°C higher than the degradation temperature of the pure poly(ε-caprolactone) at the same mass loss percentage [21].
- Currently, as the price of petroleum increases and concern for the environment becomes more prevalent, there has been a push to develop polymers from renewable bio-based materials. While some researchers have developed soybean-oil- or fatty-acid-derivative-based polyurethane thermosets and castor-oil and rapeseed-oil based waterborne polyurethane dispersions, Lu and Larock have reinforced a corn oil based block-copolymer with modified Montmorillonite [22]. As was exhibited in the petroleum based polymer composites, these composites display increased thermal stability and improvements in mechanical properties when only 2-3 wt% modified Montmorillonite is added.

In the past twenty years, numerous researchers have shown that clay can effectively reinforce polymer systems, whether petroleum or bio-based, and significantly improve the mechanical, thermal, and barrier properties of the pure material. The reinforcement of polyurethanes with clay appears to be a feasible method to enhance the thermomechanical properties of polyurethane and develop synthetic spider silk analogs—high performance, flexible, strong, energy absorbing, multi-functional composites.

The major challenge in developing polymer/clay nanocomposites is fully dispersing and exfoliating inorganic, hydrophilic clay platelets within organic and often hydrophobic polymer matrices. Numerous clays, including Montmorillonite, Hectorite, and Saponite among others, have been investigated as polymer filler. Whether natural or synthetic, these silicates contain alkali and alkaline earth cations absorbed on the negatively charged silicate faces which act as glue binding the silicates in stacks [21]. If the silicates and polymer matrix do not interact and the silicates remain aggregated in stacks, the mechanical properties of the material are poor [23]. However, if the silicate and polymer interact favorably the silicate stacks can be delaminated and the small-volume, high aspect-ratio, stiff platelets can offer a large surface on to which the soft polymer can transfer stress and can provide a torturous path in which permeants must traverse [17]. Consequently, it is important that when clay is blended with polymer that the silicates are delaminated and well-dispersed, so that the maximal enhancements are obtained.

Three different techniques are employed to disperse the clay within the polymer: melt dispersion, in situ polymerization, and use of a common solvent. Each technique as well as a new, solvent exchange technique is discussed in Chapter 3. The effectiveness of these dispersal methods depends on numerous factors, including the polarity of the clay and/or organic modification, the reactivity of the clay and/or organic modification, as well as the mobility of the polymer chains.

The extent of the clay dispersal in the polymer is defined by the gallery spacing (distance between silicate faces) and the orientation of the silicate platelets. When the silicate stacks are not delaminated at all and, instead, remain in tight aggregated tactoids, the clay acts as macro-scale filler and the resultant material can be considered a conventional composite [17]. These aggregates may increase the stiffness of the polymer at the expense of elongation, strength, and toughness and are unfavorable. When the gallery spacing of the clay increases because a few molecular layers of polymer have been inserted between the silicates, the clay is intercalated. In some instances the edges of the intercalated clay interact and the clay flocculates and is considered intercalated-and-flocculated [21]. When the clay is delaminated and the individual layers are separated throughout the polymer matrix and there are few to no steric interactions between platelets, the clay is considered exfoliated [24]. However, as the clay content increases, the average spacing between platelets necessarily decrease. In some instances, an ordered exfoliated structure, which is detected by wide angle X-ray diffraction (WAXD), can result [24]. Various possible clay dispersals are depicted in Figure 2-4.

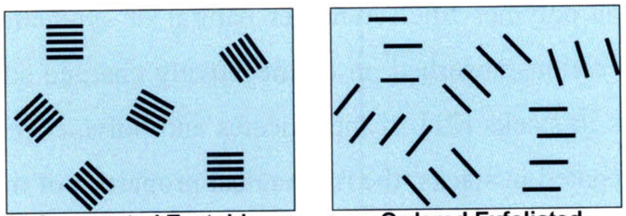

Aggregated Tactoids Ordered Exfoliated

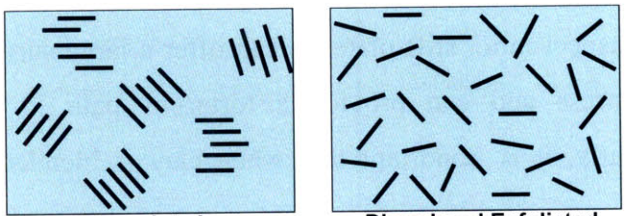

Intercalated Disordered Exfoliated

Figure 2-4: Schematic illustrations of various polymer-clay nanocomposites with different extents of clay dispersal.

Typically, research groups use very large aspect-ratio ($\alpha = L / t$) clays, like Montmorillonite ($\alpha \sim 70$ to 218), that are approximately 1 nm thick to fill their polymers [19, 25]. Because the lateral dimensions of these silicates are large, often when exfoliation is achieved at small weight fractions, intercalation persists at higher concentrations. These large thin platelets are substantially bigger than the hard domains within polyurethanes. Consequently, I chose to reinforce polyurethane with the smallest aspect ratio clay available, Laponite (D = 25 nm, t = 1 nm), so that the lateral dimension of the silicate was similar to the lateral dimension of the polyurethane hard domain. Therefore, just as spiders reinforce silk with β-sheets, and tire-makers reinforce rubber with carbon black, we reinforce polyurethanes with Laponite [26].

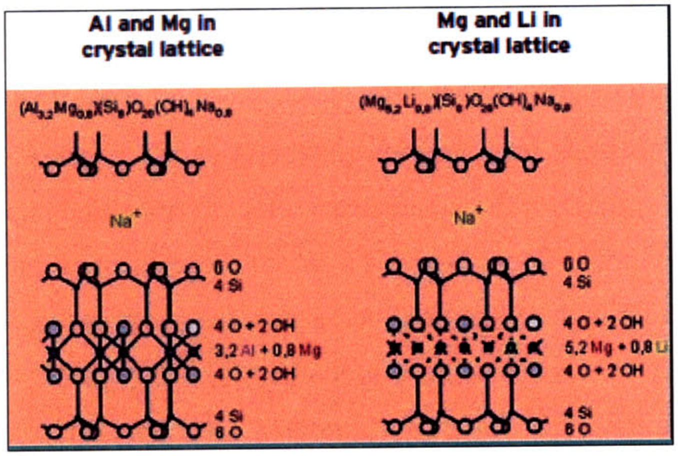

Montmorillonite **Laponite**

Figure 2-5: Comparison of the Montmorillonite and Laponite crystal structure as shown in [27].

2.4 Brief Synopsis of Previous Polyurethane Nanocomposite Research

The following section will briefly review a random selection of approximately 25% of the polyurethane/clay nanocomposite literature published and listed in the ISI Web of Science database. These articles do not constitute all polyurethane/clay nanocomposite literature, but are a representative subset. The versatility of polyurethanes and the previously exhibited potential of clay nanocomposites have made polyurethane/clay nanocomposites very desirable.

After the dramatic thermomechanical enhancement exhibited by Montmorillonite in Nylon-6, numerous research groups began investigating the affects of clay reinforcement in other polymer matrices [18]. It was not until 1998 that Wang and Pinnavaia reported the first instance of successful reinforcement of elastomeric polyurethane (PU) with smectic clay [28]. In this work, Montmorillonite, organically-modified with alkylammonium ions containing either 12 or 18 carbons, were solvated in polyols—polymeric compounds containing alcoholic hydroxyl groups, of various molecular weight. The researchers found that the extent of clay intercalation was determined by the length of the onium ion, the complex cation modifying the clay, not by the molecular weight of the polyol. At a 10 wt% loading of Montmorillonite modified with the longest onium ion a more than 100% increase in modulus, strength, and extensibility was exhibited as shown in Figure 2-6 [28]. This result suggested that onium ions acted as a plasticizer, improving elasticity, an observation noted by other researchers later [28, 29].

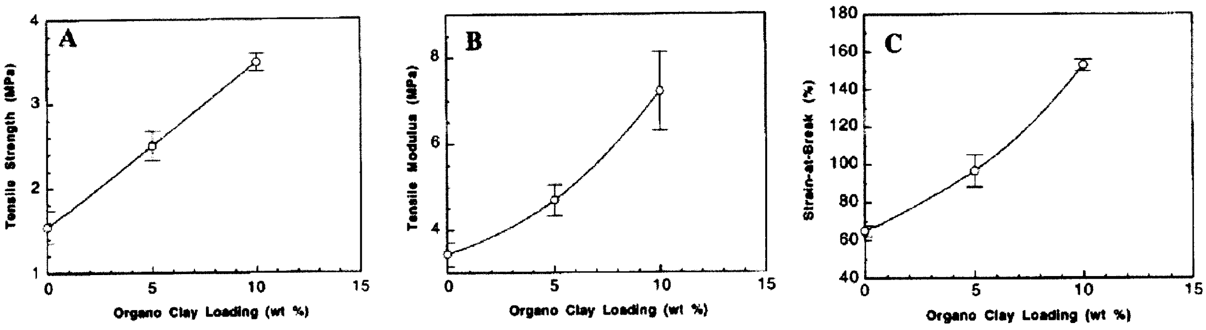

Figure 2-6: Tensile properties of the polyurethane-clay nanocomposites prepared with the longest onium ion Montmorillonite-modification at various clay loadings as reported in [28]: (A) tensile strength, (B) tensile modulus, and (C) strain-at-break.

Less than a year later Chen, Tien, and Wei published the first of a set of publications examining polyurethane/Montmorillonite nanocomposites [30]. In their first study, inspired by the Nylon-

6/Montmorillonite work nearly a decade earlier, polycaprolactone/Montmorillonite prepolymer was prepared and substituted in as chain extender during PU nanocomposite synthesis. Characterization showed that the clay was well dispersed within the polycaprolactone. However, each platelet behaved as a nucleation seed inducing crystallinity that enhanced the tensile strength of the PU nanocomposite while significantly hindering the extensibility at loadings greater than 0.74 wt% clay [30]. In a completely different PU system, five years later, Moon and colleagues found that the clay behaved in the same way, nucleating crystals in the polybutylene succinate soft segments [31].

Not wanting the clay to nucleate crystallization at the expense of the soft domain, in the following study Chen, Tien, and Wei investigated the affect of clay swelling agents, 12-aminolauric acid (12COOH) and benzidine (BZD), on a 4,4'-diphenyl methane diisocyanate (MDI), polytetramethylene glycol (PTMG, MW=1000 g mol^{-1}), and 1,4-butanediol (BDO) based PU nanocomposite [32]. Although x-ray diffraction suggested that the 12COOH better exfoliated the clay, the composites made using the BZD exhibited greater thermal stability, more than a 3-fold increase in elongation, and more than 2-fold increase in strength when compared to the pure PU [32]. However, similar to the previous study, at loadings greater than 1 wt% Montmorillonite, the mechanical enhancements deteriorated as shown in Table 2-2.

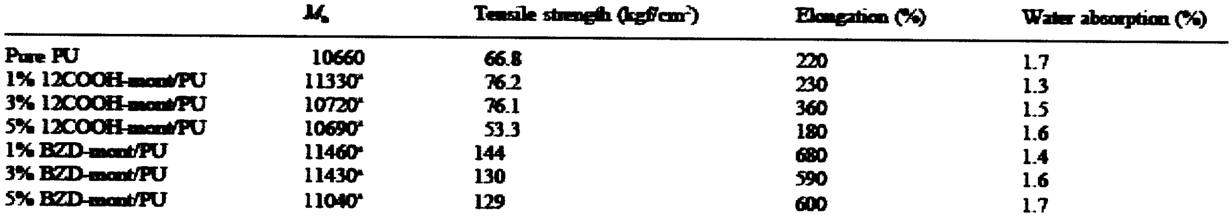

	M_n	Tensile strength (kgf/cm^2)	Elongation (%)	Water absorption (%)
Pure PU	10660	66.8	220	1.7
1% 12COOH-mont/PU	11330*	76.2	230	1.3
3% 12COOH-mont/PU	10720*	76.1	360	1.5
5% 12COOH-mont/PU	10690*	53.3	180	1.6
1% BZD-mont/PU	11460*	144	680	1.4
3% BZD-mont/PU	11430*	130	590	1.6
5% BZD-mont/PU	11040*	129	600	1.7

Table 2-2: The molecular weight, tensile strength, elongation, and water absorption of the pure polyurethane and polyurethane-Montmorillonite nanocomposites prepared in [32].

Tien and Wei extended this work, again utilizing the BZD swelling agent, and investigated the nanocomposite behavior when the hard segment content was increased from 39 wt% to 50 wt% and then to 63 wt% [33]. They found that when the hard segment fraction increased, FTIR showed that the carbonyl hydrogen bonding increased; however, as the clay content increased the hydrogen bonding decreased and the extent of intercalation diminished. Ultimately, the reinforcing ability of the clay is compromised when the hard segment hydrogen bonds are disrupted and phase mixing results, and when the more rigid PU molecules are unable to diffuse between and separate clay platelets. Consequently, the reduction in hydrogen bonding (37%) was greatest for the PU nanocomposite containing 63 wt% hard segment and 5 wt% clay [33].

Attempting to better enhance the clay-polymer interaction and further improve the thermomechanical properties, in the next investigation Tien and Wei used the same PU system with 39 wt% hard segment and evaluated four different swelling agents [34]. Three of the four swelling agents contained at least one hydroxyl group which could react with the isocyanates of the PU and tether the clay to the polymer matrix. Tien and Wei found that the extent of clay dispersion increased with swelling agent reactivity and that the mechanical enhancement was best when the clay platelets were tethered to the PU rather than trapped within it [34]. In the following publication Tien and Wei evaluated the thermomechanical and thermal degradation properties of the nanocomposites formed using the three reactive swelling agents [35]. They found that the PU soft segment glass transition temperature (T_g) remained unaffected while the hard segment T_g increased with increasing clay content [35].

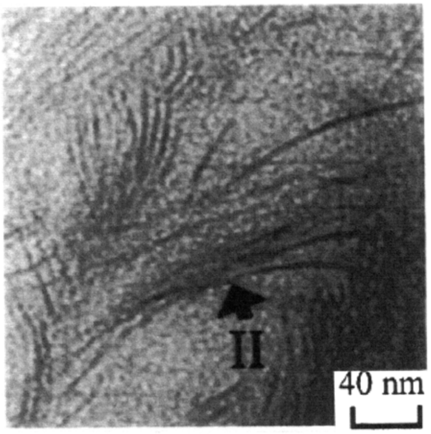

Figure 2-7: Dispersal of 1 wt% Montmorillonite modified with most reactive swelling agent in the PU containing 39 wt% hard segment as shown in [34].

The greatest improvement in degradation temperature, a 40°C increase above the degradation temperature of the pure PU, was displayed in the nanocomposite that utilized the most reactive swelling agent (containing 3 hydroxyl groups) with a loading of 1 wt% clay. This nanocomposite also exhibited the best clay dispersal as shown in Figure 2-7. Ultimately, the maximum thermomechanical enhancements are exhibited in the nanocomposites with the best clay dispersal [35].

In 2001 Xu et al, a group from Pennsylvania State University, investigated a biomedical PU system similar to that Tien and Wei studied in [30, 32-35], except the soft segment in this PU had a higher molecular weight (MW=2000 g mol^{-1}), the hard segments (22 wt%) were chain extended with 1,4-diaminocyclohexane and ethylenediamine (25:75 by mole) forming polyurethane urea segments, and the Montmorillonite (Cloisite 15A) sodium ions were exchanged with dimethyl ditallow ammonium (65% C_{18}, 30% C_{16}, and 5% C_{14}) [36]. Representative tensile behavior of the various nanocomposites is shown in Figure 2-8.

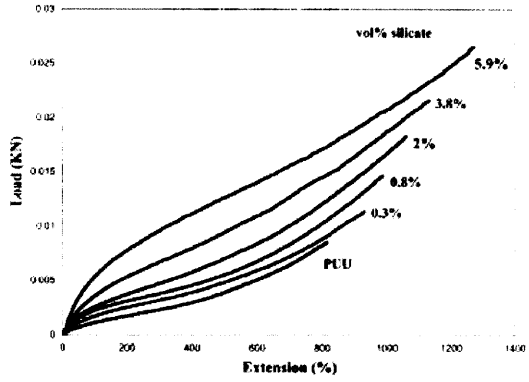

Figure 2-8: Representative force-extension curves of the polyurethane urea nanocomposites in [36].

Xu et al found that at 20 wt% clay loading the nanocomposite exhibited over a 300% increase in initial modulus, over a 30% increase in strength, over a 50% increase in extensibility, and over a 5-fold reduction in water vapor permeability when compared to the pure polyurethane urea [36].

The silicates reduce the permeability of the PU by forming torturous paths through which the water vapor molecules must diffuse. Consequently, the reduction in permeability is dependent upon the amount of clay added as well as the extent of its exfoliation. In a later publication, the authors reported that Fourier transform infrared spectroscopy (FTIR) showed that the clay platelets were kinetically trapped in the PU matrix and differential scanning calorimetry (DSC) showed that the soft segment T_g was not influenced by clay loading [37].

In 2002 Tortora et al, a group from Italy, published a study similar to the first study published by

Chen, Tien, and Wei, in which they investigated the reinforcement effects of PU composites containing poly(ε-caprolactone)/Montmorillonite prepolymer as a chain extender [38]. In this new study the prepolymer replaced di(ethylene glycol) in the hard-segment and induced the same crystallinity in the poly(ε-caprolactone) as that seen by Chen, Tien, and Wei with x-ray diffraction peaks at 21.3° and 23.7° [38]. Similarly, the nanocomposite became more brittle with increased clay content. The storage modulus increased with clay loading, particularly at temperatures above the soft segment T_g, and resultantly the material flow temperature increased by 50°C at 20 wt% clay loading as shown in Figure 2-9. Furthermore, although the elastic modulus increased by over 5-fold at 20 wt% loading, there was a significant reduction in the strain hardening slope which indicated that the clay disrupted the soft segment mobility and alignment as shown in Figure 2-9, reducing the strength and toughness of the material [38].

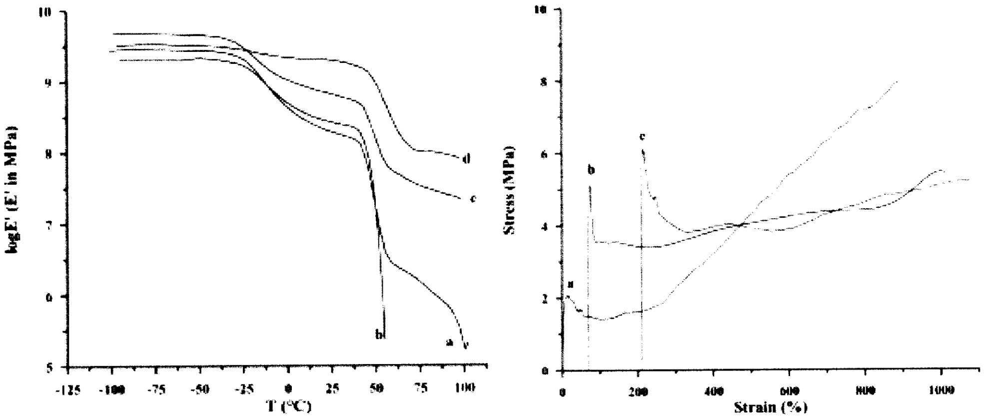

Figure 2-9: Storage moduli (left) and stress-strain plots (right) of the polyurethane containing 0 (a), 4 (b), 20 (c), and 40 (d) wt% clay from [38].

In 2003 Osman et al evaluated the gas permeability of a PU adhesive filled with Montmorillonite modified by three different ammonium ions [39]. The Montmorillonite was exchanged with organic cations that had either an aliphatic hydrocarbon nature, an aromatic moiety, or had a polarity that matched the PU polarity. They found that the water vapor permeability decreased by 40-50% at a 3 vol% clay loading for all three Montmorillonite modifications. However, the oxygen permeability decreased by 30% at 3 vol% loading only when the aromatic and polar modifications were made [39]. The nanocomposite composed of clay modified with the hydrocarbon-based ammonium ion instead increased oxygen permeability. The authors speculate that this was because the non-polar modification phase separated at the PU-silicate interface and increased the free volume at these interfaces enough that small oxygen molecules could diffuse through, but large clusters of water vapor molecules could not [39].

Also in 2003, Wang et al, who were interested in developing novel electrolytes for solid-state rechargeable batteries, investigated the influence of Montmorillonite addition on the ionic conductivity of a polyurethane electrolyte [40]. The electrolyte was filled with between 0 and 6 wt% Montmorillonite and exhibited the best ionic conductivity at 2.5 wt% loading [40]. The enhanced conductivity was due to the ability of clay to reduce the PU crystallinity, to provide more ionic transport sites, and to maintain the PU mechanical stability.

In 2004, Chen-Yang et al published work in which they examined the thermal and anticorrosive affects that Montmorillonite conferred on a PU, containing polypropylene glycol (MW=3000 g mol^{-1}), toluene diisocyanate (TDI) and 1,4-butanediol (BDO) [41]. They found that the thermal stability, char formation, and flame retardance all increased with increasing clay content. Furthermore, Montmorillonite enhanced the anticorrosive properties of the PU. The nanocomposite that exhibited the best clay dispersion, 2 wt% Montmorillonite modified with 4,4'-diaminodiphenylmethane, exhibited an order of magnitude slower corrosion rate (1.09×10^{-5} mm yr^{-1}) than that exhibited by the pure PU (2.62×10^{-4} mm yr^{-1}) [41].

Finnigan et al, a group from Australia evaluated the reinforcement effects of two different clay dispersal techniques (1. solution intercalation and 2. melt intercalation via a twin-screw extruder) in both hard (55 wt% hard segment) and soft (35 wt% hard segment) PUs composed of PTMO (MW=1000 g mol^{-1}), MDI, and BDO [42]. Finnigan et al found that clay dispersion via extrusion was slightly better as shown in Figure 2-10 because during the slow process of solvent evaporation the clay platelets had time to re-aggregate.

However, the high temperatures needed for the melt in twin-screw extrusion caused the Montmorillonite modifying surfactant and polyurethane to react and reduce the molecular weight of the nanocomposite which in turn degraded the material properties of the polyurethane. Interestingly, both dispersal methods increased the material stiffness and decreased the ultimate strength and extensibility of the composite with increasing clay content. The increase in stiffness was greater in the solvent cast films (3.2-fold increase at 7 wt% loading) [42]. The authors believe the Montmorillonite modification surfactant is responsible for the degradation of composite extensibility and strength and are currently investigating this behavior.

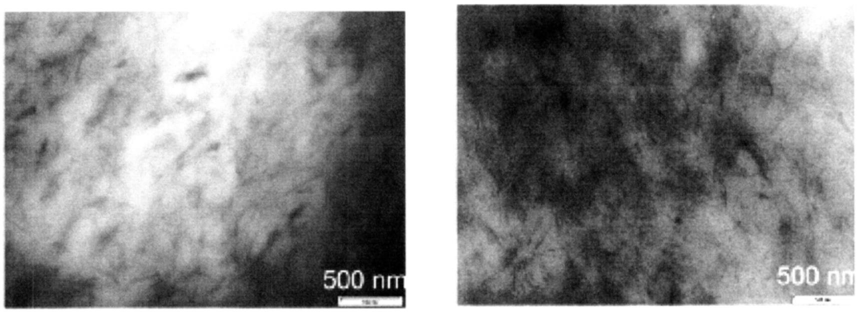

Figure 2-10: Transmission Electron Micrographs of the solvent cast (left) and melt compounded (right) soft polyurethane nanocomposites containing 3 wt% Montmorillonite depicted in [42].

In 2005, Finnigan et al utilized the same TPU with to evaluate the influence of silicate length-scale on the microphase morphology and mechanical. The TPU was filled with a single weight fraction (3 wt%) of clay (Somasif MEE, a synthetic fluoromica), but of different characteristic length: 30, 75, 200 and 650 nm. The authors show that the aspect ratio of the silicates modifies the mechanical behavior, as duplicated in Figure 2-11, but does not change the phase morphology [43]. In 2006, Finnigan et al evaluated the influence of this same filler at its smallest and largest aspect ratio on the mechanical properties and morphology of polyurethanes containing poly(hexamethylene oxide) soft segments of increasing molecular weight [44]. They found that the particle size did not affect the microphase morphology in the system either. However, the enhancement in modulus provided by the filler was greatest in the least phase-separated system. In contrast, when the smaller nano-clay was added to the polyurethane containing poly(tetramethylene oxide) soft segments, a dramatic upturn in the stress-strain curve combined with increased tensile strength resulted. This indicated that the soft segment formed secondary bonds with the filler and improved stress transfer by reducing molecular slippage [43, 44].

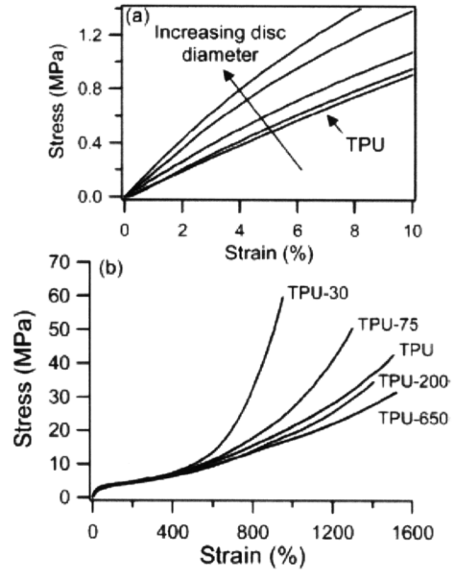

Figure 2-11: Stress-strain response of a polyurethane filled with the same concentration of synthetic fluoromica (3 wt%) but of different aspect ratio [43].

Extending their previous work, which evaluated the influence of length scale of filler on the microphase behavior and the mechanical response to failure in tension, Finnigan et al completed a more thorough analysis of the tensile mechanical behavior of these composites in the PTMO based polyurethane [45]. At strains less than 100%, as platelet size increased the relaxation rate, hysteresis, and permanent set of the composite increased.

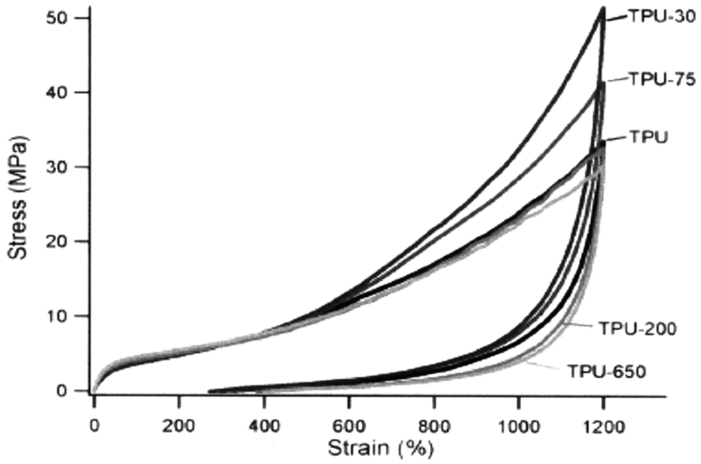

Figure 2-12: Hysteresis exhibited by a polyurethane filled with the same concentration of synthetic fluoromica (3 wt%) but of different aspect ratio [43].

However, at large strains the hysteresis became less sensitive to platelet size, while set became more sensitive as shown if Figure 2-12. This is likely due to chain slippage at the filler interface and void formation. In contrast, the smallest filler (~30 nm) reduced the permanent set, indicating that favorable interfacial interactions limited slip [45]. Also, at large strains, the slowest relaxation time of the composite (which is affiliated with hard segment rich structures) decreased when large filler particles were included.

Mishra, Kim, and Ha from Korea have used the same modified Montmorillonite (Cloisite 30B) that Finnigan et al used in their initial study in melt intercalated and compression molded nanocomposites containing low-density polyethylene and millable polyurethane [46]. In contrast to the work of Finnigan et al, they found that with increasing clay content both the stiffness and strength of the composite increased, albeit minimally, while the extensibility decreased slightly.

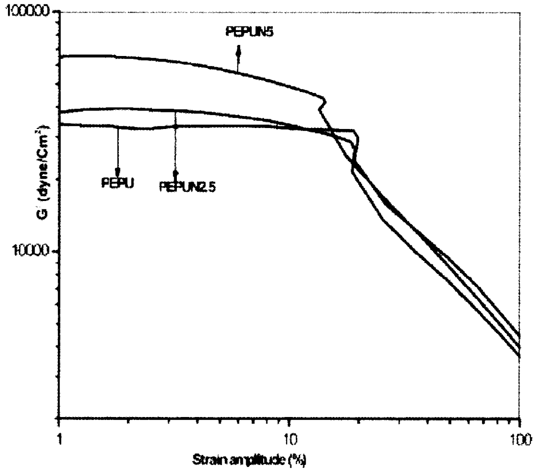

Figure 2-13: Storage modulus versus strain amplitude curves of the polyethylene-polyurethane (PEPU) nanocomposites containing 0, 2.5, and 5 wt% clay depicted in [46].

The heat shrinkability—the ability of a previously stretched, but currently unstrained, nanocomposite to reduce its length when heated—decreased with increasing filler content. Melt rheology showed that this reduction is because the Montmorillonite disturbs and deforms the entanglement network, decreasing the extent of the linear viscoelastic deformation region of the nanocomposite material as shown in Figure 2-13 [46].

Cao and Jana evaluated the influence of 1, 3 and 5 wt% of this same clay, Montmorillonite (Cloisite 30B), on the shape memory behavior of a custom synthesized polyurethane, containing polycaprolactone [47]. The melting transition of crystalline polycaprolactone was utilized as the shape memory transition trigger. At a 1 wt% loading the clay is exfoliated, but at higher concentrations the clay is intercalated. Consequently, at the 1 wt% loading, the increase in recovery stress (when strain is fixed) is 20% greater than that of the pure polyurethane as displayed in Figure 2-14. This increase in recovery stress is also greater than that exhibited by the other composites because the greater the clay loading, the greater the disruption of the hard domains and soft segment crystallinity. This disruption increases the rate of stress relaxation that the resultant composite undergoes, minimizing the achievable recovery stress.

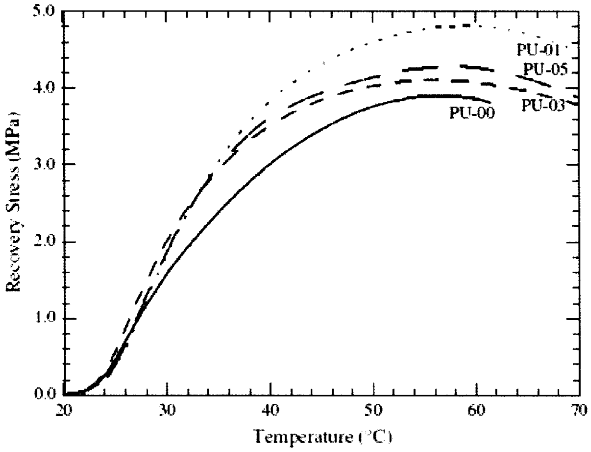

Figure 2-14: The recovery stress of the shape memory polyurethane with 0, 1, 3 and 5 wt% clay at a fixed strain of 100% while a 4°C min^{-1} heating rate is applied [47].

A majority of the polyurethane/clay nanocomposite studies published in the past ten years used solution or melt, reactive or non-reactive in situ polymerization to prepare the nanocomposites. Recently, Dan and co-workers evaluated the influence of two solvents, dimethylacetamide and tetrahydrofuran, on the resultant dispersal of 5 wt% Montmorillonite with different organic modifications (Cloisite 30B, 25A, 15A, and pristine) in polyether and polyester-based thermoplastic polyurethanes [48]. Cloisite 30B was best dispersed with dimethylacetamide, while tetrahydrofuran was the better solvent for Cloisite 15A. However, while the solvent-clay interactions are important, they are secondary when there are strong interactions between the polymer and clay. Furthermore, FTIR analysis indicates that the type of solvent as well as the polymer-clay and solvent-clay interactions play a role in the resultant phase-behavior and morphology [48].

Meng et al evaluated the roles of molecular diffusion and shear in the exfoliation process when polyurethane and organically modified Montmorillonite (Cloisite 30B) are melt-mixed [49].

While molecular diffusion plays a role initially, during the first minute of mixing, the slippage of plates due to applied shear accounts for particle exfoliation. At least three minutes of mixing is necessary to maximize separation minimize the number average length of the platelets dispersed within the composite. Prolonged mixing exposes the polyurethane matrix to the organic modifier at high temperature and leads to degradation and deterioration of the mechanical properties [49].

Tan and Nie evaluated the dispersion of montmorillonite in polyurethane urea when three different photo-polymerizable ammonium surfactants containing reactive methacrylate groups were utilized [50]. The spacing between platelet faces (*d*-spacing) increased with the length of the polymerizable surfactant. While the presence of well-dispersed silicates can form a tortuous path decreasing water permeation, the composites are still susceptible to water sorption. Tan and Nie found that the addition of the long alkyl, hydrophobic surfactant acted as a barrier to water sorption, decreasing the content uptake from 3.4% for the unmodified montmorillonite to 0.77% for the longest surfactant [50].

Rhoney et al evaluated the dispersion and reinforcement effects of nanocomposites when the various fillers, i.e. reactive Montmorillonite, non-reactive Montmorillonite, and large silicon nitride particles, were first mixed in the polyol via different agitation methods prior to in situ polymerization [51]. The mixing methods included (i) sonication with stirring at 300 rpm, (ii) high-speed mixing at 5,000 rpm, and (iii) high-shear mixing at 24,000 rpm. Steady shear rheology showed that only the Montmorillonite/polyol solutions mixed via sonication evidenced a yield stress at low shear rates and shear thinning at high shear rates, behavior that is indicative of well dispersed clay platelets [52]. From wide angle x-ray diffraction (WAXD) spectra the authors determined that the Montmorillonite with the reactive modification was well exfoliated while the non-reactive clay was aggregated. Interestingly, at 3 wt% clay loading, the reactive clay exhibited a 30% increase in storage modulus below the soft segment T_g and a 55% increase in storage modulus above the T_g when compared to the unfilled PU. Conversely, the non-reactive clay exhibited a 50% increase in storage modulus below the soft segment T_g and a 30% increase in storage modulus above the T_g [51]. The high-shear mixed nanocomposite exhibited dynamic mechanical behavior similar to the sonicated samples below the T_g but reduced moduli above the T_g, indicating that the filler was not interacting with the PU.

Song and Yao published an interesting article in 2004 in which they examined the evolution of the basal plane spacing of the clay or *d*-spacing in elastomeric polyurethane (containing polypropylene glycol, methylene biscyclohexyl isocyanate, and BDO) nanocomposites via WAXD during increasing cyclic mechanical deformations [53]. The authors found that the *d*-spacing, the distance between the basal planes of clay platelets, increased during deformation, but recovered to the original spacing upon release of the stretching force when the extent of deformation was within the elastic range (up to 100% strain). From the original state to ~200% strain the *d*-spacing of a 5 wt% filled nanocomposite increased from ~3.7 nm to ~4.4 nm. Yet, at strains greater than 200% the clay spacing exhibited less than a 0.2 nm increase as shown in Figure 2-15 [53].

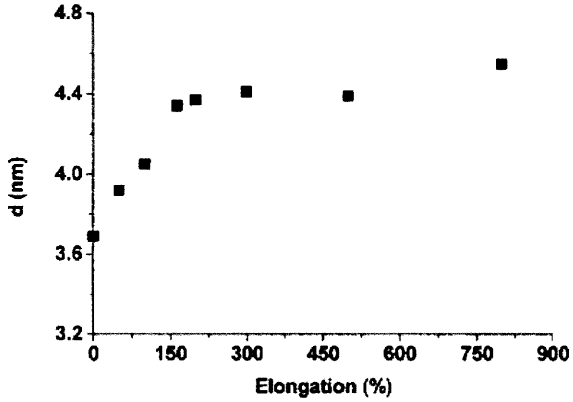

Figure 2-15: Evolution of *d*-spacing with respect to a nanocomposite loaded with 5 wt% clay during stretching [53].

The authors also evaluated the fatigue life of the nanocomposites. At 3 wt% clay loading the fatigue life increased from 55,160 cycles for the pure PU to 821,352 cycles [53]. The authors speculate that the clay intercalated between silicates forms a nano-spring and believes this type of material could extend the useful life of tires.

In a later publication pertaining to the same nanocomposite system, Song et al analyzed the morphology of the nanocomposites when the hard segment content was varied using small angle x-ray scattering and atomic force microscopy (AFM) [14]. The nanocomposites evaluated contained 18, 26, and 36 wt% hard segment. They found that the inter-domain repeat distance increased with hard segment content but decreased with increased clay content. Furthermore, the hard domain size increased with hard segment content and decreased minimally with increasing clay content. The change in hard segment size was minimal because in this PU system the clay interacts primarily with the soft, polyol segments and has little affect on hard segment formation. AFM phase images showed that the hard domains formed spherical aggregates in the PU and the aggregate size decreased from ~800 nm to ~500 nm upon the addition of clay as shown in Figure 2-16 [14].

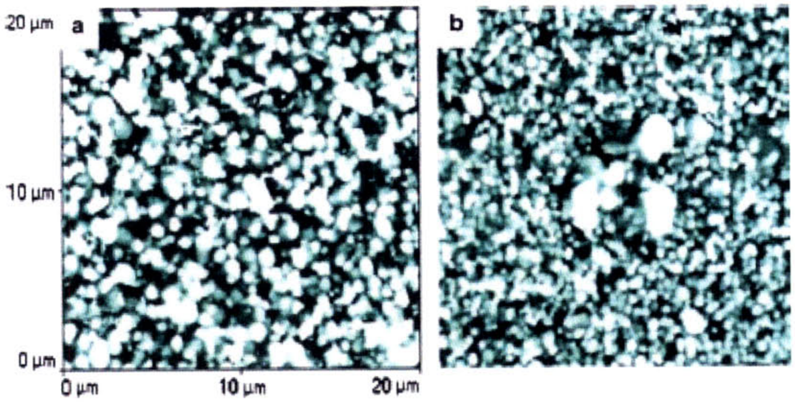

Figure 2-16: Tapping mode AFM phase images of (a) pure polyurethane containing 36 wt% hard segment and (b) the same polyurethane loaded with 1 wt% clay in [14]. The small spherical aggregates are hard domains and the large masses shown in (b) are clay tactoids.

Xia et al also evaluated the relaxation behavior of pure polyurethane of various hard segment content (16, 26, 36, and 46 wt%) and that of the pure polyurethane with 26 wt% hard segment and 1, 3 and 5 wt% modified Montmorillonite (Cloisite 20A) [54]. In contrast to the results of Finnigan et al, they found that the addition of clay encouraged phase separation and the hard domains decreased in size. As the hard segment content increased the polyurethane characteristic relaxation time decreased. However, the addition of clay, like Finnigan et al reported, too increased the relaxation time. As the applied strain increased to values above 100%, multiple relaxation mechanisms became apparent. Xia et al correlate these peaks in the relaxation spectrum to interconnected hard domain break-up, soft segment chain pullout from hard domains, and disentanglement of the chains within the soft segments [54].

Rahman et al prepared numerous waterborne polyurethane/montmorillonite (Cloisite 15A) nanocomposites with three different concentrations of 2,2-dimethylol propionic acid (DMPA): 3.75, 5.41, and 6.17 wt% [55]. They found that as the concentration of DMPA increased, and the hydrophilic nature of the pre-polymer increased, the mean particle size decreased. However, for each DMPA concentration there was a corresponding optimum clay concentration which provided the largest enhancement in tensile strength, elastic modulus, and adhesive strength: 0.5, 1, and 2 wt% respectively [55]. Surprisingly, these clay concentrations did not correlate to the smallest mean particle size.

Because polyurethane foams are the most demanded of all polymeric foams [56], Cao and colleagues investigated the affects of adding Montmorillonite to two polyurethane foams, one more rigid than the other [57]. When clay was added, it acted as nucleation sites for cell formation, creating more small cells than that formed in pure PU foams. The inclusion of clay increased the soft segment T_g of the flexible foam and decreased the soft segment T_g of the rigid foam [57]. Similarly, the clay increased the reduced (normalized with respect to density) compressive strength (780%) and reduced modulus (650%) of the flexible foam and decreased the reduced compressive strength (760%) and reduced modulus (610%) of the rigid foam. Ultimately, there appears to be a competition between the clay induced reinforcement and enhanced foam morphology and the disruption of the PU hydrogen bonding and network structure [57].

In 2005, Song et al investigated how the addition of Montmorillonite in conjunction with melamine polyphosphate powder affects the flame retardance and mechanical properties of the PU [58]. Although the clay was intercalated the tensile strength increased from 1.53 MPa to 3.85 MPa when 5 wt% clay was added with 6 wt% melamine polyphosphate [58]. Thermogravimetric analysis on this same nanocomposite showed that the mass loss rate, the CO and CO_2 release amount, specific extinction area, and the heat release rate all decreased significantly, increasing the material flame retardance. The authors speculate that the flammability is retarded because the carbonaceous-silicious-phosphorated char layers coat the materials protecting the interior polymer.

Recently, Rajendran and co-workers evaluated the release of Bifenthrin I, a termiticide, encapsulated in a polyurethane containing 0, 0.5, and 5 wt% commercial Bentonite (an impure clay composed primarily of Montmorillonite) [59]. Unless the polyurethane is subjected to a solvent that reacts with the matrix polymer and significantly swells the polyurethane, the Bifenthrin persists. Although, Bifenthrin has a high affinity for silicates and should bind to the platelets, the diffusion coefficients in the clay filled systems were faster than that of the pure polyurethane, indicating either the presence of cavities or organic carbon that results in inadequate binding [59].

In most of the work published in the past ten years, Montmorillonite was the filler of choice; however, clays other than Montmorillonite have been investigated as polyurethane fillers. Table 3.2 lists and compares the empirical formulae, the size, and the *d*-spacings of clays investigated for polyurethane reinforcement. Large aspect-ratio clays are often used and considered desirable because they can efficiently enhance the stiffness at small volume fractions due to their high surface area-to-volume ratios [60]. However, the probability that the platelets shield the matrix from straining and negatively affect load transfer is greater when the aspect ratio of the clays is large [60]. Ultimately, the aspect ratio of the clay, the interactions between the polyurethane and clay, and the resultant dispersal all influence the mechanical enhancement.

Clay	**Empirical Formula**	**Lateral dimension, *D* [nm]**	**Thickness, *t* [nm]**	***d*-spacing [nm]**
Hectorite	$Na_{0.3}Mg_{2.7}Li_{0.3}Si_4O_{10}(OH)_2$	600	1	1.53
Laponite	$Na^{+0.7}[(Si_8Mg_{5.5}Li_{0.3})O_{20}(OH)_4]^{-0.7}$	25	1	1.28
Montmorillonite	$Na_{0.2}Ca_{0.1}Al_2Si_4O_{10}(OH)_2{\cdot}10H_2O$	70-218	1	1.50
Rectorite	$Na_{0.6}Ca_{0.3}K_{0.1}Al_6Si_6O_{20}(OH)_4{\cdot}2H_2O$	200-300	1	2.22
Saponite	$Na_{0.1}Ca_{0.1}Mg_{2.25}Fe^{2+}{}_{0.75}Si_3AlO_{10}(OH)_2{\cdot}4H_2O$	165	1	1.23
Sepiolite	$(Si_{12}Mg_8O_{30})(OH)_4(OH_2)_4{\cdot}8H_2O$	25	20-1500	1.03

Table 2-3: List and comparison of the various clays investigated for polyurethane reinforcement [19, 61-64].

In 1999, Zilg et al evaluated the reinforcement capabilities of synthetic fluoromica (Hectorite) [65]. They found that the particles modified with bis(hydroxyethyl)-methyl-dodecylammonium chloride negatively influenced the Young's modulus of the nanocomposites while the unmodified fillers increased the modulus. From these results the authors inferred that the delaminated platelets were soft when compared to the original stacked platelets and did not enhance the nanocomposite stiffness [65]. However, in 2004 Varghese et al effectively reinforced polyurethane rubber (PUR) latex and PUR/natural rubber latex blends with the same unmodified Hectorite [66]. In the PUR, specifically, the inclusion of the Hectorite increased the storage modulus by 1200-1500 MPa at temperatures below the soft segment glass transition temperature ($T_g = 10°C$). Furthermore, the modulus of the PUR at 100% elongation had a 7-fold increase and at 300% elongation over a 9-fold increase when the material was filled with 10 wt% Hectorite [66].

In 2004, Ma and colleagues evaluated the reinforcement properties of Rectorite and Montmorillonite when they were ion-exchanged with three different quaternary ammonium salts and then melt intercalated in a different PUR [62]. Ma et al found that the Rectorite was as effective a filler as Montmorillonite, but that the key to successful reinforcement is choosing the right quaternary ammonium salt for ion exchange [62].

Saponite was used to reinforce a waterborne PU. When the nanocomposite was loaded with 4 wt% Saponite, the Young's modulus increased from 55.7 MPa to 126.1 MPa, the strength increased from 3.9 MPa to 7.6 MPa, the extension increased from 27.7% to 57.2%, and the wear loss was one-third that of the pure PU [67].

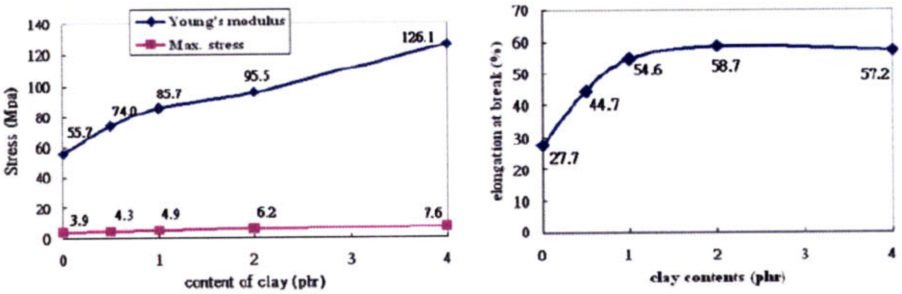

Figure 2-17: Mechanical properties of the waterborne PU filled with various weight concentrations of Saponite as shown in [68].

More recently, modified sepiolite, a fibrous or tunnel-like silicate, was dispersed within polyurethane at concentrations of 1, 3 and 5 wt% as shown in Figure 2-17 [64]. As the concentration of sepiolite increased, the tensile strength, modulus and extensibility increased, indicating strong interactions and stress transfer between the matrix and filler. The addition of sepiolite also increases the thermal stability. This increases the onset temperature of thermal degradation but also acts as an insulator and retards volatile product generation [64]. Ultimately, any clay can be as effective a reinforcing agent as Montmorillonite, if the appropriate swelling agent or ammonium salt is utilized for ion exchange and the silicates are well-dispersed.

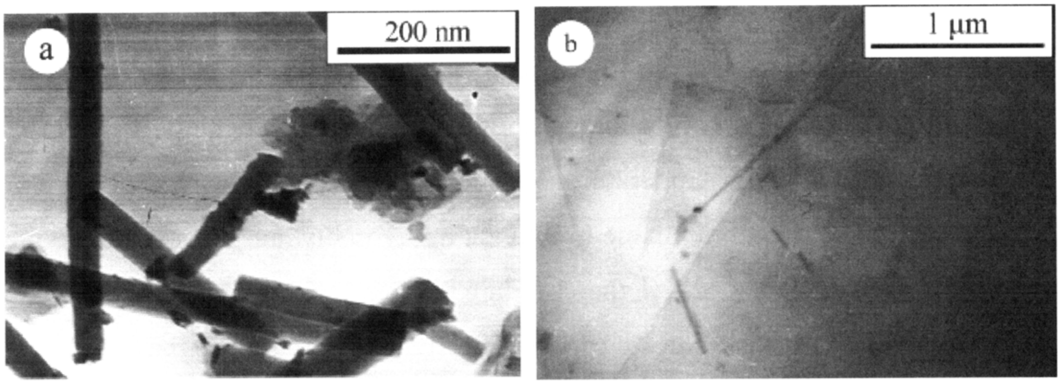

Figure 2-18: Transmission electron micrographs of sepiolite (a) and 3 wt% sepiolite in polyurethane (b) [64].

2.5 Summary

Over the past ten years researchers have investigated numerous polyurethane systems, clay fillers, chemical modifiers of clay, dispersal techniques, and nanocomposite synthesis procedures. In general, the previous research suggests that the addition of clay most effectively stiffens soft polyurethanes rather than hard polyurethanes. This is because the hard domains and soft segment crystallinity are responsible for polyurethane stiffness. When clay is added to a soft polyurethane, the rigidity of the polymer is enhanced, but when added to a hard polyurethane, the previously established hard domain network is disrupted and the rigidity compromised [12]. The resultant strength and extensibility of a polyurethane nanocomposite increases when the clay is well dispersed and the clay, the chemical modification, and the polyurethane all interact favorably. However, if the clay induces crystallinity in the soft segment, the strength and extensibility are degraded [31, 38, 69]. Furthermore, the water vapor permeability of the nanocomposites decreases with increasing clay concentration and better clay dispersal [36, 39]. The oxygen permeability, however, decreases only if the polyurethane adheres to the clay platelets [39]. These investigations show that typically the soft segment glass transition temperature is unaffected by the addition of clay while the thermomechanical and thermal degradation behavior is inconsistent and depends heavily upon the interactions between the clay, chemical modification, and polyurethane. Furthermore, the greatest thermomechanical, thermal, and barrier enhancements are exhibited in the nanocomposites with the best clay dispersal [60].

These publications also suggest that the reinforcement capability of the clay depends primarily upon the dispersal of the clay and that the type of clay is of lesser importance [65-67]. The clay dispersal tends to be best in soft polyurethanes, those containing less than 50 wt% hard segment, because it is more difficult for the rigid hard segments to diffuse between silicates [33]. While the melt processing-based dispersal technique may be more environmentally friendly than using a common solvent, the high temperatures needed for the melt can cause the chemical modification of the clay and polyurethane to interact unfavorably and deteriorate the mechanical properties of the polyurethane [42]. If the common solvent technique is used, the clay is best dispersed when the solution is sonicated [51]. Unfortunately, in all of these publications the intercalation of the large aspect-ratio clays investigated has persisted and the maximum thermomechanical, thermal, and barrier enhancements have been exhibited at small clay weight concentrations.

Ultimately, in order to develop a polyurethane/clay nanocomposite that exhibits a large increase in stiffness and strength, good dispersal of clay is necessary. To avoid possible deleterious interactions between clay chemical-modification and polyurethane, a dispersal technique that does not rely upon the chemical modification of the clay is needed. Furthermore, the reinforcement capabilities of smaller aspect–ratio clay need to be evaluated. Small aspect-ratio clays may be more easily dispersed and the thermomechanical enhancements could prove interesting since smaller aspect-ratio clay is less likely to shield the polyurethane from straining [60].

2.6 References

[1] F. Vollrath and D. P. Knight, "Liquid crystalline spinning of spider silk," *Nature*, vol. 410, pp. 541-548, 2001.
[2] J. M. Gosline, P. A. Guerette, C. S. Ortlepp, and K. N. Savage, "The mechanical design of spider silks: From fibroin sequence to mechanical function," *Journal of Experimental Biology*, vol. 202, pp. 3295-3303, 1999.
[3] M. Xu and R. V. Lewis, "Structure of a Protein Superfiber - Spider Dragline Silk," *Proceedings of the National Academy of Sciences of the United States of America*, vol. 87, pp. 7120-7124, 1990.
[4] D. T. Grubb and L. W. Jelinski, "Fiber morphology of spider silk: The effects of tensile deformation," *Macromolecules*, vol. 30, pp. 2860-2867, 1997.
[5] L. W. Jelinski, "Establishing the relationship between structure and mechanical function in silks," *Current Opinion in Solid State & Materials Science*, vol. 3, pp. 237-245, 1998.
[6] C. Y. Hayashi, N. H. Shipley, and R. V. Lewis, "Hypotheses that correlate the sequence, structure, and mechanical properties of spider silk proteins," *International Journal of Biological Macromolecules*, vol. 24, pp. 271-275, 1999.

[7] J. P. O'Brien, S. R. Fahnestock, Y. Termonia, and K. C. H. Gardner, "Nylons from nature: Synthetic analogs to spider silk," *Advanced Materials*, vol. 10, pp. 1185-+, 1998.
[8] Y. Yang, X. Chen, Z. Z. Shao, P. Zhou, D. Porter, D. P. Knight, and F. Vollrath, "Toughness of spider silk at high and low temperatures," *Advanced Materials*, vol. 17, pp. 84-88, 2005.
[9] D. Randall and S. Lee, "The Polyurethanes Book," 2nd ed. New York: Huntsman International, 2002, pp. 477.
[10] T. Thomson, *Polyurethanes as Specialty Chemicals: Principles and Applications*. Boca Raton, Florida: CRC Press, 2005.
[11] M. Michalovic, "The Macrogalleria: A Cyberwonderland of Polymer Fun," 1995.
[12] M. Szycher, *Szycher's Handbook of Polyurethanes*. Boca Raton, Florida: CRC Press, 1999.
[13] R. J. Young and P. A. Lovell, *Introduction to Polymers*. Cheltenham, U.K.: Nelson Thornes Ltd., 1991.
[14] M. Song, H. S. Xia, K. J. Yao, and D. J. Hourston, "A study on phase morphology and surface properties of polyurethane/organoclay nanocomposite," *European Polymer Journal*, vol. 41, pp. 259-266, 2005.
[15] C. D. Eisenbach, A. Ribbe, and C. Gunter, "Morphological-Studies Of Model Polyurethane Elastomers By Element-Specific Electron-Microscopy," *Macromolecular Rapid Communications*, vol. 15, pp. 395-403, 1994.
[16] D. J. Martin, G. F. Meijs, P. A. Gunatillake, S. P. Yozghatlian, and G. M. Renwick, "The influence of composition ratio on the morphology of biomedical polyurethanes," *Journal of Applied Polymer Science*, vol. 71, pp. 937-952, 1999.
[17] P. C. LeBaron, Z. Wang, and T. J. Pinnavaia, "Polymer-layered silicate nanocomposites: an overview," *Applied Clay Science*, vol. 15, pp. 11-29, 1999.
[18] J. DeGaspari, "Prospecting Paydirt," in *Mechanical Engineering Magazine*, vol. April, April 2001.
[19] K. Yano, A. Usuki, and A. Okada, "Synthesis and Properties of Polyimide-Clay Hybrid Films," *Journal of Polymer Science Part A-Polymer Chemistry*, vol. 35, pp. 2289-2294, 1997.
[20] T. Lan and T. J. Pinnavaia, "Clay-Reinforced Epoxy Nanocomposites," *Chemistry Of Materials*, vol. 6, pp. 2216-2219, 1994.
[21] S. S. Ray and M. Okamoto, "Polymer/layered silicate nanocomposites: a review from preparation to processing," *Progress in Polymer Science*, vol. 28, pp. 1539-1641, 2003.
[22] Y. S. Lu and R. C. Larock, "Bio-based nanocomposites from corn oil and functionalized organoclay prepared by cationic polymerization," *Macromolecular Materials And Engineering*, vol. 292, pp. 863-872, 2007.
[23] E. P. Giannelis, "Polymer layered silicate nanocomposites," *Advanced Materials*, vol. 8, pp. 29-35, 1996.
[24] C. M. Koo, H. T. Ham, S. O. Kim, K. H. Wang, I. J. Chung, D. C. Kim, and W. C. Zin, "Morphology evolution and anisotropic phase formation of the maleated polyethylene-layered silicate nanocomposites," *Macromolecules*, vol. 35, pp. 5116-5122, 2002.
[25] Rockwood Specialties Inc., "Nanoclay.com."
[26] Y. Termonia, "Molecular Modeling of Spider Silk Elasticity," *Macromolecules*, vol. 27, pp. 7378-7381, 1994.
[27] T. B. Murphy and A. F. Sawyer, "Advancement of natural and synthetic clays in personal

care applications," 2004.
[28] Z. Wang and T. Pinnavaia, "Nanolayer Reinforcement of Elastomeric Polyurethane," *Chemistry of Materials*, vol. 10, pp. 3769-3771, 1998.
[29] K. J. Yao, M. Song, D. J. Hourston, and D. Z. Luo, "Polymer/layered clay nanocomposites: 2 polyurethane nanocomposites," *Polymer*, vol. 43, pp. 1017-1020, 2002.
[30] T. K. Chen, Y. I. Tien, and K. H. Wei, "Synthesis and characterization of novel segmented polyurethane clay nanocomposite via poly(epsilon-caprolactone)/clay," *Journal of Polymer Science Part a-Polymer Chemistry*, vol. 37, pp. 2225-2233, 1999.
[31] S. Y. Moon, J. K. Kim, C. Nah, and Y. S. Lee, "Polyurethane/montmorillonite nanocomposites prepared from crystalline polyols, using 1,4-butanediol and organoclay hybrid as chain extenders," *European Polymer Journal*, vol. 40, pp. 1615-1621, 2004.
[32] T. K. Chen, Y. I. Tien, and K. H. Wei, "Synthesis and characterization of novel segmented polyurethane/clay nanocomposites," *Polymer*, vol. 41, pp. 1345-1353, 2000.
[33] Y. I. Tien and K. H. Wei, "Hydrogen bonding and mechanical properties in segmented montmorillonite/polyurethane nanocomposites of different hard segment ratios," *Polymer*, vol. 42, pp. 3213-3221, 2001.
[34] Y. I. Tien and K. H. Wei, "High-Tensile-Property Layered Silicates/Polyurethane Nanocomposites by Using Reactive Silicates as Pseudo Chain Extenders," *Macromolecules*, vol. 34, pp. 9045-9052, 2001.
[35] Y. I. Tien and K. H. Wei, "The Effect of Nano-Sized Silicate Layers from Montmorillonite on Glass Transition, Dynamic Mechanical and Thermal Degradation Properties of Segmented Polyurethane," *Journal of Applied Polymer Science*, vol. 86, pp. 1741-1748, 2002.
[36] R. Xu, M. Evangelos, A. J. Snyder, and J. Runt, "New Biomedical Poly(urethane urea)--Layered Silicate Nanocomposites," *Macromolecules*, vol. 34, pp. 337-339, 2001.
[37] R. J. Xu, E. Manias, A. J. Snyder, and J. Runt, "Low penneability biomedical polyurethane nanocomposites," *Journal Of Biomedical Materials Research Part A*, vol. 64A, pp. 114-119, 2003.
[38] M. Tortora, G. Gorrasi, V. Vittoria, G. Galli, S. Ritrovati, and E. Chiellini, "Structural characterization and transport properties of organically modified montmorillonite/polyurethane nanocomposites," *Polymer*, vol. 43, pp. 6147-6157, 2002.
[39] M. A. Osman, V. Mittal, M. Morbidelli, and U. W. Suter, "Polyurethane adhesive nanocomposites as gas permeation barrier," *Macromolecules*, vol. 36, pp. 9851-9858, 2003.
[40] X. J. Wang, J. J. Kang, Y. P. Wu, and S. B. Fang, "Novel composite polymer electrolytes based on poly(ether-urethane) network polymer and modified montmorillonite," *Electrochemistry Communications*, vol. 5, pp. 1025-1029, 2003.
[41] Y. W. Chen-Yang, H. C. Yang, G. J. Li, and Y. K. Li, "Thermal and anticorrosive properties of polyurethane/clay nanocomposites," *Journal Of Polymer Research*, vol. 11, pp. 275-283, 2004.
[42] B. Finnigan, D. Martin, P. Halley, R. Truss, and K. Campbell, "Morphology and properties of thermoplastic polyurethane nanocomposites incorporating hydrophilic layered silicates," *Polymer*, vol. 45, pp. 2249-2260, 2004.
[43] B. Finnigan, K. Jack, K. Campbell, P. Halley, R. Truss, P. Casey, D. Cookson, S. King, and D. Martin, "Segmented polyurethane nanocomposites: Impact of controlled particle

size nanofillers on the morphological response to uniaxial deformation," *Macromolecules*, vol. 38, pp. 7386-7396, 2005.

[44] B. Finnigan, P. Halley, K. Jack, A. McDowell, R. Truss, P. Casey, R. Knott, and D. Martin, "Effect of the average soft-segment length on the morphology and properties of segmented polyurethane nanocomposites," *Journal of Applied Polymer Science*, vol. 102, pp. 128-139, 2006.

[45] B. Finnigan, P. Casey, D. Cookson, P. Halley, K. Jack, R. Truss, and D. Martin, "Impact of controlled particle size nanofillers on the mechanical properties of segmented polyurethane nanocomposites," *International Journal Of Nanotechnology*, vol. 4, pp. 496-515, 2007.

[46] J. K. Mishra, I. Kim, and C. S. Ha, "Heat shrinkable behavior and mechanical response of a low-density polyethylene/millable polyurethane/organoclay ternary nanocomposite," *Macromolecular Rapid Communications*, vol. 25, pp. 1851-1855, 2004.

[47] F. Cao and S. C. Jana, "Nanoclay-tethered shape memory polyurethane nanocomposites," *Polymer*, vol. 48, pp. 3790-3800, 2007.

[48] C. H. Dan, Y. D. Kim, M. H. Lee, B. H. Min, and J. H. Kim, "Effect of solvent on the properties of thermoplastic polyurethane/clay nanocomposites prepared by solution mixing," *Journal Of Applied Polymer Science*, vol. 108, pp. 2128-2138, 2008.

[49] X. Y. Meng, X. H. Du, Z. Wang, W. G. Bi, and T. Tang, "The investigation of exfoliation process of organic modified montmorillonite in thermoplastic polyurethane with different molecular weights," *Composites Science And Technology*, vol. 68, pp. 1815-1821, 2008.

[50] H. L. Tan and J. Nie, "Photopolymerization and characteristics of polyurethane/organoclay nanocomposites," *Macromolecular Reaction Engineering*, vol. 1, pp. 384-390, 2007.

[51] I. Rhoney, S. Brown, N. E. Hudson, and R. A. Pethrick, "Influence of processing method on the exfoliation process for organically modified clay systems. I. Polyurethanes," *Journal of Applied Polymer Science*, vol. 91, pp. 1335-1343, 2004.

[52] R. Krishnamoorti and R. A. Vaia, "Polymer Nanocomposites: Synthesis, Characterization, and Modeling," 1st ed. Washington, D.C.: Oxford University Press, 2002, pp. 242.

[53] M. Song and K. J. Yao, "X-ray diffraction detection of compliance in polyurethane-organoclay nanocomposites," *Materials Science And Technology*, vol. 20, pp. 989-992, 2004.

[54] H. S. Xia and M. Song, "Intercalation and exfoliation behaviour of clay layers in branched polyol and polyurethane/clay nanocomposites," *Polymer International*, vol. 55, pp. 229-235, 2006.

[55] M. M. Rahman, J. H. Kim, and H. D. Kim, "Characterization of waterborne polyurethane/clay nanocomposite adhesives containing different amounts of ionic groups," *Journal Of Adhesion Science And Technology*, vol. 21, pp. 1575-1588, 2007.

[56] K. C. Khemani, "Polymeric Foams: Science and Technology," 1st ed. Washington, D.C.: American Chemical Society, 1997, pp. 236.

[57] X. Cao, L. J. Lee, T. Widya, and C. Macosko, "Polyurethane/clay nanocomposites foams: processing, structure and properties," *Polymer*, vol. 46, pp. 775-783, 2005.

[58] L. Song, Y. Hu, Y. Tang, R. Zhang, Z. Y. Chen, and W. C. Fan, "Study on the properties of flame retardant polyurethane/organoclay nanocomposite," *Polymer Degradation And Stability*, vol. 87, pp. 111-116, 2005.

[59] S. Rajendran, R. G. Gilbert, B. Cribb, R. Truss, B. Noller, A. Stewart, and M. Zalucki, "Effect of inert fillers on diffusion and controlled release of penetrant in polymer matrices," *Journal Of Applied Polymer Science*, vol. 108, pp. 3593-3600, 2008.

[60] N. Sheng, M. C. Boyce, D. M. Parks, G. C. Rutledge, J. I. Abes, and R. E. Cohen, "Multiscale micromechanical modeling of polymer/clay nanocomposites and the effective clay particle," *Polymer*, vol. 45, pp. 487-506, 2004.

[61] D. Barthelmy, "Mineralogy Database," 2004.

[62] X. Y. Ma, H. J. Lu, G. Z. Liang, and H. X. Yan, "Rectorite/thermoplastic polyurethane nanocomposites: Preparation, characterization, and properties," *Journal Of Applied Polymer Science*, vol. 93, pp. 608-614, 2004.

[63] C. Zilg, F. Dietsche, B. Hoffmann, C. Dietrich, and R. Mulhaupt, "Nanofillers based upon organophilic layered silicates," *Macromolecular Symposia*, vol. 169, pp. 65-77, 2001.

[64] H. X. Chen, M. S. Zheng, H. Y. Sun, and Q. M. Jia, "Characterization and properties of sepiolite/polyurethane nanocomposites," *Materials Science And Engineering A-Structural Materials Properties Microstructure And Processing*, vol. 445, pp. 725-730, 2007.

[65] C. Zilg, R. Thomann, R. Mulhaupt, and J. Finter, "Polyurethane nanocomposites containing laminated anisotropic nanoparticles derived from organophilic layered silicates," *Advanced Materials*, vol. 11, pp. 49-52, 1999.

[66] S. Varghese, K. G. Gatos, A. A. Apostolov, and J. Karger-Kocsis, "Morphology and mechanical properties of layered silicate reinforced natural and polyurethane rubber blends produced by latex compounding," *Journal Of Applied Polymer Science*, vol. 92, pp. 543-551, 2004.

[67] H. C. Kuan, W. P. Chuang, and C. C. M. Ma, "Synthesis and characterization of a clay/waterborne polyurethane nanocomposite," *Journal Of Materials Science*, vol. 40, pp. 179-185, 2005.

[68] H. C. Kuan, C. C. M. Ma, W. P. Chuang, and H. Y. Su, "Hydrogen bonding, mechanical properties, and surface morphology of clay/waterborne polyurethane nanocomposites," *Journal Of Polymer Science Part B-Polymer Physics*, vol. 43, pp. 1-12, 2005.

[69] A. M. Chen, Y. Tian, B. Han, G. D. Ji, S. S. Wu, and J. Shen, "Synthesis and characterization of polyurethane/montmorillonite nanocomposites," *Acta Polymerica Sinica*, pp. 591-594, 2003.

3. Nanoparticle Dispersal via Solvent Exchange Processing

[Part of this work has been published previously, in slightly different form, in "High Performance Elastomeric Nanocomposites via Solvent Exchange Processing" by S.M. Liff, N. Kumar, and G.H. McKinley, *Nature Materials,* **2007**, 6 (1): 76-83, "Preferential Association of Segment Blocks in Polyurethane Nanocomposites" by L.T.J. Korley, S.M. Liff, P.T. Hammond, and G.H. McKinley, *Macromolecules,* **2006**, 39 (20): 7030-7036, and in "Method to disperse and exfoliate nanoparticles" by N. Kumar, S. M. Liff & G.H. McKinley, U.S. Patent Application 11/253,219 (Filed October 18, 2005).]

3.1. Introduction

High performance biomaterials, such as silk [1-5] and bone [6, 7] exhibit unparalleled combinations of stiffness, strength, extensibility, and toughness by exploiting hierarchical structures in which stiff nanometer-size crystallites are embedded and dispersed in softer protein matrices [1-3, 8]. Polymer nanocomposites which utilize engineering thermoplastics as the matrix material and stiff, inorganic, anisotropic nanoparticles to tailor thermomechanical properties have been the subject of many recent studies [9, 10]. Optimal mechanical enhancement of polymer matrices via nanoreinforcement is expected only when the nanoparticles are fully exfoliated in the polymer matrix. In the present work we outline a novel solvent exchange approach to efficiently exfoliate nanoparticles, particularly synthetic smectic clays, such as Laponite® RD (Southern Clay Products, Inc.) in polymers like commercial thermoplastic polyurethane (TPU) elastomers, specifically Elasthane™ 80A (Polymer Technology Group, Inc.)

3.2 Previous Dispersal Techniques

Polymer nanocomposites have the potential to fulfill many high performance applications which require enhanced mechanical, thermal, electrical, barrier and/or optical properties, as is explained in the two previous Chapters. However, the potential for maximum enhacement occurs when the nanoparticles are fully exfoliated within the polymer matrix. For numerous nanoparticle systems, specifically clay particles, dispersion is a two part process—1) exfoliation of stacked clay particles, and 2) dispersion of the separated particles within the matrix. Incomplete exfoliation and dispersion results in nanocomposites with little or no improvement in the mechanical, thermal, electrical, barrier, and/or optical properties [11-15].

Full exfoliation of nanoparticles, specifically smectic clay particles in polymers is a major challenge. In the dry form, smectic clays exist as agglomerates of stacked platelets tightly bound to each other via strong ionic and van der Waals forces [16]. The current methods to exfoliate nanoparticles in engineering thermoplastics have been only partially successful. Exfoliation in high molecular weight and/or strongly hydrophobic polymers that are insoluble in water has proven to be particularly difficult [17, 18]. Typical methods [19] include (i) compounding and melt extrusion of the polymer melt with unmodified and organically modified clay and (ii) dispersion of organically modified clay in organic solvent followed by in-situ polymerization [20] or dissolution of the matrix polymer followed by solvent casting or precipitation. Organic modification of the particle surface has been found to be necessary to increase the affinity of clay with hydrophobic polymers or organic solvents [21]; however, disadvantages such as premature degradation of the polymer and/or decreased thermomechanical properties have been reported [21]. Even with organic modification, good exfoliation remains a challenge [21-23] as previously reported in Chapter Two and further discussed here.

3.2.1 Dispersion Via Melt and Mixing

Dispersion via melt and mixing describes generally those nanoparticle dispersion techniques that rely upon application of high temperatures and in most cases additional mechanical work input (such as extruding or compounding). The nanoparticles may be chemically modified to promote favorable interactions with the polymer matrix; however, selection of a modifier that does not degrade at the high processing temperatures is critical. This technique is advantageous because it is environmentally friendly; hazardous solvents (which are used in the other methods below) are not needed. Consequently, numerous thermoplastic polymers may be processed in this way with a wide variety of nanoparticles. Significant drawbacks still remain. When the matrix polymer and reinforcing particle do not interact favorably e.g. a polarity mismatch, large quantities of mechanical work are needed to disperse the particles. Not only is this extra work costly, but too much deformation of the polymer may cause cleavage of the polymer chains and an irreversible reduction in the molecular weight, resulting in inferior mechanical properties. Another drawback is that the concentration of nanoparticles is limited to concentrations below or near the percolation threshold. Otherwise, not only does the jammed particle network prevent further particle migration within the matrix, but jamming can cause instruments used to apply deformation, such as a twin-screw extruder, to fail. These jamming concentrations may be quite small (~2 vol%) for large aspect ratio particles.

3.2.2 In-Situ Polymerization

In-situ polymerization as a method to disperse nanoparticles is necessary in many thermoset polymers, but may also be used with thermoplastics. Again, chemical modification of the nanoparticle is not always necessary with this technique, but often helps target the particle placement within the polymer. The nanoparticles with or without modification can be swollen within the monomer. The particles can then be used either as the catalyst, as cross-linking sites or chain extenders, or as reinforcement embedded within the non-cross-linked phase [24, 25]. Meanwhile, polymerization can be induced via heat, radiation, diffusion of a suitable initiator, or catalysis. In-situ polymerization was first successful and demonstrated when Toyota developed Nylon-6 and Montmorillonite composites with enhanced thermal and mechanical properties [26]. While much of the chemistry needed to develop such systems is published, reproducible synthesis of large batches of materials for characterization can be difficult. This is due to inconsistencies that arise during the scale-up of polymerization processes that include nano-filler, e.g. impurities, nucleation sites, and kinetic limitations.

3.2.3 Common Solvent Process

A common solvent that disperses the nanoparticles and in which the polymer or pre-polymer is soluble is the third method often utilized to exfoliate nanoparticles. Chemical modification of the nanoparticles is often necessary in order for the same solvent that solubilizes the matrix polymer to also disperse the particles. The resulting nanocomposites can then be prepared by solvent casting or precipitating out the molecularly-mixed solids and then compression molding or melt compounding the precipitate. Obviously, the limiting factor is determination of a good solvent or chemical modifier that does not have a deleterious impact on the morphology or thermo-physical properties of the matrix polymer. Mackay et al have also shown that it is considerably easier to disperse nanoparticles within linear polymer solutions when the radius of gyration of the polymer is larger than the radius of the nanoparticle because there is an enthalpy gain when more molecular contacts become available [27].

Each of the methods discussed above is not consistently reliable for multiple polymer-nanoparticle pairs, nor are the resulting modifications inexpensive. For example, chemical modification of nanoparticles may result in the early onset of thermal degradation of the polymer. Furthermore, the modifying agent may be incompatible with and alter the matrix polymer morphology. The extra processing steps needed for dispersal and exfoliation, like monomer modification, adds to production costs. Some of these methods are of limited usefulness because of the limited number of solvents that can both dissolve polymers and disperse nanoparticles. As a result, a new method to effectively and uniformly disperse nanoparticles in polymers, and consistently improve the mechanical, thermal, electrical, barrier, and/or optical properties of composites is desirable.

3.3 Solvent Exchange Approach

This new dispersal technique does not rely upon chemical modification, but exploits the affinity of unmodified polar nanoparticles, like Laponite for the polar segments of block copolymers, i.e. the hard micro-domains of polyurethanes, like Elasthane. Laponite powder can be dispersed in many organic, polar solvents due to its hydrophilic character which promotes the separation of clay platelets via osmotic pressure produced by the hydration of intercalated ions [20]. In non-polar solvents, the large energy barrier created by the reduced wettability and the absence of osmotically driven platelet separation prevents direct dispersion of Laponite. A novel solvent exchange method [28] was developed to disperse charged discotic nanoparticles, such as Laponite or Montmorillonite, in organic solvents. This procedure requires the use of two solvents, denoted *A* and *B*, that meet four criteria; (i) solvent *A* must fully disperse the hydrophilic clay, (ii) solvent *B* must dissolve the polymer matrix and not cause re-aggregation of the nano-clay, (iii) solvents *A* and *B* must be fully miscible, and (iv) solvent *B* must have a higher boiling point than solvent *A*. Solvents with high dipole moments and dielectric constants were found to be the most suitable *B* solvents. Once the nanoparticle-solvent pair is prepared, solvent *A* may be removed via evaporation and the desired polymer subsequently dissolved in the nanoparticle-solvent *B* solution. Once the nanoparticle-solvent *B*-polymer solution is prepared the polymer nanocomposites can either be prepared via slow solvent casting or fast precipitation and compression molding.

Solvent *A* may include aqueous or polar solvents or solvent mixtures. A particularly suitable solvent *A* is water, but alcohols and other volatile polar solvents in which the particles are dispersible may be used as well. Other solvent *A* possibilities include methanol, ethanol, chloroform, and ethylene glycol among others [28]. Salts, surfactants, and/or other additives may be utilized to increase the solubility of the particles or optimize another property of the dispersion, e.g. ionic strength, pH, or viscosity. Various salts, including sodium chloride and sodium citrate, may be added to the dispersion to change its ionic strength. Likewise, ionic or non-ionic surfactants may be employed. Alternatively or in addition, acids or bases, such as potassium hydroxide, sodium hydroxide, or sulfuric acid, may be added to the dispersion to change its pH [28]. Low molecular weight polyethylene glycol or polypropylene glycol may also be added and used to modify the viscosity of the nanodispersion.

The concentration of nanoparticles added to form the nanoparticle-solvent *A* solution varies from one system to the next. The particle shape and dispersity are significant factors governing the concentration limit. The theoretical maximum volume fraction achievable for the random packing of monodisperse spherical particles is 0.56 [29]. However, higher concentrations may be achieved when bimodal regularly shaped particles are utilized [30, 31]. More irregularly shaped particles will jam, or form a percolated network at low concentrations, depending on their aspect ratio. The dispersion of the nanoparticles and the ability of the nanoparticles to remain in a stable and non-aggregated state is a result of the surface charge, surface chemistry, and wettability of the nanoparticles, and the ion solvation, dipole moment and dielectric constant of solvent *A* [28]. Chemical modification is not necessary before dispersion of the nanoparticles in solvent *A* but may be utilized, if necessary.

Solvent *B* is a second solvent or solvent mixture that when added to the nanoparticle-solvent *A* solution does not disrupt the nanoparticle dispersion or stability. Solvent *B* may be, but is not limited to, n-methyl pyrrolidinone (NMP), dimethylacetamide (DMAC), dimethylformamide (DMF), dimethylsulfoxide (DMSO), dichlorobenzene, or ethylene glycol. For polyurethane-Laponite composites, dimethylacetamide and dimethylformamide are excellent *B* solvents. In some instances, solvent *B* could be a polymerizable reagent. Consequently, it may be desirable to agitate or heat the dispersion as solvent *B* is added. Solvent *B* may be added to solvent *A* in practically any ratio, as long as when solvent *A* is removed the resultant concentration of nanoparticles in solvent *B* does not result in sample gelation—as a consequence the matrix polymer will not dissolve without thermal energy or mechanical work.

3.3.1 Method to Disperse Laponite in Thermoplastic Polyurethanes

In advance of preparing the polyurethane-Laponite thin-film nanocomposites, the Laponite had to be completely dispersed and the agglomerated platelet stacks delaminated without chemical modification. This is done by hydrating the Laponite with deionized water at concentrations less than 1 wt% Laponite: at larger concentrations the solution forms a gel. However, the matrix polyurethanes investigated were not soluble in water, so a process was needed to disperse the Laponite in a polyurethane solution.

For the polyurethane-Laponite systems discussed in this thesis, the optimal solvent pair determined was deionized water (DI; *A*) and dimethylacetamide or dimethylformamide (DMAc or DMF; *B*), depending on the ease of solubility of the polyurethane in solvent *B*. When Elasthane or custom synthesized polyurethanes were utilized solvent *B* was DMAc; the shape memory polyurethane discussed in Chapters Six and Seven employed DMF as solvent *B*. The following method details the procedure for Laponite dispersal when Elasthane is utilized, but the procedure remains nearly the same when a different polyurethane and DMF is utilized.

Initially, Laponite is mixed with deionized water at a concentration of ~0.70 wt% and the solution is stirred with a Teflon-coated, magnetic stirbar on a hot plate stirrer at a moderate stir speed for at least two days. Then, solvent *B* was added to the solution so that if all the water were removed, the weight fraction of Laponite would be between 0.50% and 0.65%. Again the solution was stirred at a moderate speed for two to three days. Then the liquid-vapor phase equilibrium of the binary solvent system was utilized in order to evaporate off all the water from the Laponite-H_2O-DMAc solution.

From examination of the liquid-vapor phase equilibrium curves of DMAc and H_2O separately, it was clear that at any temperature, the vapor pressure of DMAc was an order of magnitude less than H_2O. For example, at 75°C, the vapor pressure of DMAc is 4.2 kPa while the vapor pressure of H_2O is 38.6 kPa as shown in Figure 3-1 [32]. This difference could be exploited to remove all the water from the solution if the liquid-vapor phase equilibrium curve of the binary system did not exhibit significant hydrolysis or the formation of an azeotrope. In 1972, Carli and colleagues investigated two binary solvents pairs—acetic acid-DMAc and H_2O-DMAc at two different pressures and varied the temperature. They found that the H_2O-DMAc system displayed only a slight negative deviation from Raoult's Law and unlike the other system, no azeotrope formation [33]. Consequently, we assumed that at a constant temperature of 75°C the vapor pressure would change linearly from 38.6 kPa with 100% H_2O to 4.2 kPa at 100% DMAc and used a rotary evaporator (Rotovap) to remove the water.

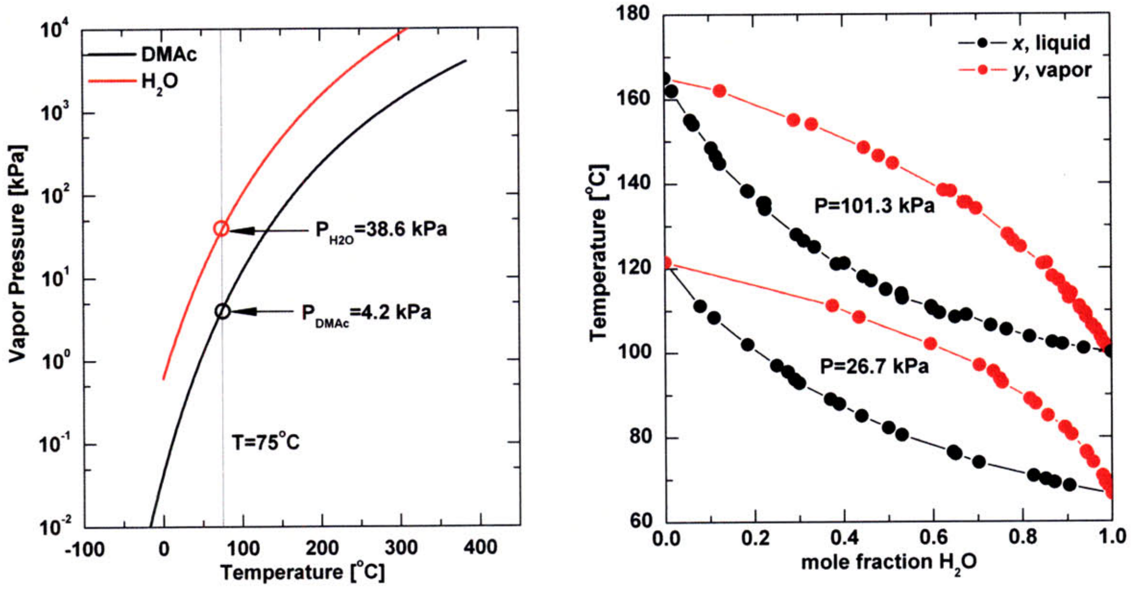

Figure 3-1: Vapor-Liquid equilibrium curve for H_2O and for DMAc (left) and vapor-liquid equilibria of H_2O-DMAc determined via experiment in [33].

The flask containing the Laponite-H_2O-DMAc solution with the spin bar was lowered into a hot water bath at 75°C and connected to the Rotovap at the attachment point. The flask was rotated at 85 rpm. This rotation and the inclusion of the spin bar, which acted as a bubble nucleation point, ensured that the solution did not char or thermally decompose. A vacuum was applied and the pressure immediately set at 25.0 kPa. At this point, in a solution containing 40% DMAc, boiling begins and water vapor begins to rise up toward the condenser, where the condensate is then caught in a second flask. The vacuum was increased very slowly until the pressure decreased to less than 4.0 kPa. The small incremental changes in pressure ensured that no splashing occurred and no DMAc or Laponite was lost in the Rotovap attachment. When all water appeared to be removed the mass of the flask was measured. The evaporation step was not considered to be complete until the mass removed from the flask through evaporation was greater than or equal to the mass of the H_2O added initially. Typically the pressure was further reduced to 3.0 kPa as a precautionary measure to ensure all H_2O was removed. When dimethylformamide was utilized the pressure was drawn down to 5.5 kPa because the vapor pressure of DMF at 75°C is 7.9 kPa [32].

To ensure complete removal of the water using the Rotovap it was necessary to remove some DMAc as well. However, it was important not to remove so much DMAc that the concentration of Laponite in the DMAc solution was greater than 0.70 wt%. At concentration higher than this it was found that the resultant solution does not reliably dissolve the polyurethane. When concentrations greater than 0.70 wt% were prepared, heat was necessary to dissolve the polyurethane in solution. Occasionally, even after a few hours at an elevated temperature, even as high as 140°C, the solution appeared to be emulsion-like and cloudy rather than completely dissolved and the resultant films were lumpy and discontinuous. This emulsion-like state may indicate that at Laponite weight fractions greater than 0.007 in DMAc, the system is more of a gel rather than a solvent dispersion. To avoid such situations, concentrations below 0.70 wt% were utilized.

This DMAc-Laponite solution was then mixed with various quantities of pure DMAc and approximately 0.5 g of polyurethane in 60 ml, thick-walled, glass vials. The total amount of solution necessary was determined by the mass of the polyurethane in the vial and the desired polyurethane concentration in solution, which was approximately 1 wt%. The final concentration of nanoparticle has a dramatic affect on the resulting composite material properties and therefore was kept constant from one nanocomposite to the next. Nanocomposites containing, 0, 1, 2, 4, 6, 8, 10, 15, and 20 wt% Laponite in Elasthane were made. The amount of DMAc-Laponite mixture was determined by the desired Laponite concentration in polyurethane. The amount needed could be calculated by solving the following equation

$$\varphi_m = \frac{CA}{CA + m_{PU}}, \tag{3.1}$$

where φ_m specifies the weight fraction of Laponite in the PU desired, C is the resultant weight fraction of Laponite in the DMAc-Laponite mixture, m_{PU} is the mass of the polyurethane, and A is the mass of the DMAc-Laponite mixture needed. The mass of pure DMAc needed is determined by taking the difference between the total mass of solvent needed less the mass of the of the DMAc-Laponite mixture needed. The resultant PU-DMAc-Laponite mixture was then rolled on a Wheaton mixer for 24 hours or until the PU was completely dissolved. In a few instances when the concentration of Laponite in DMAc was excessively high (≥ 0.70 wt%) or when custom synthesized polyurethanes were used it was necessary to heat the solutions to 140°C for 3-6 hours. After complete dissolution the solution was sonicated at room temperature for 60 minutes. At this point, each vial contained a transparent PU-DMAc-Laponite mixture in which the Laponite was fully dispersed.

3.4 Proof of Exfoliation

3.4.1 Materials

Biomedical polyetherurethane, Elasthane^{TM} 80A, was obtained from the Polymer Technology Group, Inc. (Berkeley, CA). Elasthane contains poly(tetramethylene oxide) (PTMO) soft segments and 4,4'-methylene bisphenyl diisocyanate (MDI) hard segments chain extended with 1,4-butanediol (BDO), as depicted in Fig 3-2. The hard-to-soft segment ratio of Elasthane 80A is 40:60 wt%, its molecular weight is 290,000 g mol^{-1}, and its density is 1.12 g cm^{-3} [34].

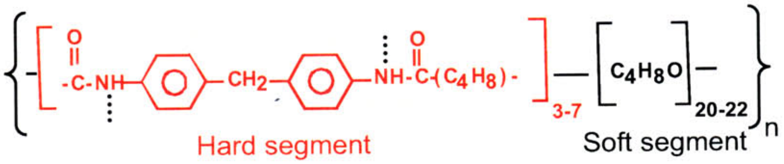

Figure 3-2: Structure of Elasthane 80A based on available non-proprietary information. Elasthane 80A is an elastomeric block-copolymer composed of MDI-BDO hard segments and PTMO soft segments. Hard segments (length 3-11 nm[35, 36]) phase segregate to form hard crystalline domains via hydrogen bonding[21].

Laponite® RD, a synthetic smectic clay with a density of 2.65 g cm^{-3} [37] was obtained from Southern Clay Products, Inc. (Gonzales, TX). Dimethylacetamide (DMAc; B.P. 165°C) was obtained from Sigma Aldrich Co. (St. Louis, MO) and used as received. Laponite was dispersed in DMAc via the solvent exchange procedure detailed above. The Elasthane concentration in the solution was maintained at 1.4-1.6 wt%. Elasthane/Laponite nanocomposite films with 120-150 μm thicknesses were prepared in Teflon® containers (6 cm x 4 cm) by controlled evaporation of DMAc. The final Laponite concentration in the dry film was controlled by varying the Laponite concentration in the Laponite-Elasthane-DMAc solution according to eq 3.1. Note, for a discotic clay such as Laponite, the percolation threshold, $\tilde{\phi}_P$, can be approximated by dividing the random-close-packed hard sphere percolation volume fraction (~0.64) by the aspect-ratio, α, of the clay. The evaporation rate of DMAc was maintained by keeping the films in a closed 60°C oven with a 0.02 m^3 hr^{-1} N_2 purge flow.

3.4.2 Dispersal Characterization

3.4.2.1 Transmission Electron Microscopy

The 10 wt% Elasthane-Laponite nanocomposite transmission electron microscope (TEM) sample was cut on a RMC MT-χ Cryo-capable Ultramicrotome with a diamond knife at -170°C and collected on 400 mesh copper grids. The other polyurethane-Laponite nanocomposite TEM samples were prepared in a JEOL JEM 9310 focused ion beam (FIB) instrument. These samples were first sputter-coated with ~200 nm of gold, and then a localized ~1 μm thick carbon protective film was deposited atop the selected area for lamella preparation. The samples were milled and polished in the FIB to give lamella measuring 10 μm by 10 μm by 80 nm. These samples were transferred to the copper grids using a micromanipulation system which consisted of a position-controlled polished glass rod that allowed for electrostatic pick-up of the lamella. The Elasthane lamellae filled with 4 wt% and 20 wt% Laponite as well as the custom synthesized polyurethane composites described in 3.5.2 were observed in a JEOL 2010 TEM containing a LaB6 filament and imaged using a Gatan digital camera. The TEM image of the nanocomposite containing 10 wt% Laponite was obtained using a JEOL 200CX operated at 200 kV.

3.4.2.2 Atomic Force Microscopy

On a separate occasion, atomic force microscope (AFM) phase images of the nanocomposite was taken in tapping mode on the 10 wt% Laponite cryo-microtomed TEM sample at a different time with a unique NanoProbe (amplitude set point = 0.85 Volts, scale = 20°).

3.4.2.3 Wide Angle X-ray Diffraction

Wide angle x-ray diffraction (WAXD) spectra from 10° to 80° were obtained using a Rigaku RU300 with an 18 kW rotating CuKα anode x-ray generator, a 185 mm diffractometer, and a scintillation counter, in the Bragg-Brettano mode. WAXD spectra from 2° to 38° were obtained using a Molecular Metrology small-angle X-ray scattering system with a custom-machined attachment so that WAXD *d*-spacings could be obtained.

3.4.3 Results and Discussion

The efficacy of the solvent exchange approach for exfoliating the Laponite is demonstrated in the TEM micrographs, AFM phase images, and WAXD data of the resultant Elasthane/Laponite composites presented in Figures 3-3 and 3-4. The TEM images show exfoliated and randomly oriented single Laponite platelets.

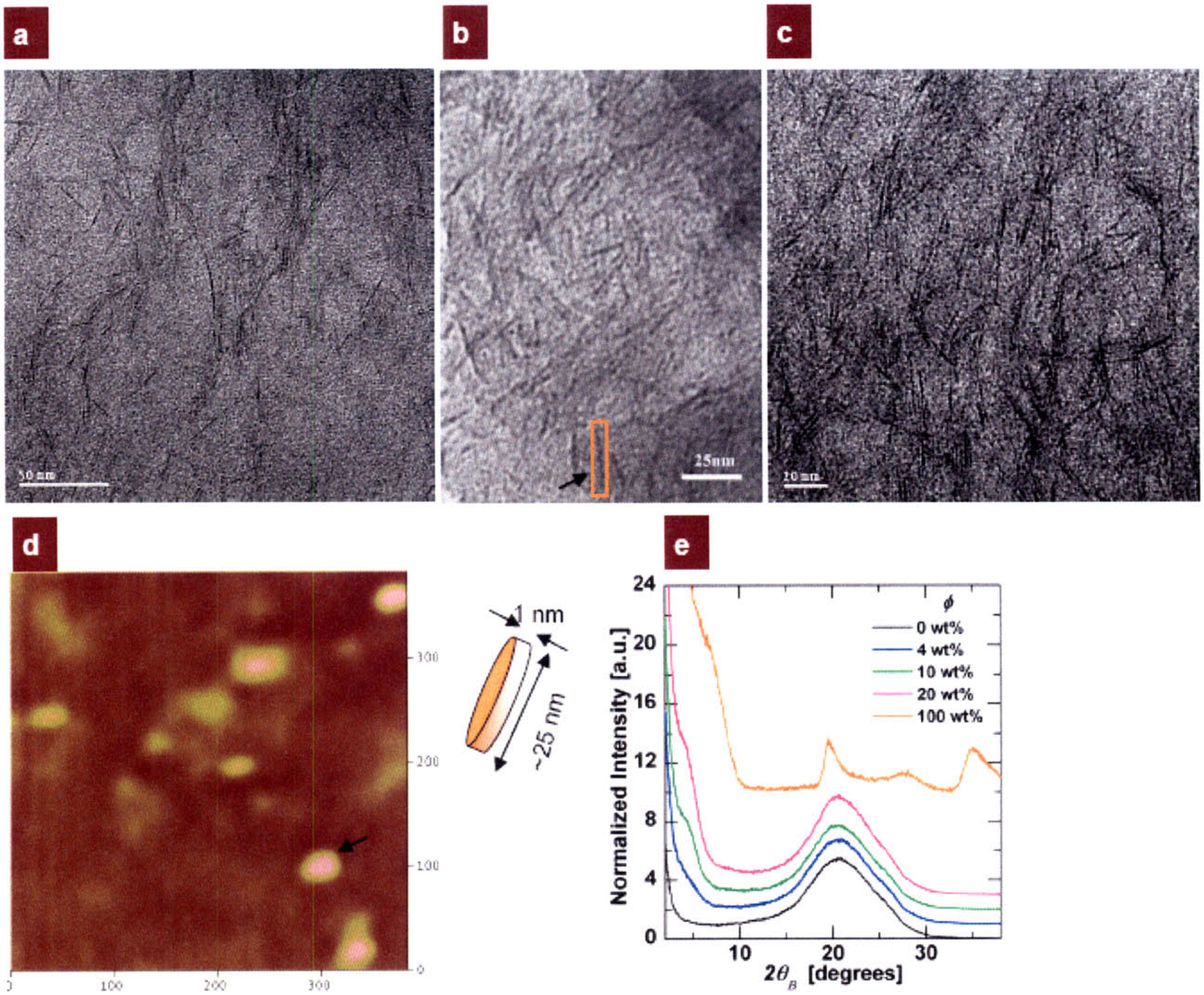

Figure 3-3: a, b, & c, Transmission electron micrographs (TEM) of nanocomposites containing 4, 10, and 20 wt% Laponite show fully exfoliated, uniformly dispersed and randomly oriented, Laponite platelets. Above the percolation concentration (ϕ_P = 5.9 wt%) jamming of Laponite platelets is observed. In the ϕ = 20 wt% micrograph some instances of intercalation are evident with a 2 nm spacing between platelets. d, Atomic Force Microscope (AFM) phase image of the surface of the same ϕ = 10 wt% TEM sample shows stiff, single Laponite particles (bright fields) cut at different orientations. Image width is 383 nm. e, Wide angle x-ray diffraction (WAXD) spectra of nanocomposites containing 0, 4, 10 and 20 wt% Laponite and of Laponite powder[38] (from bottom to top).

As the Laponite concentration, ϕ, exceeds the percolation threshold, $\phi_P \approx 5.9$ wt% (or $\tilde{\phi}_P \approx 2.5$ vol%), particle-particle interactions become increasingly important during the slow solvent evaporation and the instances of intercalated platelets with a spacing of 2 nm, however infrequent, increase. The percolation threshold, ϕ_P, represents the concentration at which the average inter-particle spacing is less than one particle diameter. The d001 spacing of Laponite is 1.28 nm ($2\theta = 6.92°$) according to Southern Clay Products, Inc. the provider. This diffraction shoulder is observed in the ϕ = 10 and 20 wt% samples with increased intensity at a spacing of

2.02 nm ($2\theta = 4.36°$), indicating the instances of Laponite intercalation increase as ϕ surpasses ϕ_p. The incomplete exfoliation at $\phi \geq \phi_p$ is a consequence of the increased Laponite volume fraction and the slow solvent evaporation which results in weak particle-particle interactions [17, 21] (See Figure 3-3e and 3-4). The peak at $2\theta = 20°$ corresponds to hard segment crystallites with lattice spacing of 4.43 Å [21, 38].

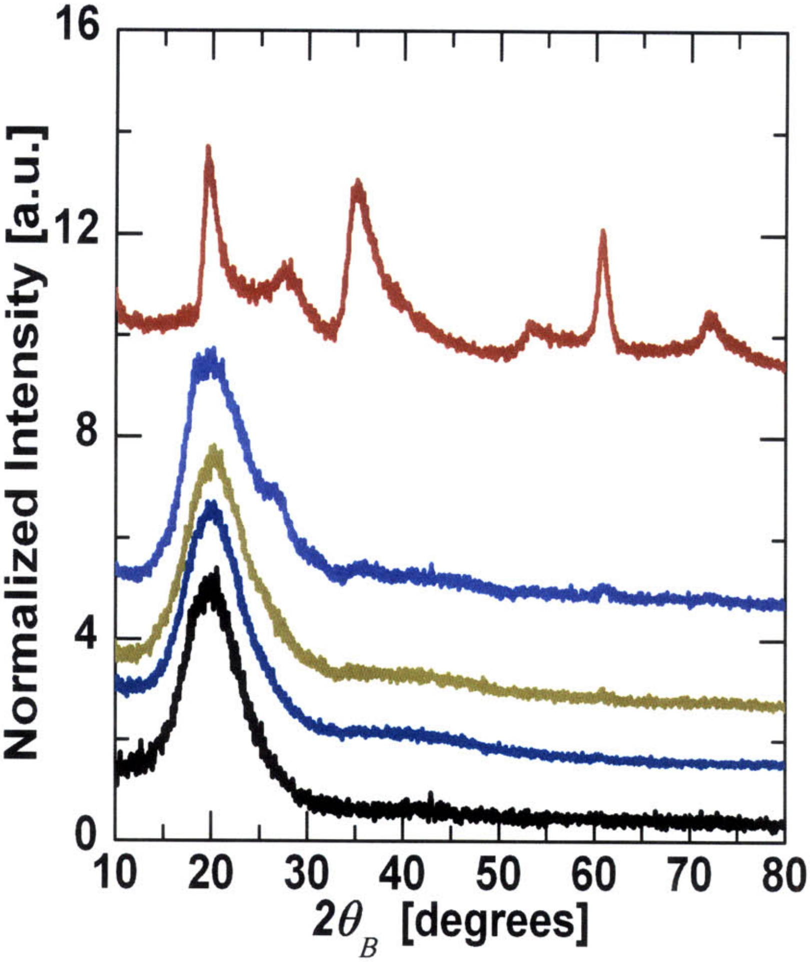

Figure 3-4: Laponite dispersal within the polyurethane matrix via WAXD, using a different diffraction instrument and different nanocomposite samples (Dispersal Characterization). Spectra from $2\theta = 10°$ to $80°$ of nanocomposites containing 0, 4, 10 and 20 wt% Laponite and of Laponite powder [39] (from bottom to top).

Because Laponite has only weak reflections due to imperfect platelet registration and its small size, the broad diffraction halo of the Elasthane would mask the peak at $2\theta = 19.5°$. Although no large angle peaks are observed in the $\phi < 20$ wt% samples, the Laponite peak at 27.4° is observed in the $\phi = 20$ wt% spectra shifted to 26.4°. At this high Laponite volume fraction, particle-particle interactions developed over the long time allowed for slow solvent removal cause the platelets to re-aggregate in an intercalated state. Note, the WAXD spectra of numerous nanocomposite samples at various Laponite concentration have been examined using numerous WAXD instruments, including the G1 beamline at the Cornell high-energy synchrotron source (CHESS) [40], and are broadly consistent. This will be discussed in Chapter Five. In numerous instances at Laponite concentrations above the percolation threshold, but below 20 wt% ($\phi_P \leq \phi \leq 20$ wt%), nanocomposite spectra did not exhibit any peaks or shoulders corresponding to the pure Laponite spectra, indicating that the platelets were well dispersed and no longer in agglomerated stacks.

3.5 Influence of Processing Parameters

The solvent exchange method is an effective way to disperse nanoparticles in solution and exfoliate nanoparticles in a solid polymer matrix, as is detailed in the previous section. The exfoliation and resultant property enhancement can be further tailored by exploiting polymer polarity and processing time.

3.5.1 Influence of Segment Polarity

To verify that segment polarity and hydrophilicity determine the location of preferential reinforcement in either the soft or hard domain, thermoplastic polyurethane/Laponite nanocomposites were prepared using two custom-synthesized thermoplastic polyurethanes (TPUs) that differed in soft segment (SS) polarity and hydrophilicity[41].

3.5.1.1 Materials

Two custom synthesized polyurethanes were synthesized and differ from Elasthane in composition. One is poly(ethylene oxide) based while the other is poly(tetramethylene oxide) based. They were each filled with 10 wt% Laponite as discussed previously using our solvent-exchange process. The PEO-based polyurethane contains a 1,6-hexamethylene diisocyanate—1,4-butanediol (HDI-BDO) hard segment (33 wt%) and a poly(ethylene oxide)-poly(propylene oxide)-poly(ethylene oxide) (PEO-PPO-PEO) soft segment (1900 g mol^{-1}) [42].

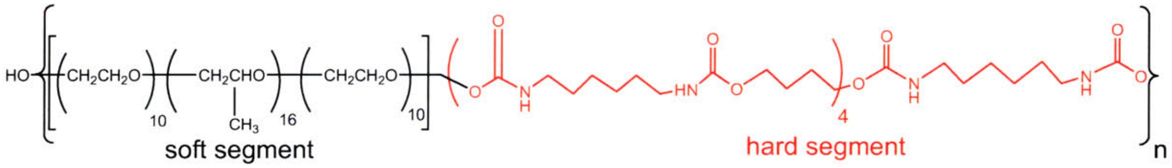

Figure 3-5: Structure of PEO-based polyurethane [42].

The total weight-average molecular weight of this crystalline, aliphatic hard segment polyurethane was determined to be 110,000 g mol^{-1} using gel permeation chromatography. This polyurethane displays a soft segment glass transition at -61°C, a hard segment melting transition at 146°C, and a hard segment crystallization transition at 108°C [42]. Like Elasthane, the novel PTMO-based polyurethane contained poly(tetramethylene oxide) soft segments but the soft segment was of higher molecular weight (2000 g mol^{-1}) and was more crystalline at room temperature. Note soft segment crystallinity is dependent upon segment molecular weight [43]. The hard segment (37 wt%) is composed of HDI chain extended with BDO, as in the PEO-based polyurethane [44].

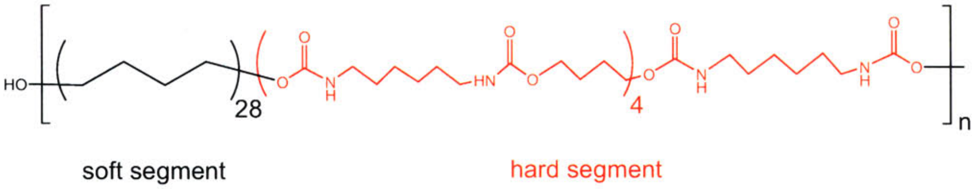

Figure 3-6: Structure of PTMO-based polyurethane [44].

The total weight-average molecular weight of this polyurethane is 233,000 g mol^{-1}. The HDI-PTMO PU displays a soft segment glass transition at -65°C, a hard segment melting transition at 174°C, and a hard segment crystallization transition at 146°C [44].

The following section details the characterization results of these two custom-synthesized polyurethane-Laponite nanocomposites. These composites were characterized in the same manner as the Elasthane-Laponite nanocomposites described in 3.4.2.

3.5.1.2 Evidence of Exfoliation

Both wide angle x-ray diffraction (WAXD) and transmission electron microscopy (TEM) provide evidence that the Laponite is well dispersed throughout the custom-synthesized polyurethanes, further supporting the efficacy of the novel solvent exchange procedure.

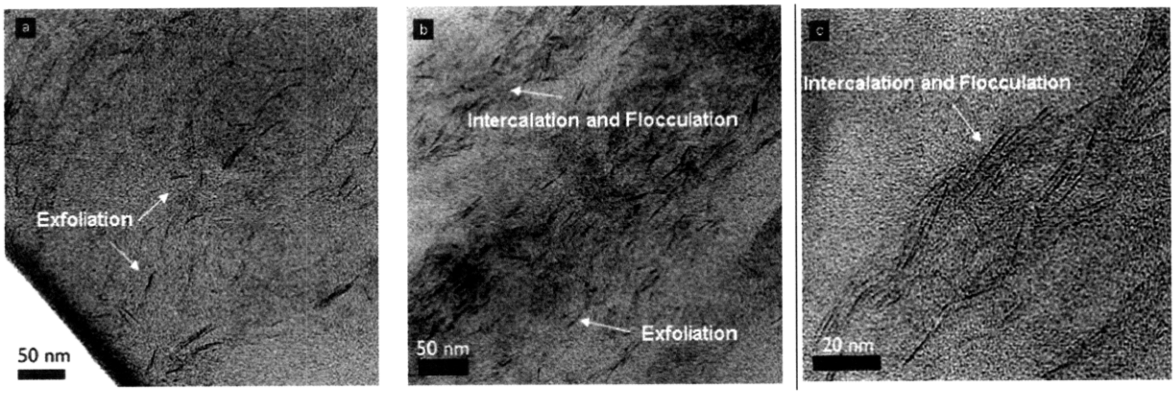

Figure 3-7: (a) TEM image of 10 wt % Laponite dispersed in PTMO:HDI-BDO PU; 50 nm scale bar. (b)TEM image of 10 wt % Laponite dispersed in PEO-PPO-PEO:HDI-BDO PU; 50 nm scale bar. (c) TEM image of 10 wt % Laponite dispersed in PEO-PPO-PEO:HDI-BDOPU; 20 nm scale bar.

However, the Laponite appears to be fully exfoliated in the HDI-PTMO PU system, while in the PEO-based system there is evidence of some platelet flocculation. Although the clay is randomly dispersed throughout the PEO-based matrix, regions of more closely packed Laponite platelets are observed as well as regions of more even, random dispersal. The HDI-PTMO PU nanocomposite does not display phase separated regions of clay dispersal, but instead even, random dispersal throughout the image. The differences in the Laponite dispersal can be seen in the TEM micrographs displayed in Figure 3-7.

WAXD spectra between a scattering angle of 5° and 80° further confirm the extent of Laponite dispersion observed in the TEM images. The WAXD spectra of the pure HDI:BDO hard segments of these polyurethanes, the pure polyurethanes, and the nanocomposites filled with 10 wt% Laponite, as well as the pure Laponite are shown below in Figure 3-8.

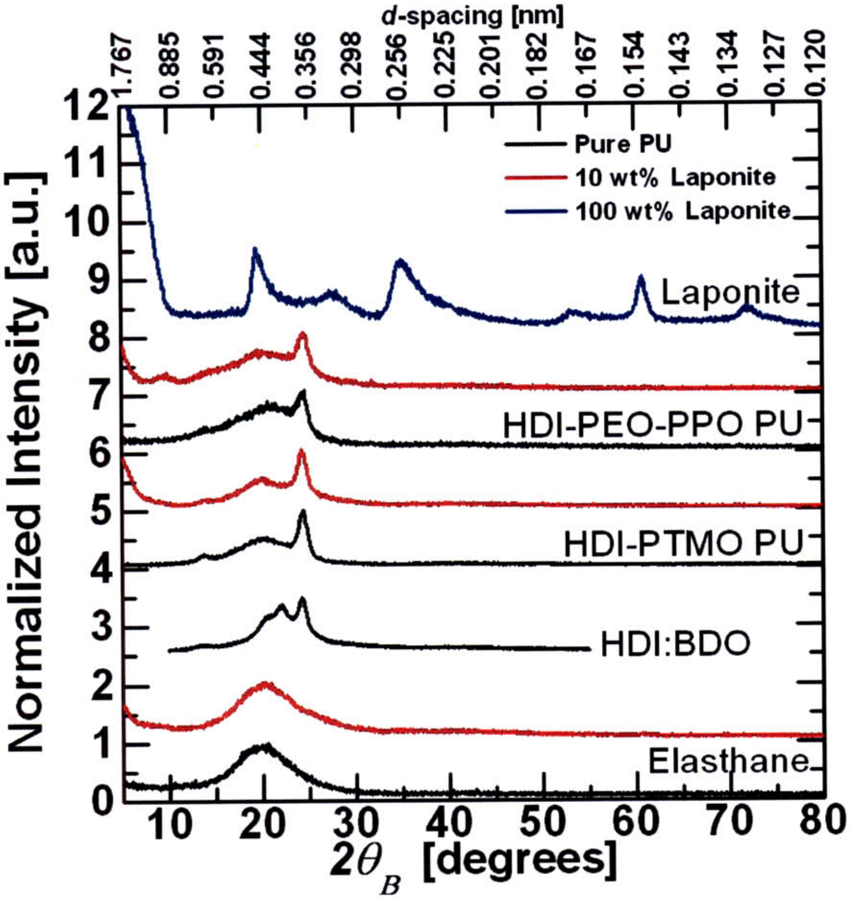

Figure 3-8: WAXD spectra of HDI:BDO hard segment, of pure Laponite and of the pure and 10 wt % Laponite-filled polyurethane nanocomposites.

There is virtually no difference in the pure HDI- PTMO PU and corresponding nanocomposite spectra above 5°. The absence of the Laponite basal plane spacing peak ($2\theta = 6.92°$) and *d*020 reflection ($2\theta = 19.5°$) in the HDI-PTMO PU nanocomposite spectrum indicates that the platelets have been separated and the gallery spacing increased to a random undetectable distance with this apparatus, indicating full exfoliation. However, there are differences between the spectra of pure PEO-based polyurethane and its corresponding nanocomposite. In the PEO-based polyurethane-Laponite nanocomposite spectrum there is a small peak at approximately 10°. If the clay was intercalated and the gallery spacing increased, the peak in the scattering angle at 6.9°, indicating the Laponite basal plane spacing when the platelets are stacked, should shift to lower angles. Consequently, the presence of a peak at a higher scattering angle implies either that the clay platelets are stacking more tightly than exhibited when Laponite is in a dry powder state or that the peak is a higher-order reflection of a peak present below a scattering angle of 5°. Based on the TEM image, it is reasonable to assume that the peak is a secondary reflection of an intercalation peak or ordered exfoliation peak. However, to determine with any certainty the cause of the peak, an investigation utilizing small angle x-ray scattering is necessary, as will be described in Chapter Five.

3.5.1.3 Evidence of Preferential Reinforcement

The results of characterization of these polyurethane/Laponite nanocomposites suggest that by increasing the polarity and/or hydrophilicity of the polyurethane soft segment the Laponite can be directed away from the hard domain and attracted into the polar soft domains. When polyurethanes containing highly polar, hydrophilic soft segment constituents, such as polyethylene oxide (PEO), are employed, the Laponite is directed away from the hard domains and embedded within the soft domain. The resulting material is less extensible than the pure polyurethane and very brittle. The other polyurethane investigated utilized the same hard segment at similar weight concentrations, but the soft segments, although of similar molecular weight, had different polarities and hydrophilicities. One polyurethane contained poly(tetramethylene oxide) (PTMO) soft segments while the other polyurethane contained polyethylene oxide-polypropylene oxide-polyethylene oxide (PEO-PPO-PEO) soft segments. As can be seen from Table 3-1 PEO is more polar and has a higher solubility parameter than the other soft segment constituents and attracts the Laponite platelets.

Polyurethane	Soft Segment Constituent	Solubility Parameter $[J^{1/2}cm^{-3/2}]$
Elasthane	PTMO	18.039
HDI-PTMO PU		
HDI-PEO-PPO-PEO PU	PEO	19.625
	PPO	16.873
	PEO-PPO-PEO	18.493

Table 3.1: Polyurethane soft segment polarity expressed in terms of the solubility parameter which was calculated using the group contribution method and values given in [45].

Consequently, the novel polyurethane/Laponite nanocomposite that has a PTMO soft segment but hexamethylene diisocyanate (HDI) hard segment behaves similar to Elasthane/Laponite nanocomposites—exhibiting an increase in strength, toughness, and stiffness without a loss in extensibility when Laponite is added. This will be described in the next Chapter. Furthermore, like the Elasthane nanocomposites, the HDI-PTMO PU nanocomposite exhibits a disruption in the hard segment crystallinity seen in DSC and a decrease in lossiness (tan δ) at the glass transition in DMA. There is no change in the value of the soft segment glass transition temperature when Laponite is added (See Figures 3-9 and 3-10). Therefore, as in the Elasthane/Laponite nanocomposites, the Laponite is preferentially embedded within the hard domains of the HDI-PTMO PU and effectively strengthening and toughening the polyurethane.

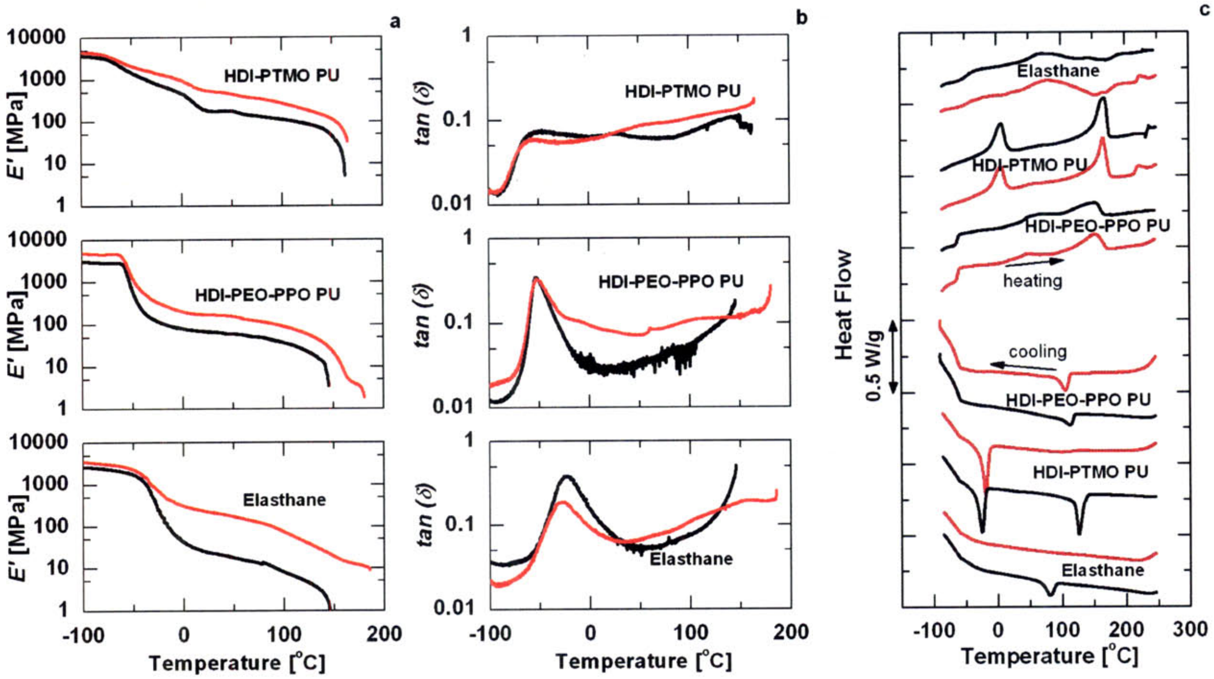

Figure 3-9: Flexural storage modulus, *E'* (a), and loss tangent, tan *δ* (b), both determined via DMA and DSC thermograms and (c) during initial heating and cooling cycles of the pure (black) and 10 wt % Laponite-filled PUs (red).

The novel polyurethane/Laponite nanocomposite that has the same HDI-based hard segments but a more polar and hydrophilic, PEO-based soft segment exhibits contrasting behavior. The extensibility of this polyurethane decreases dramatically when Laponite is added while the stiffness of the material exhibits no distinct change. The dramatic reduction in extensibility decreases the strength and toughness of the material significantly, and the nanocomposite behaves like a brittle plastic rather than as a stronger, tougher elastomer as is displayed in Figure 3-10. Furthermore, DSC shows that the hard segment is unaffected by the addition of Laponite. DMA shows that the value of the soft segment glass transition temperature is unchanged, although the transition is broadened significantly, indicating a restriction in soft segment mobility as shown in Figure 3-9b. Characterization of this PEO-based Laponite nanocomposite suggests that the Laponite is embedded within the soft domain of polyurethane, where it restricts soft segment mobility and negatively affects the extensibility of the material.

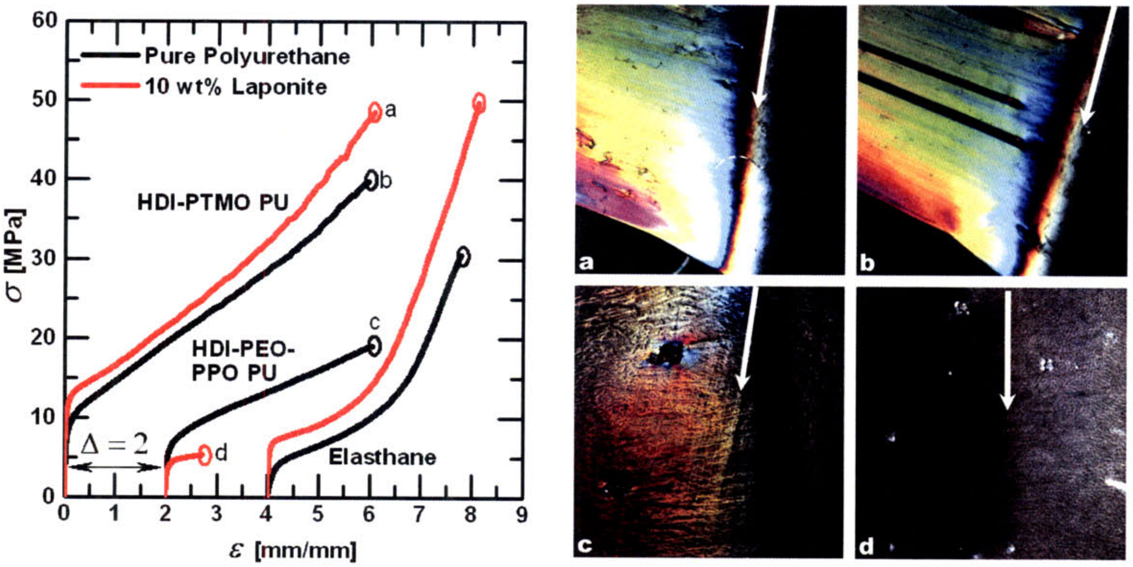

	HDI-PTMO PU	HDI-PTMO PU & 10 wt% Laponite	HDI-PEO-PPO PU	HDI-PEO-PPO PU & 10 wt% Laponite
Initial Modulus (MPa)	260 ± 18	474 ± 26	181 ± 26	157 ± 3
Ultimate Strength (MPa)	40 ± 5	48 ± 2	16 ± 3	5.0 ± 0.4
Failure Strain	6.28 ± 0.35	6.17 ± 0.26	3.85 ± 0.35	0.62 ± 0.21
Toughness at 30% Strain (MJ m^{-3})	2.57 ± 0.23	3.51 ± 0.12	1.60 ± 0.26	1.16 ± 0.04
Total Toughness, (MJ m^{-3})	149 ± 21	170 ± 13	43 ± 9	2.7 ± 1.1

Figure 3-10: Representative engineering stress-strain tensile curves of the pure and 10 wt % Laponite filled polyurethanes are presented, and the correspondingly labeled cross-polarized image (height) 2.2 mm) of four of the six samples is shown (a-d), where (a) is unfilled PTMO:HDIBDO PU, (b) is 10 wt % Laponite filled PTMO:HDI-BDO PU, (c) is unfilled PEO-PPO-PEO:HDI-BDO PU, and (d) is 10 wt % Laponite filled PEO-PPO-PEO:HDI-BDO PU. Note that the stress-strain curves are offset by Δ = 2.0 for ease of viewing. The cross-polarized images of PTMO:MDI-BDO and PTMO:HDI-BDO PU thin films after deformation are similar. A white arrow runs tangent along the grip locale, separating the undeformed portion of the polyurethane (right) from the deformed portion (left) which was stretched in a direction perpendicular to the white arrow.

In summary, this novel solvent exchange approach can produce fully-exfoliated dispersions of nanoparticles that enhance the thermomechanical properties of polyurethanes which contain non-polar soft segments without hindering material extensibility. If the soft segment attracts the nanoparticles (in this case the charged clay discs) the Laponite preferentially segregates into the soft micro-domains. This significantly hinders soft segment mobility and therefore dramatically reduces the TPU extensibility [41]. Ultimately, the solvent exchange approach combined with the thermodynamic attraction of the unmodified Laponite platelets to polar and/or hydrophilic constituents afford material engineers the ability to select and control the location of nanoreinforcement. Thus, the thermomechanical properties of polar block-copolymers such as polyurethanes and polyureas can be tailored.

3.5.2 Influence of Processing Time

When this novel solvent exchange approach is utilized, the solvent is removed slowly over three to four weeks at elevated temperature. Ultimately, the polyurethane and nano-filter has an extended period of time in which to preferentially self-assemble. Consequently, when the matrix contains non-polar soft segments, the Laponite is preferentially embedded within the polyurethane hard domains, where it significantly enhances the thermomechanical properties of the material while maintaining material extensibility. A small fraction of Laponite may be embedded within the soft domain, but this is not enough to negatively influence the material behavior. However, when the matrix polyurethane contains polar constituents, such as polyethylene oxide, the Laponite is preferentially embedded within the soft domain, restricting soft segment mobility and decreasing the material extensibility. Again, a small fraction of the Laponite may be embedded within the hard domain, but the Laponite within the soft domain dominates the material behavior.

This same extent of preferential reinforcement can not be achieved if a quicker processing method is utilized. The physical properties of the solvent cast films were observed to depend on the evaporation rate. As noted in section 3.4.1 a constant evaporation rate was maintained for all nanocomposite samples by keeping the films in a closed 60°C oven with a 0.02 $m^3 hr^{-1}$ N_2 purge flow. This rate was maintained because when the study was initiated the evaporation rate was not strictly monitored and the mechanical properties from one batch of composites to the next displayed significant differences. Those composites that were prepared under more rapid evaporative conditions exhibited inferior properties. Consequently, when comparatively fast processes like electrospinning and precipitation with compression molding are utilized, there is less time for microphase segregation and preferential reinforcement. Inferior mechanical properties are then inevitable.

These solvent-based nanodispersion methods are further complicated when Laponite or other high aspect ratio particles are used, because the nanoparticles induce gelation at low concentrations. When nanocomposite solutions for precipitation in solvents like methanol are prepared the concentration of polyurethane in solution is constrained by the solubility limit. This limit is further constrained when nanoparticles are added. For example, 5 grams of polyurethane will not fully dissolve in a 100 gram solution that contains greater than 0.3 grams of Laponite (or a concentration of Laponite that is greater than or equal to 6 wt% of the resulting solid). The same solution without the Laponite will easily dissolve the polyurethane. Similar solutions that contain concentrations of Laponite in the resulting solid that are greater than the percolation limit are not able to be successfully electrospun because addition of such high concentration of Laponite particles leads to jamming. This limits the extent of the solution viscoelasticity and promotes capillary break-up. So while the solvent exchange approach successfully exfoliates nanoparticles, the resultant property enhancement can only be achieved but at a cost—long processing time and utilization of a lot of environmentally unfriendly solvents, such as dimethyl acetamide and dimethylformamide. Should an environmentally-friendly solvent, like α-tocopherol or supercritical carbon dioxide be able to be utilized instead to maintain nanoparticle dispersion, the resultant solution could be used as an additive to numerous polymeric products. For example, nano-reinforced polyurethanes and polyureas could increase the strength and wear resistance of prosthetics or protective eye-wear. Polyolefins too could be reinforced and the barrier resistance and flame retardance of cable sheathing improved

3.6 Conclusions

The new solvent exchange method outlined here allows block-copolymers with polar constituents, like thermoplastic polyurethanes, to be preferentially nanoreinforced with inorganic nanoparticles, like smectic clays. This method utilizes a combination of solvents; one solvent separates and disperses the nanoparticles and the second solvent maintains the dispersion stability but also dissolves the matrix polymer. While this technique may be applied to numerous nanoparticle-polymer systems, the extent of property enhancement depends on the time allowed for phase-segregation and preferential reinforcement and the concentration limits of solution feasibility relies heavily on the aspect ratio of the nanoparticles employed. Ultimately, the use of block polarity in conjunction with this solvent exchange approach offers an avenue toward the development of high performance materials that rival natural materials.

3.7 References

[1] D. P. Knight and F. Vollrath, "Biological liquid crystal elastomers," *Philosophical Transactions of the Royal Society of London Series B-Biological Sciences*, vol. 357, pp. 155-163, 2002.

[2] F. Vollrath and D. P. Knight, "Liquid crystalline spinning of spider silk," *Nature*, vol. 410, pp. 541-548, 2001.

[3] Y. Termonia, "Molecular Modeling of Spider Silk Elasticity," *Macromolecules*, vol. 27, pp. 7378-7381, 1994.

[4] A. H. Simmons, C. A. Michal, and L. W. Jelinski, "Molecular orientation and two-component nature of the crystalline fraction of spider dragline silk," *Science*, vol. 271, pp. 84-87, 1996.

[5] J. D. van Beek, L. Beaulieu, H. Schafer, M. Demura, T. Asakura, and B. H. Meier, "Solid-state NMR determination of the secondary structure of Samia cynthia ricini silk," *Nature*, vol. 405, pp. 1077-1079, 2000.

[6] H. J. Gao, B. H. Ji, I. L. Jager, E. Arzt, and P. Fratzl, "Materials become insensitive to flaws at nanoscale: Lessons from nature," *Proceedings of the National Academy of Sciences of the United States of America*, vol. 100, pp. 5597-5600, 2003.

[7] B. L. Smith, T. E. Schaffer, M. Viani, J. B. Thompson, N. A. Frederick, J. Kindt, A. Belcher, G. D. Stucky, D. E. Morse, and P. K. Hansma, "Molecular mechanistic origin of the toughness of natural adhesives, fibres and composites," *Nature*, vol. 399, pp. 761-763, 1999.

[8] J. Gosline, P. Guerette, C. Ortlepp, and K. Savage, "The mechanical design of spider silks: from fibroin sequence to mechanical function," *J Exp Biol*, vol. 202, pp. 3295-3303, 1999.

[9] H. Koerner, G. Price, N. A. Pearce, M. Alexander, and R. A. Vaia, "Remotely actuated polymer nanocomposites - stress-recovery of carbon-nanotube-filled thermoplastic elastomers," *Nature Materials*, vol. 3, pp. 115-120, 2004.

[10] R. A. Vaia and H. D. Wagner, "Framework for nanocomposites," *Materials Today*, vol. 7, pp. 32-37, 2004.

[11] A. M. Chen, Y. Tian, B. Han, G. D. Ji, S. S. Wu, and J. Shen, "Synthesis and characterization of polyurethane/montmorillonite nanocomposites," *Acta Polymerica Sinica*, pp. 591-594, 2003.

[12] S. Y. Moon, J. K. Kim, C. Nah, and Y. S. Lee, "Polyurethane/montmorillonite nanocomposites prepared from crystalline polyols, using 1,4-butanediol and organoclay hybrid as chain extenders," *European Polymer Journal*, vol. 40, pp. 1615-1621, 2004.

[13] M. Song, D. J. Hourston, K. J. Yao, J. K. H. Tay, and M. A. Ansarifar, "High performance nanocomposites of polyurethane elastomer and organically modified layered silicate," *Journal of Applied Polymer Science*, vol. 90, pp. 3239-3243, 2003.

[14] Z. Z. Yu, C. Yan, M. S. Yang, and Y. W. Mai, "Mechanical and dynamic mechanical properties of nylon 66/montmorillonite nanocomposites fabricated by melt compounding," *Polymer International*, vol. 53, pp. 1093-1098, 2004.

[15] X. M. Zhang, R. J. Xu, Z. G. Wu, and C. X. Zhou, "The synthesis and characterization of polyurethane/clay nanocomposites," *Polymer International*, vol. 52, pp. 790-794, 2003.

[16] S. S. Ray, K. Okamoto, and M. Okamoto, "Structure-property relationship in biodegradable poly(butylene succinate)/layered silicate nanocomposites," *Macromolecules*, vol. 36, pp. 2355-2367, 2003.

[17] S. Sinha Ray and M. Okamoto, "Polymer/layered silicate nanocomposites: a review from preparation to processing," *Progress in Polymer Science*, vol. 28, pp. 1539-1641, 2003.

[18] M. Alexandre and P. Dubois, "Polymer-layered silicate nanocomposites: preparation, properties and uses of a new class of materials," *Materials Science and Engineering: R: Reports*, vol. 28, pp. 1-63, 2000.

[19] J. Njuguna and K. Pielichowski, "Polymer nanocomposites for aerospace applications: Fabrication," *Advanced Engineering Materials*, vol. 6, pp. 193-203, 2004.

[20] D. Burgentzle, J. Duchet, J. F. Gerard, A. Jupin, and B. Fillon, "Solvent-based nanocomposite coatings: I. Dispersion of organophilic montmorillonite in organic solvents," *Journal of Colloid and Interface Science*, vol. 278, pp. 26-39, 2004.

[21] B. Finnigan, D. Martin, P. Halley, R. Truss, and K. Campbell, "Morphology and properties of thermoplastic polyurethane nanocomposites incorporating hydrophilic layered silicates," *Polymer*, vol. 45, pp. 2249-2260, 2004.

[22] X. H. Dai, J. Xu, X. L. Guo, Y. L. Lu, D. Y. Shen, N. Zhao, X. D. Luo, and X. L. Zhang, "Study on structure and orientation action of polyurethane nanocomposites," *Macromolecules*, vol. 37, pp. 5615-5623, 2004.

[23] I. Rhoney, S. Brown, N. E. Hudson, and R. A. Pethrick, "Influence of processing method on the exfoliation process for organically modified clay systems. I. Polyurethanes," *Journal of Applied Polymer Science*, vol. 91, pp. 1335-1343, 2004.

[24] P. C. LeBaron, Z. Wang, and T. J. Pinnavaia, "Polymer-layered silicate nanocomposites: an overview," *Applied Clay Science*, vol. 15, pp. 11-29, 1999.

[25] S. S. Ray and M. Okamoto, "Polymer/layered silicate nanocomposites: a review from preparation to processing," *Progress in Polymer Science*, vol. 28, pp. 1539-1641, 2003.

[26] Y. Kojima, A. Usuki, M. Kawasumi, A. Okada, Y. Fukushima, T. Kurauchi, and O. Kamigaito, "Mechanical-Properties Of Nylon 6-Clay Hybrid," *Journal Of Materials Research*, vol. 8, pp. 1185-1189, 1993.

[27] M. E. Mackay, A. Tuteja, P. M. Duxbury, C. J. Hawler, B. Van Horn, Z. Guan, G. Chen, and R. S. Krishnan, "General strategies for nanoparticle dispersion," *Science*, vol. 311, pp. 1740, 2006.

[28] N. Kumar, S. M. Liff, and G. H. McKinley, " Method to disperse and exfoliate nanoparticles," U. S. P. Office, Ed. United States: Massachusetts Institute of Technology, Filed October 18, 2005.

[29] R. G. Larson, *The Structure and Rheology of Complex Fluids*. New York, NY: Oxford University Press, 1998.

[30] C. S. O'Hern, L. E. Silbert, A. J. Liu, and S. R. Nagel, "Jamming at zero temperature and zero applied stress: The epitome of disorder," *Physical Review E*, vol. 68, pp. 011306, 2003.

[31] V. Trappe, V. Prasad, L. Cipelletti, P. N. Segre, and D. A. Weitz, "Jamming phase diagram for attractive particles," *Nature*, vol. 411, pp. 771-772, 2001.

[32] C. L. Yaws, X. Lin, L. Bu, D. R. Balundgi, and S. Tripathi, "Vapor Pressure," in *Chemical Properties Handbook*, C. L. Yaws, Ed. New York: McGraw-Hill, 1999, pp. 784.

[33] A. Carli, S. Di Cave, and E. Sebastiani, "Thermodynamic characterization of vapour--liquid equilibria of mixtures acetic acid--dimethylacetamide and water--dimethylacetamide," *Chemical Engineering Science*, vol. 27, pp. 993-1001, 1972.

[34] M. J. Wiggins, M. MacEwan, J. M. Anderson, and A. Hiltner, "Effect of soft-segment chemistry on polyurethane biostability during in vitro fatigue loading," *Journal Of Biomedical Materials Research Part A*, vol. 68A, pp. 668-683, 2004.

[35] D. J. Martin, G. F. Meijs, P. A. Gunatillake, S. P. Yozghatlian, and G. M. Renwick, "The influence of composition ratio on the morphology of biomedical polyurethanes," *Journal of Applied Polymer Science*, vol. 71, pp. 937-952, 1999.

[36] C. D. Eisenbach, A. Ribbe, and C. Gunter, "Morphological-Studies Of Model Polyurethane Elastomers By Element-Specific Electron-Microscopy," *Macromolecular Rapid Communications*, vol. 15, pp. 395-403, 1994.

[37] I. Grillo, P. Levitz, and T. Zemb, "Insertion of small anisotropic clay particles in swollen lamellar or sponge phases of nonionic surfactant," *European Physical Journal E*, vol. 5, pp. 377-386, 2001.

[38] M. M. Malwitz, S. Lin-Gibson, E. K. Hobbie, P. D. Butler, and G. Schmidt, "Orientation of platelets in multilayered nanocomposite polymer films," *Journal of Polymer Science Part B-Polymer Physics*, vol. 41, pp. 3237-3248, 2003.

[39] Cornell University, "Cornell High Energy Synchrotron Source - G-Line,"http://www.chess.cornell.edu/gline/index.htm, 2007: Accessed August 20, 2005.

[40] A. Aneja and G. L. Wilkes, "A systematic series of 'model' PTMO based segmented polyurethanes reinvestigated using atomic force microscopy," *Polymer*, vol. 44, pp. 7221-7228, 2003.

[41] L. T. J. Korley, S. M. Liff, N. Kumar, G. H. McKinley, and P. T. Hammond, "Preferential association of segment blocks in polyurethane nanocomposites," *Macromolecules*, vol. 39, pp. 7030-7036, 2006.

[42] L. J. Korley, *PEO-containing Copolymers as Polyurethane Soft Segments in the Development of High Performance Materials*, Ph.D. in Program in Polymer Science and Technology, Cambridge, MA:Massachusetts Institute of Technology, 2005.

[43] M. Szycher, *Szycher's Handbook of Polyurethanes*. Boca Raton, Florida: CRC Press, 1999.

[44] G. Pollock, *Synthesis and Characterization of Mechanically Enhanced, Nanostructured Thermoplastic Polyurethane Elastomers*, Ph.D. in Program in Polymer Science and Technology, Cambridge, MA:Massachusetts Institute of Technology, 2005.

[45] D. W. van Krevelen, *Properties of Polymers: Their Correlation with Chemical Structure; Their Numerical Estimation and Prediction From Additive Group Contributions*, 3rd ed. Amsterdam, NL: Elsevier Science, 1997.

4. High Performance Elastomeric Nanocomposites via Solvent Exchange Processing

[Part of this work has been published previously, in slightly different form, in "High Performance Elastomeric Nanocomposites via Solvent Exchange Processing" by S.M. Liff, N. Kumar, and G.H. McKinley, *Nature Materials,* **2007**, 6 (1): 76-83 and in "Preferential Association of Segment Blocks in Polyurethane Nanocomposites" by L.T.J. Korley , S.M. Liff, P.T. Hammond, and G.H. McKinley, *Macromolecules,* **2006**, 39 (20): 7030-7036.]

4.1 Introduction

The incorporation of nanoparticles into engineering thermoplastics affords engineers an opportunity to synthesize polymer nanocomposites that potentially rival the most advanced materials in nature. Development of these materials is difficult since thermodynamic and kinetic barriers inhibit the dispersal of inorganic, often hydrophilic nanoparticles in hydrophobic polymer matrices. Using the new solvent exchange approach, detailed thoroughly in Chapter 3, we preferentially nanoreinforce the hard micro-domains of thermoplastic elastomers with a smectic clay of similar characteristic dimensions. The strong adhesion between the clay and the hard micro-domains of the block copolymer coupled with the formation of a percolative network not only stiffens and toughens, but increases the heat distortion temperature of the material and induces reversible thermotropic liquid-crystalline transitions. The discotic clay platelets induce morphological ordering over a range of length scales that results in significant thermomechanical enhancement and expands high temperature applications. Merging block-copolymer processing techniques with this method for nanoparticle preferential-ordering facilitates the development of new, hierarchically-ordered materials or "'molecular-composite hybrids'" [1].

High performance biomaterials, such as silk [2-6] and bone [7, 8] exhibit unparalleled combinations of stiffness, strength, extensibility, and toughness by exploiting hierarchical structures in which stiff nanometer-size crystallites are embedded and dispersed in softer protein matrices [2-4, 9]. Polymer nanocomposites which utilize engineering thermoplastics as the matrix material and stiff, inorganic, anisotropic nanoparticles to tailor thermomechanical properties have been the subject of many recent studies as discussed in Chapter 2 [10, 11]. Successful mechanical enhancement of polymer matrices via nanoreinforcement is expected only when the nanoparticles are fully exfoliated in the polymer matrix. This is difficult since the organic, hydrophobic polymer matrices thermodynamically and kinetically inhibit the dispersal of the inorganic, hydrophilic clay. Despite numerous advances synthetic polymer nanocomposites have yet to display the superior toughness of natural biomaterials, such as silk. Like a majority of engineering materials the nanocomposites are either stiff but not extensible, like steel, or extensible but not stiff, like rubber. In this Chapter, we present the material characterization of a high performance nanocomposite prepared via the novel solvent exchange approach of Chapter Three composed of synthetic smectic clay, Laponite® RD, and a commercial thermoplastic polyurethane (TPU) elastomer, Elasthane^{TM} 80A.

4.2 Materials and Characterization Methods

4.2.1 Materials

Biomedical polyetherurethane, Elasthane^{TM} 80A was obtained from the Polymer Technology Group, Inc. (Berkeley, CA). Elasthane contains poly(tetramethylene oxide) (PTMO) soft segments and 4,4'-methylene bisphenyl diisocyanate (MDI) hard segments chain extended with 1,4-butanediol (BDO). The hard-to-soft segment ratio of Elasthane 80A is 40:60 wt%, its molecular weight is 290,000 g/mol, and its density is 1.12 g.cm^{-3} [12]. Laponite® RD, a synthetic smectic clay with a density of 2.65 g.cm^{-3} [13] was obtained from Southern Clay Products, Inc. (Gonzales, TX). Dimethylacetamide (DMAc; B.P. 165°C) was obtained from Sigma Aldrich Co. (St. Louis, MO) and used as received. Laponite was dispersed in DMAc via the new solvent exchange procedure [14] explained in the previous Chapter. Solutions of Elasthane, Laponite, and DMAc were prepared from the resulting Laponite-DMAc dispersion. The Elasthane concentration in the solution was maintained at 1.4-1.6 wt%. Elasthane/Laponite nanocomposite films with 120-150 μm thicknesses were prepared in Teflon® containers (6 cm x 4 cm) by controlled evaporation of DMAc. The final Laponite concentration in the dry film was controlled by varying the Laponite concentration in the Laponite-Elasthane-DMAc solution. Note, for a discotic clay such as Laponite, the percolation threshold, $\tilde{\phi}_P$, can be approximated by dividing the random-close-packed hard sphere percolation volume fraction (~0.64) by the aspect-ratio, α, of the clay. Because the diameter and thickness of Laponite platelets are 25 nm and 1nm, respectively, the aspect ratio of Laponite is 25 and the percolation threshold is 2.5 vol% or 6 wt%. The evaporation rate of DMAc was maintained by keeping the films in a closed 60°C oven with a 0.02 m^3.hr^{-1} N_2 purge flow. A constant evaporation rate was maintained for all samples because the physical properties of the dry films were observed to depend on the evaporation rate. The mechanical properties of films prepared at higher evaporation rates proved repeatedly to be inferior (see section 3.5.2.).

4.2.2 Atomic Force Microscopy

Atomic force microscope (AFM) phase images of the nanocomposite samples (which were sandwiched between epoxy and cryo-microtomed) were taken in tapping mode using moderate force (Amplitude Set Point = 0.7 Volts, scale = 60°) and high force (0.3 Volts, 15°) on a Veeco Instruments Dimension 3100 AFM with the same Veeco NanoProbe (130 μm, 280-361 Hz).

4.2.3 Mechanical Characterization

Tensile tests were performed on thin film samples approximately 45 x 5 x 0.1 mm^3 and were carried out on an Zwick/Roell Z010 mechanical tester with a 500 N load cell at a constant crosshead speed of 100% initial length per minute. Dynamic mechanical analysis (DMA) measurements were made at 1 Hz and at a heating rate of $3°C.min^{-1}$ using the TA Instruments Q800 DMA. To demonstrate the thermomechanical integrity of these nanocomposites two films containing 0 and 20 wt% Laponite were held in improvised grips under a constant load equal to 1.08 N (initial stress of 1.75 MPa) and heated from 45°C to 125°C at $\sim 1°C.min^{-1}$. Photographs were captured as the experimental set-up underwent heating in an oven with a transparent window.

4.2.4 Thermal Characterization

Differential scanning calorimetry (DSC) measurements were performed on a TA Instruments Q1000 DSC at heating rate of $10°C.min^{-1}$. The theoretical Laponite concentration in the films was verified by thermogravimetric analysis (TGA). TGA was performed under a $20\ ml.min^{-1}$ N_2 purge at a heating rate of $10°C.min^{-1}$ with a Perkin Elmer TGA7. Multiple samples at each Laponite concentration were prepared and all DMA, DSC, and tensile tests were repeated a minimum of three times. A Carl Zeiss Axioskop 2MAT Polarizing Microscope was used to obtain birefringent images of the nanocomposites.

4.3 Results and Discussion

Elasthane, an elastomeric block-copolymer, is composed of hard segments (HS) and soft segments (SS) which combine to give the TPU moderate stiffness, high rubber-like extensibility, and easy processibility [12, 15] (See Figure 4-1). Thermodynamic incompatibility of the HS and SS drives the polymer system into a two-phase morphology in which hydrogen-bonded, crystalline hard micro-domains form amid the rubbery soft domains. Depending on the specific segmental composition and the interaction between soft and hard segments, the hard micro-domains can form fibrillar, globular, or lamellar structures within a continuous soft matrix or form an interconnected hard domain network [16, 17]. The hard segments (length 3-11 nm [18, 19]) are observed to phase segregate in polyurethanes similar to Elasthane and form hard cylindrical crystalline domains via hydrogen bonding [20]. Because the polyurethane HS has a high melting temperature ($T_{m,HS} > T_{room}$) and the SS has a low glass transition temperature ($T_{g,SS} < T_{room}$), at room temperatures the hard and soft domains are in crystalline and rubbery states, respectively. The stiffness (or elastic modulus, E) and strength (tensile stress at break, σ_{max}) of the TPU increases with HS content while the extensibility (strain at failure, ε_{max}) increases with SS content [18, 21-24]. The flexibility of urethane chemistry enables the chemical structure of the HS and SS domains to be varied to control the thermal transition temperatures and thermomechanical properties of the polyurethane [25, 26]. Synthetically it is difficult to increase the elastic modulus of a polyurethane and maintain its high extensibility, or vice-versa—an increase in one often results in a decrease in the other [15].

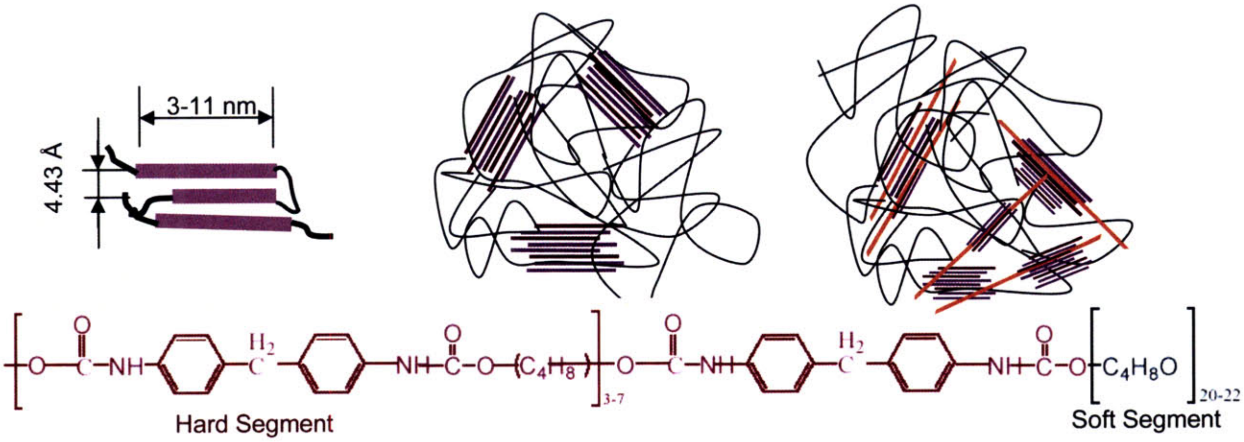

Figure 4-1: Structure of Elasthane 80A and Laponite dispersal within the polyurethane matrix. Elasthane 80A is an elastomeric block-copolymer composed of MDI-BDO hard segments and PTMO soft segments. Hard segments (length 3-11 nm [18, 19]) phase segregate to form hard crystalline domains via hydrogen bonding [20]. The charged Laponite platelets (in orange) preferentially reinforce the polar hard domains.

Recent studies of high performance biomaterials such as spider silk show that araneid spiders modify the stiffness and strength of silk by regulating ordering of polypeptide chains and/or through formation of nano-crystallites during spinning [27, 28]. Following previous polymer nanocomposite work [10, 11, 29, 30], we thus chose to stiffen and strengthen a commercial synthetic TPU with low aspect-ratio clay platelets. Very recently, Finnigan et al. have studied a similar TPU (but with higher soft segment weight fraction and with a spherical morphology) filled with a single weight fraction of clay (3 wt%) [16]. They show that the aspect-ratio of the silicates modifies the mechanical behavior but does not change the phase morphology. To increase E and σ_{max} of Elasthane while maintaining its high ε_{max}, it is necessary to preferentially nanoreinforce the polyurethane hard micro-domains with unmodified Laponite nanoparticles. The stronger affinity of the hydrophilic, non-surface-modified Laponite with the more polar HS rather than with the SS allows the Laponite to segregate into the hard micro-domains during the processing of the TPU. By preferentially restricting the Laponite particles to the hard micro-domains the undesired stiffening of the soft domain is avoided and the large ε_{max} of the polyurethane composite remains uncompromised. To optimize this micro-segregation it is key that the dimension of the discotic clay platelets is similar in magnitude to the natural dimensions of the HS domains that microphase separate (HS length $= 3\text{-}11$ nm [18, 19], Figure 4-1). Consequently, Laponite (diameter, $d = 25$ nm, thickness $l = 1$ nm, aspect-ratio $\alpha = d / l = 25$) is more suitable for the preferential nanoreinforcement of the hard micro-domains than other high aspect-ratio clays (*e.g.* Montmorillonite and Hectorite with d=100-300 nm [29]) that are commonly used in polymer nanocomposites.

AFM phase imaging is often used to distinguish hard and soft micro-domains in polyurethanes because there is often insufficient contrast in electron density between phases and effective staining procedures prove too time-consuming to make TEM effective [31, 32]. Extensive analysis of AFM images showed repeatedly that as more of the high modulus Laponite is added the bright areas brighten and grow in size, indicating that the Laponite imposes a change in hard domain texture. As the Laponite concentration increases the discrete hard micro-domains become interconnected, and in conjunction with the Laponite this accounts for the increased initial modulus and distinct yield point. The bright white regions on the left hand column, which correspond to regions occupied by the very highest modulus moieties on the right, are believed to be a combination of Laponite and hard polyurethane micro-domains at the surface. With AFM it is difficult to distinguish the Laponite platelets from the hard polyurethane micro-domains due to the preferential association of the Laponite and the irregular shape formation of the hard micro-domains. The hard micro-domains in the bulk Elasthane are unlike the fibrillar hard micro-domain structures observed in AFM phase images of piperazine-butanediol-poly(tetramethylene oxide) and hexamethylene diisocyanate-butanediol-poly(ethylene oxide)-poly(propylene oxide)

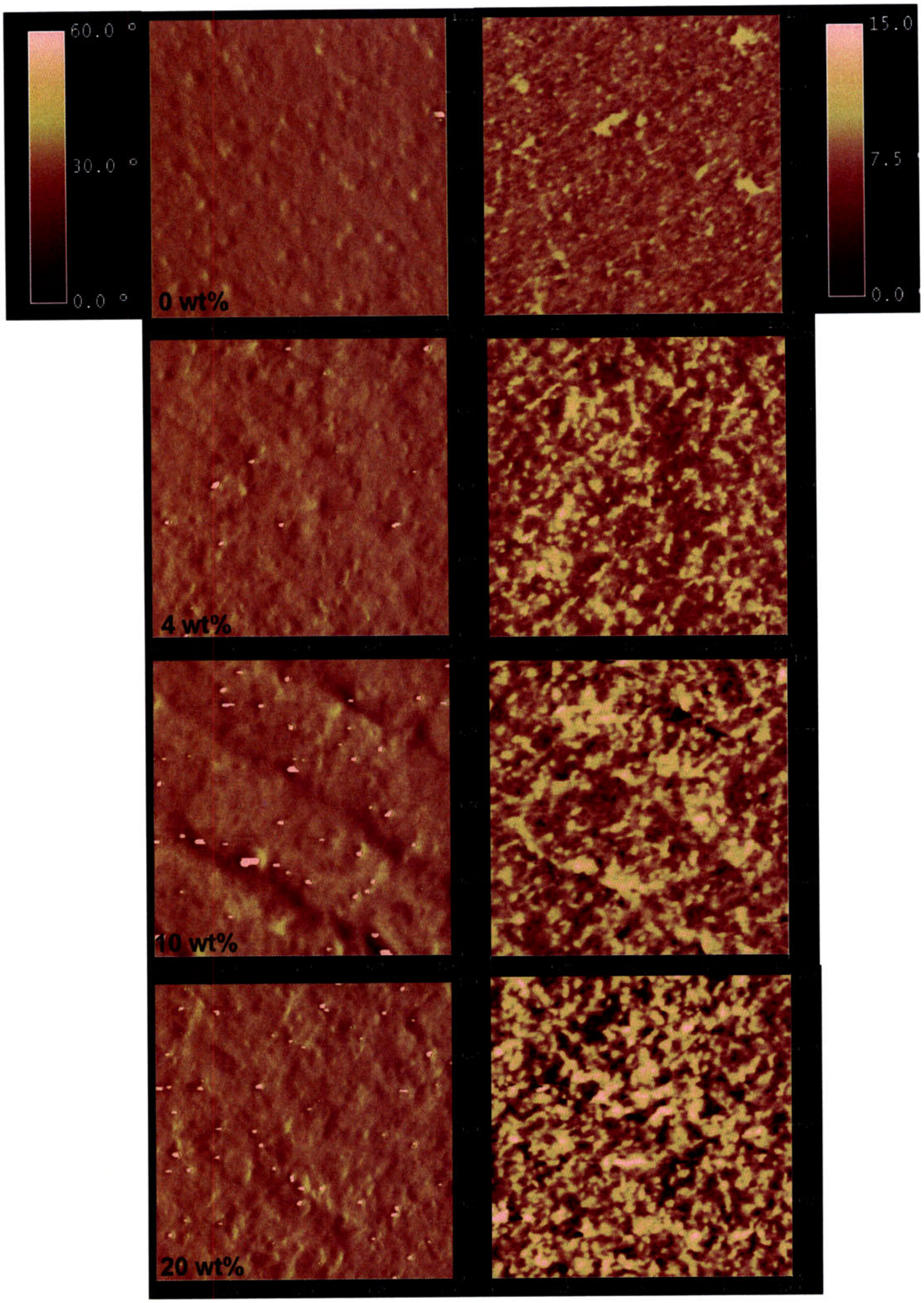

Figure 4-2: Hard and soft micro-domain distribution in nanocomposites containing 0, 4, 10, and 20 wt % Laponite as observed via AFM phase imaging. The same areal extent (1 μm x 1 μm) on each nanocomposite was imaged with moderate tapping force (amplitude set point = 0.7 Volts, scale = 60°, left) and with high tapping force (0.3 Volts, 15°, right). The bright regions correspond to material of high modulus within the softer matrix material.

poly(ethylene oxide) polyurethanes [33] or the large, spherical hard micro-domain structures observed in methylene-bis(cyclohexyl isocyanate)-butanediol-poly(propylene glycol) [34]. The soft domains observed in the present study do not form the irregular spherical soft micro-domains which are observed in AFM phase images of bisphenyl methylene diisocyanate-dendrimer-poly(tetramethylene oxide) polyurethanes [19, 35]. Instead the hard micro-domain morphology observed in these images is similar to the morphology observed by Eisenbach et al. via element-specific electron-microscopy and by McLean and Sauer using tapping-mode AFM in polyurethanes of similar composition [19, 35, 36].

Because Laponite preferentially reinforces the hard micro-domains of Elasthane and concentrations greater than 5.9 wt% induce jamming, the influence on the mechanical properties of Elasthane is profound. The tensile curve of pure Elasthane (ϕ = 0 wt%) shown in Figure 4-3a is similar to that of other TPUs [37, 38] in which three distinguishable deformation regions are readily identified. The first region where the stress, σ, increases linearly with strain, ε, is a region of elastic deformation and is governed by TPU crystallinity, hard segment content and ordering [38].

Yield corresponds to break-up of an interconnected hard domain network and is followed by two distinct regions of plastic deformation [17, 38]. The region of moderate slope is indicative of soft domain deformation plus rotation and alignment of the smaller hard micro-domains. The last region characterized by the steep upturn in the σ-ε curve corresponds to the stretching and strain-induced crystallization of the soft-segments as well as further break-up of the hard micro-domains [17], later discussed in Chapter Five. The addition of Laponite significantly increases the initial modulus of the material and the magnitude of the plateau and ultimate stress, but does not affect the slope of the curve due to soft segment stretching after yield or the slope of the curve due to soft-segment strain-induced crystallization or hardening. However, the onset of plastic deformation and strain-hardening both occur at smaller deformations with increasing Laponite concentration (see Chapter Five).

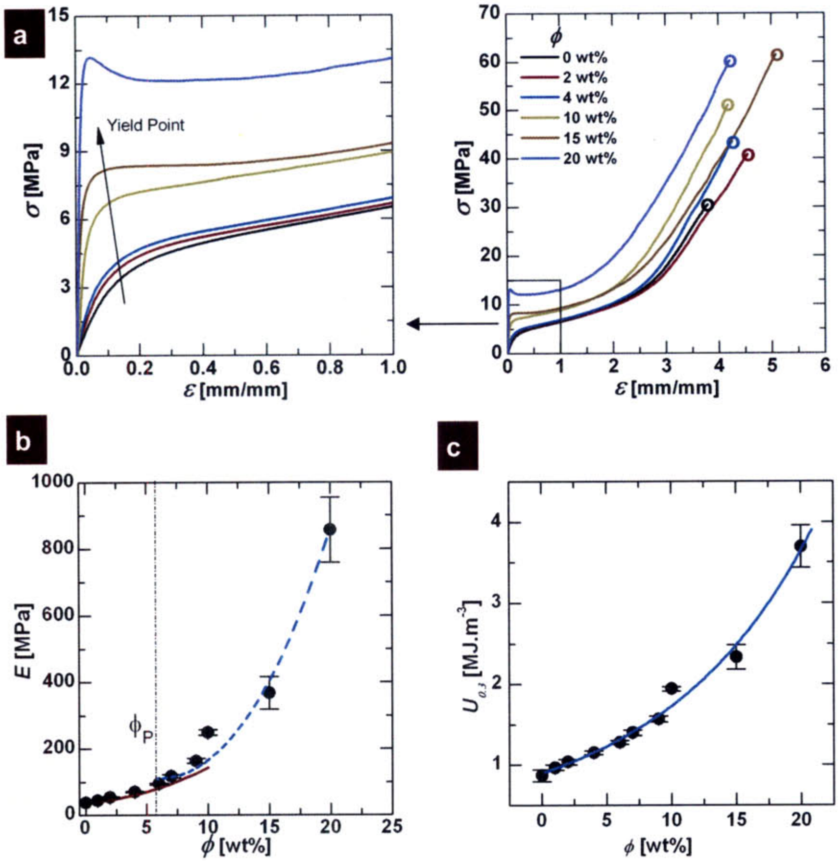

Figure 4-3: Impact of Laponite concentration on the mechanical properties of Elasthane. a, Representative engineering stress-strain (σ–ε) curves of thin film nanocomposites containing between 0 and 20 wt% Laponite. b, Initial elastic modulus, *E*, increases with increasing Laponite concentration, ϕ. For $\phi < \phi_P$ the prediction of Guth's model (Equation 1; red line) is in excellent agreement with experimental values. The agreement of Guth's model using $\alpha = 25$ further demonstrates that the Laponite is completely exfoliated. For $\phi > \phi_P$ the sharp increase in *E* follows the typical scaling (Equation 2; blue dashed-line) of jammed systems[18, 20]. c, Toughness, $U_{0.3}$, (defined as the area under the σ–ε curve up to $\varepsilon = 0.3$) increases quadratically with ϕ (Equation 3; blue line), so $U_{0.3}$ of a nanocomposite containing 20 wt% Laponite is 4.25 times greater than that of pure Elasthane. The error bars in b and c are equal to one standard deviation (minimum of five samples) plus the contribution based on instrument imprecision.

The dramatic impact of Laponite on the elastic modulus of the polyurethane is shown in Figure 4-3. The modulus, *E,* increases with increasing Laponite concentration from 38 MPa at $\phi = 0$ wt% to 70.5 MPa at $\phi = 4$ wt% to 856 MPa at $\phi = 20$ wt%. This 23-fold increase in modulus, and specifically the sharp increase in *E* at $\phi \geq 6$ wt%, is a consequence of the percolative Laponite network. Below ϕ_P the platelets are randomly dispersed with an average inter-particle spacing greater than one particle diameter. Above ϕ_P, the Laponite forms a sample-spanning jammed structure which significantly hinders the mobility of hard and soft micro-domains during imposed deformation. Note the nanocomposites containing 15 and 20 wt% Laponite exhibit a sudden decrease in σ after yield, a behavior typical of glassy polymers [39]. This result corresponds to the sudden collapse of the jammed structure at which point the yield stress exceeds the stress that can be supported by the soft domains without significant reorientation and alignment.

The increase in E below the percolation limit can be modeled by Guth's equation [40] which was extended for anisotropic particles:

$$E = E_0(1 + 0.67\alpha\tilde{\phi} + 1.62\alpha^2\tilde{\phi}^2), \quad \text{for } \tilde{\phi} < \tilde{\phi}_P \qquad (4.1)$$

Above the percolation limit, a power law scaling typical of jammed systems, such as gels [36] and glasses [41], is observed:

$$E = E_1 + A(\tilde{\phi} - \tilde{\phi}_P)^n \quad \text{for } \tilde{\phi} > \tilde{\phi}_P \qquad (4.2)$$

where $\tilde{\phi}$ is the volume fraction of Laponite, $\tilde{\phi}_P$ is the percolation threshold volume fraction of Laponite, E_0 is the elastic modulus of pure Elasthane, and A and n are model parameters. The predicted values of E using Eq. 4.1 with E_0 = 38 MPa and $\alpha = 25$ agree with experimental data. The aspect ratio, $\alpha = 25$, of a single Laponite platelet further indicates that the Laponite platelets are fully exfoliated. Above the percolation threshold Eq. 4.2 is used with $\{E_1, A, n\}$ = {110 MPa, 1.54x10^5 MPa, 2}. This power-law scaling is typical of critical-like behavior systems. While this behavior is similar to equilibrium critical phenomena, jamming is clearly a non-equilibrium transition [36]. The scaling factor, n, depends on numerous system properties including particle size, shape, polydispersity, and the particle-particle interaction potential [36, 41]. The magnitude of the scaling factor increases with the extent of particle-particle interactions [42]. As shown in Figure 4-3c the toughness at ε = 0.3 increases quadratically with $\tilde{\phi}$ in a manner similar to the Guth prediction for modulus. Thus

$$U_{0.3} = U_{0.3}^0\left(1 + 0.415\alpha\tilde{\phi} + 0.345\alpha^2\tilde{\phi}^2\right) \qquad (4.3)$$

where $U_{0.3}^0$ = 0.916 MJ.m^{-3} and $U_{0.3}$ increases from 0.86 MJ.m^{-3} at ϕ = 0 wt% to 3.7 MJ.m^{-3} at ϕ = 20 wt%.

The impact of Laponite concentration on the extensibility (ε_{max}), strength (σ_{max}), and overall toughness (U_{max}) is not as dramatic. There is no significant change in the extensibility (ε_{max}) of Elasthane with Laponite—all nanocomposites exhibit $\varepsilon_{max} = 4.23 \pm 0.4$. This suggests that the ultimate extensibility of the elastic network of soft domains is not compromised by reinforcing the hard domains. Both σ_{max} and U_{max} increase when Laponite is added to Elasthane. In comparison, other elastomeric nanocomposites reinforced with either smectic clays [20, 43-45], carbon nanotubes [46], or fullerene [47] have only exhibited up to a six-fold increase in E and these enhancements are often accompanied by reductions in either ε_{max}, σ_{max}, or both. In the Elasthane/Laponite nanocomposite, the ultimate tensile strength σ_{max} plateaus at $\phi = 10$ wt%, exhibiting a 50% increase from 32 MPa at $\phi = 0$ wt% to 50 MPa at $\phi = 10$ wt%. Similarly, U_{max} plateaus at $\phi = 15$ wt% and exhibits a 100% increase, raising U_{max} from 48 MJ m^{-3} at $\phi = 0$ wt% to 95 MJ m^{-3} at $\phi = 15$ wt%. The Laponite toughens the Elasthane matrix in a manner similar to that in which hard, crystalline, mineral platelets toughen bone and nacre [7, 48]. The successful toughening of the Elasthane with Laponite is a result of the strong affinity, and consequent strong interfacial adhesion, of the Laponite with the polyurethane hard domain.

The 23-fold increase in E and increase in σ_{max}, $U_{0.3}$ and U_{max} (without a concomitant reduction in ε_{max}, or any change in the slope of the tensile curve during strain-hardening) arises because the Laponite is preferentially embedded within the polyurethane hard micro-domains rather than in the soft domain and drives interconnections between the hard micro-domains as observed with AFM (Figure 4-2). As shown in Figure 4-4a and Figure 4-5 the insignificant change in the soft segment glass transition temperature, $T_{g,SS}$, combined with the large increase in heat distortion temperature (HDT) and large increase in the magnitude of the flexural storage modulus, $E'(\phi, T)$, for temperatures $T > T_{g,SS}$, confirms that Laponite platelets are preferentially embedded in the hard micro-domains. Only at $\phi \geq 15$ wt% does Laponite begin to observably enter the soft domains of the Elasthane and induce soft segment crystallinity.

In addition to identifying the location of preferential nanoreinforcement, the dynamic mechanical analysis (DMA) data for the various nanocomposites depicted in Figure 4-4b elucidates the influence of Laponite concentration on the flexural storage modulus, $E'(\phi, T)$.

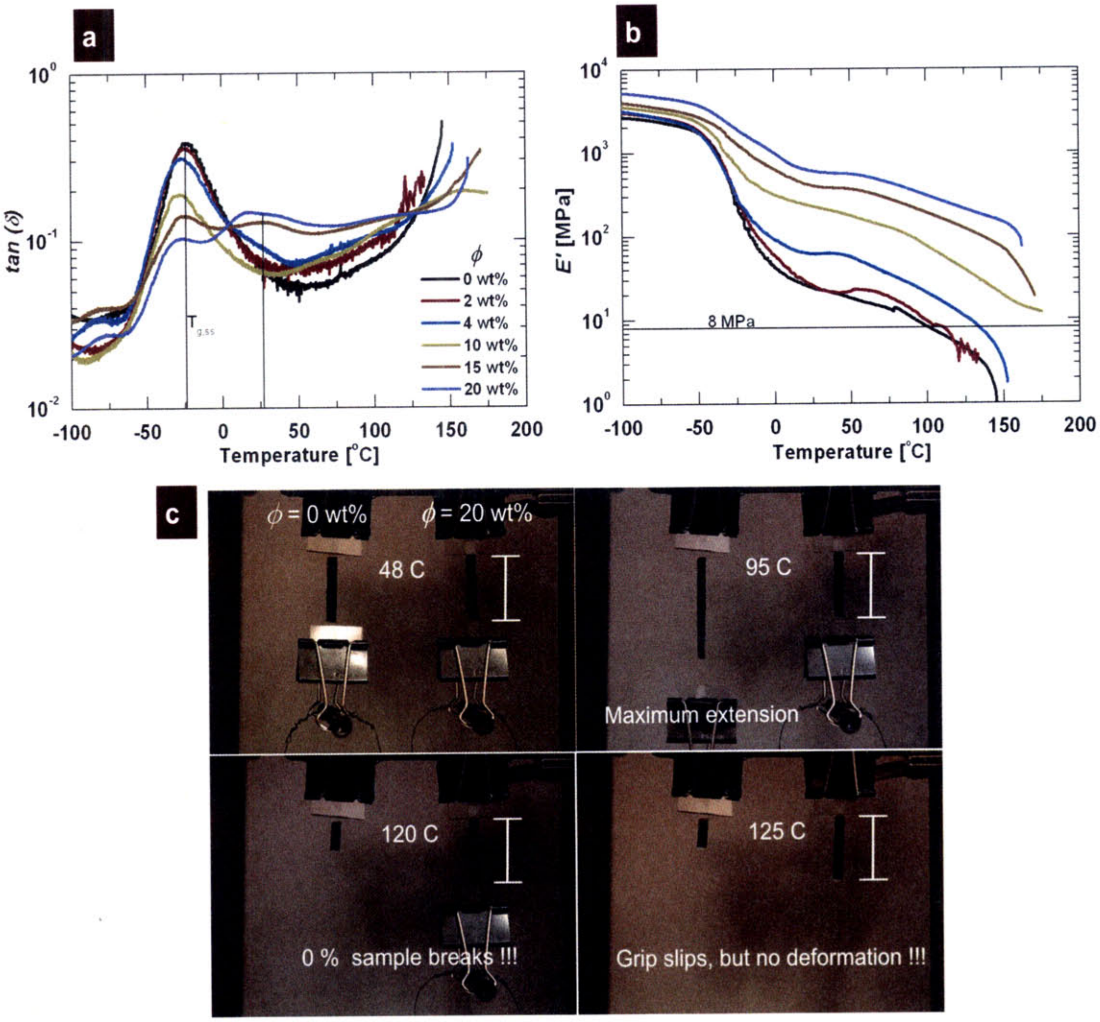

Figure 4-4: Impact of Laponite concentration on the thermomechanical properties of Elasthane. a, The ratio of the flexural storage modulus to the loss modulus at various temperatures, or *tan(δ)* curve, for nanocomposites containing between 0 and 20 wt% Laponite measured by Dynamic Mechanical Analysis (DMA). The soft segment glass transition temperature ($T_{g,SS}$), indicated by the peak at –25°C in the curve, does not change significantly with increasing ϕ. A new peak at 29°C observed in nanocomposites with $\phi \geq 15$ wt% suggests the onset of crystallization in soft domains. Equivalent transitions also appear in the DSC data shown in Figure 4-5. b, Increasing the concentration of Laponite in the nanocomposite does not significantly change the magnitude of the flexural storage modulus (E') prior to the onset of the soft segment glass transition at –50°C. Above this temperature the magnitude of E' increases significantly with ϕ. The steep fall in E' at high temperatures ($T > 130$°C) is due to the softening of the Elasthane caused by the melting of the hard domains. The heat distortion temperatures (HDT), which may be defined as the temperature at which $E' = 8$ MPa (see ISO 75—method C) for nanocomposites with $\phi = 0$, 2, 4, 8, 10, and 20 wt% are 101,111, 134, 161, >160, >200°C, respectively. The exact values of the HDT for nanocomposites with $\phi > 10$ wt% could not be measured due to instrument limitations. c, Demonstration of the mechanical enhancement of Elasthane at high temperature by the addition of Laponite (See Appendix A-1). The pure Elasthane exhibits little resistance to heat distortion, deforming significantly with increase in temperature, reaching the maximum allowable extension at 95°C, and finally breaking at 120°C. The nanocomposite containing 20 wt% Laponite resists heat distortion and does not show visually any deformation upon heating; however, at 125°C the grips slipped from the sample. Length of scale bar: 46 mm.

The magnitude of the rubbery plateau modulus at 25°C scales like the elastic modulus, *E*, and exhibits a 25-fold enhancement from $E' = 24$ MPa at $\phi = 0$ wt% to $E' = 600$ MPa at $\phi = 20$ wt%. Again, this enhancement is due to the percolative network established by the exfoliated Laponite platelets which are preferentially embedded within the TPU hard micro-domains. Consequently, the addition of Laponite to shape memory polyurethanes may significantly improve performance, offering a means to enhance the rubbery modulus and thus the restoring force [10] without changing the glass transition temperature.

The addition of 20 wt% Laponite to Elasthane induces an increase in the HDT of more than 100°C. This allows the nanocomposite to be used potentially in higher temperature applications without risk of permanent sagging or deformation. Figure 4-4c and the movie in Appendix A-1 illustrate that under a constant load Elasthane films elongate by more than 100% and break at 120°C. In contrast, thin films containing 20 wt% Laponite exhibit no deformation at temperatures as high as 125°C. Furthermore, because the Laponite platelets are not organically modified, TGA shows that there is no risk of thermal degradation or decomposition at temperatures below 250°C (Figure 4-6).

Further investigation is necessary to determine what thermo-physical mechanism is responsible for the dramatic increase of the HDT when Laponite is added to the polyurethane—presumably both the percolative Laponite network and the enhancement in magnitude and intensity of the hard segment melting temperature which is observed in DSC data (Figure 4-5) play a role. In general, the melting temperature of a material increases if the intermolecular cohesive bonds holding the material together are strengthened, and the intensity of a hard segment melting endotherm increases when the crystallite is more perfect [39]. Consequently, Laponite platelets must amplify a crystalline morphology with the hard micro-domains which accounts for the HS strengthening and the enhancement in melting endotherm intensity.

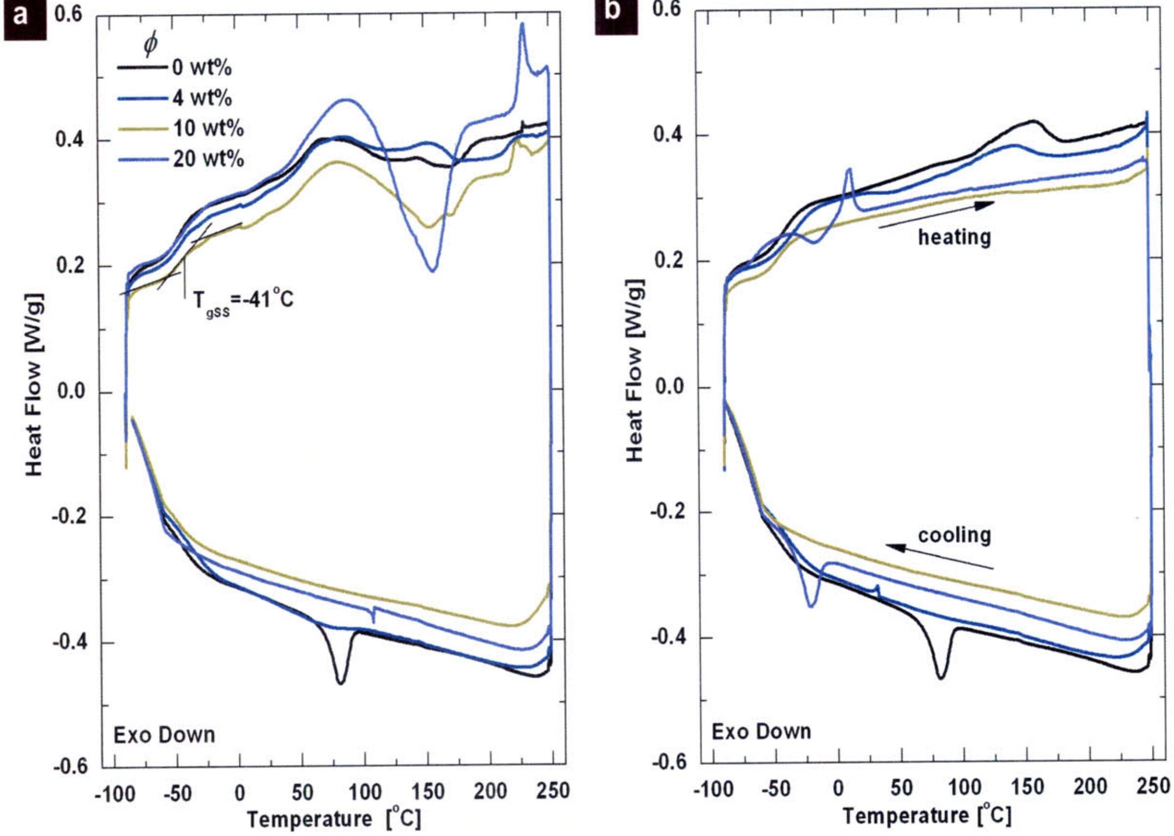

Figure 4-5: DSC of the nanocomposites containing 0, 4, 10, and 20 wt% Laponite. a, DSC curves during the first heating and cooling cycle show both reversible and irreversible transitions. b, Subsequent heating and cooling cycles show reversible transitions. Pure Elasthane exhibits a reversible hard segment melting endotherm and crystallization exotherm at 150°C and 77°C, respectively, which agree with the values reported in literature. With increasing Laponite concentration, ϕ, this peak reduces in intensity, and finally disappears in nanocomposites with $\phi > 6$ wt%. This behavior is attributed to the restricted motion of the hard segments due to the disruption by and jamming of Laponite above the percolation concentration ($\phi_P = 5.9$ wt%). Furthermore, an irreversible melting peak observed in the first heating cycle near 227°C is not observed in the samples during the subsequent heating cycles. The increased intensity of this peak is attributed to interactions between the hard segment and the Laponite since the peak intensity increases with ϕ. The origin of the broad dip in the first heating cycle near 150°C observed in the 10 wt% and 20 wt% nanocomposite thermograms cannot be resolved but may result from soft segment and Laponite interactions. The glass transition temperature of the soft segment, $T_{g,SS}$ at -41°C does not change, but nanocomposites with $\phi \geq 15$ wt% exhibit an interphase reversible melting/crystallization peak at 10°C and –25°C during the heating and cooling cycles, respectively. Similar results are observed in DMA measurements (Figure 4-4a).

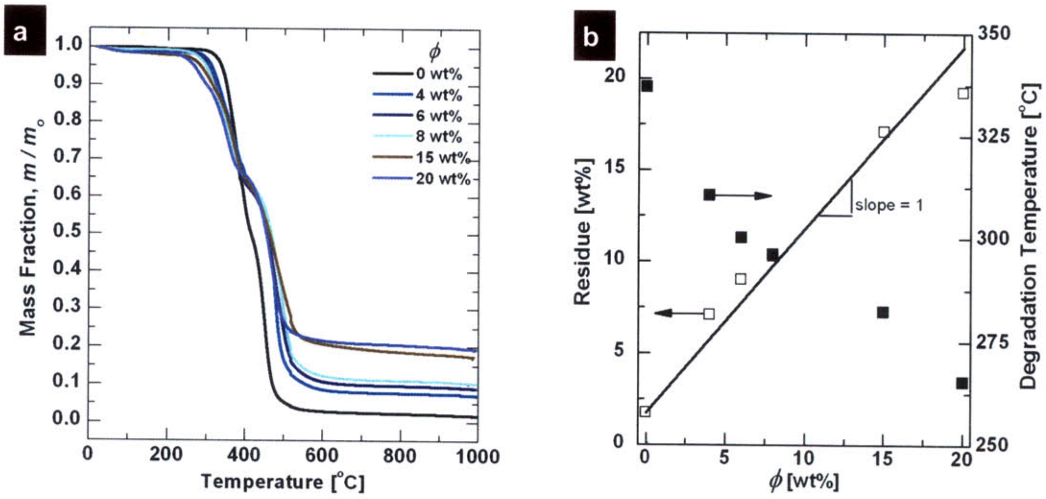

Figure 4-6: Laponite concentration and impact on thermal degradation. a, Thermogravimetric analysis (TGA) of nanocomposites containing 0 to 20 wt% Laponite. The rapid loss in weight at T = 350°C is due to the degradation of the Elasthane. b, Residue weight fraction at 1000°C of the various nanocomposites is nearly equal to the weight fraction of Laponite blended with Elasthane in each case. This is demonstrated by the agreement of the experimental data with a line of slope one. Increasing Laponite fraction decreases the thermal degradation temperature which is defined as the temperature at which the sample weight decreases by 5%.

Microscopic images of the nanocomposite films taken under cross-polarized light like those depicted in Figures 4-7 and 4-8 help to elucidate the influence of Laponite on the morphology of the polyurethane nanocomposite. The local mechanical properties and morphology of the ordered domains and the amorphous matrix are very different from one another. The birefringence and fractal-like shape of the ordered domains depicted in Figure 4-7b and Figure 4-8 suggest a quenched phase transition process [49]. The spatial scale of these ordered domains (20-100 μm) is much larger than the size of the hard micro-domains (20-175 nm) [20, 31]. The fraction of the image area occupied by these ordered-domains increases slightly with ϕ; however, this increase was close to the sample-to-sample variation with the same ϕ. As shown in Figure 4-7a, there is a rapid reduction in the fractional area of bright regions upon heating between 100°C and 120°C. This transition is similar to the local melting transition in thermotropic liquid-crystalline polymers. This long-range ordering is the result of an isotropic-nematic (I-N) transition of the hard micro-domains with, and without, the Laponite discs. Upon annealing the samples at 60°C, new, ordered, crystalline domains appeared after numerous days of annealing as shown in Figure

4-7c. This re-crystallization behavior was not observed in the pure Elasthane sample even after annealing for many days.

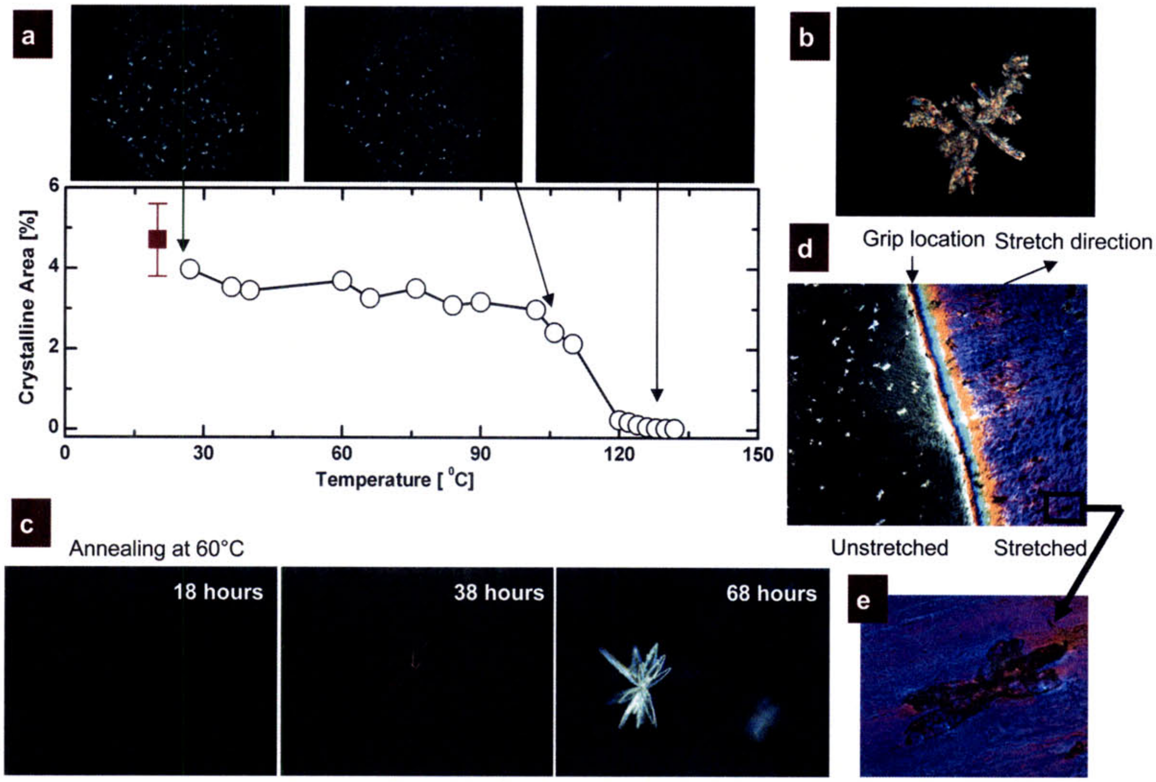

Figure 4-7: Evidence of long range order or crystallization in the nanocomposites is apparent in images obtained with a cross-polarized microscope. a, Bright crystalline domains in a nanocomposite containing 20 wt% Laponite are due to the long-range ordering of the Elasthane hard domains. b, The fractal-like shape of the crystalline domains is typical of a quenched phase transformation. Upon heating, the bright domains undergo a nematic-isotropic transition between 100 and 120°C. c, Crystalline domains reappeared upon annealing the sample for a few days at 60°C. d, Birefringent image of a nanocomposite containing 10 wt% Laponite after tensile testing. The unstretched region on the left side of the grip line exhibits these same bright domains. Upon stretching the amorphous matrix becomes birefringent as a result of strain induced alignment and crystallization of the polymer chains during plastic deformation[50]. e, The ordered domains become disordered upon stretching as evidenced by the darkening of these previously bright domains. Similar birefringence results are also obtained in pure Elasthane films. Image widths are as follow: (a) 2700 μm, (b) 337 μm, (c) 270 μm, (d) 2700 μm, and (e) 337 μm.

The re-crystallization behavior is again similar to that observed in thermotropic liquid-crystalline polymers in which mesogens are chemically attached to the polymer chains [51]. In our nanocomposites it appears that the Laponite platelets act as mesogens that are physically embedded in the hard micro-domains rather than chemically attached to the polymer chain.

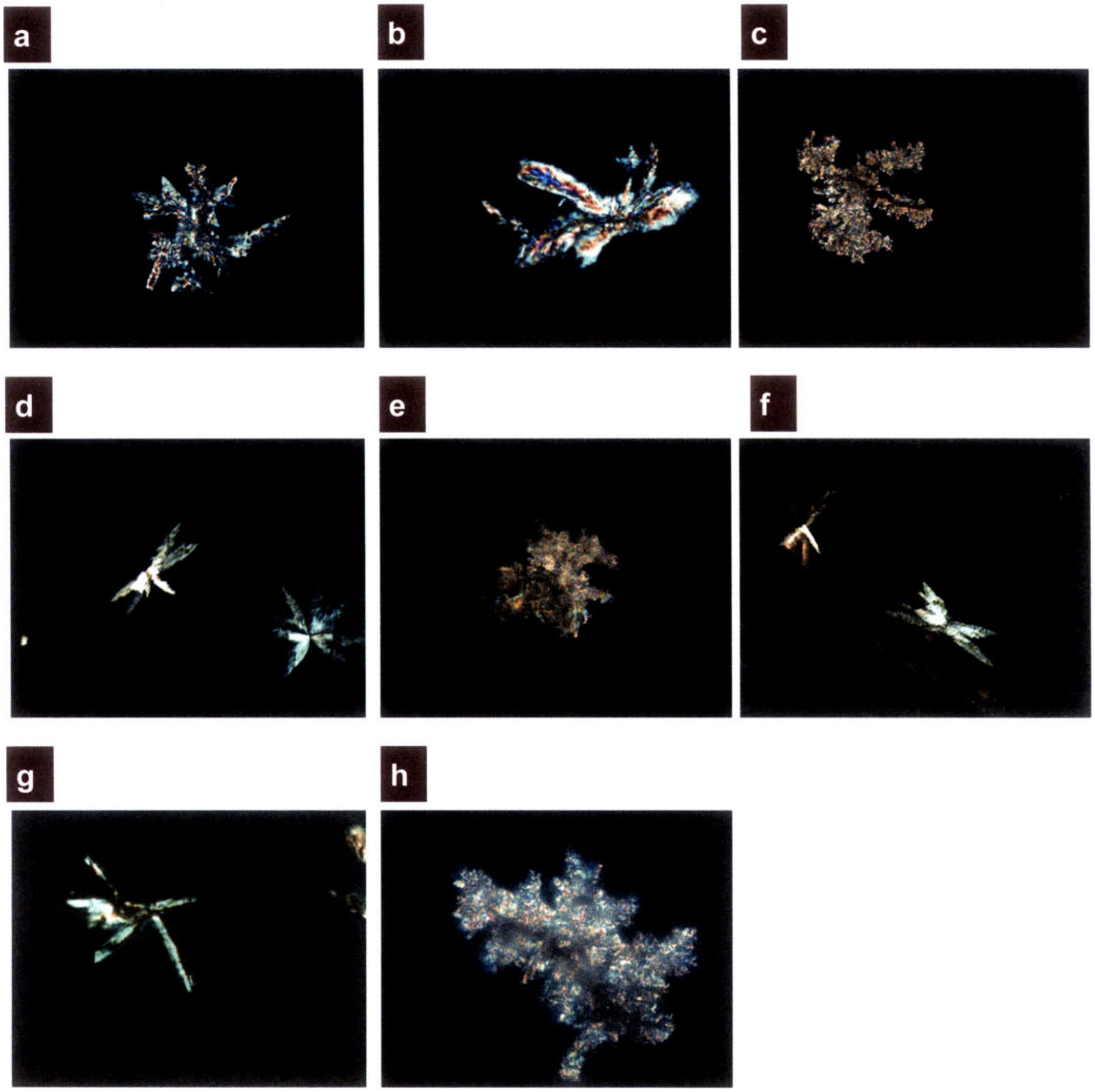

FIGURE 4-8: Polarized optical microscopy images of the ordered, fractal-like domains in various nanocomposite films exhibit birefringence. Image width is as follows: (a) 270 μm, (b) 135 μm, (c) 675 μm, (d) 270 μm, (e) 675 μm, (f) 270 μm, (g) 135μm, and (h) 337 μm.

These ordered domains did not exhibit the Maltese cross pattern indicative of spherulites observed in some polyurethane systems [31]. Spherulites which consist of numerous crystallites that grow radially outward form spheres that measure approximately 10 μm in diameter [39]. Instead these ordered domains maintain non-descript, fractal-like shapes that measure approximately 200 μm in size until they are disrupted by stretching. After stretching the amorphous matrix becomes birefringent via strain induced alignment and crystallization of the polymer chains during plastic deformation [50]. The ordered domains become disordered during stretching as evidenced by the darkening of the previously bright fields (Figures 4-7d-e).

4.4 Conclusion

The new solvent exchange method outlined in Chapter Three allows block-copolymers with polar constituents, like thermoplastic polyurethanes, to be preferentially nanoreinforced with organic nanoparticles, like smectic clays. The efficacy of nanoreinforcement on thermomechanical properties hinges upon the close matching of characteristic length scale and the adhesion of the nanoparticles to the targeted polymer phase morphology. The hierarchical order induced by the addition of discotic Laponite platelets creates a percolated network that significantly stiffens and toughens the elastomer without reducing its extensibility. The use of block polarity in conjunction with this solvent exchange approach and processing techniques, such as electrospinning (later discussed in Chapter Seven), offers an avenue toward the development of high performance materials that rival natural materials. Furthermore, the addition of Laponite to shape memory polyurethanes or other actuating polymers may significantly improve performance, offering a means to enhance the restoring force without changing the glass transition temperature.

4.5 References

[1] E. Manias, "Stiffer by design," *Nature Materials*, vol. 6, pp. 9-11, 2007.

[2] D. P. Knight and F. Vollrath, "Biological liquid crystal elastomers," *Philosophical Transactions of the Royal Society of London Series B-Biological Sciences*, vol. 357, pp. 155-163, 2002.

[3] F. Vollrath and D. P. Knight, "Liquid crystalline spinning of spider silk," *Nature*, vol. 410, pp. 541-548, 2001.

[4] Y. Termonia, "Molecular Modeling of Spider Silk Elasticity," *Macromolecules*, vol. 27, pp. 7378-7381, 1994.

[5] A. H. Simmons, C. A. Michal, and L. W. Jelinski, "Molecular orientation and two-component nature of the crystalline fraction of spider dragline silk," *Science*, vol. 271, pp. 84-87, 1996.

[6] J. D. van Beek, L. Beaulieu, H. Schafer, M. Demura, T. Asakura, and B. H. Meier, "Solid-state NMR determination of the secondary structure of Samia cynthia ricini silk," *Nature*, vol. 405, pp. 1077-1079, 2000.

[7] H. J. Gao, B. H. Ji, I. L. Jager, E. Arzt, and P. Fratzl, "Materials become insensitive to flaws at nanoscale: Lessons from nature," *Proceedings of the National Academy of Sciences of the United States of America*, vol. 100, pp. 5597-5600, 2003.

[8] B. L. Smith, T. E. Schaffer, M. Viani, J. B. Thompson, N. A. Frederick, J. Kindt, A. Belcher, G. D. Stucky, D. E. Morse, and P. K. Hansma, "Molecular mechanistic origin of the toughness of natural adhesives, fibres and composites," *Nature*, vol. 399, pp. 761-763, 1999.

[9] J. Gosline, P. Guerette, C. Ortlepp, and K. Savage, "The mechanical design of spider silks: from fibroin sequence to mechanical function," *J Exp Biol*, vol. 202, pp. 3295-3303, 1999.

[10] H. Koerner, G. Price, N. A. Pearce, M. Alexander, and R. A. Vaia, "Remotely actuated polymer nanocomposites - stress-recovery of carbon-nanotube-filled thermoplastic elastomers," *Nature Materials*, vol. 3, pp. 115-120, 2004.

[11] R. A. Vaia and H. D. Wagner, "Framework for nanocomposites," *Materials Today*, vol. 7, pp. 32-37, 2004.

[12] M. J. Wiggins, M. MacEwan, J. M. Anderson, and A. Hiltner, "Effect of soft-segment chemistry on polyurethane biostability during in vitro fatigue loading," *Journal Of Biomedical Materials Research Part A*, vol. 68A, pp. 668-683, 2004.

[13] I. Grillo, P. Levitz, and T. Zemb, "Insertion of small anisotropic clay particles in swollen lamellar or sponge phases of nonionic surfactant," *European Physical Journal E*, vol. 5, pp. 377-386, 2001.

[14] N. Kumar, S. M. Liff, and G. H. McKinley, "Method to disperse and exfoliate nanoparticles," U. S. P. Office, Ed. United States: Massachusetts Institute of Technology, Filed October 18, 2005.

[15] M. Szycher, *Szycher's handbook of polyurethanes*. Boca Raton: CRC Press, 1999.

[16] B. Finnigan, K. Jack, K. Campbell, P. Halley, R. Truss, P. Casey, D. Cookson, S. King, and D. Martin, "Segmented polyurethane nanocomposites: Impact of controlled particle size nanofillers on the morphological response to uniaxial deformation," *Macromolecules*, vol. 38, pp. 7386-7396, 2005.

[17] F. Yeh, B. S. Hsiao, B. B. Sauer, S. Michel, and H. W. Siesler, "In-situ studies of structure development during deformation of a segmented poly(urethane-urea) elastomer," *Macromolecules*, vol. 36, pp. 1940-1954, 2003.

[18] D. J. Martin, G. F. Meijs, P. A. Gunatillake, S. P. Yozghatlian, and G. M. Renwick, "The influence of composition ratio on the morphology of biomedical polyurethanes," *Journal of Applied Polymer Science*, vol. 71, pp. 937-952, 1999.

[19] C. D. Eisenbach, A. Ribbe, and C. Gunter, "Morphological-Studies Of Model Polyurethane Elastomers By Element-Specific Electron-Microscopy," *Macromolecular Rapid Communications*, vol. 15, pp. 395-403, 1994.

[20] B. Finnigan, D. Martin, P. Halley, R. Truss, and K. Campbell, "Morphology and properties of thermoplastic polyurethane nanocomposites incorporating hydrophilic layered silicates," *Polymer*, vol. 45, pp. 2249-2260, 2004.

[21] H. D. Kim, T. J. Lee, J. H. Huh, and D. J. Lee, "Preparation and properties of segmented thermoplastic polyurethane elastomers with two different soft segments," *Journal of Applied Polymer Science*, vol. 73, pp. 345-352, 1999.

[22] B. R. Nair, V. G. Gregoriou, and P. T. Hammond, "FT-IR studies of side chain liquid crystalline thermoplastic elastomers," *Polymer*, vol. 41, pp. 2961-2970, 2000.

[23] H. Yeganeh and M. A. Shamekhi, "Poly(urethane-imide-imide), a new generation of thermoplastic polyurethane elastomers with enhanced thermal stability," *Polymer*, vol. 45, pp. 359-365, 2004.

[24] J. L. Stanford, R. H. Still, and A. N. Wilkinson, "Effects of soft-segment prepolymer functionality on structure - property relations in RIM copolyurethanes," *Polymer*, vol. 44, pp. 3985-3994, 2003.

[25] A. J. Ryan, J. L. Stanford, and A. J. Birch, "Copolyureas formed by reaction injection moulding: correlations between chemical structure, thermal properties and microphase separation," *Polymer*, vol. 34, pp. 4874-4881, 1993.

[26] D. K. Lee and H. B. Tsai, "Properties of segmented polyurethanes derived from different diisocyanates," *Journal of Applied Polymer Science*, vol. 75, pp. 167-174, 2000.

[27] D. P. Knight, M. M. Knight, and F. Vollrath, "Beta transition and stress-induced phase separation in the spinning of spider dragline silk," *International Journal Of Biological Macromolecules*, vol. 27, pp. 205-210, 2000.

[28] D. Porter, F. Vollrath, and Z. Shao, "Predicting the mechanical properties of spider silk as a model nanostructured polymer," *European Physical Journal E*, vol. 16, pp. 199-206, 2005.

[29] S. Sinha Ray and M. Okamoto, "Polymer/layered silicate nanocomposites: a review from preparation to processing," *Progress in Polymer Science*, vol. 28, pp. 1539-1641, 2003.

[30] E. T. Thostenson, C. Li, and T.-W. Chou, "Nanocomposites in context," *Composites Science and Technology*, vol. 65, pp. 491-516, 2005.

[31] A. Aneja and G. L. Wilkes, "A systematic series of 'model' PTMO based segmented polyurethanes reinvestigated using atomic force microscopy," *Polymer*, vol. 44, pp. 7221-7228, 2003.

[32] L. T. J. Korley, B. D. Pate, E. L. Thomas, and P. T. Hammond, "Effect of the degree of soft and hard segment ordering on the morphology and mechanical behavior of semicrystalline segmented polyurethanes," *Polymer*, vol. 47, pp. 3073-3082, 2006.

[33] M. Song, H. S. Xia, K. J. Yao, and D. J. Hourston, "A study on phase morphology and surface properties of polyurethane/organoclay nanocomposite," *European Polymer Journal*, vol. 41, pp. 259-266, 2005.

[34] C. P. Chen, S. A. Dai, H. L. Chang, W. C. Su, T. M. Wu, and R. J. Jeng, "Polyurethane elastomers through multi-hydrogen-bonded association of dendritic structures," *Polymer*, vol. 46, pp. 11849-11857, 2005.

[35] R. S. McLean and B. B. Sauer, "Tapping-mode AFM studies using phase detection for resolution of nanophases in segmented polyurethanes and other block copolymers," *Macromolecules*, vol. 30, pp. 8314-8317, 1997.

[36] V. Trappe, V. Prasad, L. Cipelletti, P. N. Segre, and D. A. Weitz, "Jamming phase diagram for attractive particles," *Nature*, vol. 411, pp. 772-775, 2001.

[37] H. S. Lee, S. R. Yoo, and S. W. Seo, "Domain and segmental deformation behavior of thermoplastic elastomers using synchrotron SAXS and FTIR methods," *Journal of Polymer Science Part B-Polymer Physics*, vol. 37, pp. 3233-3245, 1999.

[38] C. B. Wang and S. L. Cooper, "Morphology and properties of segmented polyether polyurethaneureas," *Macromolecules*, vol. 16, pp. 775-786, 1983.

[39] R. J. Young and P. A. Lovell, *Introduction to Polymers*, 2nd ed. London: Chapman and Hall, 1991.

[40] E. Guth, "Theory of filler reinforcement," *Journal of Applied Physics*, vol. 16, pp. 20-25, 1945.

[41] C. S. O'Hern, L. E. Silbert, A. J. Liu, and S. R. Nagel, "Jamming at zero temperature and zero applied stress: The epitome of disorder," *Physical Review E (Statistical, Nonlinear, and Soft Matter Physics)*, vol. 68, pp. 011306, 2003.

[42] B. N. H. Wang, *Rheological and morphological characterization of hierarchically nanostructured materials*, Ph.D. in Chemical Engineering, Cambride, MA:Massachusetts Institute of Technology, 2007.

[43] X. H. Dai, J. Xu, X. L. Guo, Y. L. Lu, D. Y. Shen, N. Zhao, X. D. Luo, and X. L. Zhang, "Study on structure and orientation action of polyurethane nanocomposites," *Macromolecules*, vol. 37, pp. 5615-5623, 2004.

[44] Z. S. Petrovic, I. Javni, A. Waddon, and G. Banhegyi, "Structure and properties of polyurethane-silica nanocomposites," *Journal of Applied Polymer Science*, vol. 76, pp. 133-151, 2000.

[45] I. Rhoney, S. Brown, N. E. Hudson, and R. A. Pethrick, "Influence of processing method on the exfoliation process for organically modified clay systems. I. Polyurethanes," *Journal of Applied Polymer Science*, vol. 91, pp. 1335-1343, 2004.

[46] M. D. Frogley, D. Ravich, and H. D. Wagner, "Mechanical properties of carbon nanoparticle-reinforced elastomers," *Composites Science and Technology*, vol. 63, pp. 1647-1654, 2003.

[47] T. Zhang, K. Xi, X. Yu, M. Gu, S. Guo, B. Gu, and H. Wang, "Synthesis, properties of fullerene-containing polyurethane-urea and its optical limiting absorption," *Polymer*, vol. 44, pp. 2647-2654, 2003.

[48] Z. Y. Tang, N. A. Kotov, S. Magonov, and B. Ozturk, "Nanostructured artificial nacre," *Nature Materials*, vol. 2, pp. 413-U8, 2003.

[49] I. Dierking, "Liquid crystalline fractals: dilatation invariant growth structures in the phase ordering process of 'banana-phases'," *Liquid Crystals Today*, vol. 12, pp. 1-10, 2003.

[50] K. Kojio, S. Nakamura, and M. Furukawa, "Effect of side methyl groups of polymer glycol on elongation-induced crystallization behavior of polyurethane elastomers," *Polymer*, vol. 45, pp. 8147-8152, 2004.

[51] D. Acierno, E. Amendola, C. Carfagna, S. Concilio, P. Iannelli, L. Incarnato, and P. Scarfato, "Synthesis and characterisation of a nematic homo-polyurethane," *Polymer*, vol. 44, pp. 4949-4958, 2003.

5. Influence of Nano-Clay on Morphology and Mechanics of High Performance Elastomeric Nanocomposites

5.1 Introduction

Hierarchical order induced by the addition of discotic platelets creates a percolated network that significantly stiffens and toughens an elastomer without reducing its extensibility when its hard micro-domains are preferentially reinforced. As is described in Chapter 4, the addition of 20 wt% Laponite not only increases the initial modulus of Elasthane 23-fold, but strengthens and toughens the commercial polyurethane and induces an increase in the heat distortion temperature of more than 100°C. The remarkable thermomechanical enhancement and hierarchical order exhibited in this model segmented, block-copolymer polyurethane nanocomposite prompts two questions: (1) what thermo-physical interactions between nano-clay and elastomeric thermoplastic polyurethane are taking place? and (2) can these thermo-physical interactions be exploited further?

To answer these questions, the Laponite-hard micro-domain morphology during deformation is interrogated and evaluated and extensive mechanical testing and characterization completed. Quantifying the influence of nano-clay on the hysteresis, time-dependence and stress-softening behavior typical of elastomers is imperative for these materials to be utilized in thermomechanical applications. Furthermore, by utilizing various characterization techniques, i.e. x-ray scattering, fourier transform infrared spectroscopy, and cross-polarized microscopy in conjunction with various mechanical tests, the local orientational changes of Laponite within the thin film and the influence of the nano-clay on the soft and hard micro-domains can be inferred.

Small and wide angle x-ray scattering allows the spacing between hard micro-domains and the spacing between Laponite platelets and between hard segments to be determined as well as the extent of soft segment orientation [1-4]. Using x-ray scattering with in situ stretching allows the spacing between the Laponite platelets, hard segments, and hard micro-domains to be interrogated as the thin film is progressively deformed. Song et al have completed a small angle x-ray scattering (SAXS) study in which they found that within the elastic regime of the matrix material the *d*-spacing of the clay platelets varied in a reversible manner, increasing upon deformation but recovering to the original spacing upon removal of the imposed load [4]. Ultimately, the pairs of platelets with interspersed polymers acted as tiny nano-springs. Quantifying the variation in the resultant platelet *d*-spacing, soft segment orientation, and hard segment spacing with respect to macro-scale deformation when the nano-clay is preferentially embedded with the polyurethane hard micro-domains allows the physical influence of the nano-clay to be determined.

Not only is x-ray scattering with in situ stretching useful, but FTIR and cross-polarized light microscopy can be used to correlate morphological changes in the jammed Laponite network to the thermomechanical behavior. By monitoring the intensity of the IR signals associated with the pure and nanocomposite bond signature, such as the free and hydrogen-bonded carbonyl bonds of the hard segment at 1733 cm^{-1} and 1712 cm^{-1}, respectively, the association of Laponite with the polyurethane hard micro-domains can be determined [5, 6]. Subsequent observations monitoring how the bond signature changes with respect to deformation can provide clues regarding clay-segment association and matrix damage.

Ordered, fractal-like domains are observed within the Elasthane nanocomposites under cross-polarized light. Monitoring these birefringent regions in the thin-film nanocomposite during a tensile test visually ties the various regions of tensile deformation, i.e. Laponite jamming, soft segment alignment, strain hardening or hard micro-domain break-up within the nanocomposite, to the disruption of the crystallite structures observed under cross-polarized light (shown in Figure 5-23). These domains are comprised of polyurethane hard micro-domains, Laponite, and conformationally-confined soft domains. These domains, which measure approximately 20-100 μm in size, are disrupted upon large deformations as shown in the previous chapter. The scale of these ordered domains is much larger than the size of the hard micro-domains (20-175 nm) [7, 8], indicating that the local mechanical properties and morphology of the ordered domains and the amorphous matrix are very different from one another.

The above morphological evaluation provides evidence to help explain how the nano-clay interacts with the elastomer to modify the mechanical response. Physical attachment between the elastomer and nano-clay can be verified with attenuated reflectance Fourier transform spectroscopy (ATR-FTIR). X-ray scattering and cross-polarized microscopy help tie the morphological evolution upon deformation to the mechanical behavior of an elastomer when nano-clay preferentially reinforces the hard micro-domains. It is important for the continued advancement of engineering thermoplastics that these thermo-physical interactions between the elastomer and nano-clay are not only understood but able to be modeled. A one-dimensional constitutive model that augments the previous polyurethane model developed by Qi and Boyce [9] is discussed in Appendix A-3. This knowledge coupled with the appropriate model offers a means for the development of new devices that exploit the thermo-physical interactions between elastomers and nano-clay.

5.2 Mechanical and Morphological Characterization Techniques

Thermoplastic polyurethanes demonstrate strong hysteresis, time dependence, and cyclic softening [9]. In section 5.2 a series of uniaxial tensile tests as well as morphological characterization techniques are described. In the following section, 5.3, the results which quantify these features in the model nano-clay filled elastomer are conveyed and discussed.

5.2.1 Mechanical Test Descriptions

Uniaxial tensile tests were conducted using a computer controlled Zwick mechanical tester, model Z010, with screw tightened grips (Model No. 8133). Each grip had one flat polyurethane jaw face and one convex aluminum face. The jaw faces ensured a line of contact across the width of the thin film specimen and eliminated slip. Specimens were subjected to constant nominal strain rate loading and unloading cycles. Test specimens were rectangular and approximately 5 mm in width and measured 120-180 μm in thickness. The specimen thickness did vary through the length by ±20 μm. Measurements made with a video extensometer proved that the modulus calculated via engineering stress-strain results utilizing the average specimen thickness and the Zwick crosshead as the means to measure the change in specimen length was valid (See Appendix A-2). Consequently, the results reported are in terms of engineering stress-strain and when true stress-strain is reported, the material was assumed incompressible. True strain was defined as the logarithm of the current length over the initial length, where the current length of the sample was taken to be the crosshead distance. True stress was calculated by multiplying nominal stress by the stretch ratio. Elastomers are generally incompressible. Consequently it is reasonable to assume the Poisson ratio ranges from 0.48 to 0.50. The nominal strain rate maintained for each test was 0.0167s^{-1} unless otherwise noted.

5.2.1.1 Hysteresis

The polyurethane nanocomposites were stretched to 1.8 and 2.6 times the original specimen lengths and then unloaded. Additional strain recovery occurred with time after unloading, so the specimens were unloaded to a slightly positive force of 15 mN so that specimen buckling was avoided. This 'no-load condition' was held for 180 seconds before subsequent loading. Each load-unload cycle was completed twice at a specified specimen stretch before the larger subsequent stretch was applied. The response after the first and second cycle (N=1 and N=2) are reported and the residual strains were measured prior to re-loading.

5.2.1.2 Softening

The polyurethane nanocomposites were stretched to 1.1, 1.2, 1.4, 1.8, 2.2, 2.6, and 3.0 times the original specimen length and then unloaded. Additional strain recovery occurred with time after unloading, so the specimens were unloaded to a slightly positive force of 15 mN so that specimen buckling was avoided. This 'no-load condition' was held for 180 seconds before subsequent loading. Each load-unload cycle was completed five times at a specified specimen stretch before the larger subsequent stretch was applied. The response after the first and fifth cycle (N=1 and N=5) are reported and the residual strains were measured prior to re-loading.

5.2.1.3 Rate Dependence

The rate dependence of the material at low strain rates was evaluated. Each nanocomposite specimen was stretched 2.0 times the original specimen length and unloaded five times at three different nominal tensile strain rates: 0.0017 s^{-1}, 0.0167 s^{-1}, and 0.1667 s^{-1}.

5.2.1.4 Time Dependence

During loading or unloading if the test is suspended, time dependence in the stress response (if the strain is held constant) or in the creep behavior (when the stress is held constant) ensues. Stress relaxation tests were conducted during loading and unloading up to a maximum stretch of 2.0 in one instance and 3.0 in another instance. These load-unload cycles with intermittent holds were repeated four times and stretched at a nominal strain rate of 0.0167 s^{-1} with intermittent 600 second holds at stretches of 1.1, 1.2, 1.4, 1.6, 1.8, and 2.0 in one instance and 1.1, 1.2, 1.4, 1.8, 2.2, 2.6 and 3.0 in another instance.

5.2.1.5 Relaxed Response and Equilibrium Paths

In stress relaxation tests, the stress relaxes towards an equilibrium state during the intermittent holds. The stress relaxation behavior during the 1st cycle and the subsequent cycles of the test differ after cycling between stretches of 1.0 and 2.0. Consequently, the stress relaxes towards two distinct softened paths. The softened stress at each intermittent hold was taken as the stress value prior to loading or unloading to the subsequent stretch. The equilibrium paths then are defined to fall halfway between the softened response of the first softened load-unload path at each applied strain and the subsequent softened load-unload path.

5.2.2 Morphological Characterization Techniques

5.2.2.1 Wide Angle X-ray Scattering

WAXS data was acquired at the G1 beamline at the Cornell High-Energy Synchrotron Source (CHESS). At the CHESS G1 beamline, λ = 1.23 Å, the beam was collimated to a horizontal divergence of 1 mrad via the wiggler 'K' factor and horizontal-focusing optics. This natural collimation was supplemented by use of two 1 mm slits and a third, which functioned as a guard slit. The relative X-ray intensity was measured at positions (0) just before the sample, using a helium-filled proportional counter, and (2) upstream of the collimation slits, using a nitrogen-filled proportional counter. A MedOptics CCD detector was used to measure the scattered radiation, with pixel size 47.19 μm pixel^{-1} and size 1024 x 1024 pixels.

A home-built stretcher was used to elongate the 0.1-0.2 mm thick samples to static positions that subsequently increased the specimen length to 1.1, 1.2, 1.4, 1.6, 1.8, 2.0, 2.5, 3.0, 4.0, 5.0, 6.0, 7.0, 8.0, and 9.0 times the original specimen length. Obviously, the samples slipped because tensile failure data presented in the previous Chapter indicates that the films fail consistently at nominal stretches of approximately 5.0. Consequently, the resulting scatter patterns can only be qualitatively associated with various tensile deformation regions, rather than correlated to specific strains. Scattering patterns were collected for 20 seconds in WAXS (time-averaged). A background pattern was collected for each sample environment, for a collection time equal to the sample collection time. A dark (blocked beam) pattern was measured for each collection time employed. The appropriate dark pattern was subtracted from each sample and background scattering pattern. Each sample pattern was then corrected using the following formula:

$$\textit{Correlated Scattering Pattern} = \textit{Sample Pattern} - T \cdot \textit{Background Pattern}. \qquad (5.1)$$

The transmission ratio, T, was taken to be the following ratio

$$T = \frac{I'_{0,\,sample}}{I'_{0,\,background}}\left[\frac{\left(I_2/I_0\right)_{sample}}{\left(I_2/I_0\right)_{background}}\right], \qquad (5.2)$$

where I_0 and I_2 is the measured beam intensity at the positions denoted by numerical subscript 0 and 2 mentioned previously and I_0' is the intensity measured at position 0 during collection. Data was reduced from 2D (intensity vs. 2θ, χ) to 1D (intensity vs. 2θ) format by integrating over all values of χ, for each value of 2θ, where 2θ is the scattering angle and χ is the azimuthal angle. The data was also reduced to 1D format by integrating over values of 2θ between 15.09° and 15.83° (*d*-spacing = 0.447 nm to 0.468 nm) and 16.56° and 17.28° (*d*-spacing = 0.409 nm to 0.427 nm) for each value of χ.

Small angle x-ray scattering data with in-situ stretching was also collected, but the distinct SAXS peaks observed in the pure polyurethane were not identifiable in the Laponite filled sammple (See Appendix A-4). This is most likely the result of electron-density contrast matching between the soft and hard blocks due to the disrupted morphology encouraged by the addition of the rigid clay platelets as seen in atomic force microscopy phase images [10]. If a fraction of the soft segment chains are constrained within the Laponite-hard micro-domain substructures, as is suggested via cross-polarized microscopy, the pseudo electron density of the continuous domain is raised, limiting the perceived contrast between the soft and hard domains. Consequently, the SAXS data is not reported.

5.2.2.2 Attenuated Total Reflectance Fourier Transform Infrared Spectroscopy

The nanocomposite films were stretched to a static position using a home-built, manual stretcher and characterized with attenuated total reflectance Fourier transform infrared spectroscopy (ATR-FTIR). A Nicolet Nexus 870 spectrometer with a DuraSampl*IR* II Diamond ATR from SensIR Technologies was used to collect data between wave numbers of 4 cm^{-1} and 4000 cm^{-1}. The home-built stretcher was comprised of a digital caliper with cylindrical rods used as grips attached to the jaws of the caliper. The grip on each jaw consisted of a small cylindrical rod with two threaded holes at either end set parallel to the measuring flat of the jaw. A specimen, measuring 25 x 5 x ~0.15 mm^3 was placed between the threaded holes and as the screws through the rod were tightened the rod made a line of contact along the width of the specimen. Then the thin-film specimen was deformed by manually opening the jaws of the caliper. Each position was held by tightening the screw on the caliper that stops the lower jaw from moving and the thin film characterized. The area in which the film was characterized was circled with a black permanent marker. Upon deformation, the marker smeared, making it difficult to interrogate the same area at each subsequent increasing stretch. As a consequence, the bond signatures did not change systematically, but seemed to hover around the static signature despite the magnitude of stretch. Therefore, only the static signature is reported.

5.2.2.3 Cross-Polarized Microscopy

The long range order, deformation, and crystalline morphologies of the nanocomposites during deformation were examined using a Carl Zeiss Axioskop 2MAT Polarizing Microscope with cross-polarized light and the same home-built, manual stretcher used with ATR-FTIR. The nanocomposite films were stretched to a static position and then the mid-section was imaged. Although the grips did induce local deformation at the line of contact, specimen slip was eliminated. Because the middle of the specimen was imaged, the resultant stretches reported describe the overall specimen stretch and the value is greater than that actually achieved by the area interrogated.

5.3 Results and Discussion

5.3.1 Hysteresis

Figure 5-1 shows the tensile engineering stress-engineering strain behavior of Elasthane/Laponite nanocomposite films at engineering strains equal to 0.8 and 1.6. The loading curves exhibit an initial stiff response that increases its magnitude with Laponite concentration and rolls over to a more compliant behavior. This rollover in the 15 wt% nanocomposite appears as a yield point typical of amorphous polymers due to the jamming of nano-clay platelets and initiation of localized deformation. As the Laponite concentration increases, the rollover occurs at smaller and smaller strains. The pure polyurethane rolls over at a strain of ~0.15 while the 15 wt% Laponite filled rolls over at ~0.03. The unloading paths exhibit large hysteresis and significant residual strain that both increase with increasing Laponite concentration. This behavior is obvious in Figure 5-2 when the behavior of the pure and 15 wt% Laponite-filled behavior is compared directly.

When the Laponite concentration is less than the percolation limit, the increase in hysteresis, or energy absorbed, compared to that of the pure polyurethane increases significantly without considerably increasing the residual strain. In contrast, when the Laponite concentration is greater than the percolation limit, there is both a marked increase in energy absorbed and residual strain. The addition of nano-clay reinforces the stress response of Elasthane, but also locally damages the polyurethane matrix, especially at concentrations above the percolation threshold.

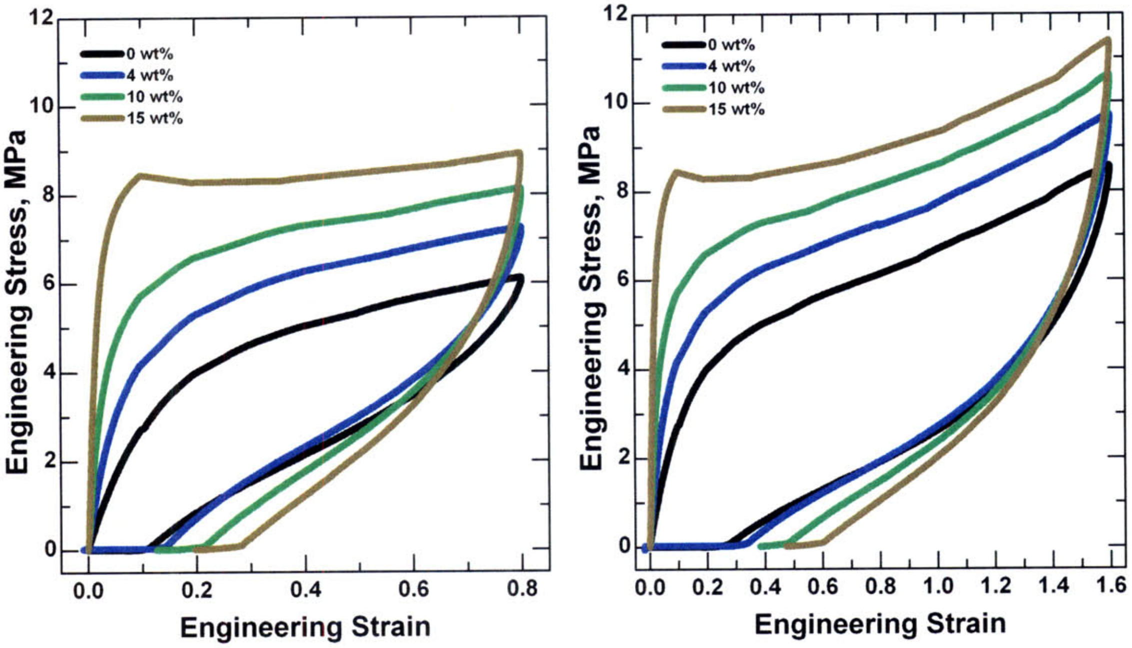

Figure 5-1: Hysteresis of pure Elasthane to composites filled with 4, 10, and 15 wt% Laponite when thin-film specimens are stretched 80% and 160%.

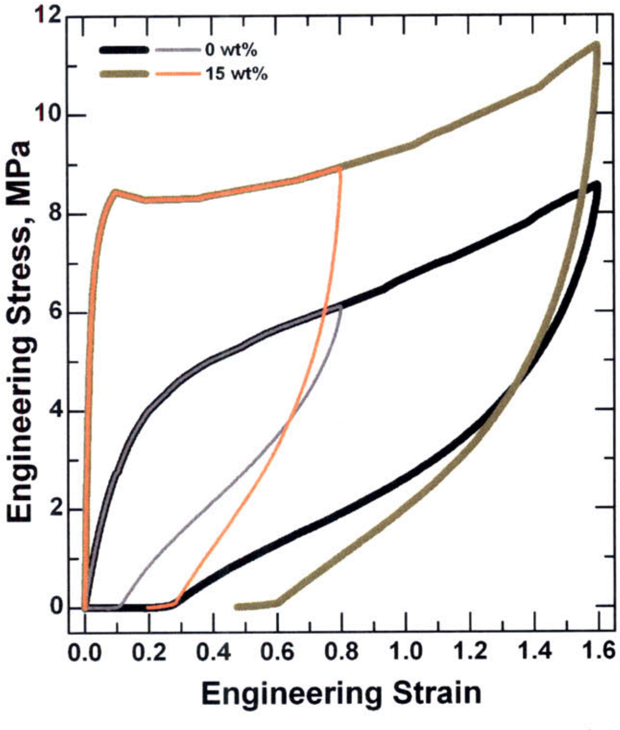

Figure 5-2: Comparison of the hysteresis of pure Elasthane and a composite filled with 15 wt% Laponite when thin-film specimens are stretched 80% and unloaded and then to 160%.

5.3.2 Softening

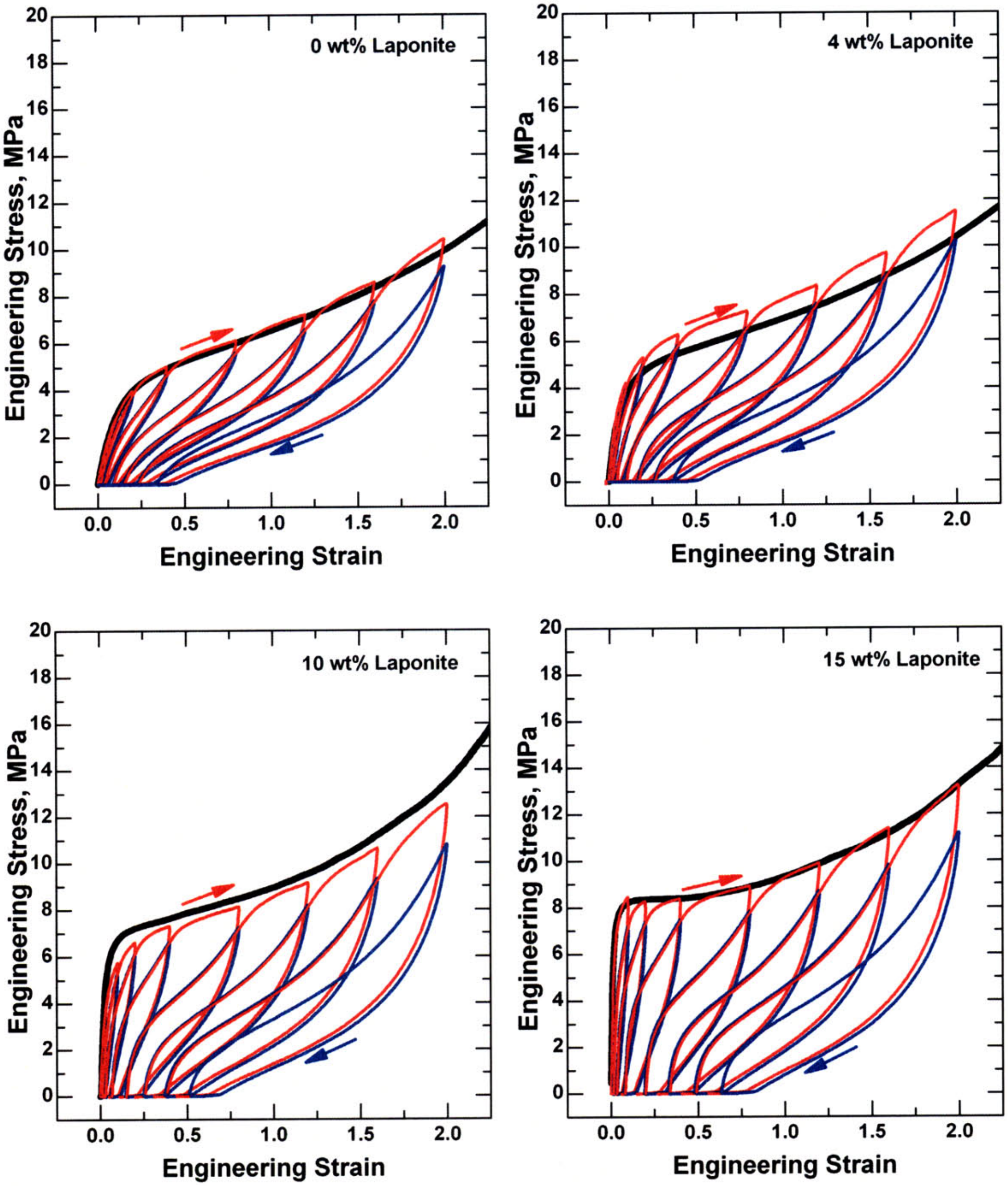

Figure 5-3: Cyclic softening behavior of pure Elasthane and nanocomposites filled with 4, 10, and 15 wt% Laponite when the specimens are stretched to nominal or engineering strains equal to 0.1, 0.2, 0.4, 0.8, 1.2, 1.6 and 2.0. The response shown in black is that of an independent sample stretched to failure. The stress-strain response shown in red is that upon the first cycle of loading and unloading at each stretch (N=1) and that in blue corresponds to the fifth cycle (N=5).

Figure 5-3 exhibits the engineering stress-strain response of Elasthane filled with 0, 4, 10 and 15 wt% Laponite during the first and fifth cycle of loading-unloading tests to engineering strains of

0.1, 0.2, 0.4, 0.8, 1.2, 1.6, and 2.0. Typical of most elastomers, the response of the subsequent cycle is more compliant than that observed in the first deformation cycle [11, 12]. The extent of softening that occurs between the first and second deformation cycle is greatest, but after a few cycles the softened response stabilizes, as shown in Figure 5-4. The residual or plastic strain too exhibits the largest increase between the first and second deformation cycle and then stabilizes during subsequent cycling. There is slight softening in the material response upon unloading, but when compared to the softening upon loading it can be considered negligible. When the previous maximum strain achieved during previous cycles is surpassed the stress response approaches that typical of a non-softened specimen and the extent of softening increases with applied stretch.

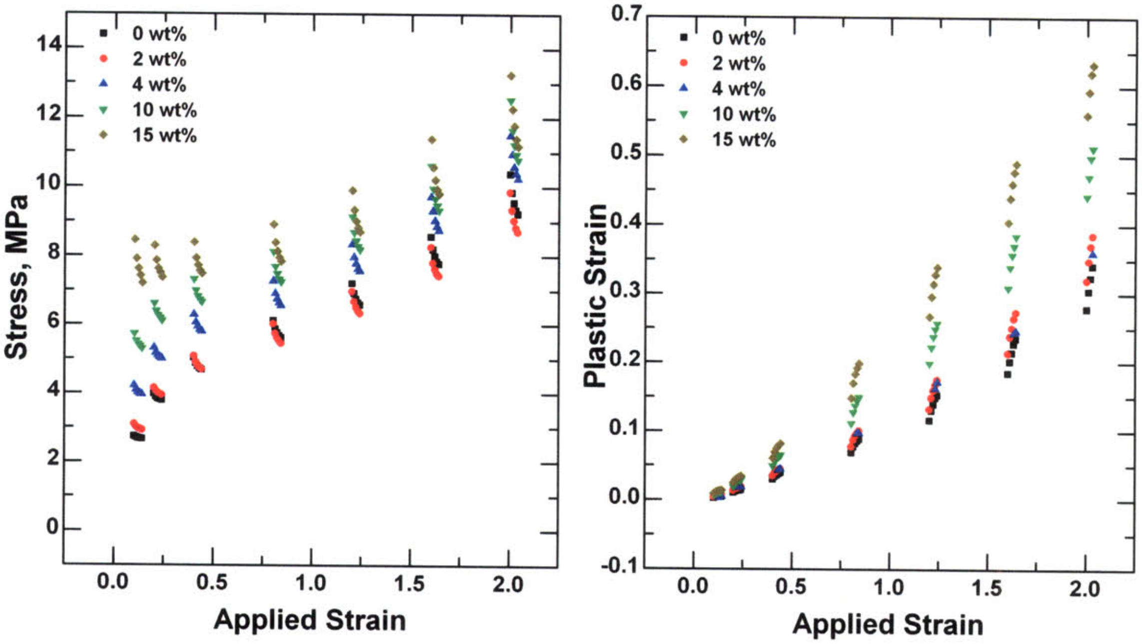

Figure 5-4: Evolution of the maximum stress and plastic strain as 0, 2, 4, 10, and 15 wt% Laponite-filled nanocomposites are cycled 5 times at applied nominal strains equal to 0.1, 0.2, 0.4, 0.8, 1.2, 1.6, and 2.0. The plastic strain is that obtained after the specimen is held under a no-load condition for 180 s. For ease of viewing the resulting trends of maximum stress and plastic strain are plotted against modified applied strain (modified applied strain = applied strain + 0.01).

When nano-clay is added to the polyurethane the softening behavior typical of elastomers is still apparent. However, increasing the nano-clay concentration increases the magnitude of the softened, stress-strain response of the nanocomposites from that exhibited by the pure polyurethane. The extent of softening between the first and fifth cycle too increases with Laponite concentration, particularly when concentrations exceed the percolation limit. The addition of Laponite similarly increases the plastic strain. Obviously the material response of these elastomers with and without nano-clay depends strongly upon the material strain history.

5.3.3 Rate Dependence

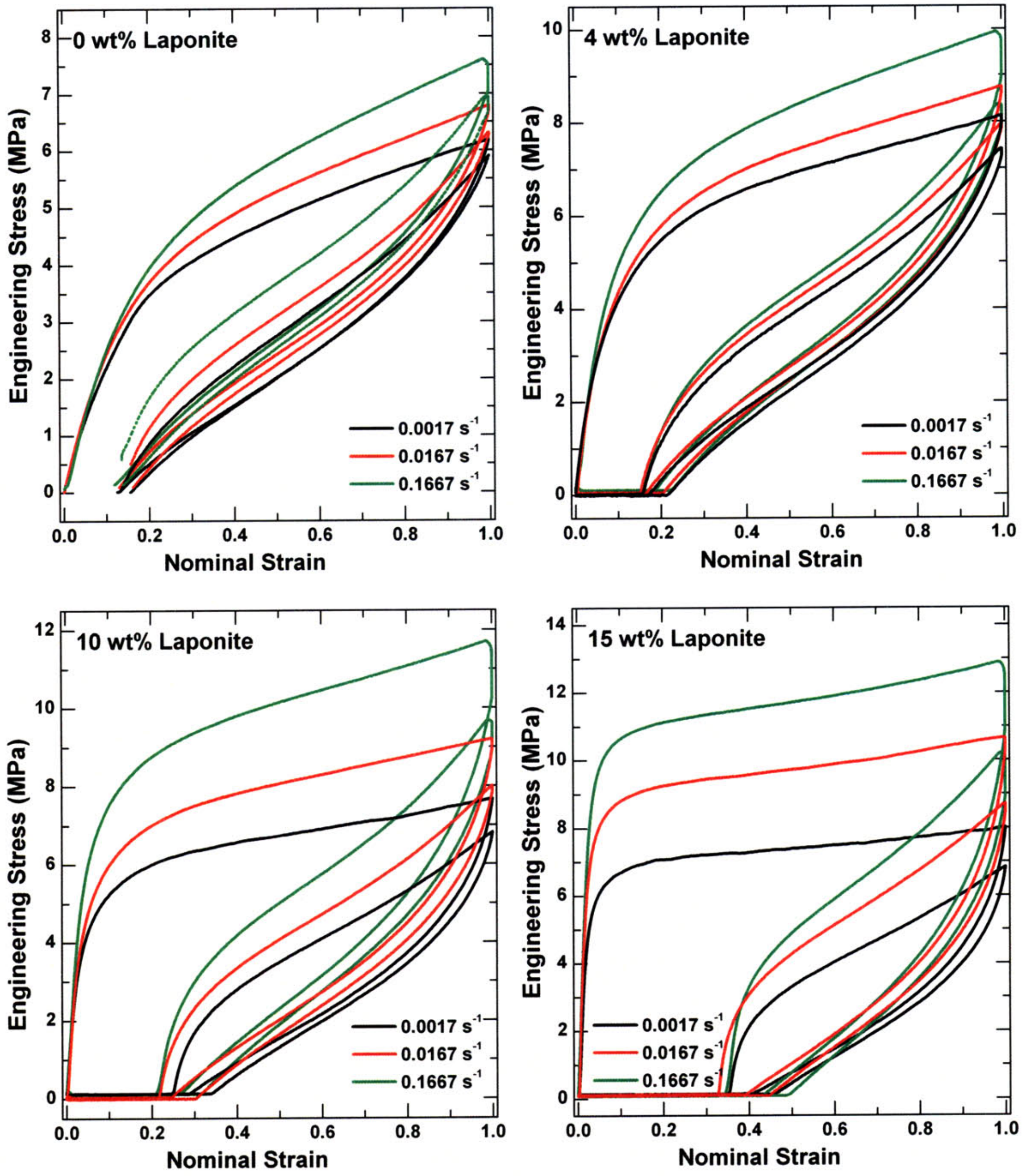

Figure 5-5: Rate dependence of 0, 4, 10, and 15 wt% Laponite-filled Elasthane when stretched to a nominal strain of 1.0 at three different nominal strain rates: 0.0017 s^{-1}, 0.0167 s^{-1}, and 0.1667 s^{-1}.

The stress-strain behavior of the Elasthane/Laponite nanocomposites at three low strain rates is shown in Figures 5-5, 5-6 and 5-7. Upon loading the stress-response increases with increased strain rate, a response typical of polymers [13]. The observed increase in stress with rate is greatest upon loading, enhancing the flow stress by 1-2 MPa with each order of magnitude increase in rate. Meanwhile the increase is so slight upon unloading that it can be assumed negligible. Consequently, loading is more rate dependent than unloading.

The flow stress or engineering stress at an engineering strain equal to 0.3 at each strain rate increases with the Laponite volume fraction as shown in Figure 5-6. This increase in flow stress is similar to the increase in viscosity exhibited in filled solutions. Einstein showed that the viscosity of a dilute solution filled with spheres increases linearly with the filler volume fraction [14]. Similarly, the flow stress increases linearly, indicating the higher concentration solids are more rate sensitive.

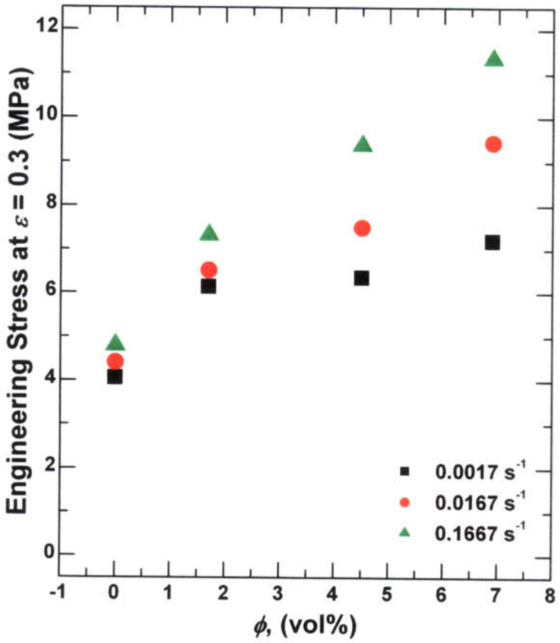

Figure 5-6: The flow stress, or engineering stress at $\varepsilon = 0.3$, at the various strain rates is plotted against the Laponite concentration. The flow stress appears to increase linearly with volume fraction.

At the slowest strain rate the stress-strain response deviates from that reported in Chapter Four (nominal strain rate = $0.0167\,s^{-1}$) where the modulus and flow stress increases with Laponite concentration and the slope of soft segment stretch and re-orientation region remains constant despite the addition of nano-clay. As shown in Figure 5-7, at the slowest rate the 0 and 4 wt% filled nanocomposite exhibits a larger hardening slope than that of the more concentrated nanocomposites. Deformation at this slow strain rate is like testing the specimen at a slightly elevated temperature ($T > T_{amb}$); the Laponite and hard micro-domains are able to re-orient with the soft segment and retard the hardening.

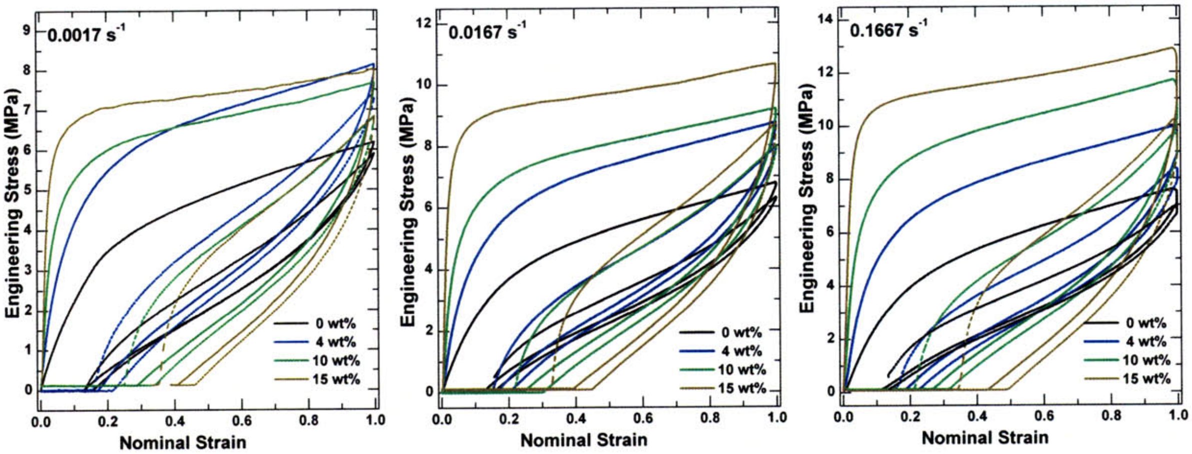

Figure 5-7: Comparison of the engineering stress-strain response of 0, 4, 10, and 15 wt% Laponite-filled Elasthane when stretched to a nominal strain of 1.0 at three different nominal strain rates: 0.0017 s^{-1}, 0.0167 s^{-1}, and 0.1667 s^{-1}.

For a more complete analysis of the rate dependence of these nanocomposites evaluation at moderate and high strain rates are needed [15].

5.3.4 Time Dependence

Tensile stress relaxation tests were conducted at sequentially increasing nominal strains and then unloaded at those same strains. Figure 5-8 show the corresponding strain profile, stress response and stress-strain response. A majority of the stress relaxation occurs within the first 20 seconds. During loading, the stress decreases while the strain is held constant and upon unloading, the stress increases. Note that there was no intermittent hold at a nominal strain of 2.0 prior to unloading. Consequently, the stress-recovery during unloading is masked by the material relaxation that continues to evolve. The extent of stress-relaxation is greater than that of stress-recovery due to evolving chain orientation and matrix damage.

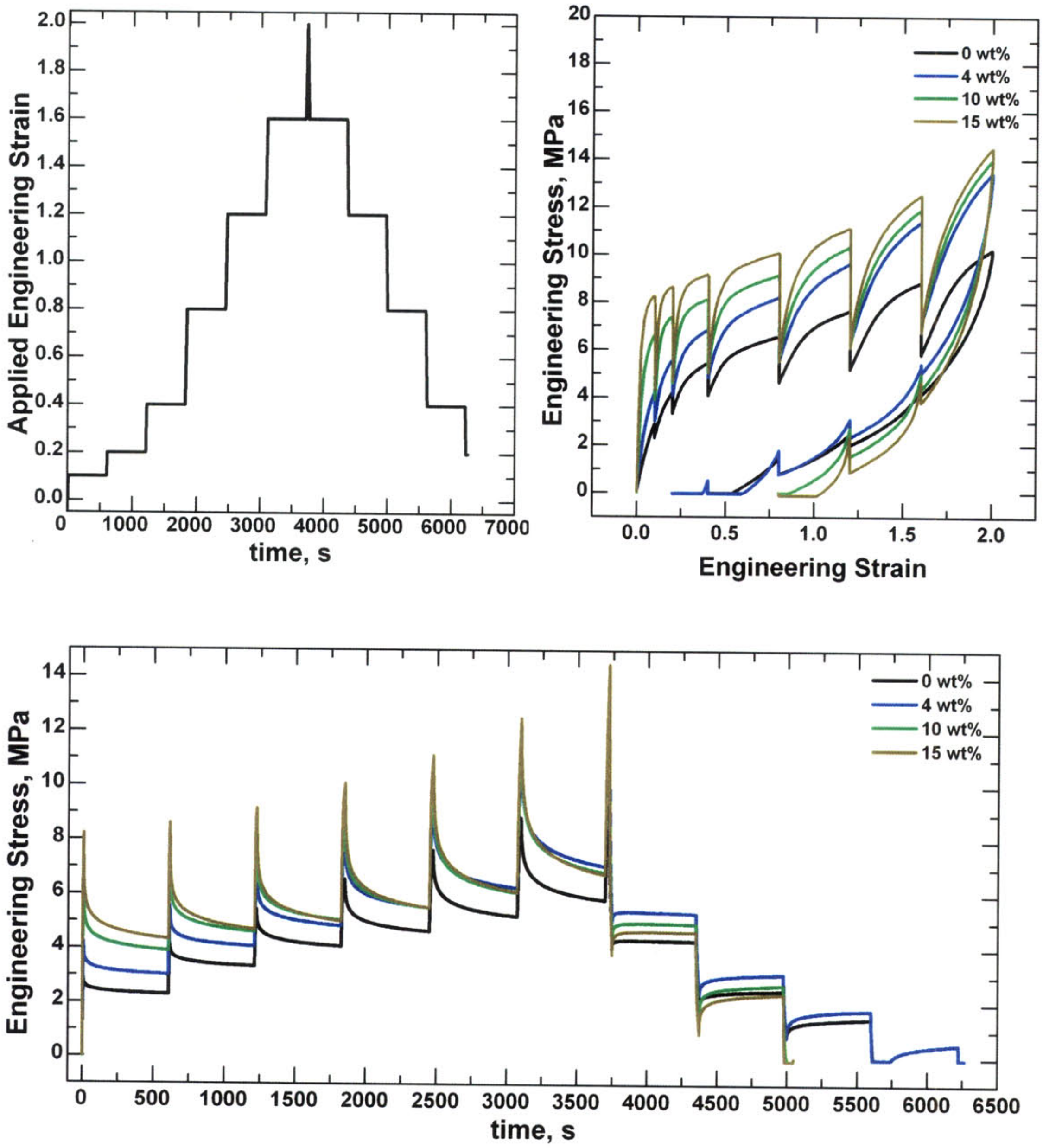

Figure 5-8: Applied strain history for stress relaxation tests as well as the engineering stress response vs. time and applied strain for nanocomposites containing 0, 4, 10 and 15 wt% Laponite.

As the magnitude of the applied strain increases, the relaxed stresses of the Laponite-filled nanocomposites appear to converge to a value greater than the pure polyurethane. There also appears to be two relaxation mechanisms and consequently two relaxation time constants that depend on both Laponite concentration and the magnitude of stretch applied. It is difficult to clearly distinguish the influence of Laponite on the stress relaxation behavior without further analysis. The experimental relaxation data at each nominal or engineering strain was fit to the following equation that describes the rheological model in Figure 5-9:

$$\sigma = \left[E_0 + E_1 \exp\left(\frac{-t}{\tau_1}\right) + E_2 \exp\left(\frac{-t}{\tau_2}\right) \right]\left(\lambda - \frac{1}{\lambda^2}\right) \tag{5.3}$$

where the specimen stretch, λ, is equal to $1+\varepsilon$, where ε is the applied engineering strain.

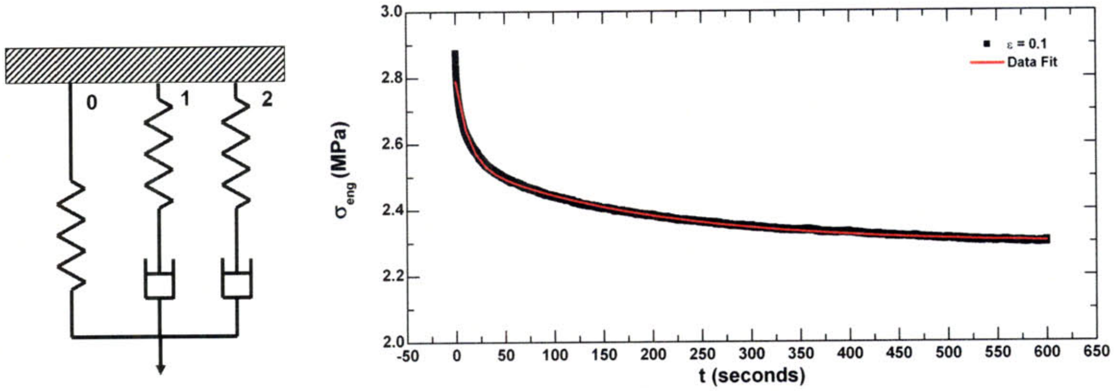

Figure 5-9: One-dimensional description of the rheological model of the experimental stress relaxation and corresponding fit to the pure Elasthane stress relaxation after the specimen is stretched 10%.

After fitting the relaxation data for composites containing 0, 4, 10 & 15 wt% Laponite upon loading to stretches equal to 1.1, 1.2, 1.4, 1.8, 2.2, and 2.6 the resulting moduli and time constants were plotted against the applied stretch. Below in Figure 5-10, find the time constants, τ_1 and τ_2. The short relaxation time constant (12-16 s) appears to depend on the magnitude of the stretch applied. The long relaxation time constant displays significant scatter, but appears to remain constant at ~200 s despite the magnitude of stretch applied. The magnitude of these relaxation times are within the same range that Xia et al observe for a similar polyurethane [16]. The long relaxation time corresponds to the hard micro-domains and the short relaxation time corresponds to the soft segment. As the magnitude of the applied stretch increases but does not reach the strain hardening regime, the soft segments stretch, align and orient while the hard segments rotate but do not break-up. Consequently, the long relaxation time exhibits scatter and remains constant while the short relaxation time increases with stretch. It is important to note that the initial data point taken at a nominal stretch of 1.1 falls within the region of yield for the nano-clay filled materials. This flow, in conjunction with the stress relaxation, combines to exhibit effectively smaller relaxation time constants. In future analyses these three data points are excluded.

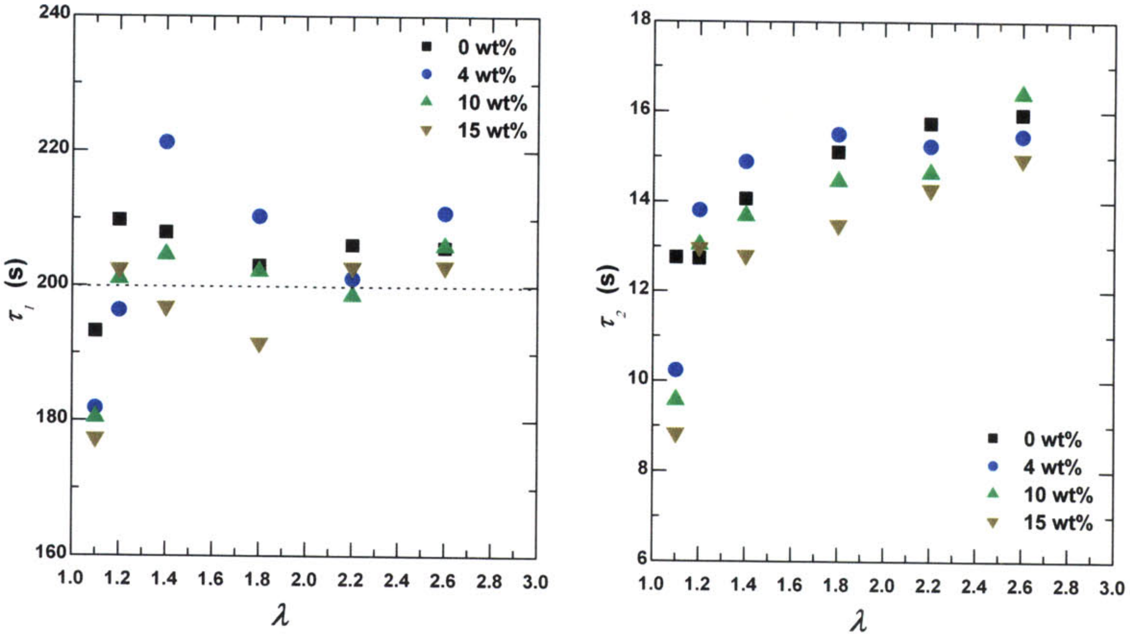

Figure 5-10: Two characteristic time constants observed in the stress relaxation behavior of the polyurethane nanocomposites. The first relaxation time constant corresponds to the hard micro-domain relaxation and the second faster relaxation constant corresponds to the soft segment that becomes less mobile upon stretch and orientation.

In order to extend the analysis of the stress relaxation behavior exhibited by these nanocomposites in tension to other modes of deformation, the relaxation behavior was examined as a function of orientation [17]. Arruda and Boyce have shown that the eight-chain network model depicted in Figure 5-11 captures the finite strain behavior of polymers subject to complex deformations using only two model parameters [18].

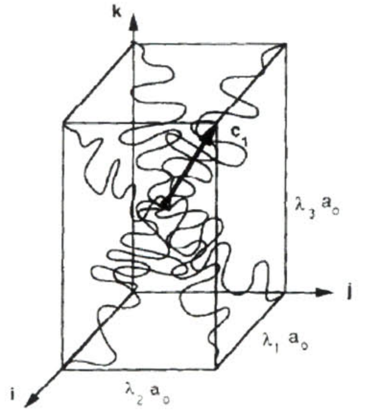

Figure 5-11: Schematic of the stretched eight-chain network as depicted in [18].

The three chain angles that correspond to the angles between the three principal directions (1, 2 and 3) and a vector pointing from the center of the representative volume element (RVE) along one of the eight chains to its vertex can be described by

$$\beta_i = \operatorname{acos}\left[\frac{\lambda_i}{\sqrt{\sum_{i=1}^{3} \lambda_i^2}}\right], \tag{5.4}$$

where β_i is the chain angle with respect to a principal direction, i, and λ_i is the stretch describing the RVE deformation with respect to a principal direction [19]. Dupaix and Boyce found it useful to utilize a physically based orientation parameter, α, to describe the molecular relaxation observed in amorphous polymers like poly(ethylene terephthalate)-glycol [17]. They define the orientation parameter as the compliment of the maximum chain angle:

$$\alpha = \frac{\pi}{2} - \beta_{\max} . \tag{5.5}$$

The orientation parameter as a function of principal stretch for an incompressible material deformed in tension, compression and equibiaxial tension and compression is shown in Figure 5-12. Note that the orientation parameter when a polymer solid is not deformed is equal to 0.615 rad and decreases upon deformation. It is not convenient to plot the stress relaxation time constants and moduli against a non-linear, decreasing function that starts at a maximum value and approaches zero. For ease, the orientation parameter was normalized by the undeformed orientation parameter (α_0-α), so that the undeformed normalized orientation parameter starts at 0 rad and monotonically increases to 0.615 rad.

When the two, characteristic relaxation time constants are plotted against the normalized orientation parameter in Figure 5-13 it is clear that $\tau_1 = 200$ s and τ_2 increases as the soft segment stretches and aligns. Initially the soft segment exhibits a relaxation time constant of ~12 s but upon deformation the value increases according to the following relation:

$$\tau_2 = 12.3 + 9(\alpha_0 - \alpha) . \tag{5.6}$$

This trend is observed in the pure Elasthane as well as nanocomposites filled with 4, 10, and 15 wt% Laponite.

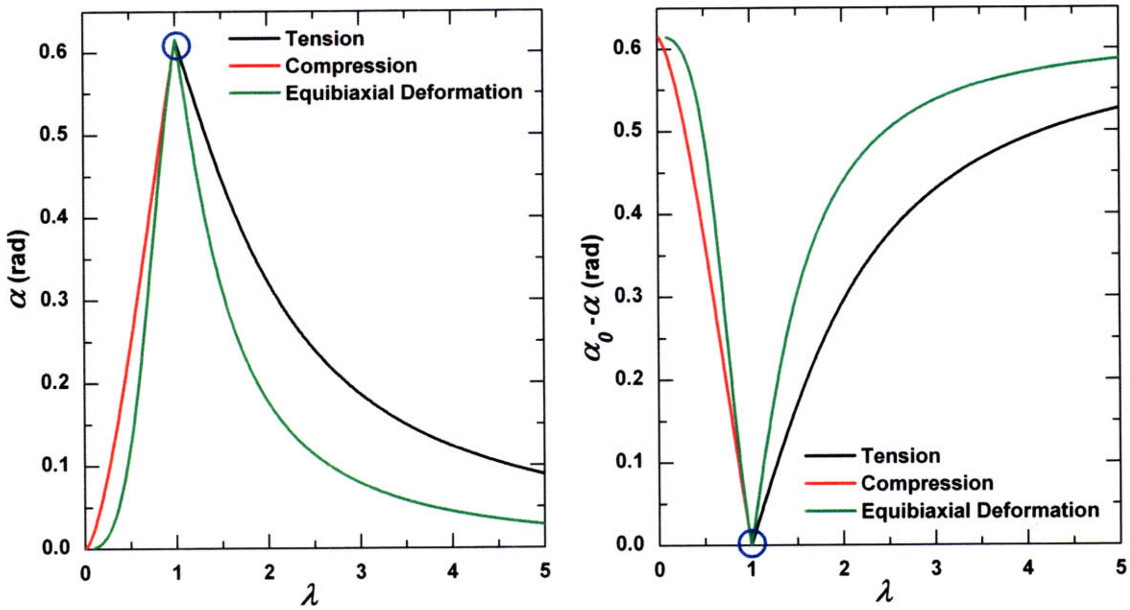

Figure 5-12: Relationship between the orientation parameter, α, as well as the normalized orientation parameter, α_0-α, and the principal stretch of an eight-chain RVE for an incompressible material. Note that equibiaxial compression is equivalent to tension but the principal stretch is given by a value less than unity.

This increase in relaxation time with soft segment stretch and alignment is either due to strain induced crystallization (the specimen film transitions from transparent to opaque upon stretching) or interrogation of the longer soft segment chains upon increased stretch [20-22].

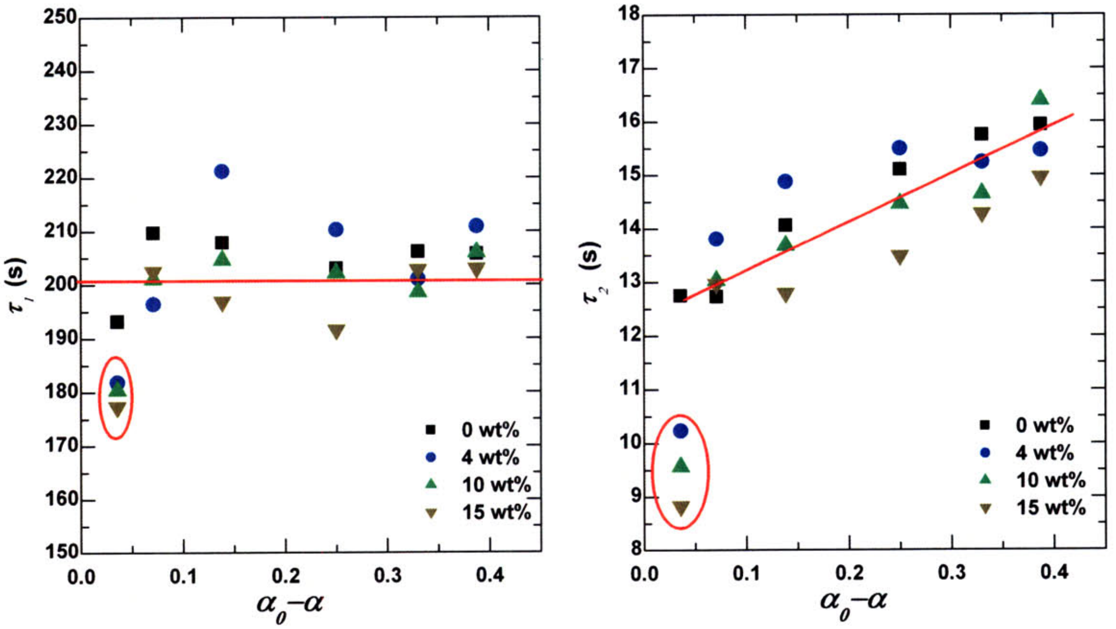

Figure 5-13: Evolution of the two characteristic time constants observed in the stress relaxation behavior of the polyurethane nanocomposites with orientation.

The three relaxation moduli given in equation 5.3 are plotted against the tensile stretch, as depicted in Figure 5-14.

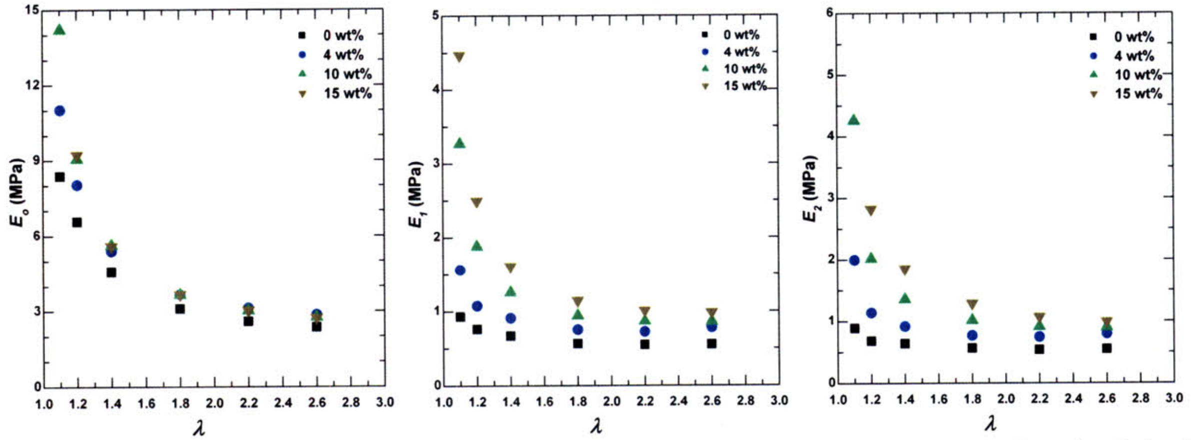

Figure 5-14: Evolution with tensile stretch of the three moduli that capture the stress relaxation behavior of the polyurethane nanocomposites.

The resultant moduli (given by E_0, E_1, and E_2) decay with increasing stretch. The addition of nano-clay increases the moduli significantly at small stretches and minimally at large stretches. When the natural logarithm of the moduli is plotted against the natural logarithm of the normalized orientation parameter the trends fall linearly, indicating that the moduli scale with orientation following a power-law. The addition of nano-clay increases the sensitivity of the material to orientation induced softening. This behavior is exhibited by the increasing slope of the linear fits shown in Figure 5-15. The parameters, *A* (the y-intercept) and *m (*the slope) of these fits are given in Table 5-1. The parameters were plotted against the Laponite volume fraction and equations capturing their dependence on concentration and aspect ratio determined.

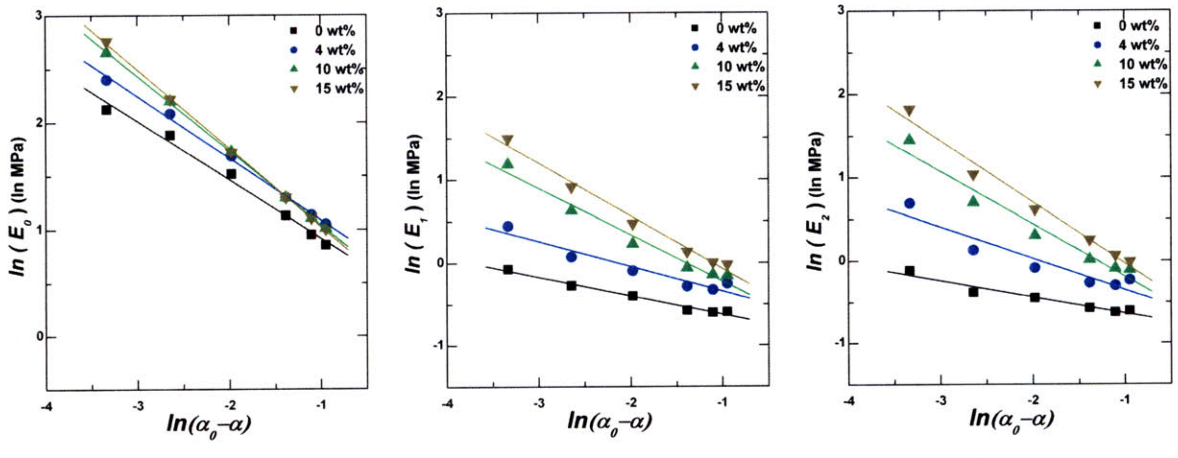

Figure 5-15: Power-law decay of the polyurethane nanocomposite moduli with orientation. The magnitude of the modulus and the extent of softening with increased orientation depend upon the Laponite concentration.

Laponite Fraction, φ		**Fit Parameters**					
wt	**vol**	E_0		E_1		E_2	
		A	**m**	**A**	**m**	**A**	**m**
0.00	0.000	0.37	-0.55	-0.85	-0.23	-0.84	-0.20
0.04	0.017	0.51	-0.58	-0.64	-0.30	-0.73	-0.38
0.10	0.045	0.34	-0.70	-0.78	-0.56	-0.83	-0.63
0.15	0.069	0.29	-0.74	-0.71	-0.64	-0.77	-0.74

Laponite Fraction, φ		**Parameters Based on ϕ and α**					
wt	**vol**	E_0		E_1		E_2	
		A	**m**	**A**	**m**	**A**	**m**
0.00	0.000	0.44	-0.54	-0.78	-0.22	-0.80	-0.23
0.04	0.017	0.44	-0.59	-0.78	-0.33	-0.80	-0.37
0.10	0.045	0.44	-0.67	-0.78	-0.51	-0.80	-0.59
0.15	0.069	0.44	-0.74	-0.78	-0.66	-0.80	-0.78

Table 5-1: Parameters describing the power-law decay of the polyurethane nanocomposite moduli with increased orientation. The parameters in the upper table are determined via fits to experimental data. The parameters in the lower table are approximations to the experimental fit values given by empirical trends that quantify the influence of Laponite concentration, *φ*, and aspect ratio, *α*.

The linear decay of the log-log plot of polyurethane moduli with orientation provides the following relation:

$$\ln E_i = A_i + m_i \ln\left(\alpha_0 - \alpha\right), \tag{5.7}$$

where A_i is the y-intercept and m_i is the slope. The resulting relationship between each of the three moduli, which capture the nanocomposite stress relaxation behavior, and the normalized orientation parameter is given by

$$E_i = C_i \left(\alpha_0 - \alpha\right)^{m_i}, \tag{5.8}$$

where the constant, $C_i = e^{A_i}$ and the slope, m_i prescribes the extent of decay. It is assumed that the contribution to each modulus, E_0 the softened polyurethane response, E_1 the hard micro-domain contribution, and E_2 the soft segment contribution is independent of nano-filler concentration or aspect ratio. The parameters A_i can be assumed constant: $A_{E_0} = 0.44$, $A_{E_1} = -0.78$, and $A_{E_1} = -0.80$. The validity of this assumption relies upon evidence that the addition of nano-filler does not significantly increase or disrupt polyurethane crystallinity or microphase segregation (discussed further in 5.3.9). The extent of modulus decay with orientation is likely dependent upon nano-filler concentration, aspect ratio and polydispersity. Consequently, the slopes obtained for composites containing 0, 4, 10, and 15 wt% Laponite (with aspect ratio: $\alpha = 25$) for each distinct modulus was plotted against the nano-filler volume fraction, $\tilde{\phi}$, and the equation below fit:

$$m_i = c_{1,i}\left(1+\alpha\tilde{\phi}c_{2,i}\right), \tag{5.9}$$

where $c_{1,i}$ and $c_{2,i}$ are constants empirically determined and α is the nano-filler aspect ratio [23]. The empirical relations for the parameter m_i are described in the following three equations:

$$m_{E_0} = \text{-}0.54\left(1\text{+}0.21\alpha\tilde{\phi}\right) \tag{5.10}$$

$$m_{E_1} = \text{-}0.22\left(1\text{+}1.14\alpha\tilde{\phi}\right) \tag{5.11}$$

$$m_{E_1} = \text{-}0.22\left(1\text{+}1.40\alpha\tilde{\phi}\right). \tag{5.12}$$

The resultant parameter values determined from these relations are listed in the lower portion of Table 5-1. There is good agreement between the moduli calculated from these empirical relations and the experimental data as shown in Figure 5-16.

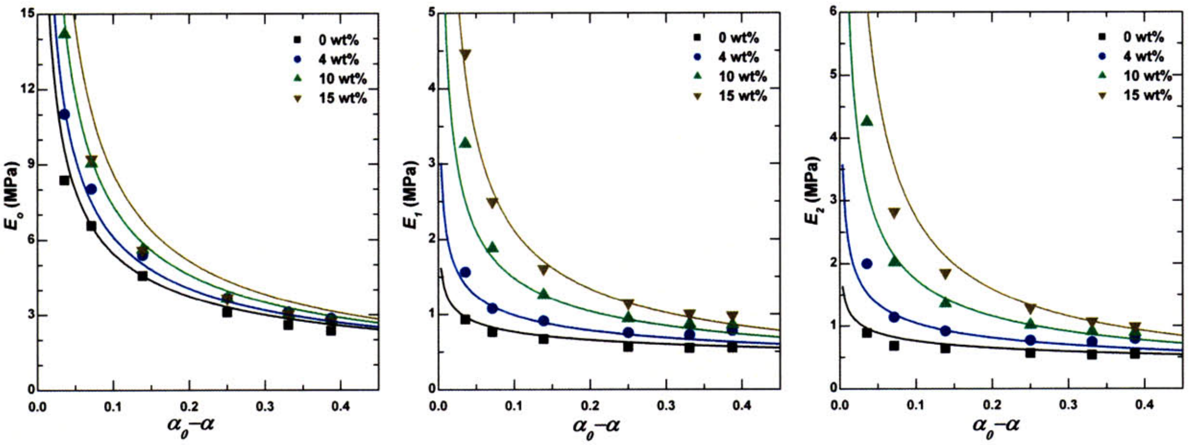

Figure 5-16: Comparison of the polyurethane nanocomposite moduli evolution with increased orientation determined from experimental data (solid symbols) and that predicted via empirical relations (solid thin line).

The stress relaxation behavior of the 0, 4, 10, and 15 wt% Laponite-filled nanocomposites indicates that the polyurethane behavior can be captured well using two characteristic relaxation mechanisms. The first corresponds to the hard micro-domain relaxation ($\tau_1 \sim 200$s) and remains constant despite Laponite concentration when the extent of matrix deformation and orientation has not induced hard segment break-up. The second mechanism corresponds to the uncoiling and relaxation of the soft segments ($\tau_2 \sim 12$ s). This characteristic relaxation time constant increases with deformation and soft segment orientation. The moduli governing the material stress response exhibits a power-law decay with orientation. Ultimately, a constitutive model that accounts for these two distinct relaxation mechanisms is necessary.

5.3.5 Relaxed Response and Equilibrium Paths

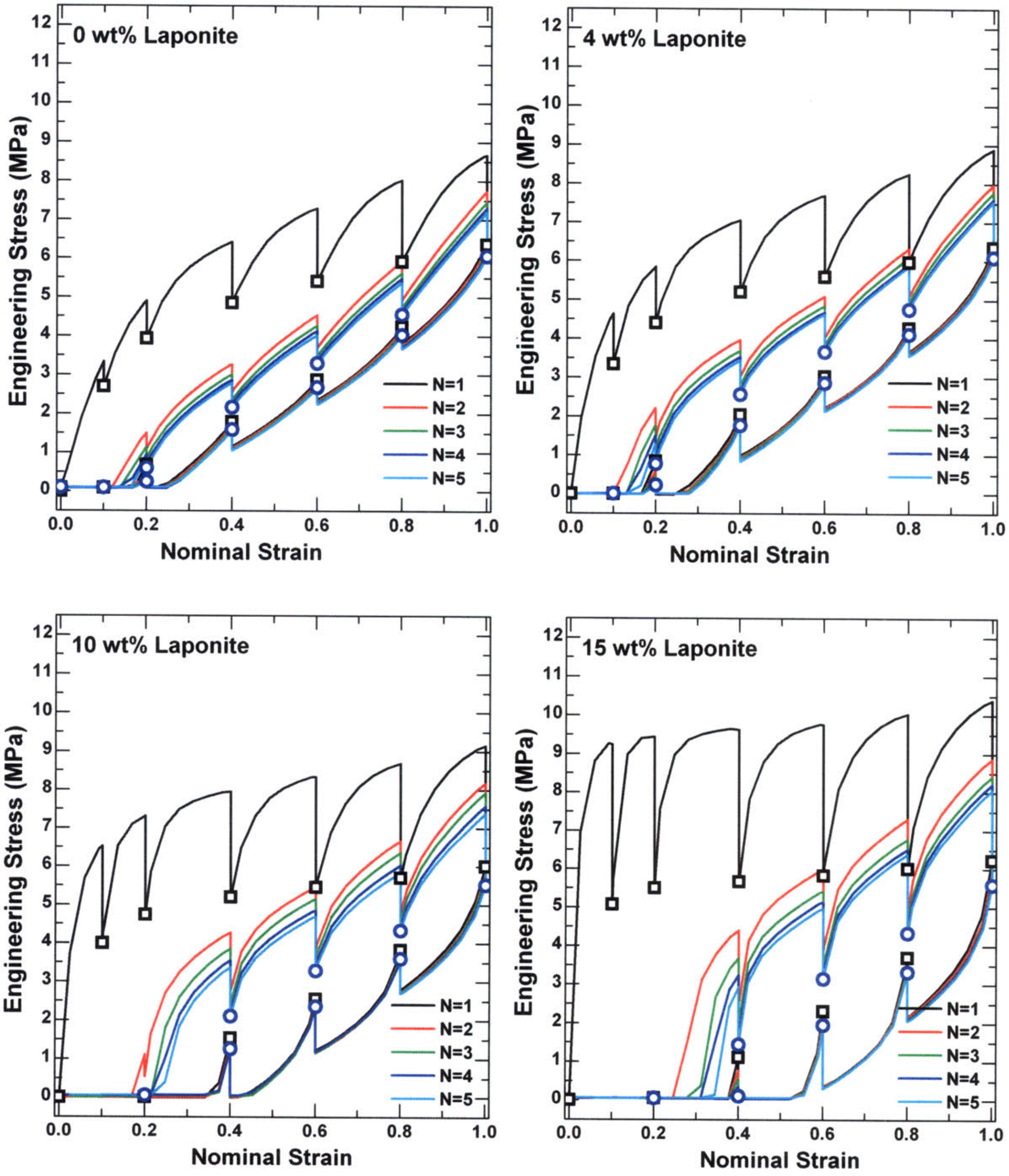

Figure 5-17: Stress relaxation behavior of pure polyurethane and that filled with 4, 10, and 15 wt% Laponite through five load-unload cycles. The points used to distinguish the softened response after the 1st and 5th cycle.

Figure 5-17 depicts the stress relaxation behavior of the 0, 4, 10, and 15 wt% Laponite filled composites during the first and fifth cycle of testing. The relaxed value of stress at a particular strain depends upon the deformation history of the material. Similar to the softening results discussed previously, the recovered response upon unloading in each cycle is virtually the same. Similarly, the subsequent relaxed stresses achieved upon loading for all loading cycles that do not surpass the maximum stretch achieved upon initial loading are nearly identical. The softened or relaxed responses for each of the Elasthane nanocomposites are compared in Figure 5-18.

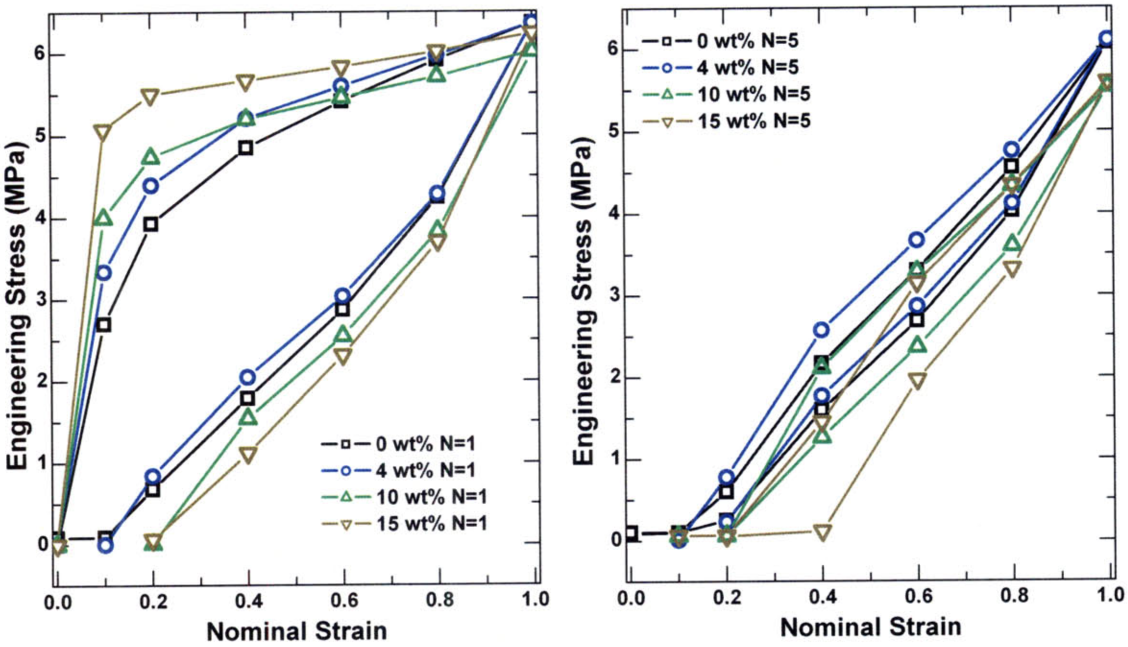

Figure 5-18: Softened response of the 0, 4, 10, and 15 wt% Laponite-filled nanocomposites determined from the stress relaxation behavior during the 1st and 5th cycle. The equilibrium path falls halfway between the softened loading and unloading response.

Increasing the Laponite concentration increases the initial stiffness and flow stress exhibited by the relaxed or softened path upon initial loading. The addition of Laponite at concentrations above the percolation limit decreases the hardening slope of the relaxed response as well as the stress achieved upon un-loading. This is likely due to increased localized plastic deformation caused by the presence of the rigid filler. As a consequence the softened responses converge at a nominal strain equal to unity upon initial loading and the second path converges to the same stress. The softened path upon subsequent loading for each composite is quite similar. Despite these differences upon initial loading, Laponite does not significantly influence the equilibrium path as shown in Appendix A-3.

5.3.6 X-ray Scattering

Morphological studies allow for further elucidation of the structural characteristics of these semicrystalline polyurethane nano-clay composites while undergoing tensile deformation. Martin et al have reported that Elasthane 80A exhibits a broad, weak hard segment diffraction pattern when the material is compression molded and annealed at 135°C [24]. The broad peak suggests minimal long range order and the peak which corresponds to a hard segment lattice *d*-spacing of 0.439 nm falls within the expected range exhibited by 4,4'-methylene diphenyl diisocyanate hard segments chain extended with 1,4-butanediol (MDI-BDO) [3, 25]. WAXS spectra of a pure and 8 wt% Laponite-filled composite are shown below in Figure 5-19 as the materials are stretched. The diffraction patterns are analyzed at four positions that correlate to the undeformed, yield, soft segment orientation, and strain hardening regimes of the stress-strain profile. The diffraction patterns are displayed in full in Appendix A-4. The pure polyurethane exhibits a broad peak at a *d*-spacing of 0.447 nm ($2\theta = 15.8°$) and shoulder at 0.421 nm ($2\theta = 16.8°$). The presence of two peaks is a result of slow solvent casting and microphase segregation. When the material is stretched the intensity of this peak decreases, indicating hard domain disruption and re-orientation as well as specimen thinning. When the stretch achieved corresponds to that within the strain hardening regime, a broad peak that spans 10° and peaks at a *d*-spacing of 1.21 nm ($2\theta = 5.8°$) results. It is not clear what structure feature this peak corresponds to because the inter-domain spacing between hard domains upon significant stretch and re-orientation is typically 10-20 nm and between crystallized soft segments is ~0.4 nm. However, this peak it is not observed in the Laponite-filled samples.

Reflections indicative of Laponite powder are not observable in the 8 wt% Laponite-filled nanocomposite diffraction pattern; specifically the absence of the *d*001 diffraction peak suggests the nano-clay is fully exfoliated. It is important to note that the *d*001 and *d*020/110 peak reported by the manufacturer as 1.28 nm and 0.452 nm are instead observed at 1.38 nm and 0.390 nm respectively. This discrepancy is unexpected and may result due to a difference in specimen preparation. Typically powders are ground to a fine dust before x-ray interrogation, but because a sharp pattern was captured from the powder as constituted this step was avoided. However, the addition of nano-clay does increase the intensity of the hard segment reflections when compared to those of the pure specimen. Similarly, the hard segment melting endotherms observed with differential scanning calorimetry exhibit increased intensity when nano-clay is added.

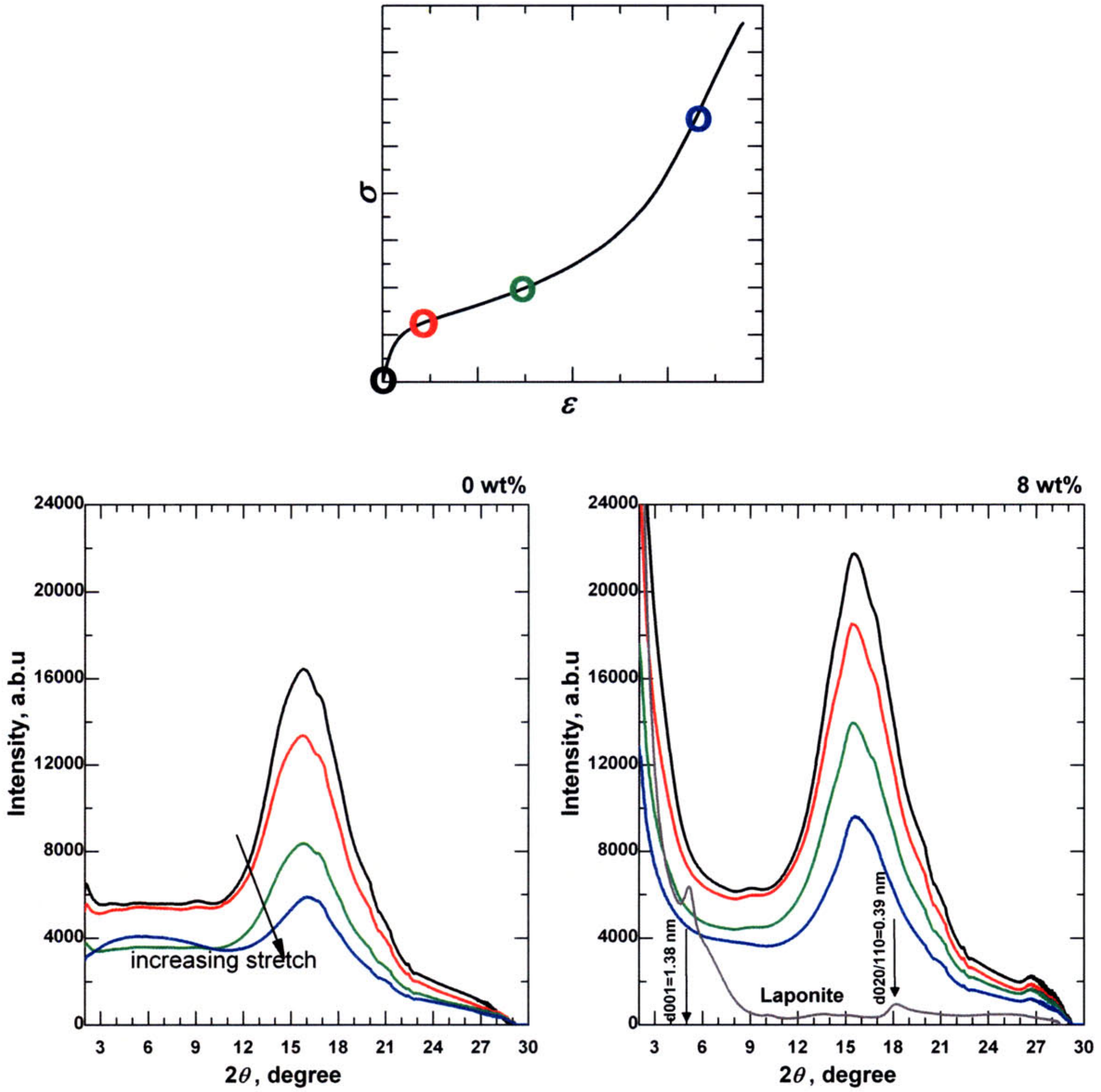

Figure 5-19: WAXS spectra of pure and 8 wt% Laponite-filled Elasthane as the material is deformed. The spectra shown corresponds to four positions along the stress-strain curve: 1. undeformed (black circle), 2. yield (red), 3. soft segment re-orientation (green), and 4. strain hardening (blue). The diffraction pattern of Laponite powder is included with the 8 wt% Laponite-filled composite spectra.

The intensity of a hard segment melting endotherm increases when the crystallite is more pure and/or perfect [26]. The preferential association of the Laponite platelets to the hard micro-domains at a concentration greater than the percolation limit likely restricts mobility and prevents crystallite adulteration. The addition of nano-clay increases the hard segment lattice spacing from 0.447 nm (2θ = 15.8°) to 0.456 nm (2θ = 15.5°) and maintains the secondary spacing at 0.421 nm (2θ = 16.8°). Upon increased deformation the intensity of the broad peak indicative of hard segment lattice spacing too decreases in the 8 wt% sample. If a broad peak of low intensity does occur near 6°, like that in the pure polyurethane at the greatest extent of deformation, it is masked by the presence of Laponite. Small angle x-ray scattering would help to further identify the hard micro-domain evolution, but as mentioned in the previous section this data in the Laponite filled samples was indistinguishable (See Appendix A-4). Consequently, inference from azimuthal analysis of the WAXS spectra must be relied upon.

Azimuthal scans within *d*-spacings of 0.447 nm and 0.468 nm (15.09° to 15.83°) and 0.409 nm and 0.427 nm (16.56° and 17.28°) help to elucidate the how the hard segments evolve upon deformation, shown in Figures 5-20 and 5-21. The peaks at 0.447 nm for pure Elasthane and 0.456 nm for the 8 wt% filled nanocomposite are initially randomly oriented indicating the matrix is isotropic prior to deformation. Upon deformation, they orient with the equator. The shoulder at 0.421 nm in both materials also begins randomly distributed but upon deformation orients with the equator. A six-fold symmetry begins to develop in the composite, typical of soft segment alignment, at the largest stretch. This result indicates that the nano-clay does not restrict soft segment alignment, but rather its presence amplifies the chain alignment as well as the hard segment intensity.

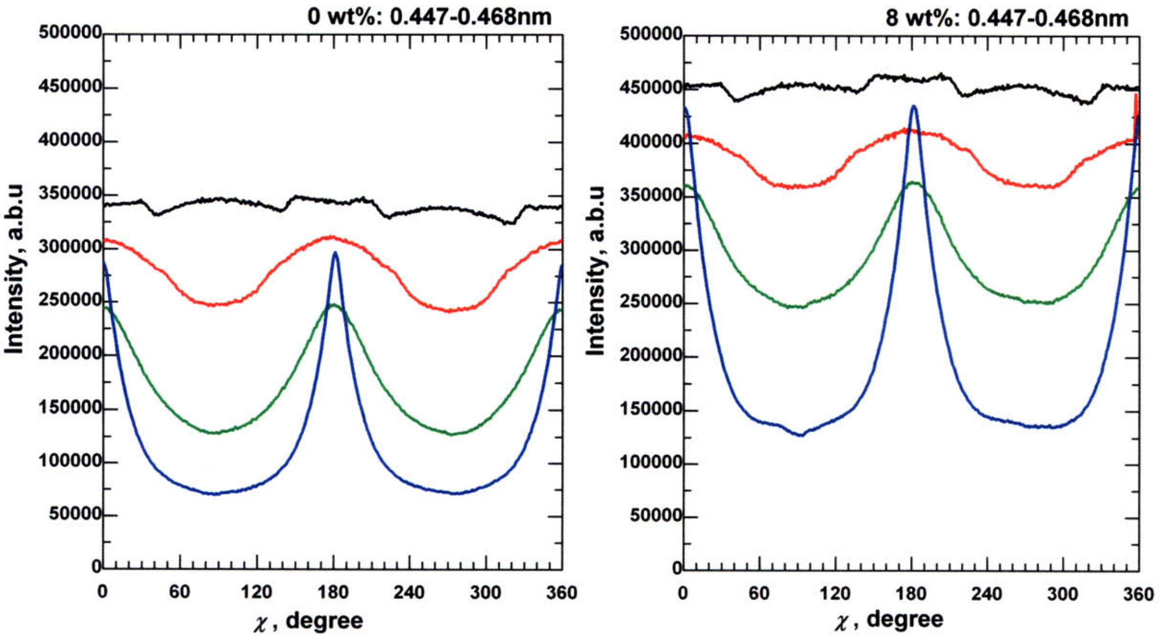

Figure 5-20: Azimuthal scan of the pure and 8 wt% Laponite-filled polyurethane composite as the deformation increases at *d*-spacing between 0.447 and 0.468 nm ($2\theta = 15.09°$ to $15.83°$).

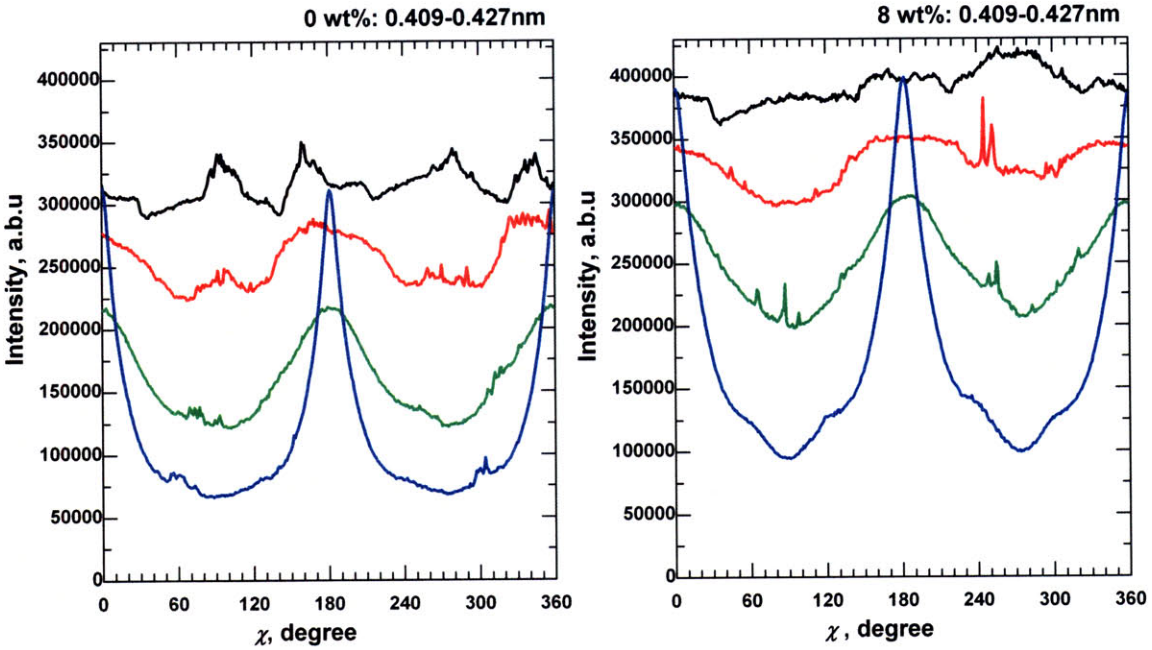

Figure 5-21: Azimuthal scan of the pure and 8 wt% Laponite-filled polyurethane composite as the deformation increases at *d*-spacing between 0.409 and 0.427 nm (2θ = 16.56° to 17.28°).

The preferential association of Laponite to the hard micro-domains imposes spatial restrictions and/or constraints on the hard segments. Upon deformation re-orientation of the hard micro-domain/Laponite structures encourage local soft segment alignment. The hard micro-domain/Laponite structures act like rigid fillers around which the soft chains must stretch. As observed in the previous section, the consequence of this amplified orientation is increased plastic strain and matrix damage.

5.3.7 Attenuated Total Reflectance Fourier Transform Infrared Spectroscopy

From the dynamic mechanical analysis results detailed in Chapter Four, it is clear that the heat distortion temperature of the Elasthane increases with increasing Laponite concentration. However, it is not clear whether this behavior is a consequence of Laponite jamming or enhancement of hard segment melting temperature. In general the melting temperature of a material is increased if the intermolecular cohesive bonds holding the material together are stronger [26]. Furthermore, the intensity of a hard segment melting endotherm increases when the crystallite is more pure and/or perfect [26]. Both of these characteristics are exhibited in the first heating cycle of DSC analysis when the Laponite concentration increases as shown in Chapter Four. Attenuated total reflectance Fourier transform infrared spectroscopy (ATR-FTIR) can be used to measure how the intensity of the free and hydrogen-bonded NH and C=O of the

Elasthane varies with increasing Laponite concentration [5, 6]. If as the clay concentration increases, the ratio of the areas under the peaks at 1703 cm^{-1} and 1730 cm^{-1}, corresponding to the hydrogen-bonded and non-bonded carbonyl group of the urethane, increases, it can be concluded that the degree of hydrogen-bonding in Elasthane is increasing [5, 27]. By evaluating the ratio of the intensities of the bonded and free peaks of the ATR-FTIR spectrum the origin of the enhancement in heat distortion temperature can be determined and the preferential association of the nano-clay with the hard micro-domains of Elasthane can be further confirmed [5].

The ATR-FTIR spectrum of the Elasthane/Laponite composites are shown in Figure 5-22. The spectral signature of this polyurethane has been characterized previously by Christenson et al and is displayed in Table 5-2 [28]. The peak at 1000 cm^{-1}, absent in the pure polyurethane spectrum, corresponds to the presence of stretched Si-O bonds in the Laponite platelets [29]. Consequently as the Laponite concentration increases the intensity of the peak at this wavelength increases. The ratio of the areas under the peaks corresponding to the hydrogen and non-bonded (or free) carbonyl bonds (HCO and FCO subscripts respectively) decreases initially upon the addition of 6 wt% Laponite as shown in Table 5-3. As the Laponite concentration increases the ratio approaches that of pure Elasthane. However, if the extent of the free or hydrogen-bonded carbonyl bond absorbance to the total carbonyl bond absorbance is instead compared, as explained in [30], the addition of Laponite does not appear to influence inter-urethane bonding. This trend is the same as that when the –NH bond of the urethane linkages (3325 cm^{-1}: not shown) is evaluated against the standard –CH stretching signature of the polyether (2860-2940 cm^{-1}: not shown) [27].

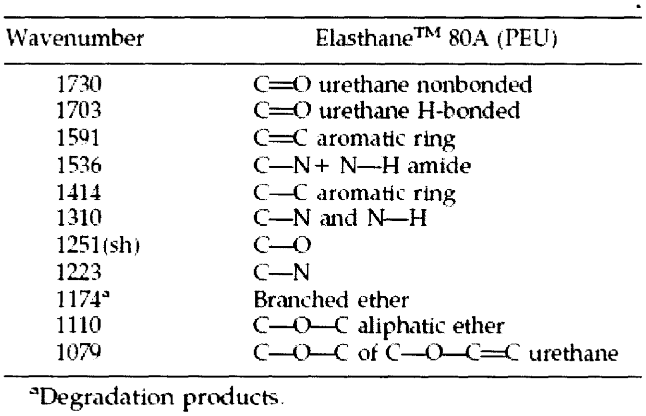

Wavenumber	Elasthane™ 80A (PEU)
1730	C=O urethane nonbonded
1703	C=O urethane H-bonded
1591	C=C aromatic ring
1536	C—N + N—H amide
1414	C—C aromatic ring
1310	C—N and N—H
1251(sh)	C—O
1223	C—N
1174^a	Branched ether
1110	C—O—C aliphatic ether
1079	C—O—C of C—O—C=C urethane

^{a}Degradation products.

Table 5-2: ATR-FTIR spectral assignments for Elasthane determined by Christenson et al in [28].

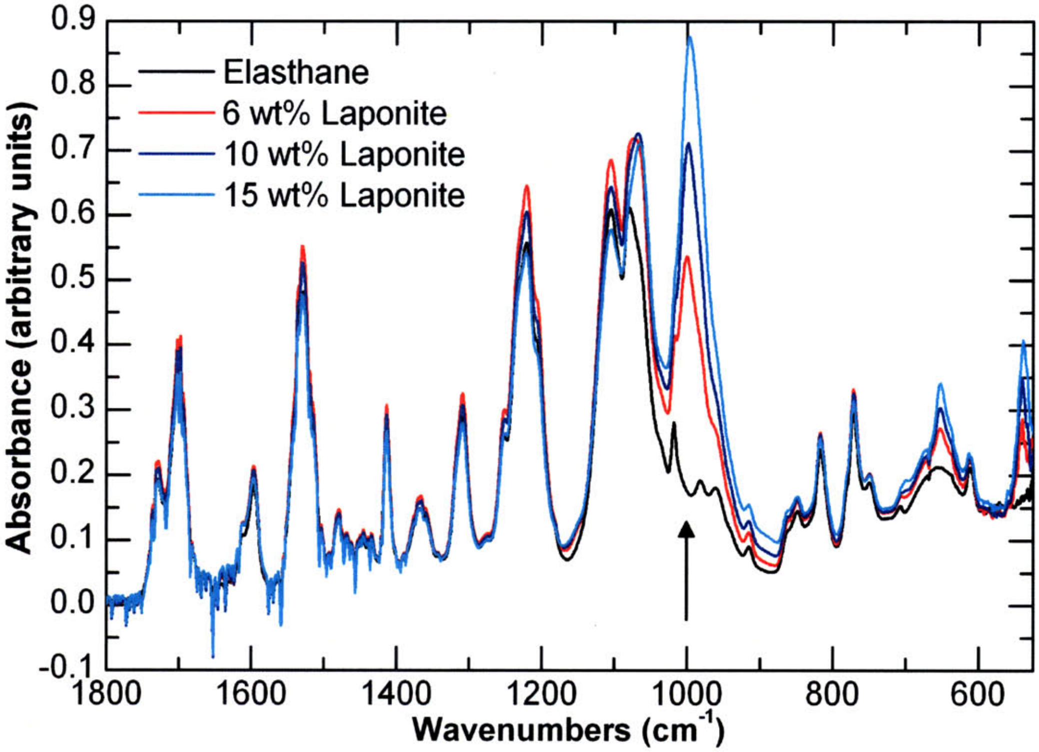

Figure 5-22: ATR-FTIR spectrum of pure Elasthane 80A and that filled with 6 wt%, 10 wt% and 15 wt% Laponite.

Laponite	A_{HCO}/A_{FHO}	A_{HCO}/A_{CO}	A_{FCO}/A_{CO}
0	2.72	0.73	0.27
4	2.66	0.73	0.27
10	2.67	0.73	0.27
15	2.69	0.73	0.27

Table 5-3: Ratio of area under the absorbance peaks of the hydrogen-bonded carbonyl bonds and the free carbonyl bonds (A_{HCO}/A_{FCO}) as well as the ratio of these areas to the total absorbance area constituting carbonyl bonds described by [30].

These results indicate that the addition of clay does not reduce the hard segment inter-urethane hydrogen bonding and order, nor does it reduce the hydrogen bonding between the hard segment and soft segment. Whether the Laponite platelets are physically linked to the matrix or kinetically trapped, which can not be determined conclusively from these results, Laponite does not influence microphase separation. Ultimately, the long processing time utilized via slow solvent casting allows for self-assembly and complete microphase separation irregardless of Laponite concentration. Furthermore, the preferential association of the nano-clay with the hard micro-domains adds further order via spatial constraint.

5.3.8 Cross-Polarized Microscopy

Ordered, fractal-like domains are observed under cross-polarized light which are comprised of polyurethane hard micro-domains, Laponite, and conformationally-confined soft domains. These domains which measure approximately 20-100 μm in size are disrupted upon yield and continue to break up with increasing stretch as shown in Figure 5-23 and 5-24. Micrographs taken under cross-polarized light of a pure Elasthane film and a nanocomposite film containing 10 wt% Laponite elucidate this behavior. The bright ordered domains seen in the undeformed specimens become dark and amorphous upon deformation. At yield, these ordered domains or sub-structures are stressed and stretched. Consequently, the bright domains intensify and begin to break up, expanding in size as shown in Figure 5-23. It proved difficult to capture this point of initial domain break-up in nanocomposites containing a percolated Laponite network because the onset of yield begins almost immediately upon deformation. Upon greater tensile deformation these bright domains continue to stretch parallel to the stretch direction and break-up further. As a result, the bright, ordered domains become dark and amorphous. Complete disruption of the ordered domains is observed prior to strain hardening, but after significant soft segment orientation.

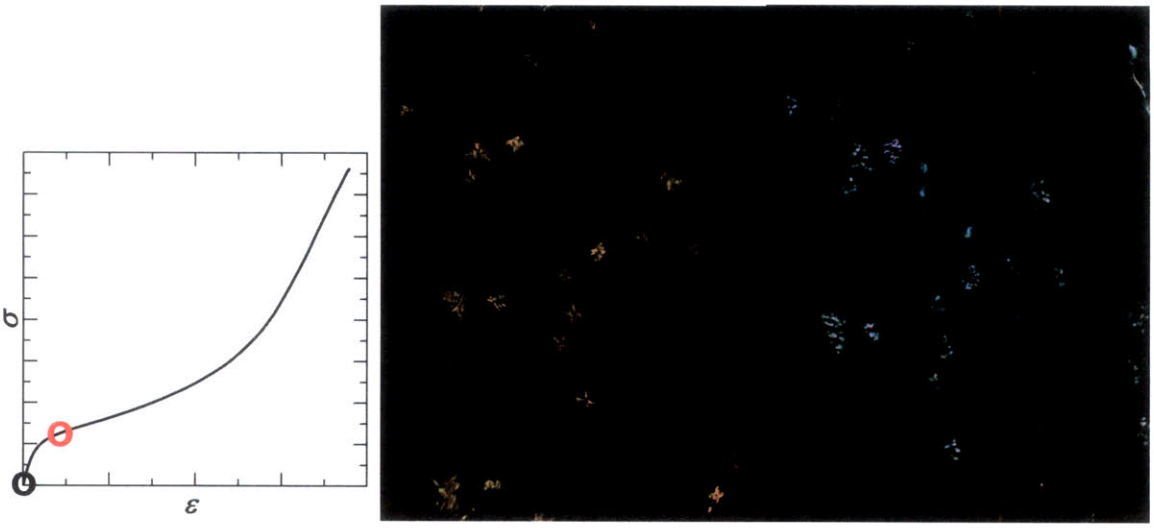

Figure 5-23: Comparison of the long range order exhibited through cross-polarized microscopy of pure Elasthane prior to deformation (left) and after deformation to yield (image width is 2.14 mm). The bright ordered domains increase intensity and begin to crack and separate upon yield.

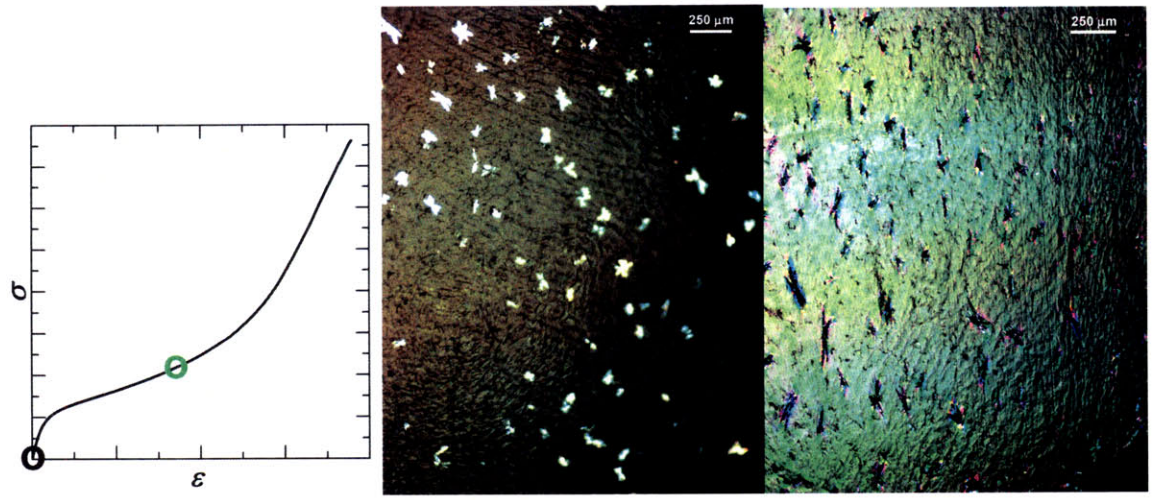

Figure 5-24: Comparison of the long range order exhibited through cross-polarized microscopy of 10 wt% Laponite-filled Elasthane prior to deformation (left) and after significant stretch and soft-segment re-orientation and alignment. The bright ordered domains become dark and amorphous indicating that these sub-structures have been completely disrupted at large stretch.

Ultimately, upon deformation these ordered domains are irreparably damaged—after inelastic stretch and mechanical unloading, the original ordered domains remain disrupted and unrecoverable. These cross-polarized images provide visual evidence that indeed the matrix does undergo irreparable damage upon deformation, especially in the localized areas where Laponite and hard micro-domains constrain the soft segment.

5.4 Conclusions

Thermoplastic polyurethane filled with nano-clay demonstrates strong hysteresis, time dependence, and cyclic softening. The rate sensitivity of the polyurethane increases with Laponite concentration as does the extent of softening between the first and fifth cycle of loading. Similarly, the addition of Laponite increases the residual or plastic strain, particularly when concentrations exceed the percolation limit. The pure and Laponite filled polyurethanes exhibit two characteristic relaxation times. The long relaxation time corresponds to the hard micro-domains and the short relaxation time corresponds to the soft segment. As the magnitude of the applied stretch increases the soft segments stretch, align and orient while the hard segments rotate but do not break-up. Consequently, the long relaxation time exhibits scatter and remains constant while the short relaxation time increases with stretch. The addition of nano-clay too increases the sensitivity of the material to orientation induced softening. The extent of modulus decay with orientation is dependent upon nano-filler concentration, aspect ratio and polydispersity. Ultimately, nano-clay reinforces the stress response of Elasthane, but also locally damages the polyurethane matrix, especially when concentrations above the percolation threshold are utilized. Laponite does not influence the hyperelastic or equilibrium response of the material—that is matrix dependent. Instead, the nano-clay influences the non-equilibrium response—the rate sensitivity and time dependence—much like rigid particles influence the viscosity of dilute solutions.

ATR-FTIR results indicate that the addition of clay does not reduce the hard segment inter-urethane hydrogen bonding and order, nor does it reduce the hydrogen bonding between the hard segment and soft segment. Laponite does not influence microphase separation. This confirms that the equilibrium matrix polyurethane response is unaffected by the addition of nano-clay. Ultimately, the long processing time utilized via slow solvent casting allows for self-assembly and complete microphase separation irregardless of Laponite concentration. The preferential association of Laponite to the hard micro-domains imposes spatial restrictions and/or constraints on the hard segments. Wide angle x-ray scattering indicates that upon deformation the hard micro-domain/Laponite structures re-orient and encourage local soft segment alignment. The hard micro-domain/Laponite structures act like rigid fillers around which the soft chains must stretch. As is observed via mechanical characterization, the consequence of this amplified orientation is increased plastic strain and matrix damage. Cross-polarized images provide visual evidence that indeed the matrix does undergo irreparable damage upon deformation, especially in the localized areas where Laponite and hard micro-domains conformationally constrain the soft segment initially. Ultimately, understanding the morphological and mechanical influence of nano-clay on the elastomeric behavior is important for the continued advancement of engineering thermoplastics.

5.5 References

[1] L. J. Korley, B. D. Pate, E. L. Thomas, and P. T. Hammond, "Effect of the degree of soft and hard segment ordering on the morphology and mechanical behavior of semicrystalline segmented polyurethanes," *Polymer*, vol. 47, pp. 3073-3082, 2006.

[2] D. J. Martin, G. F. Meijs, P. A. Gunatillake, S. J. McCarthy, and G. M. Renwick, "The effect of average soft segment length on morphology and properties of a series of polyurethane elastomers.2. SAXS-DSC annealing study," *Journal of Applied Polymer Science*, vol. 64, pp. 803-817, 1997.

[3] J. T. Koberstein, A. F. Galambos, and L. M. Leung, "Compression-molded polyurethane block copolymers. 1. Microdomain morphology and thermomechanical properties,"

Macromolecules, vol. 25, pp. 6195-6204, 1992.

[4] M. Song and K. J. Yao, "X-ray diffraction detection of compliance in polyurethane-organoclay nanocomposites," *Materials Science And Technology*, vol. 20, pp. 989-992, 2004.

[5] X. H. Dai, J. Xu, X. L. Guo, Y. L. Lu, D. Y. Shen, N. Zhao, X. D. Luo, and X. L. Zhang, "Study on structure and orientation action of polyurethane nanocomposites," *Macromolecules*, vol. 37, pp. 5615-5623, 2004.

[6] Y. I. Tien and K. H. Wei, "Hydrogen bonding and mechanical properties in segmented montmorillonite/polyurethane nanocomposites of different hard segment ratios," *Polymer*, vol. 42, pp. 3213-3221, 2001.

[7] A. Aneja and G. L. Wilkes, "A systematic series of 'model' PTMO based segmented polyurethanes reinvestigated using atomic force microscopy," *Polymer*, vol. 44, pp. 7221-7228, 2003.

[8] B. Finnigan, D. Martin, P. Halley, R. Truss, and K. Campbell, "Morphology and properties of thermoplastic polyurethane nanocomposites incorporating hydrophilic layered silicates," *Polymer*, vol. 45, pp. 2249-2260, 2004.

[9] H. J. Qi and M. C. Boyce, "Stress-strain behavior of thermoplastic polyurethanes," *Mechanics of Materials*, vol. 37, pp. 817-839, 2005.

[10] L. J. Korley, *PEO-containing Copolymers as Polyurethane Soft Segments in the Development of High Performance Materials*, Ph.D. in Program in Polymer Science and Technology, Cambridge, MA:Massachusetts Institute of Technology, 2005.

[11] J. Diani, M. Brieu, and J. M. Vacherand, "A damage directional constitutive model for Mullins effect with permanent set and induced anisotropy," *European Journal of Mechanics A: Solids*, vol. 25, pp. 483-496, 2006.

[12] H. J. Qi and M. C. Boyce, "Constitutive model for stretch-induced softening of the stress-stretch behavior of elastomeric materials," *Journal of the Mechanics and Physics of Solids*, vol. 52, pp. 2187-2205, 2004.

[13] J. D. Ferry, *Viscoelastic Properties of Polymers*, 3rd ed. New York, NY: John Wiley & Sons, Inc., 1980.

[14] A. Einstein, "Investigations on the Theory of Brownian Movement," *Annalen der Physik*, vol. 4, pp. 371-381, 1906.

[15] J. Yi, M. C. Boyce, G. F. Lee, and E. Balizer, "Large deformation rate-dependent stress-strain behavior of polyurea and polyurethanes," *Polymer*, vol. 47, pp. 319-329, 2006.

[16] B. Finnigan, P. Casey, D. Cookson, P. Halley, K. Jack, R. Truss, and D. Martin, "Impact of controlled particle size nanofillers on the mechanical properties of segmented polyurethane nanocomposites," *International Journal Of Nanotechnology*, vol. 4, pp. 496-515, 2007.

[17] R. B. Dupaix and M. C. Boyce, "Constitutive modeling of the finite strain behavior of amorphous polymers in and above the glass transition," *Mechanics of Materials*, vol. 39, pp. 39-52, 2007.

[18] E. M. Arruda and M. C. Boyce, "A three-dimensional constitutive model for the large stretch behavior of rubber elastic materials," *Journal of the Mechanics and Physics of Solids*, vol. 41, pp. 389-412, 1993.

[19] J. S. Bergström and M. C. Boyce, "Deformation of elastomeric networks: relation between molecular level deformation and classical statistical mechanics models for rubber elasticity," *Macromolecules*, vol. 34, pp. 614-626, 2001.

[20] M. Niesten and R. J. Gaymans, "Tensile and elastic properties of segmented copolyetheresteramides with uniform aramid units," *Polymer*, vol. 42, pp. 6199-6207, 2001.

[21] M. Niesten, J. W. ten Brinke, and R. J. Gaymans, "Segmented copolyetheresteraramids with extended poly(tetramethyleneoxide) segments," *Polymer*, vol. 42, pp. 1461-1469, 2001.

[22] J. P. Flory, *Principles of Polymer Chemistry*. Ithaca, NY: Cornell University Press, 1953.

[23] E. Guth, "Theory of Filler Reinforcement," *Journal of Applied Physics*, vol. 16, pp. 20-25, 1945.

[24] D. J. Martin, G. F. Meijs, P. A. Gunatillake, S. P. Yozghatlian, and G. M. Renwick, "The influence of composition ratio on the morphology of biomedical polyurethanes," *Journal of Applied Polymer Science*, vol. 71, pp. 937-952, 1999.

[25] B. Finnigan, D. Martin, P. Halley, R. Truss, and K. Campbell, "Morphology and properties of thermoplastic polyurethane nanocomposites incorporating hydrophilic layered silicates," *Polymer*, vol. 45, pp. 2249-2260, 2004.

[26] R. J. Young and P. A. Lovell, *Introduction to Polymers*. Cheltenham, U.K.: Nelson Thornes Ltd., 1991.

[27] C. H. Dan, Y. D. Kim, M. H. Lee, B. H. Min, and J. H. Kim, "Effect of solvent on the properties of thermoplastic polyurethane/clay nanocomposites prepared by solution mixing," *Journal Of Applied Polymer Science*, vol. 108, pp. 2128-2138, 2008.

[28] E. M. Christenson, M. Dadsetan, M. Wiggins, J. M. Anderson, and A. Hiltner, "Poly(carbonate urethane) and poly(ether urethane) biodegradation: In vivo studies," *Journal of Biomedical Materials Research*, vol. 69A, pp. 407-416, 2004.

[29] J. A. Caulfield, T. A. Wells, and K. E. Miller, "Novel method for transmission infrared analysis of clay minerals using silicon wafer substrates," *Clays and Clay Minerals*, vol. 55, pp. 213-219, 2007.

[30] I. Yilgor, E. Yilgor, I. G. Guler, T. C. Ward, and G. L. Wilkes, "FTIR investigation of the influence of diisocyanate symmetry on the morphology development in model segmented polyurethanes," *Polymer*, vol. 47, pp. 4105-4114, 2006.

6. Influence of Laponite on the Shape Memory Behavior of Polyurethane

6.1 Introduction

Materials that exhibit shape change, whether metal alloy, ceramic, polymer or gel, have generated great interest in the past decade as actuators in the aerospace, textile and biomedical industries. For instance shape memory polymer foams have attracted attention as space deployable support structures, shelters for space habitation, and rover components, as well as embolic sponges due to the low density, increased surface area, and compressibility of the foam [1]. Should actuating polymers be able to respond as quickly and with as much strength as natural skeletal muscle, numerous devices that were previously unattainable could be realized—such as artificial muscle, haptic devices, electronic Braille screens, rehabilitation gloves, tremor suppressors, and micro-wings [2, 3]. Shape memory is the ability of a material to maintain a deformed shape and upon external stimulus recover the original, pre-deformed shape. The actuating external stimulus is most often thermal inducing entropic recovery, but for polymeric materials and gels light may also be employed. Ionic strength, pH, and solvent quality may also be used to induce shape transitions in gels [4]. Shape memory polymers which include amorphous polymers as well as chemically or physically cross-linked multi-block copolymers with either a melting transition or glass transition above the storage temperature (often ambient temperature, T_{amb} or 37°C in the human body) are attractive actuated materials because they exhibit moderate strength and significant strain recovery. Actuation stresses span the range from kilopascals to megapascals and recovery strains extend from 10% to 100% depending on the polymer employed.

Shape memory capability in polymers is attributed to both its chemical components and morphology. Linear multi-block polymers are often utilized in shape memory applications because they allow the actuation temperature, or transition temperature (T_{trans}) to be tuned via synthetic methods. These block copolymers contain at least two distinct, immiscible morphological phases. One phase is characterized by thermal transitions above the programming temperature of the shape memory polymer (SMP) and acts as a permanent physical link to the other phase, maintaining memory of the original shape prior to deformation. The second phase is characterized by either a melting or glass transition temperature (T_{trans}) above the storage temperature. Typical operation of a SMP includes production of the material in some specified and desired permanent configuration, e.g. as a cylindrical fiber of length l_o and radius r_o. Then the SMP is programmed or deformed to meet specifications of the desired temporary shape, e.g. a cylindrical fiber of longer length l ($l > l_o$) and radius r ($r < r_o$). Often the deformation temperature is set above the inherent transition temperature ($T_{trans}=T_g$ or T_m) of the polymer—the temperature which triggers entropic recovery—so that less work is needed to deform the material. If deformed at an elevated temperature, the polymer is then cooled to the storage temperature, vitrifying or crystallizing the second phase and holding the deformed, temporary shape. This temporary shape is maintained while the temperature is held below T_{trans}; however, upon an increase in temperature to a value greater than or equal to T_{trans} the mobile chains of the second phase entropically return to their previous configuration and the permanent shape is recovered—the fiber returns to its original length l_o and radius r_o. In order to obtain the temporary shape specified a second time, or a different temporary shape, the programming cycle must be repeated and more work applied to deform the material.

Polyurethanes are attractive shape memory polymers because they are well-studied linear multi-block copolymers consisting of soft segments with melting transition greater than ambient temperature ($T_{m,\,SS} > T_{amb}$) or hard segments with glass transition temperature greater than ambient temperature ($T_{g,\,HS} > T_{amb}$) that are either covalently cross-linked to the soft segment in thermosets or linked to the soft segment through hydrogen or ionic bonding in thermoplastics. This linkage between the soft and hard blocks of the polyurethane maintains the permanent shape unless the programming temperature approaches the hard segment melting temperature ($T_{m,\,HS}$) or the programmed deformation is to such an extent that the cross-links are permanently damaged. Versatile polyurethane chemistry allows the soft segment glass transition and melting temperature to be tailored for specific mechanical responses and surface character such as biocompatibility, hydrophilicity, or blood compatibility [5]. For instance, polyurethanes containing poly(ε-caprolactone) diol (PCL) soft segments are desirable for biomedical applications, i.e. as sutures or in drug delivery applications due to its biocompatibility and its melting transition temperature ($T_{m,PCL}$= 44-55°C depending on molecular weight) that is just greater than the temperature of the human body, T_{body}=37°C [4].

The capability of nano-clay to significantly enhance the thermomechanical properties of polyurethane is discussed in Chapter 4. The fact that the addition of Laponite increases the flexural storage modulus of Elasthane above and below its glass transition indicates that it may be possible to reinforce shape memory polyurethane with nano-clay and enhance the recovery stress when the material is subjected to a fixed strain and actuated. However, it has also been shown that Laponite forms a percolated network at concentrations above 2.5 vol% or 6 wt% and, upon deformation this network is disrupted, as is the polyurethane network which undergoes irreparable damage. Likely, there will be an optimum loading in which the free strain recovery and stress recovery at constrained strain are maximized.

Rezanejad and Kokabi showed in [6] that modified-Montmorillonite nano-clay (Closite 15A) enhanced the recovery stress of cross-linked, low-density polyethylene (LDPE) by ~200%. However, as a consequence the added nano-filler hinders chain motion and disrupts chain recovery so that in the 8 wt% filled LDPE nanocomposite there is a 12% decrease in recoverable strain. Similarly, Cao and Jana evaluated the influence of 1, 3 and 5 wt% of modified-Montmorillonite (Cloisite 30B), on the shape memory behavior of a custom synthesized polyurethane, containing polycaprolactone [7]. The melting transition of crystalline polycaprolactone was utilized as the shape memory transition trigger. At a 1 wt% loading, the clay is exfoliated, but at higher concentrations the clay is intercalated. At the 1 wt% loading, the increase in recovery stress (when strain is fixed) is 20% greater than that of the pure polyurethane. Cao and Jana believe this increase in recovery stress is greater than that exhibited by the other composites because the larger clay loadings further disrupt the hard micro-domains and soft segment crystallinity. This disruption in turn increases the rate of stress relaxation the resultant composite undergoes, minimizing the achievable recovery stress. In this study we utilized commercial, biocompatible, thermoplastic polyurethane, MM 5510 from the DiAPLEX Series provided by Mitsubishi Heavy Industries, Ltd. and Laponite to evaluate the influence of nano-clay on the shape memory properties of polyurethane.

6.2 Materials and Experimental Methods

6.2.1 Materials

The shape memory polyurethane MM 5510 (Mitsubishi Heavy Industries, Ltd.) was supplied in pellet form and used as received. This polyurethane is composed of diphenylmethane-4,4-diisocynate, adipic acid, ethylene oxide, polypropylene oxide, 1,4-butanediol, and bisphenol A [8]. The glass transition temperature, T_{trans}, of the soft segment is specified by the provider as 55°C. Dimethyl formamide (DMF) from Sigma Aldrich was used as received to dissolve the polyurethane pellets. Nano-clay platelets, Laponite RD (Southern Clay Products, Inc.), with diameter of ~25 nm and thickness of 1 nm were used as received in powder form.

6.2.2 Composite Preparation

Polyurethane-Laponite-DMF solutions were prepared via the solvent exchange method discussed in Chapter 3 so that the final concentration of polyurethane in solution was 1 wt% and the final Laponite concentration in polyurethane was 0, 4, 10 and 15 wt%. The solutions were then roll-mixed at a moderate speed for two days prior to use to ensure that the polyurethane was completely dissolved. MM5510/Laponite nanocomposite films with 120−180 μm thicknesses were prepared in Teflon containers (6 cm × 4 cm) by controlled evaporation of DMF. Solvent casting took place immediately after the solutions were sonicated for 60 minutes to ensure complete dispersal of the Laponite in solution. The evaporation rate of DMF was maintained by keeping the films in a closed 50°C oven with a 0.02 $m^3 h^{-1}$ N_2 purge flow. The resultant films were characterized using the following procedures.

6.2.3 Characterization Methods

6.2.3.1 Laponite Dispersal

The 4 wt%, 10 wt% and 15 wt% Laponite nanocomposite TEM samples were prepared in a JEOL JEM 9310 focused ion beam (FIB) instrument. These samples were first sputter-coated with ~200nm of gold, and then a localized ~1μm-thick carbon protective film was deposited atop the selected area for lamella preparation. The samples were milled and polished in the FIB to give lamellae measuring 10 μm x 10μm x 80 nm. These samples were transferred to the copper grids using a micromanipulation system that consisted of a position-controlled polished glass rod that allowed for electrostatic pick-up of the lamellae. These lamellae were observed in a JEOL 200CX TEM operated at 200 kV.

6.2.3.2 Thermal Transitions

To determine the influence of Laponite on the glass transition and melting transitions of the polyurethane differential scanning calorimetry measurements were carried out on a TA Instruments Q1000 DSC at a heating rate of 10°C min^{-1} between -90° and 250°C, using aluminum pans. Dynamic mechanical measurements were also made at a frequency of 1 Hz and at a heating rate of 3°C min^{-1} from -150°C to 200°C using the TA Instruments Q800 DMA.

6.2.3.3 Thermal Expansion Coefficient

The thermal expansion coefficient of the nanocomposites was determined using TA Instruments Q800 DMA. A controlled force test was run from -150°C to 150°C at 2°C min^{-1} and a tensile force was applied so that the nominal stress in the sample would be 10 kPa based on the initial width and thickness of the rectangular specimen. The length displacement data was used to calculate the linear axial coefficient of thermal expansion,

$$\alpha = \frac{1}{l_0}\frac{dl}{dT}, \tag{6.1}$$

where l/l_0 is the axial thermal stretch and l_0 the original length prior to testing. Each test was repeated on a minimum of two, unique samples and only at temperatures above 80°C were there discrepancies in behavior. This can be attributed to instrument difficulty in holding the 10 kPa load while the sample was undergoing significant thermal softening.

6.2.3.4 Stress-Strain Behavior Above and Below the Transition Temperature

Various tensile tests were completed on each of the nanocomposites using the EnduraTEC ELF 3200 with heat chamber. One test procedure required that each specimen be stretched 150% and unloaded to its initial length five times. Each nanocomposite was tested at room temperature (~25°C) and at 70°C, a temperature above the glass transition or trigger temperature of the polyurethane. A second procedure required that each specimen be stretched to 1.2, 1.4, 1.7, 2.0 and 2.5 times its original length and unloaded five times at each stretch before proceeding to the larger deformation. The second procedure was also completed at room temperature and at the elevated temperature. The third procedure required that each nanocomposite be stretched at an elevated temperature to 1.4, 1.7, or 2.5 times its original length and unloaded five times. Upon completion each specimen was cooled to room temperature (approximately 10 minutes of forced air flow was needed to cool the sample) and then stretched to a value equal to or greater than the previous stretch and again unloaded. For all tests the gauge length of the specimens was 8 mm and the crosshead speed was 0.13 mm s^{-1}.

During testing, using the ELF 3200, the thin-film sample was lit with a fiber optic light and videoed using a Qimaging Retiga 1300 CCD camera equipped with a 200 mm Canon f14.0 Canon lens and a Nikon 200 mm extension. Dots using a fine tip black permanent marker were placed in alternating pattern along the length of the sample as shown below in Figure 6-1 and the specimen width and thickness at each location were measured with a micrometer. The camera was placed at a distance of approximately 1 m from the specimen and images captured every 0.5 s. The images were analyzed with a digital image correlation algorithm developed by Correlated Solutions Incorporated (CSI). The deformed image was correlated to the reference image via two distinct points of interest, i.e. two black dots, connected by a straight line. The software then output the x and y pixel position of these two distinct points. The change in longitudinal distance was used to calculate the true strain while the change in horizontal distance was used to calculate the true stress as shown below:

$$\varepsilon_{true} = \ln\left(\frac{y_2 - y_1}{y_{2,0} - y_{1,0}}\right) \tag{6.2}$$

and

$$\sigma_{true} = \frac{F}{(wt)} = \frac{F}{(w_0 t_o)}\left(\frac{w_0}{w}\right) = \frac{F}{(w_0 t_o)}\left(\frac{x_{2,0} - x_{1,0}}{x_2 - x_1}\right) \tag{6.3}$$

when changes in thickness are assumed negligible, $t \approx t_0$. This video extensometer was used because strain localization was common within these samples since the thickness of the specimen varied ±20 μm through the length due to processing.

It is important to note that the grips used in ELF 3200 were not best suited for this material; however, time did not allow for procurement of another pair. The grips were screw tightened and the jaw faces were serrated. If the films were placed in these grips by themselves the serrated faces cut and damaged the sample, causing the data that was collected on that particular sample to be invalid. So instead a soft, slightly tacky elastomer was placed on either side of the specimen as a means to prevent specimen damage.

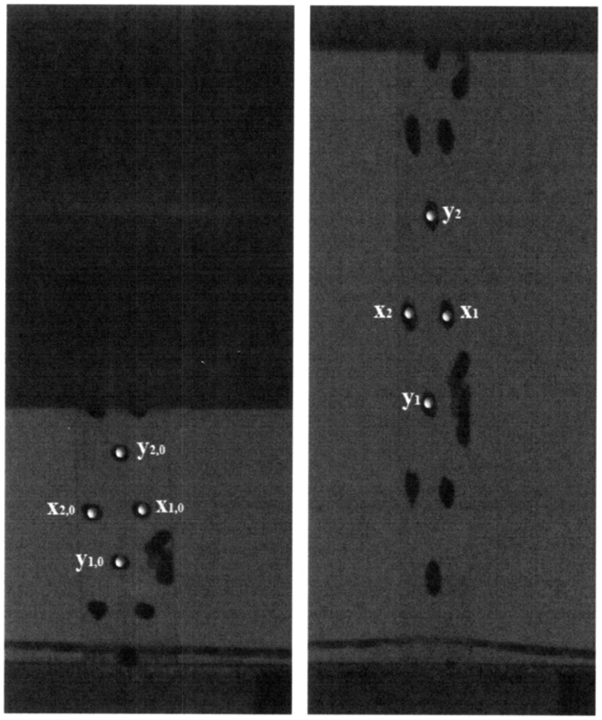

Figure 6-1: Images of a pure MM5510 polyurethane film inside the ELF 3200 as seen with the video extensometer. On the left is the un-deformed film with an 8 mm gauge length. On the right is the same film stretched to the instruments upper limit; the upper grip moves 12 mm upward, however, there are localized areas of deformation so the true strain in the sample does not reach 0.92 as is evidenced by the highlighted markers.

While the inclusion of this elastomer prevented puncture and tear of the specimen, it encouraged slippage at the grip locale or localized deformation there due to over-tightening of the grip screws. Often, the contact line or surface where the grip held the specimen was not even with the grip ends and could not be visualized from start to finish, as is the case in Figure 6-1. The extent of deformation that takes place within these regions cannot be accounted for. These problems manifested in the later tests which required thermal cycling. Consequently, when the instrument was programmed to stretch the specimen a certain amount, often the local deformations visualized from start to end within the specimen were not realized. Instead there was some slip or localized deformation outside the initial gauge length of the specimen and a lesser amount of strain was accounted for using the video extensometer. Therefore, throughout this chapter the specimen stretch programmed is reported as $\lambda_{specimen}$ and the local, true strain measured using the video extensometer is reported as true strain or λ_{true}.

6.2.3.5 Free Strain Recovery

The free strain recovered in these nanocomposites under virtually no load was examined two ways. The first method utilized the ELF 3200 with heat chamber. Each specimen was stretched to 1.4, 1.7, or 2.5 times it original length using displacement control at room temperature. Upon reaching the desired stretch the instrument feedback was changed to force control and the load was manually reduced over approximately five minutes time to virtually no load without buckling the specimen (in actuality a small positive tensile force in the specimen exists). Then while this load was maintained the temperature in the oven was increased from room temperature, ~25°C to 70°C over approximately 30 seconds and then held constant until the specimen stopped recovering strain and began lengthening. The second method utilized the TA Instruments Q800 DMA and did not allow for visualization of the specimen deformation. A custom program was made which equilibrated the temperature in the oven at 70°C for one minute and then the nominal strain was ramped at 0.0167 s^{-1} to 10%, 20%, 40%, 70% or 100% nominal or engineering strain. After holding this length for one minute the temperature was ramped to 25°C at -10°C min^{-1}. The force was then reduced to and held at 0.001 N and the temperature ramped back up to 70°C at 10°C min^{-1} and the strain recovery monitored. This procedure was repeated five times on each sample. This allowed the extent of strain recovery, total strain recovery and strain fixity defined below by Landlein and Kelch in [4] to be determined.

The extent of strain recovery, $R_r(N)$, compares the strain recovered from one cycle to the previous cycle:

$$R_r(N) = \frac{\varepsilon_m - \varepsilon_p(N)}{\varepsilon_\mathrm{m} - \varepsilon_p(N-1)}, \tag{6.4}$$

where ε_m is the maximum nominal strain applied, ε_p is the nominal irrecoverable strain during the specified cycle denoted by the integer *N*.

The extent of total strain recovery, $R_{r,\,total}(N)$, compares the strain recovered during one cycle to the deformed state:

$$R_{r,\,total}\left(N\right)=\frac{\varepsilon_m-\varepsilon_p\left(N\right)}{\varepsilon_{\mathrm{m}}}, \tag{6.5}$$

where ε_m is the maximum nominal strain applied, ε_p is the nominal irrecoverable strain during cycle number N.

The extent of strain fixity, $R_f\left(N\right)$, quantifies the ability of the material to hold its temporary shape after consecutive deformation cycles:

$$R_f\left(N\right)=\frac{\varepsilon_u\left(N\right)}{\varepsilon_{\mathrm{m}}}, \tag{6.6}$$

where ε_m is the maximum nominal strain applied, ε_u is the nominal strain realized under the no load condition prior to actuation and recovery during cycle number N. The positions of ε_m, ε_u, ε_p are described visually in the three dimensional deformation plot shown in Figure 6-2.

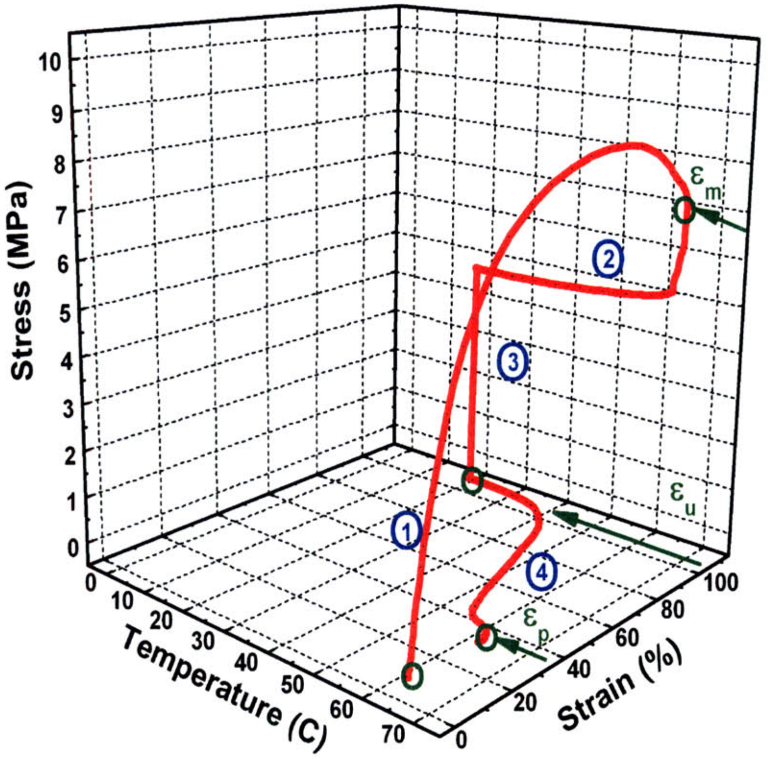

Figure 6-2: Visual description of the free strain recovery test and the locations of ε_m, ε_u, ε_p with respect to engineering stress, strain and temperature. The first step demarks deformation at an elevated temperature above T_{trans}. The second step demarks cooling to a temperature below T_{trans}. The third step demarks unloading to a no load condition. The fourth and final step demarks entropic recovery during the temperature ramp to a temperature above T_{trans}.

6.2.3.6 Constrained Strain, Stress Recovery

The constrained strain, stress recovery test also utilized the ELF 3200 with heat chamber. Each specimen is stretched to 1.4, 1.7, or 2.5 times its original length at room temperature and held at that stretch and allowed to relax for five minutes. Then, the length of the specimen is manually reduced until there is virtually no load without buckling the sample (in actuality a small positive tensile force in the specimen exists). This manual reduction in length is a slow process that takes approximately five minutes in order to allow for the time-dependent stress-recovery (opposite to stress relaxation) at room temperature to plateau. After the load is removed, the displacement is held constant and the temperature is increased from 25°C to 70°C over approximately thirty seconds and then held constant for ten minutes. Meanwhile, the load, which increases when the specimen attempts to shrink because the specimen is restricted, is monitored. The engineering stress is reported.

6.3 Results and Discussion

6.3.1 Laponite Dispersal

The Laponite platelets, which measure approximately 25 nm in diameter and 1 nm in thickness, are well dispersed within the polyurethane matrix even at concentrations above the percolation threshold ($\tilde{\phi}_p \approx$ 2.5 vol% or 6 wt%). Transmission electron micrographs of the nanocomposites containing 4, 10 and 15 wt% (shown in Figure 6-3) nano-clay further elucidate the efficacy of the solvent exchange technique to fully exfoliate the clay particles. In the 4 wt% sample the platelets are randomly oriented and separated by more than one particle diameter. At 10 wt% nano-clay necklaces span the sample, exemplifying a percolated network. It proved difficult to solvent cast the 10 wt% sample in particular because the percolated clay network encouraged crack growth upon solvent removal and often rather than a smooth continuous film, numerous film pieces resulted. In contrast, the 15 wt% sample starts to exhibit an aligned network of clay platelets due to volume restrictions. Just as it is impossible to re-fill a matchbox with matches once they have been removed without aligning them, the clay platelets must align and orient within the polyurethane matrix at this high concentration. This effect, coupled with the slow solvent removal and the presence of polar constituents such as ethylene oxide, promotes intercalation and flocculation as is observed in the lower left corner of the 10 wt% micrograph and the upper right corner of the 15 wt% micrograph. This clay dispersal is similar to that seen in the custom synthesized polyurethane containing poly(ethylene oxide) and 10 wt% Laponite discussed in Chapter 3. These micrographs visually suggest that the Laponite is not only reinforcing the hard micro-domains, but embedded within the soft domain as well.

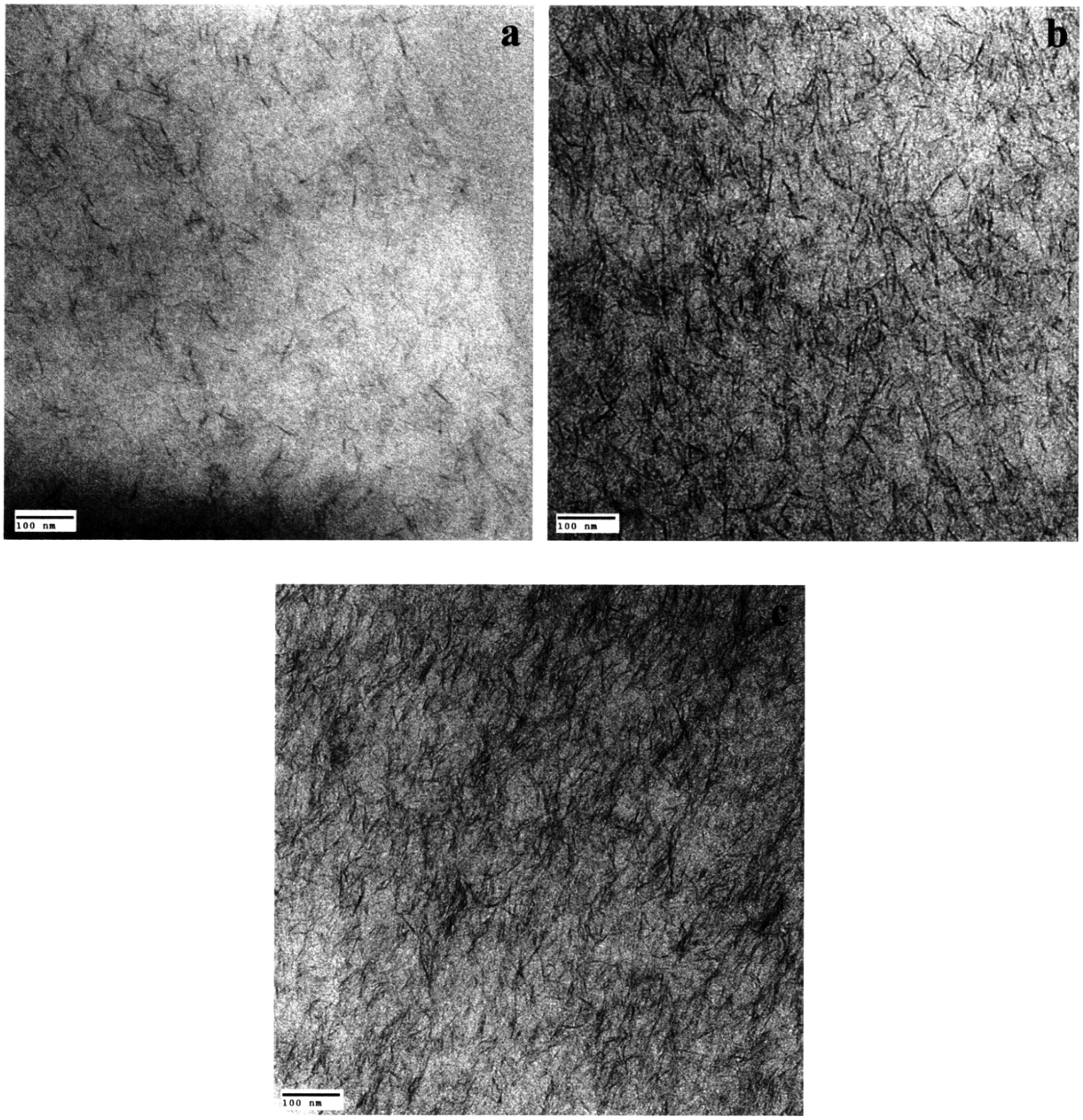

Figure 6-3: Transmission electron micrographs of MM5510 PU nanocomposites containing 4, 10, and 15 wt% Laponite (a, b and c, respectively). Note the Laponite platelets in the 15 wt% specimen are more aligned and there are instances of intercalation and flocculation in the specimens containing Laponite concentrations greater than the percolation threshold.

6.3.2 Thermal Transitions

Differential scanning calorimetry was used to verify that the transition temperature of the polyurethane was in fact 55°C as the manufacture reported. However, instead the complex nature of this multi-block polyurethane was revealed after solvent casting. Three glass transitions were observed upon the first heating cycle between 0°C and 100°C in addition to the hard segment melting endotherm near 200°C as shown in Figure 6-4.

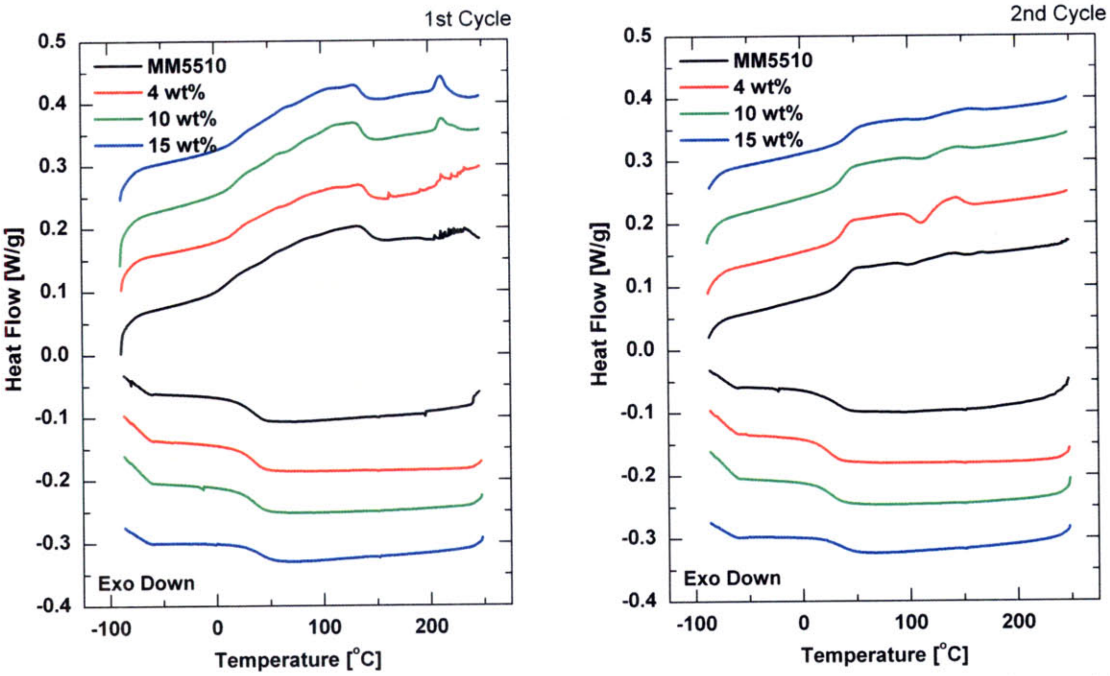

Figure 6-4: First and second heat flow cycles of pure MM5510 polyurethane and composites filled with 4, 10, and 15 wt% Laponite using differential scanning calorimetry.

Upon cooling and then reheating one soft segment glass transition dominates at ~35°C and then ~45°C, respectively. Aware of the results of Yang et al, who found that similar Mitsubishi shape memory polyurethane was plasticized upon soaking in a water, great care was taken to avoid water sorption [9]. All specimens were kept in a polycarbonate case and then within a desiccator when not being tested or zip-locked within two bags between tests. These results, in conjunction with dynamic mechanical analysis, suggest that the slow solvent removal and annealing at 50°C is responsible for the presence of the multiple glass transition temperatures at approximately 20°C, 50°C, and 75°C upon initial heating rather than water sorption.

Like in the Elasthane-Laponite composites upon initial heating, the hard segment melting temperature of the nanocomposite increases as does the intensity of the melting endotherm as the concentration of nano-clay increases. But upon cooling, a corresponding exotherm is unnoticeable. Upon reheating, the endotherm is broadened due to incomplete and imperfect re-crystallization due to the fast 10°C min^{-1} temperature ramp. However, it is not clear whether this behavior is a consequence of Laponite jamming and constrained motion or a change in morphology and hard micro-domain texture. In general the melting temperature of a material is increased if the intermolecular cohesive bonds holding the material together are stronger [10]. Furthermore, the intensity of a hard segment melting endotherm increases when the crystallite is more pure and/or perfect [10].

The thermal transitions observed with dynamic mechanical analysis, while within the same temperature range as the differential scanning calorimetry results, only illuminate one glass transition in freshly prepared samples and two transitions in aged samples. After numerous tests on thin-film nanocomposite samples prepared following the same procedure but at different dates there were discrepancies in the glass transition behavior. In some instances, particularly when samples were tested soon after preparation, only one soft segment glass transition was observed between 44°C and 54°C, depending on Laponite concentration. When numerous days passed these same nanocomposite samples exhibited different transition behavior, often exhibiting two transitions separated by 10°C in the pure sample and 30-40°C in the highly-filled samples although the nanocomposites were carefully stored in a dessicator and sealed from laboratory humidity (which ranged from 17% to 42% relative humidity). Despite these discrepancies, the magnitude of the flexural storage and loss moduli were consistent from one sample to the next. The addition of nano-clay enhances the flexural storage modulus most significantly at temperatures above the transition temperature. While water sorption has been shown by Yang et al to decrease the glass transition temperature in similar shape memory polyurethanes, only one transition was observed, not two or three transitions as was observed in these nanocomposites [9, 11]. Due to the care taken to store these samples in a desiccator, it is believed the multiple transitions are a result of processing and aging in the pure sample as well as due to the addition of nano-clay to the composites.

The glass transition temperature can be defined as either the temperature at which the flexural loss modulus reaches a local maximum or the temperature at which the ratio of the flexural storage modulus to the flexural loss modulus (*tan δ*) reaches a local maximum. The value determined via the flexural loss modulus is typically less than that determined via *tan δ*. In this case there was as much as an 18°C discrepancy as is shown in Table 6-1. Consequently, while the *tan δ*-based soft segment glass transition is observed at 45-55°C, the peak in E'' is closer to

30°C (as seen in Figure 6-5). This indicaties that these polyurethanes could in fact be used in biomedical applications since the body temperature is of similar magnitude (37°C). The addition of nano-clay too decreases the soft segment glass transition; however, the influence is not systematic. Likely, preferential reinforcement of the more polar soft segment creates a second sub-structure or morphology that develops further while the sample is stored at room temperature.

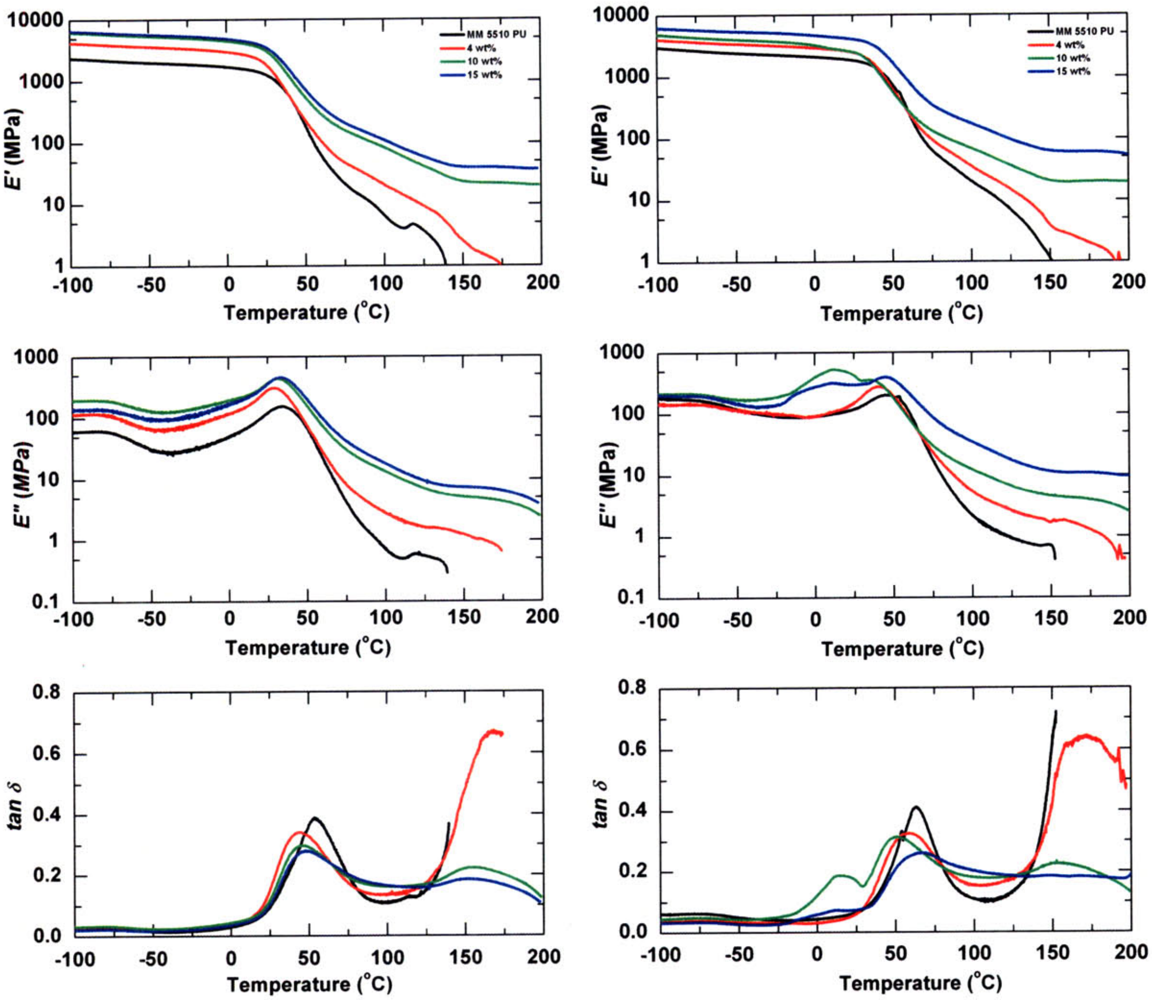

Figure 6-5: Dynamic mechanical response of pure MM5510 polyurethane and composites filled with 4, 10, and 15 wt% Laponite soon after preparation (left) and nine months later (right).

Glass Transition(s)						
	DMA (new)		DMA (aged)		DSC	
	E" peak	*tan δ* peak	*E"* peak	*tan δ* peak	1st Cycle	2nd Cycle
MM5510 PU	35.2°C	53.5°C	45.0°C, 54.0°C	53.5°C, 63.3°C	14.5°C, 51.9°C, 73.3°C	42.9°C
4 wt%	29.3°C	44.0°C	42.3°C	59.6°C	22.0°C, 52.4°C, 74.6°C	40.0°C
10 wt%	31.4°C	45.4°C	11.6°C, 36.4°C	14.0°C, 50.6°C	18.6°C, 54.7°C, 77.5°C	38.7°C
15 wt%	32.7°C	47.7°C	10.4°C, 46.3°C	10.4°C, 63.5°C	13.1°C, 51.9°C, 73.5°C	45.9°C

Table 6-1: Analysis of the glass transition temperatures observed between 0°C and 100°C via dynamic mechanical analysis and differential scanning calorimetry upon heating on freshly prepared and aged samples.

6.3.3 Thermal Expansion Coefficient

The addition of nano-clay to these polyurethane films not only alters the transition temperature, but decreases the in-plane thermal expansion coefficient at temperatures above and below the transition temperature, as seen in Figure 6-6. The transition temperature is demarked by the

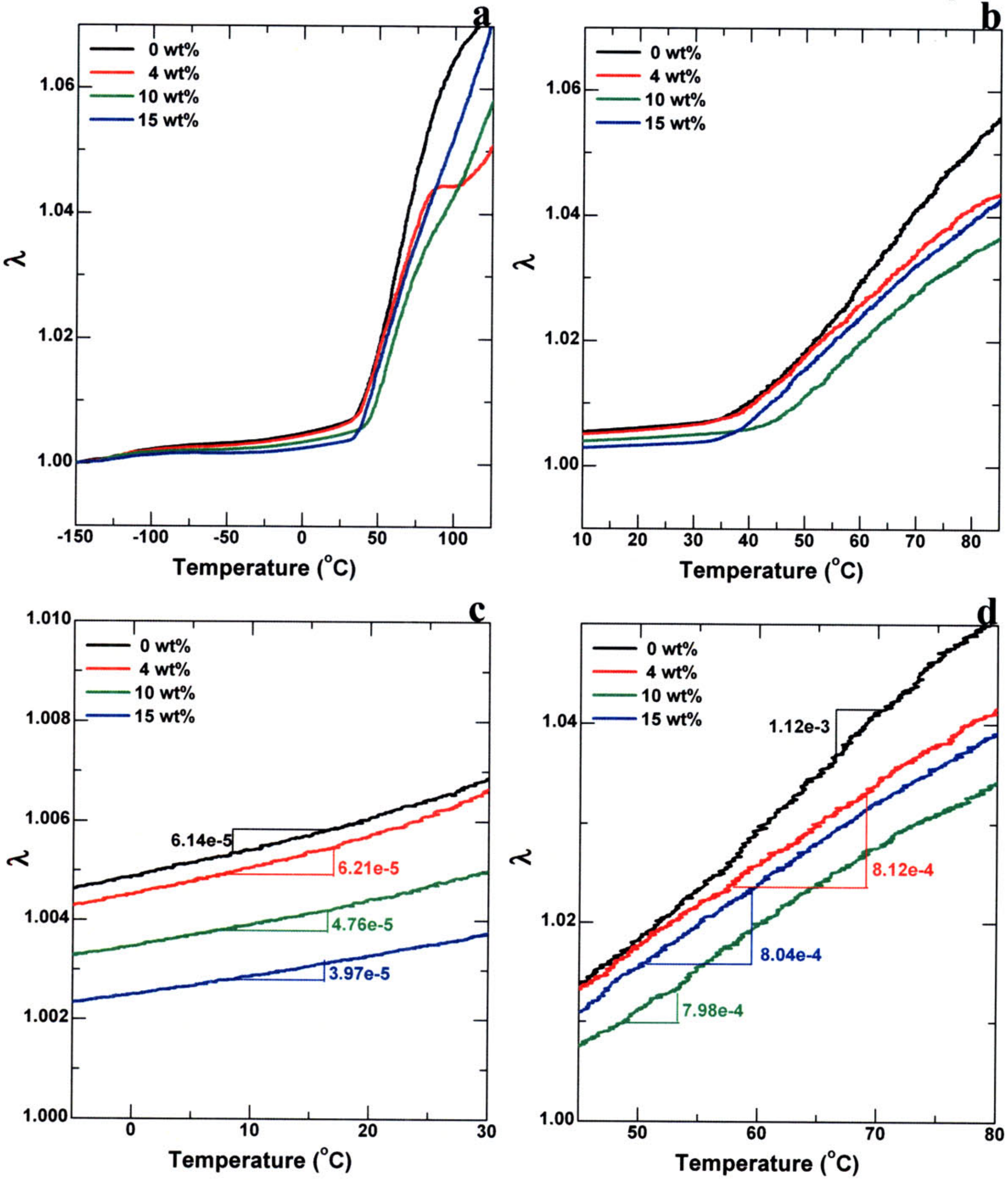

Figure 6-6: a) Thermal expansion of pure MM5510 polyurethane films and composites filled with 4, 10, and 15 wt% Laponite from -150°C to 125°C while under a 10 kPa tensile load. b) Enlarged view of the thermal expansion behavior within the shape memory operational temperature range interrogated. c & d) The thermal expansion coefficients below and above the transition temperature (55°C), respectively, are elucidated.

change in slope of the axial thermal stretch of the specimens at temperatures between 35°C and 45°C. The influence of nano-clay observed via the axial thermal stretch behavior is opposite to that seen with DSC and DMA. The addition of 15 wt% nano-clay does not appear to significantly change the transition temperature, but the addition of 4 wt% and 10 wt% systematically increases the transition temperature from 33°C to 35° and 42°C, respectively. The expansion behavior of the sample filled with 4 wt% Laponite, a concentration less than the percolation threshold, is similar to that of the pure polyurethane. At concentrations above the percolation threshold the influence of the nano-clay is more dramatic. The addition of 10 wt% and 15 wt% nano-clay decreases the coefficient of thermal expansion from $6.2\text{x}10^{-5}$ $°C^{-1}$ to $4.8\text{x}10^{-5}$ $°C^{-1}$ and $4.0\text{x}10^{-5}$ $°C^{-1}$, respectively, at temperatures below the transition temperature. At temperatures above the transition temperature, despite the Laponite concentration, the addition of nano-clay reduces the coefficient of thermal expansion 28% to $8.0\text{x}10^{-4}$ $°C^{-1}$ from $1.1\text{x}10^{-3}$ $°C^{-1}$. It is important to note that the influence of Laponite is most significant in the in-plane directions, through the width and length, rather than in the transverse direction through the thickness [12]. Based on these results, it is clear that within the operating range of 25°C and 70°C thermal expansion accounts for only 4% or less of the specimen lengthening and recovery.

6.3.4 Stress-Strain Behavior Above and Below the Transition Temperature

The preferential insertion of nano-clay within the soft domains of this shape memory polyurethane is elucidated in the hysteretic tensile results above and below the transition temperature. As the concentration of nano-clay increases, so does the modulus of the polyurethane composite. The 15 wt% composite, due to the incomplete exfoliation and tendency for intercalation and flocculation of the nano-clay, exhibits an increase in modulus when compared to the pure polyurethane and a decrease when compared to the 10 wt% composite. In the results both above and below the transition temperature (Figure 6-7), it is obvious that the addition of nano-clay suppresses strain-hardening, further indicating that the nano-clay is preferentially embedded within the soft domain of the polyurethane. Strain-hardening is demarked by an incline in slope of the stress-strain behavior after yield. The pure polyurethane appears to strain harden immediately after yield, while the addition of nano-clay systematically increases the onset of strain hardening and decreases the resulting slope. Greater deformation is necessary in order to rotate, re-orient and order the Laponite filled soft segment in order to release soft segments constrained by the clay platelets and allow those chains to fully uncoil and stretch.

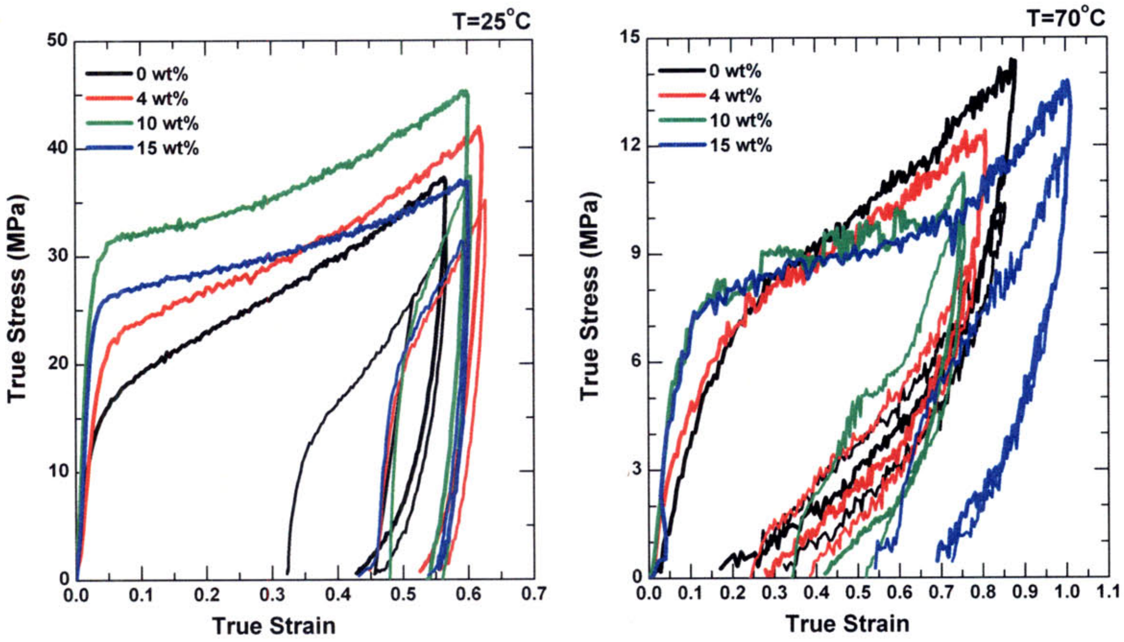

Figure 6-7: True stress-strain response of the MM5510 polyurethane composites at 25°C, a temperature below the transition temperature (55°C), and 70°C, a temperature above the transition temperature when the films are stretched 2.5 times their original length.

Interestingly, at temperatures below the transition temperature the addition of nano-clay increases the plastic strain contribution and energy absorbed upon the first loading-unloading cycle, but decreases the absorbable energy upon re-loading and unloading. In contrast, at temperatures above the transition temperature the plastic strain too increases as does the absorbable energy upon re-loading and unloading.

In the hysteresis results collected within an oven at 70°C, depicted in Figure 6-8, there is quite a discrepancy in flow stress achieved when the specimens are stretched to 1.4 and 1.7 times their original length. This discrepancy is likely due to a change in the way in which the oven heated. The previous data reported was collected prior to an event that changed the oven configuration. While in all instances the heating rate prescribed was a step function to 70°C from room temperature, these initial tests took approximately ten minutes to equilibrate at 70°C and there was no thermal overshoot. For these initial tests the thermocouple inside the oven which monitored the temperature and controlled the feedback loop was surrounded by an insulator.

Consequently, the monitored thermal response was more gradual and smooth. After a change in configuration and the thermocouple insulator irreversibly eliminated, as was the case for the later tests, the thermal response of the oven was more choppy and coarse. As a result, the feedback

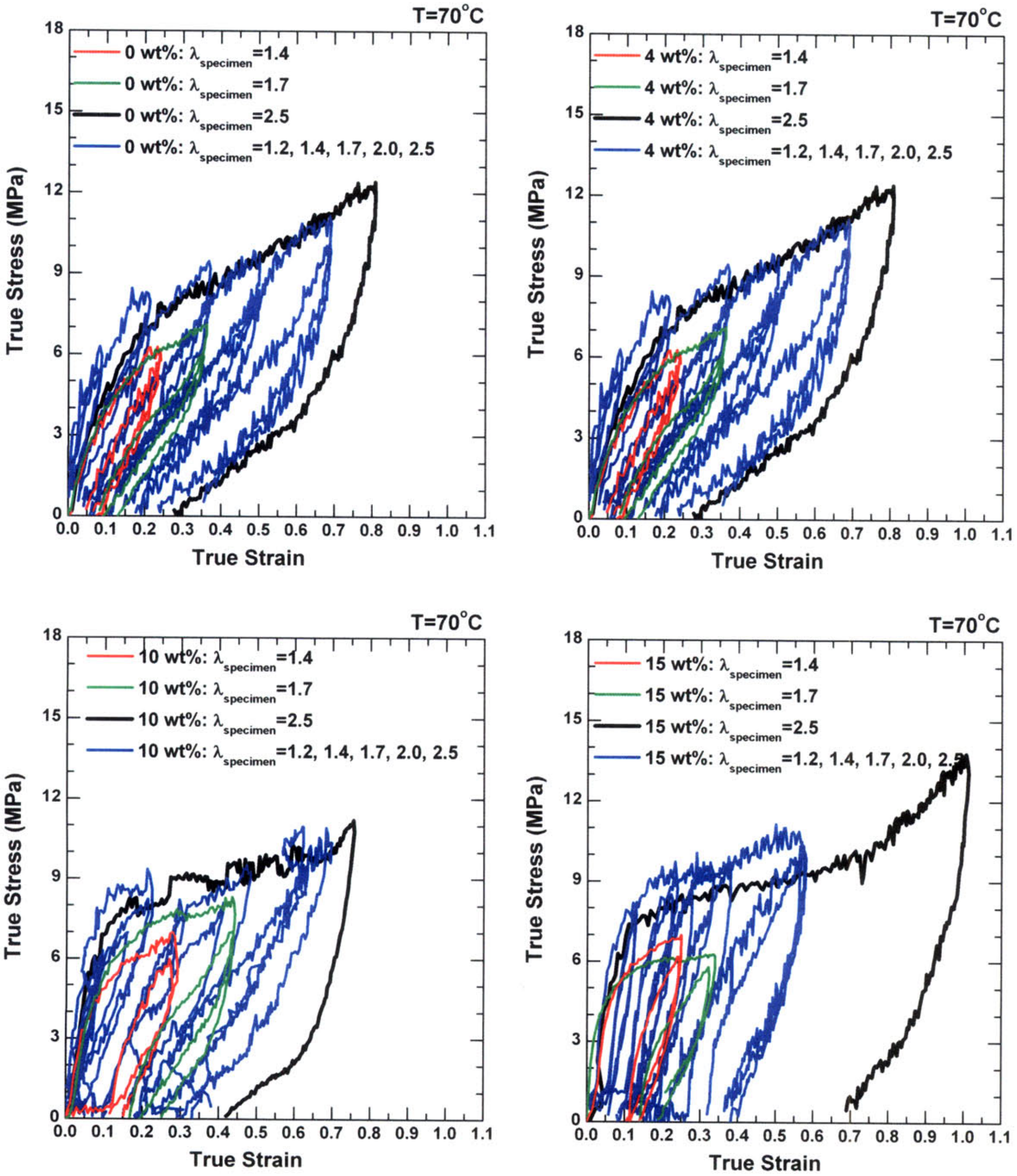

Figure 6-8: Uniaxial tensile response of the various nanocomposites at 70°C, a temperature above the transition temperature. The red curve depicts the response of the 1st and 5th cycle stretching the specimen 1.4 times its original length and unloading. The green curve depicts the response of the 1st and 5th cycle stretching the specimen 1.7 times its original length. The black curve depicts the response of the 1st cycle stretching the specimen 2.5 times its original length. The blue curve depicts the response of the 1st and 5th cycle as the specimen is stretched to 1.2, 1.4, 1.7, 2.0, and 2.5 times its original length, consecutively.

loop to the oven forced faster heating initially and the prescribed temperature of 70°C was consistently overshot. While the thermocouple measured an equilibrated temperature ranging between 72°C and 75°C an independent thermometer placed within the oven read 80°C and 85°C. This discrepancy leads to greater thermal softening and accounts for the variation in response. While the thermocouple output a temperature value within 5°C of the prescribed value the actual temperature could have been 10°C warmer and fully accounted for the drop in flow stress in these later tests. Despite the discrepancy in flow stress the nanocomposites at temperatures above the glass transition temperature exhibit the stretch-induced softening typical of elastomers like rubber [13].

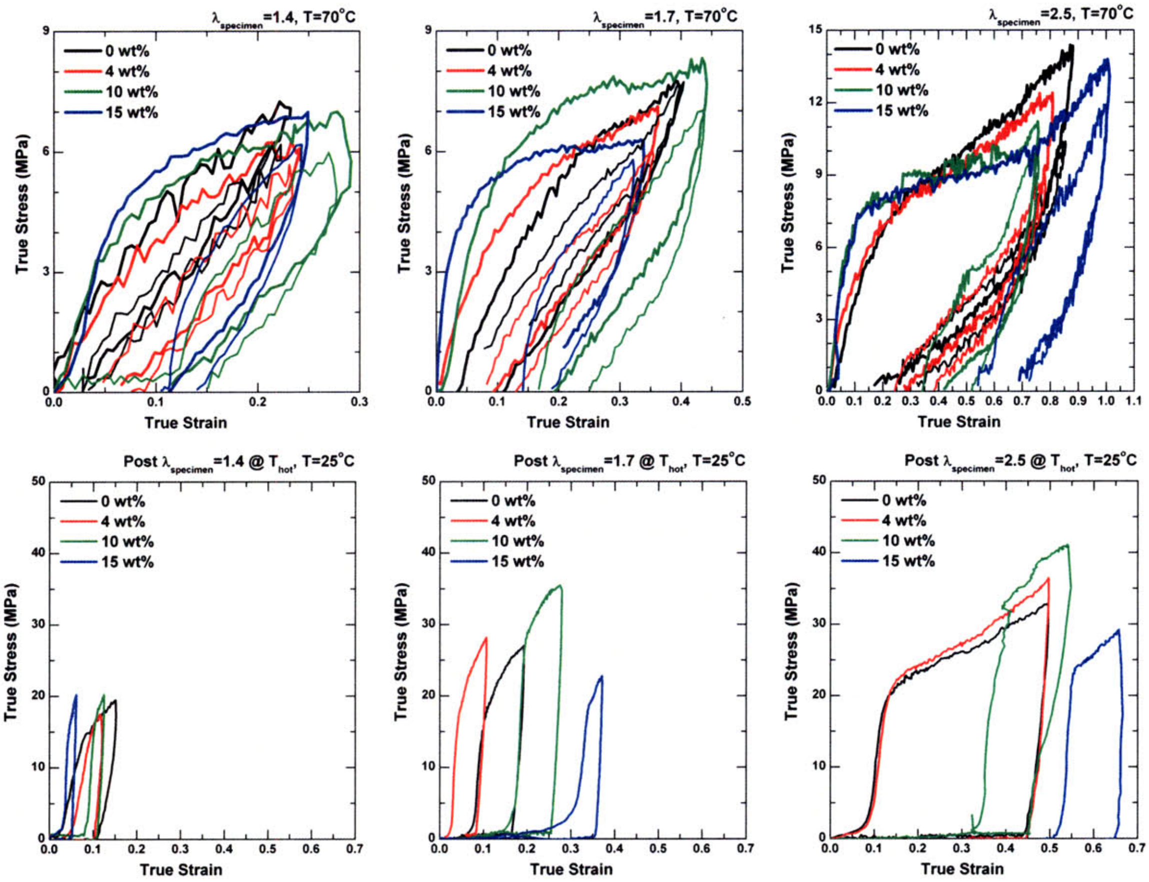

Figure 6-9: Uniaxial tensile response of the various nanocomposites at 70°C and the corresponding response at 25°C after five cycles of deformation at the elevated temperature.

Because shape memory polymers are often programmed for initial deformation at an elevated temperature and then cooled for storage in order to reduce the amount of work needed to deform the material, the response of the polyurethane nanocomposites at the colder, storage temperature after deformation at the elevated temperature is of interest. Like many elastomers, we observed that as the applied specimen stretch increased cyclically at elevated temperature, the initial modulus subsequently softened and the amount of plastic strain incurred increased.

After undergoing a small amount of plastic deformation at 70°C, the nanocomposites exhibit increasing initial moduli with nano-clay concentration at 25°C, as is depicted in the bottom left image in Figure 6-9. The locations of these responses with respect to the mechanical behavior of the polyurethane composites at room temperature are visualized in Figure 6-10. The plastic strain, given by the location of increasing stress in the bottom images of Figure 6-9, also increases with nano-clay concentration, except in the 15 wt% specimen. This discrepancy is likely due to the occurrence of localized deformation that takes place outside the observable range of the video extensometer and within the specimen grips. A similar discrepancy is observed when the specimens are stretched to 1.7 times the original length at an elevated temperature in the 4 wt% filled sample. Again, at this stretch and the larger stretch, the plastic deformation incurred increases with nano-clay concentration, especially when the concentration is greater than the percolation limit. However, after deformation at these larger applied strains, the moduli of the nanocomposites are essentially constant at room temperature no matter the nano-clay concentration.

The response of these materials from one sample to the next at room temperature is generally compatible. However, there were a few discrepancies, especially in the magnitudes of the flow stress of the 10 wt% and 15 wt% nano-clay filled specimens after deformation at elevated temperatures. These discrepancies can be attributed to natural differences that occurred during sample preparation, post-processing, and aging. As mentioned in section 6.3.2, multiple soft-segment glass transitions between 10°C and 65°C were observed via dynamic mechanical analysis when the samples were allowed to age within desiccators. This behavior was easily observed in the highly filled composites because the transitions present in no two specimens of a particular concentration coincided exactly. So while the samples were protected from atmospheric humidity, due to limited accessibility to the ELF 3200, two months time passed between the first and last tests, and likely manifested the discrepancies in stress-strain behavior.

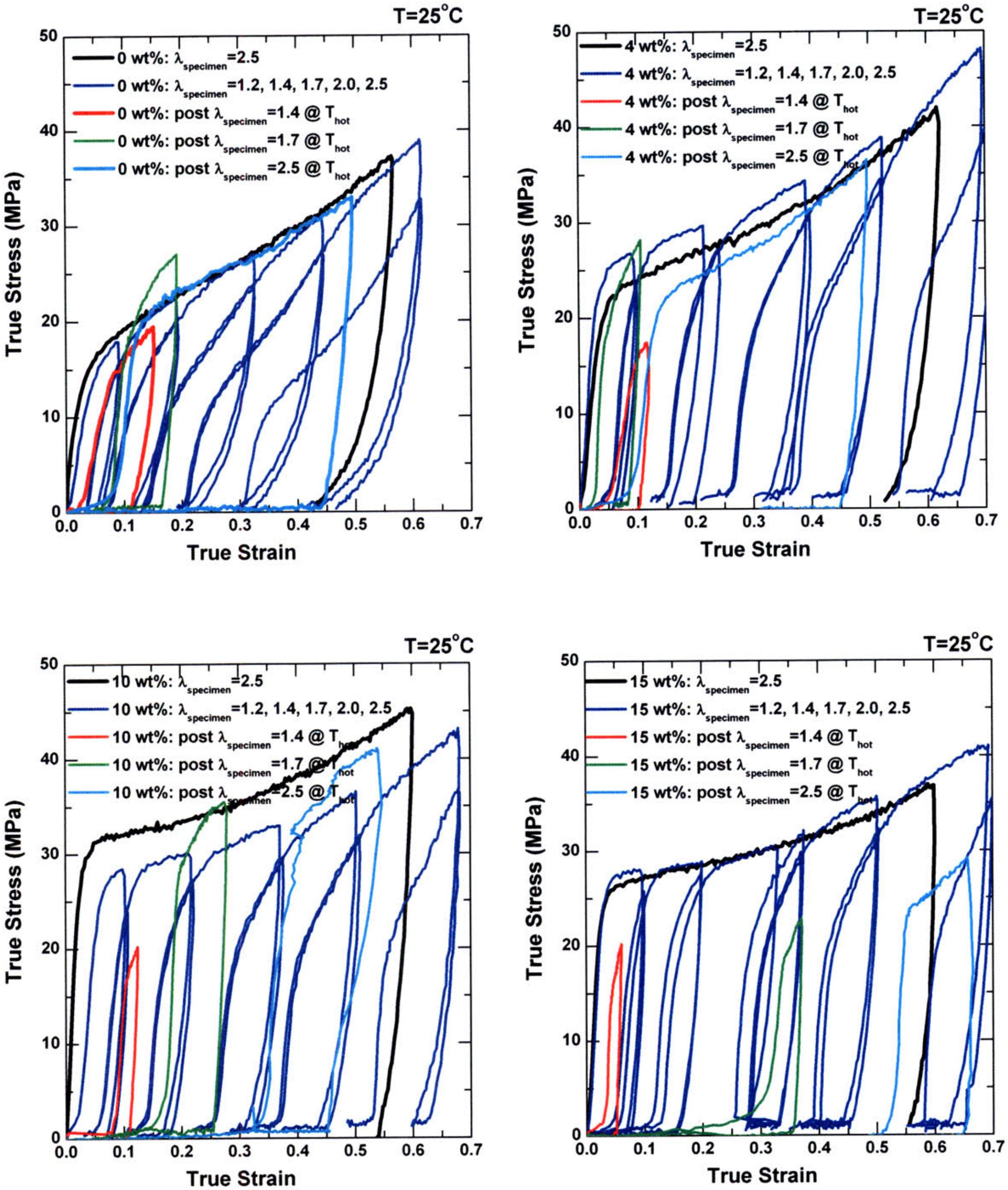

Figure 6-10: Uniaxial tensile response of the various nanocomposites at 25°C, a temperature below the transition temperature. The red curve depicts the response after cyclic stretching of the specimen 1.4 times its original length at an elevated temperature. The green curve depicts the response after cyclic stretching of the specimen 1.7 times its original length at an elevated temperature. The cyan curve depicts the response after cyclic stretching of the specimen 2.5 times its original length at an elevated temperature. The black curve depicts the response of the 1st cycle stretching the specimen 2.5 times its original length. The blue curve depicts the response of the 1st and 5th cycle as the specimen is stretched to 1.2, 1.4, 1.7, 2.0, and 2.5 times its original length, consecutively.

6.3.5 Free Strain Recovery

The addition of nano-clay, particularly at concentrations above the percolation threshold, to shape memory polyurethane significantly decreases the strain recovered during thermal actuation when no load is applied. Figures 6-11 and 6-12 depict the nominal stretch recovery of the polyurethane nanocomposites when a maximum stretch of 1.1, 1.2, 1.4, 1.7, or 2.0 is applied at 70°C.

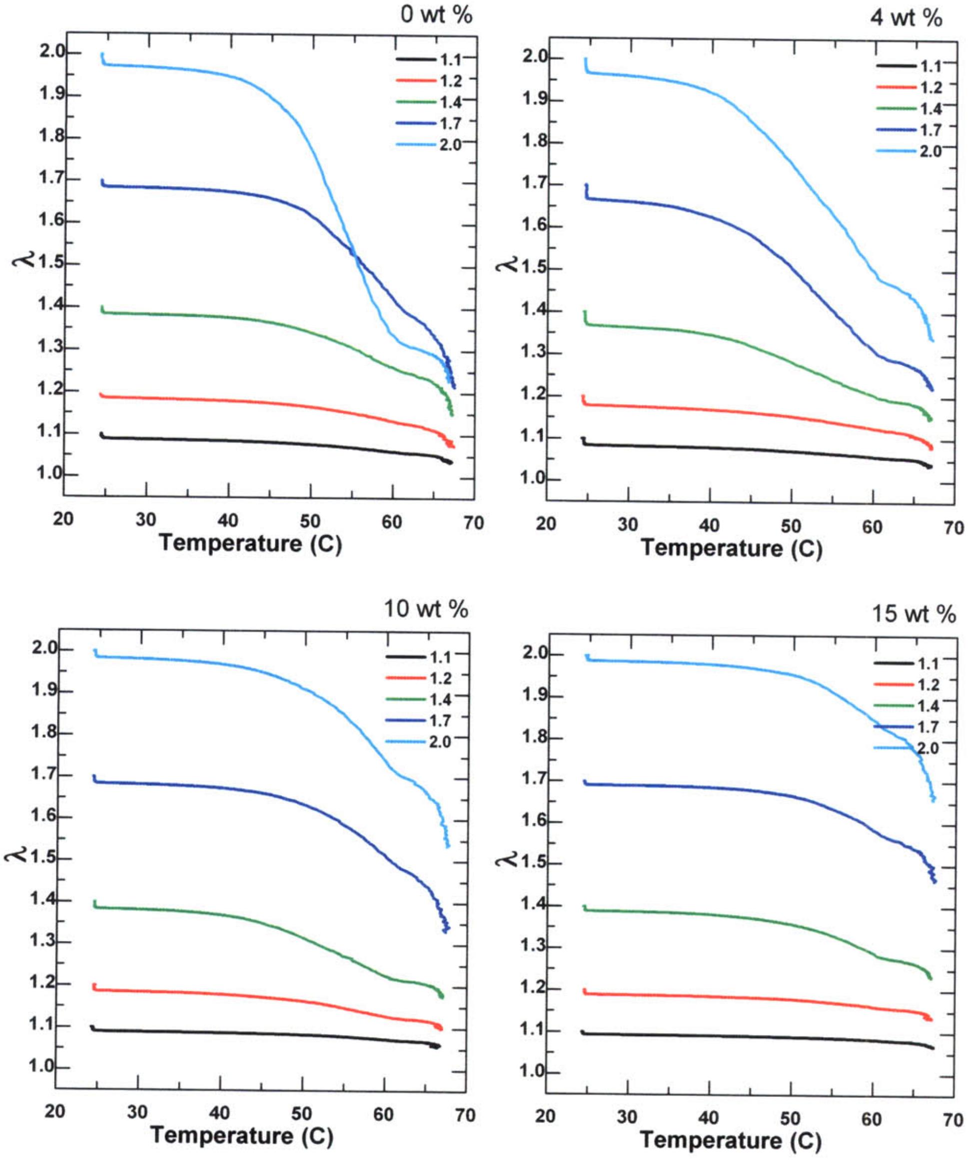

Figure 6-11: Stretch recovery of the nanocomposites after stretching the specimen to 1.1, 1.2, 1.4, 1.7, or 2.0 times its original length at 70°C using the TA Instruments Q800 DMA. The stretch reported is the nominal stretch or specimen stretch.

The initial steep drop in specimen stretch at 25°C correlates to removal of a tensile load. Then slow recovery ensues until the transition temperature of the nanocomposite is approached. At that point, the strain is recovered at a faster rate. The rate of recovery increases as the applied strain increases. This is easily observed in the pure polyurethane sample in Figure 6-12 when comparing the recovery within the 40°C-60°C temperature range at increasing applied stretch. Furthermore, the addition of nano-clay, particularly at concentrations above the percolation limit, decreases the rate at which strain is recovered during this thermal region. The addition of nano-clay at concentrations below the percolation limit decreases the temperature at which the strain recovery begins by as much as 8°C. At concentrations above the percolation limit, the nano-clay suppresses the onset of strain recovery by as much as 10°C for the 15 wt% filled sample.

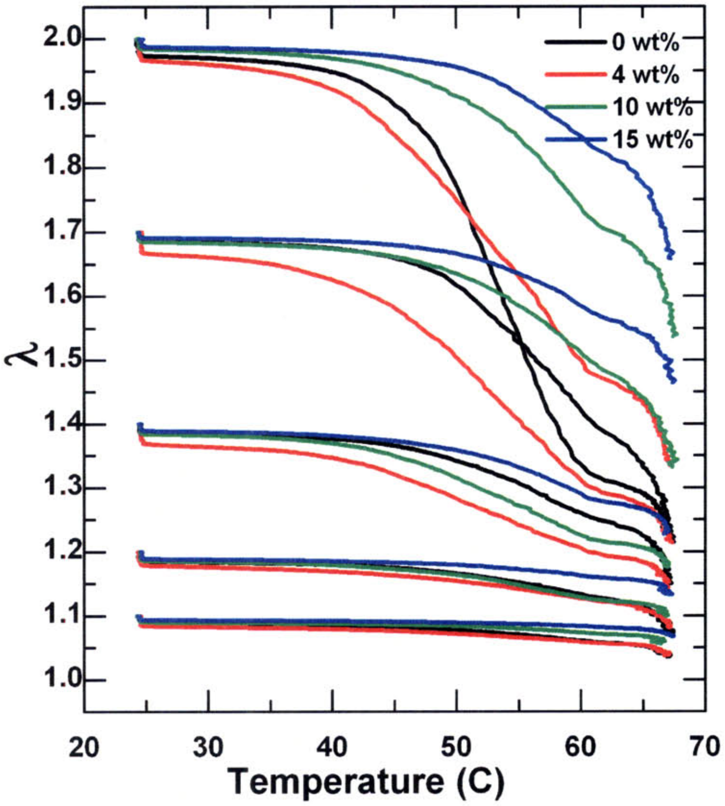

Figure 6-12: Comparison of the stretch recovery of the nanocomposites after stretching the specimens to 1.1, 1.2, 1.4, 1.7, or 2.0 times their original length at 70°C using the TA Instruments Q800 DMA. The stretch reported is the nominal stretch or specimen stretch.

At 58°C the strain recovery rate slows until 65°C when the recovery rate again increases. The temperatures at which these rates in strain recovery change correspond to the variation in transition temperature behavior observed with the DMA. The flexural storage modulus undergoes a similar behavior of slow softening, followed by a large quick drop and then gradual decay with increasing temperature through the same temperature range. While the DMA interrogates the visco-elastic response of the material, it is obvious that those same soft segment components and Laponite are responsible for the resultant recovery.

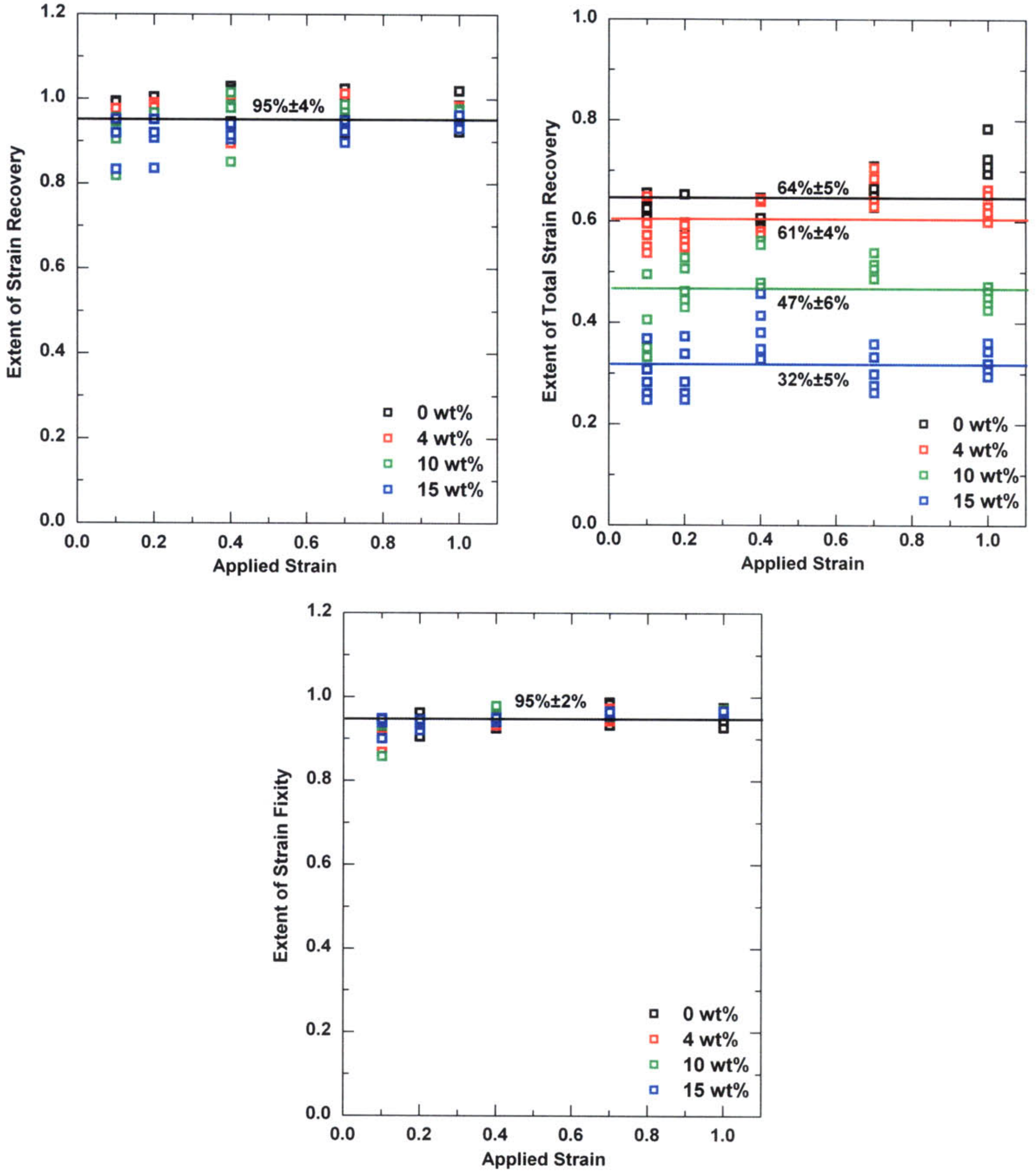

Figure 6-13: Comparison of the extent of strain recovery, total strain recovery and strain fixity for the polyurethane nanocomposites determined after deformation at elevated temperature.

Despite the concentration of Laponite added to the polyurethane the extent of strain recovery from one cycle to the next is approximately 95%. Just as when an elastomer is cycled to one stretch and unloaded the plastic strain increases with each consecutive stretch, the extent of strain recovery decreases. However, like with the increase in plastic strain, the extent of strain recovery lost eventually reaches an equilibrium value. Although, the presence of nano-clay does not influence the extent of strain fixity (~95%) when the polyurethane is quickly stretched at 70°C and then quickly cooled at 10°C min^{-1}. The influence of the nano-clay with regard to strain fixity will be more important in deformation programs where the cooling rates are slower or the specimen is left at a temperature near or above the transition temperature for longer periods of time. The greatest influence of the nano-clay as shown in Figure 6-13 is on the extent of total strain recovery, particularly at concentrations above the percolation threshold. The 4 wt% filled nanocomposite exhibits only a slight decrease in the extent of total strain recovery from 64% for the pure sample to 61%. When 10 wt% and 15 wt% nano-clay is dispersed within the polyurethane matrix, the extent of total strain recovery drops to 47% and 32%, respectively. As is observed in the previous Chapter, the addition of nano-clay, particularly at concentrations above the percolation threshold, causes irreparable damage. Irreparable damage upon deformation is significant in these composites where the nano-clay is preferentially embedded within the soft domain.

In contrast to the response of nanocomposites deformed at an elevated temperature of 70°C, the nanocomposites deformed at room temperature exhibit a large drop in strain when the load is removed, indicating poor strain fixity. This behavior is apparent when comparing the point of maximum applied strain in Figure 6-14, denoted by the open circle, to the initial data point of the solid line that describes the strain recovery upon thermal actuation. The difference is accounted for by greater inelastic strain recovery typically observed in glassy polymers [14]. As the concentration of Laponite increases so too does the permanent plastic strain and, consequently, the strain fixity of the most concentrated samples appears to be better than the pure polyurethane because the inelastic strain recovery is hindered. Similar to the previous results, the extent of total strain recovered increases with applied stretch, but decreases with nano-clay concentration. Furthermore, the temperature demarking the onset of strain recovery increases with nano-clay concentration.

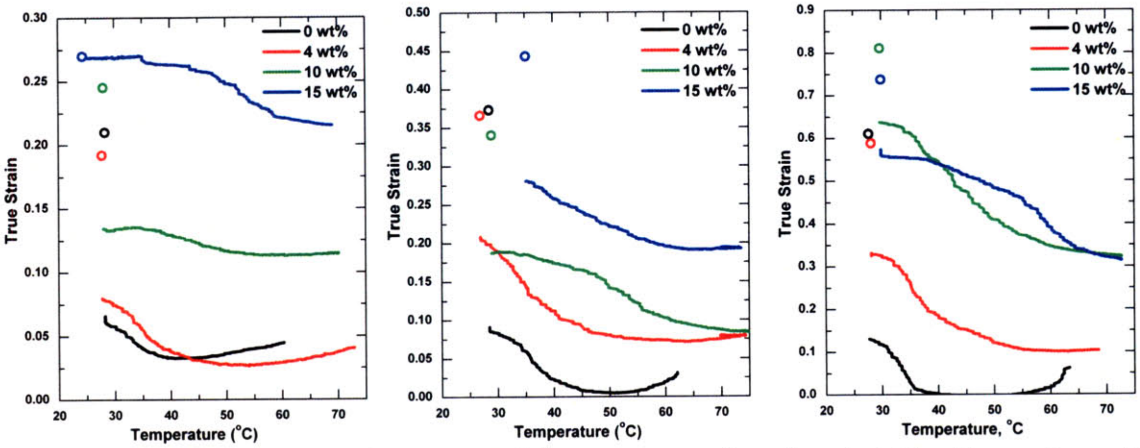

Figure 6-14: Comparison of the strain recovery of the nanocomposites after stretching the specimens to 1.4, 1.7, or 2.5 times their original length at 25°C using the ELF 3200 (from left to right). The deformation was visualized and the maximum true strain achieved was reported with an empty circle while the continuous line demarks the strain recovery during the no load condition.

In contrast to the previous results, the specimens, deformed at room temperature with the ELF 3200, exhibit strain recovery onset at temperatures as small as 30°C. At 50°C, the pure sample begins to elongate. By including a percolated network of nano-clay, the temperature at which the nanocomposites begin to elongate can be suppressed by as much as 20°C depending on the extent of strain applied. Again, it is important to note that the qualitative behavior described in Figures 6-14 and 6-15 is accurate. However, the temperatures at which the transitions take place are accurate to within ~5°C. A digital thermometer displayed as much as a 5°C discrepancy between the output results from the ELF 3200 during the thermal ramp to 70°C.

Ultimately, the greater the stretch applied to the specimen the greater the orientation and ordering of the soft chains and consequently the greater the available strain for entropic recovery. As is shown in Figure 6-15, when the strain applied does not significantly stretch the sample past yield, the extent of strain recovered is small. At stretches approximately three times greater, when the specimen has been stretched well past yield, the strain recovery is significantly increased. However, the presence of rigid nano-clay within the soft segments retards orientation and alignment. The soft segment then incurs irreparable damage in order to achieve orientation and chain alignment when the chains break, stretch or slip around the platelets, break away from the platelets, or rotate the platelets [15]. Consequently, the addition of nano-clay, at concentrations above the percolation threshold, significantly limits the extent of total strain recovery upon thermal actuation.

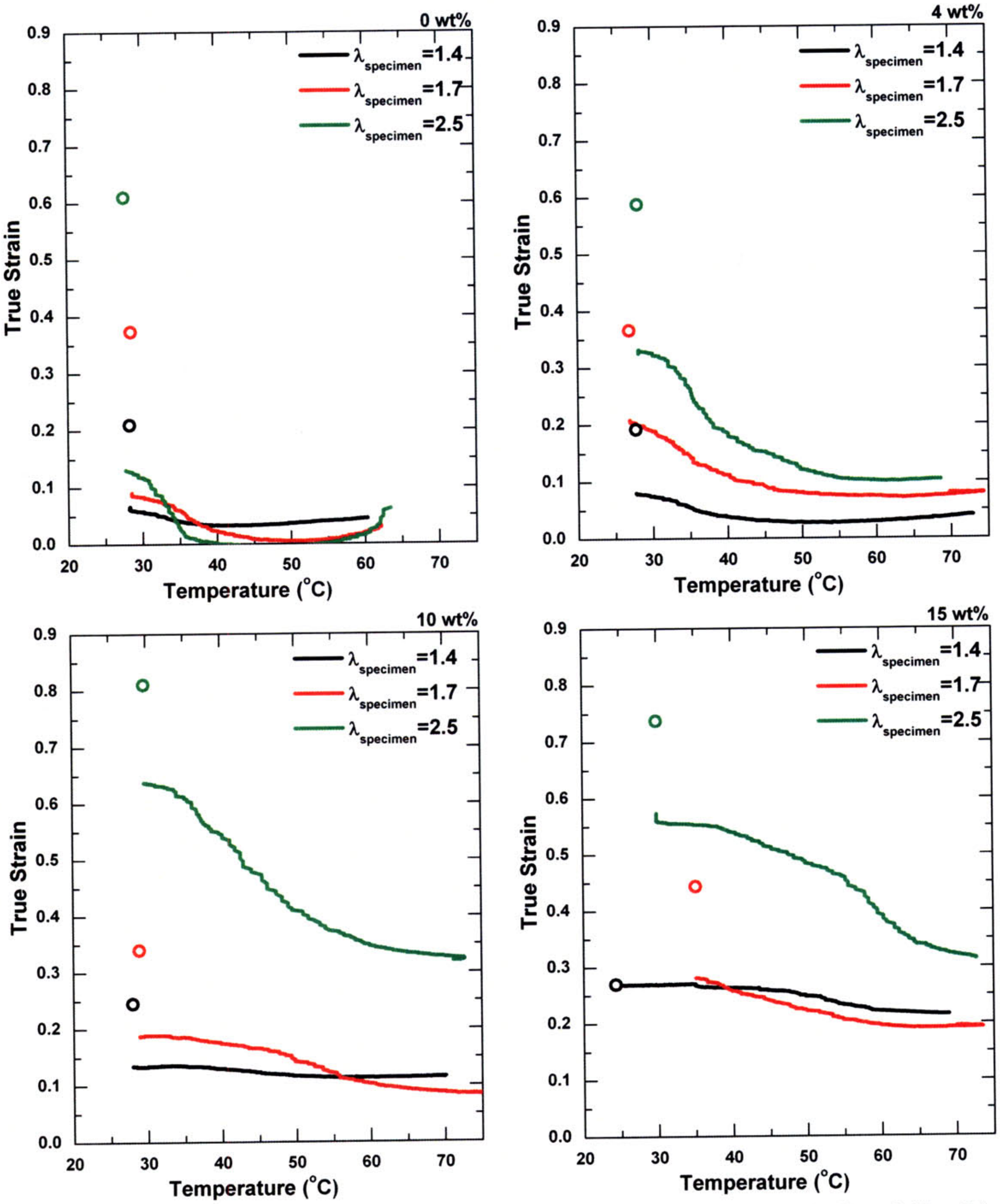

Figure 6-15: The strain recovery of the polyurethane nanocomposites containing 0, 4, 10 and 15 wt% nano-clay after stretching the specimens to 1.4, 1.7, or 2.0 times their original length at 25°C using the ELF 3200. The deformation was videoed and the maximum true strain achieved was reported with an empty circle while the continuous line demarks the strain recovery during the no load condition.

6.3.6 Constrained Strain, Stress Recovery

The attraction of researchers to shape memory polymers for numerous applications is often based on utilization of an actuation stress, or recovery stress when the polymer is constrained from recovering strain [2, 16-20]. However, it is difficult to isolate the stress due to entropic recovery under a constrained strain condition from thermal expansion/contraction stresses, thermal softening and stress relaxation. Thermal expansion, thermal softening and stress relaxation under a constrained strain conditions causes a drop in the tensile stress.

	Initial Modulus (MPa)		CTE (1/°C)		Predicted Thermal Stress (MPa)	
	T = 25°C	T = 70°C	T = 25°C	T = 70°C	min	max
0 wt%	142	29	6.14E-05	1.12E-03	0.39	1.46
4 wt%	290	34	6.21E-05	8.12E-04	0.81	1.24
10 wt%	461	81	4.76E-05	8.04E-04	0.99	2.93
15 wt%	451	137	3.97E-05	7.98E-04	0.81	4.92

Table 6-2: Predicted thermal stress of the various polyurethane nanocomposites when the length is constrained. The initial modulus at room temperature multiplied by the axial coefficient of thermal expansion at room temperature and the operating temperature difference (70°C-25°C=45°C) gives a lower estimate of the predicted thermal stress. The upper estimate is given by the initial modulus at the elevated temperature multiplied by the axial coefficient of thermal expansion at the same elevated temperature and operating temperature difference.

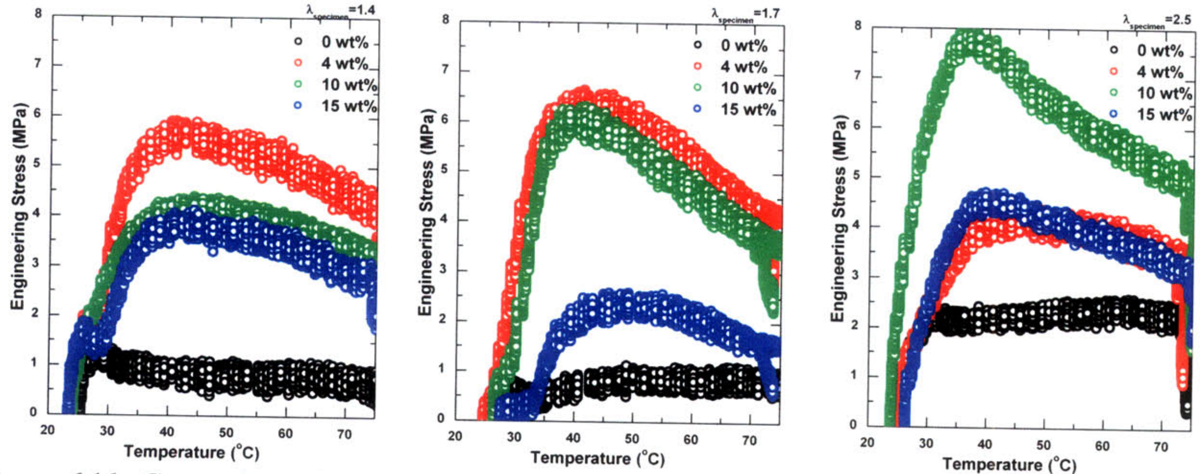

Figure 6.16: Comparison of the stress recovered when the strain is constrained after stretching the polyurethane nanocomposite specimens to 1.4, 1.7, or 2.5 times their original length at 25°C using the ELF 3200. The engineering stress is reported because the sample exhibited localized deformation that was not entirely captured by the video extensometer.

The magnitude of the drop due to thermal expansion can be estimated by multiplying the modulus of the material, *E*, by the axial coefficient of thermal expansion, α, and the change in temperature. Table 6-2 predicts the minimum and maximum thermal stress reduction. The minimum thermal stress reduction predicted for pure polyurethane is ~0.4 MPa. This drop in stress can be observed in Figure 6-16 over the 25°C to 70°C temperature range when the specimen was constrained after stretching the specimen 1.4 times its original length. The nano-clay reinforced samples exhibit drops greater in magnitude as predicted. This drop is augmented by thermal softening of the material and negated by time-dependent stress recovery.

Figure 6.16 depicts the recovery stress of each nanocomposite after stretching the specimen to 1.4, 1.7, or 2.5 times its original length. In actuality though, due to the localized deformation outside the extensometer viewing area discussed previously, the actual stretches achieved are listed in Table 6-3. Consequently, the actual stretches achieved by the 10 wt% and 15 wt% are less than that achieved by the 4 wt% sample. The resulting actuation stresses achieved are two-thirds of that achieved by the 4 wt% sample. While increasing the stretch applied increases the available energy for recovery, the addition of nano-clay also increases the available energy and, consequently, the resulting actuation stress achieved. This is confirmed when the pure polyurethane and 4 wt% filled composite stretched 1.7 times their original length are compared or when the pure and 10 wt% filled polyurethanes are stretched 2.5 times their original length. In both instances the nano-clay filled composite exhibits the greater actuation or recovery stress.

	λ_{true}			
$\lambda_{specimen}$	0 wt%	4 wt%	10 wt%	15 wt%
1.4	1.22	1.30	1.17	1.11
1.7	1.36	1.35	1.29	1.49
2.5	1.73	1.53	1.73	1.68

Table 6-3: Comparison of the true stretch achieved in each nanocomposite as seen via the video extensometer during the constrained strain, stress recovery test when the specimen was stretched to 1.4, 1.7, or 2.5 its original length.

As the nano-clay concentration increases the actuation stress too increases, except when 15 wt% nano-clay is added. This drop in actuation stress is due to the poorer Laponite dispersal and increased plastic deformation due to the increased presence of rigid, flocculated, intercalated platelets. The peak in actuation stress of the pure polyurethane occurs almost immediately at ~30°C and the stress plateaus at nearly this same value until the temperature is held at 70°C for an extended period of time, as shown in Figure 6-17. In contrast, the nanocomposite actuation stress peaks at ~40°C and then drops as the material thermally softens, and expands until 70°C, when the soft segments easily reptate and flow and the rate of softening significantly increases.

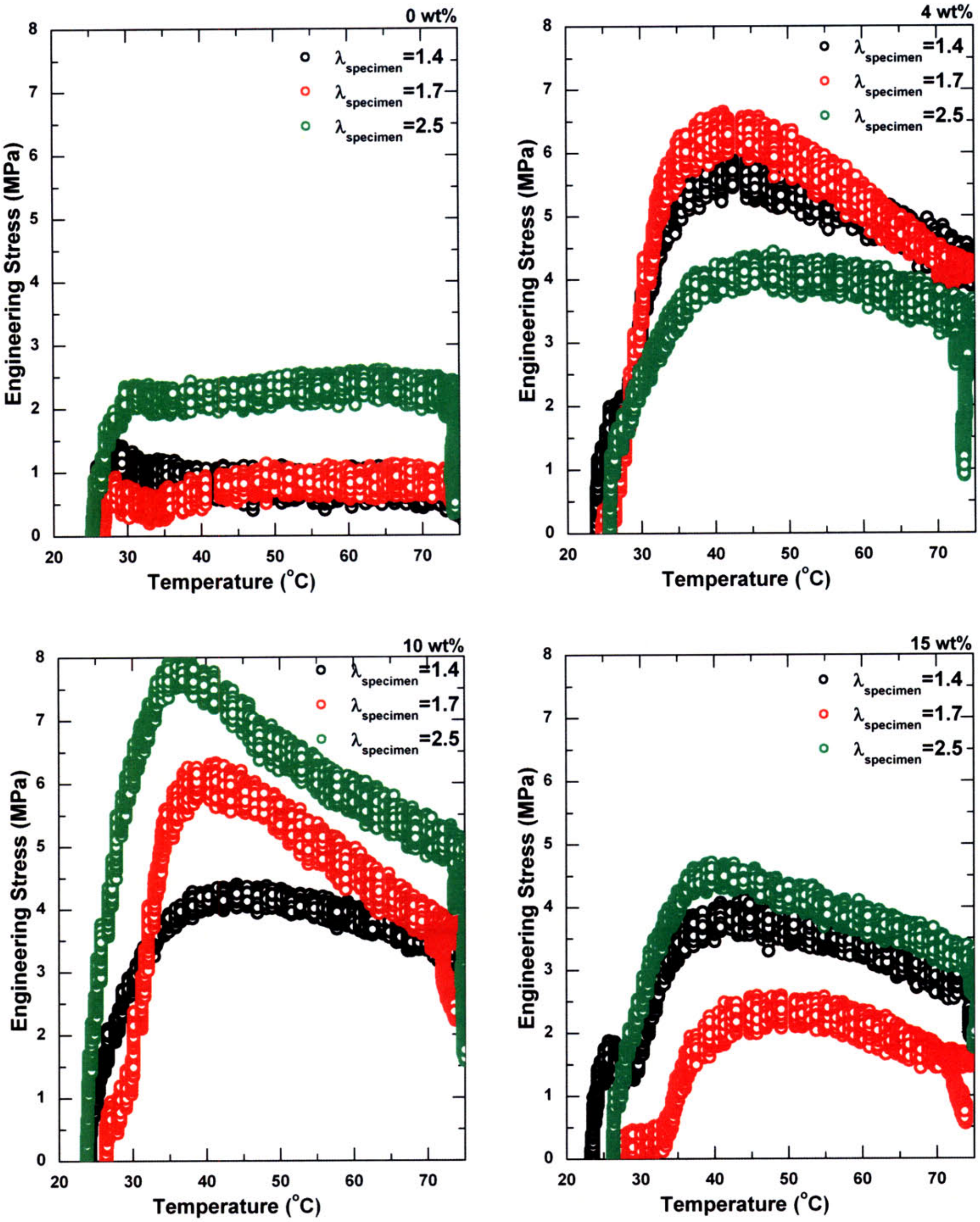

Figure 6.17: The stress recovered when the strain is constrained after stretching each polyurethane nanocomposite specimen to 1.4, 1.7, or 2.5 times their original length at 25°C using the ELF 3200. The engineering stress is reported because the sample exhibited localized deformation that was not entirely captured by the video extensometer.

This behavior contrasts the behavior reported by Miaudet et al [21] when the actuation stress of a carbon nanotube-polyvinyl alcohol peaks at a temperature roughly equal to the deformation temperature. In this polyurethane-nano-clay system, the peak in actuation stress occurs nearly

15°C above the deformation temperature or room temperature when clay is added. These peaks instead correspond to the transition behavior observed in the dynamic mechanical results.

6.4 Conclusions

Nano-clay is preferentially embedded within the soft domains of commercial shape memory polyurethane using the solvent exchange approach previously described. The nano-clay is fully exfoliated; however, at concentrations above the percolation limit, intercalation persists and flocculation amid the most polar soft segment constituents is observable in the most concentrated composite. The complex nature of this multi-block copolymer is further manifested when nano-clay is added. The manufacturer reports the soft segment glass transition as 55°C, but differential scanning calorimetry, as well as dynamic mechanic analysis, indicates that two and three transitions within 10°C and 65°C are present. At temperatures above the transition temperature, the nanocomposites behave like typical elastomers—exhibiting stretch-induced softening and hysteresis. At temperatures above and below the transition temperature, the addition of nano-clay decreases the axial coefficients of thermal expansion as well as increases the plastic strain. At temperatures below the transition temperature, the nanocomposites act like glassy polymers—exhibiting significant inelastic recovery. However, the addition of nano-clay decreases the extent of inelastic recovery. Consequently, the strain fixity of the material when stretched at temperatures below the transition temperature is poor compared to that when the nanocomposites are stretched at an elevated temperature and cooled quickly. No matter the deformation temperature, the extent of total strain recovered decreases with increasing Laponite concentration, particularly at concentrations above the percolation threshold. The addition of nano-clay also delays the onset of strain recovery as well as stress recovery. However, as the stretch applied to each specimen increases so too does the actuation stress. The addition of well dispersed nano-clay to the polyurethane increases the actuation stress; however, as the temperature increases, or is held at an elevated value, the recovery stress decays significantly while the pure polyurethane holds constant. Ultimately, the optimum nano-clay concentration where the greatest strain recovery is balanced by the largest actuation stress is equal to the percolation limit. At larger concentrations, the amount of strain able to be recovered decreases significantly while the actuation stress increases. The actuation stress will increase with filler loading until the nano-clay dispersal becomes too intercalated that plastic deformation dominates. At smaller concentrations, the strain able to be recovered is maximized, but the obtainable recovery stress is minimized. Ultimately, the addition of nano-clay to shape memory polyurethane allows another tool for the design of actuating polymers with prescribed stress and strain recovery.

6.5 References

[1] M. A. Di Prima, M. Lesniewski, K. Gall, D. L. McDowell, T. Sanderson, and D. Campbell, "Thermo-mechanical behavior of epoxy shape memory polymer foams," *Smart Materials & Structures*, vol. 16, pp. 2330-2340, 2007.

[2] G. M. Spinks, V. Mottaghitalab, M. Bahrami-Samani, P. G. Whitten, and G. G. Wallace, "Carbon-Nanotube-Reinforced Polyaniline Fibers for High-Strength Artificial Muscles," *Advanced Materials*, vol. 18, pp. 637-640, 2006.

[3] K. J. Pawlowski, H. L. Belvin, D. L. Raney, J. Su, J. S. Harrison, and E. J. Siochi, "Electrospinning of a micro-air vehicle wing skin," *Polymer*, vol. 44, pp. 1309-1314, 2003.

[4] A. Lendlein and S. Kelch, "Shape-memory polymers," *Angewandte Chemie-International Edition*, vol. 41, pp. 2034-2057, 2002.

[5] M. Szycher, *Szycher's Handbook of Polyurethanes*. Boca Raton, Florida: CRC Press, 1999.

[6] S. Rezanejad and M. Kokabi, "Shape memory and mechanical properties of cross-linked polyethylene/clay nanocomposites," *European Polymer Journal*, vol. 43, pp. 2856-2865, 2007.

[7] F. Cao and S. C. Jana, "Nanoclay-tethered shape memory polyurethane nanocomposites," *Polymer*, vol. 48, pp. 3790-3800, 2007.

[8] M. Y. Razzaq and L. Frormann, "Thermomechanical studies of aluminum nitride filled shape memory polymer composites," *Polymer Composites*, vol. 28, pp. 287-293, 2007.

[9] B. Yang, W. M. Huang, C. Li, and J. H. Chor, "Effects of moisture on the glass transition temperature of polyurethane shape memory polymer filled with nano-carbon powder," *European Polymer Journal*, vol. 41, pp. 1123-1128, 2005.

[10] R. J. Young and P. A. Lovell, *Introduction to Polymers*. Cheltenham, U.K.: Nelson Thornes Ltd., 1991.

[11] B. Yang, W. M. Huang, C. Li, C. M. Lee, and L. Li, "On the effects of moisture in a polyurethane shape memory polymer," *Smart Materials & Structures*, vol. 13, pp. 191-195, 2004.

[12] N. Sheng, *Multiscale Micromechanical Modeling of the Thermal/Mechanical Properties of Polymer/Clay Nanocomposites*, Ph.D. in Dept. of Mechanical Engineering, Cambridge, MA:Massachusetts Institute of Technology, 2006.

[13] H. J. Qi and M. C. Boyce, "Constitutive model for stretch-induced softening of the stress-stretch behavior of elastomeric materials," *Journal of the Mechanics and Physics of Solids*, vol. 52, pp. 2187-2205, 2004.

[14] O. A. Hasan and M. C. Boyce, "A constitutive model for the nonlinear viscoelastic viscoplastic behavior of glassy polymers," *Polymer Engineering And Science*, vol. 35, pp. 331-344, 1995.

[15] J. Diani, M. Brieu, and J. M. Vacherand, "A damage directional constitutive model for Mullins effect with permanent set and induced anisotropy," *European Journal of Mechanics A: Solids*, vol. 25, pp. 483-496, 2006.

[16] P. R. Buckley, G. H. McKinley, T. S. Wilson, W. Small, W. J. Benett, J. P. Bearinger, M. W. McElfresh, and D. J. Maitland, "Inductively heated shape memory polymer for the magnetic actuation of medical devices," *Ieee Transactions On Biomedical Engineering*, vol. 53, pp. 2075-2083, 2006.

[17] K. Gall, M. L. Dunn, Y. P. Liu, G. Stefanic, and D. Balzar, "Internal stress storage in shape memory polymer nanocomposites," *Applied Physics Letters*, vol. 85, pp. 290-292, 2004.

[18] K. Gall, P. Kreiner, D. Turner, and M. Hulse, "Shape-Memory Polymers for Microelectromechanical Systems," *Journal of Microelectromechanical Systems*, vol. 13, pp. 472-483, 2004.

[19] A. Lendlein and R. Langer, "Biodegradable, Elastic Shape-Memory Polymers for Potential Biomedical Applications," *Science*, vol. 296, pp. 1673-1676, 2002.

[20] D. Ratna and J. Karger-Kocsis, "Recent advances in shape memory polymers and composites: a review," *Journal Of Materials Science*, vol. 43, pp. 254-269, 2008.

[21] P. Miaudet, A. Derre, M. Maugey, C. Zakri, P. M. Piccione, R. Inoubli, and P. Poulin, "Shape and temperature memory of nanocomposites with broadened glass transition," *Science*, vol. 318, pp. 1294-1296, 2007.

7. Development of Multi-Responsive Electrospun Fabric

[This work will be submitted for publication in a slightly different form, as "Multi-Responsive Non-Woven Electrospun Polyurethane Mats Recover Intrinsic Stretch" by S.M. Liff and G.H. McKinley to *Polymer* in September 2008.]

7.1 Introduction

Electrospun, non-woven, polymer nano-fibers exhibit interesting properties due to the large surface area and large draw-ratio induced by the electric field and three-dimensional whipping instability [1-3]. The present work evaluates the entropic strain recovery of electrospun, non-woven, thermoplastic polyurethane mats composed of either smooth continuous fibers or composed of 'beads on a string' (BOAS) morphology that respond to both thermal and aqueous stimuli. The BOAS mats exhibit the greatest strain recovery and annealing the mats at a temperature near the glass transition temperature releases the intrinsic stretch 'frozen' into the material via electro-spinning. In response to either stimuli the porous, non-woven mats shrink macroscopically, maintaining mechanical integrity and simultaneously exhibiting fiber diameter growth coupled with pore diameter shrinkage that nearly eliminates all pores greater than three μm in size. Furthermore, this paper demonstrates that addition of nanoparticles to the responsive, biocompatible, thermoplastic polyurethane mats using the solvent exchange technique detailed in Chapter 3 allows the fiber morphology to be tuned and treatment of the surface with an oleophobic coating allows development of fabrics with reversible wettability.

Materials that exhibit shape change, whether metal alloy, ceramic, polymer or gel, have generated great interest in the past decade as actuators in the aerospace, textile and biomedical industries. Shape memory, as reviewed in Chapter 6, is the ability of a material to maintain a deformed shape and upon external stimulus recover the original, pre-deformed shape. The actuating external stimulus induces entropic recovery and is most often thermal but for polymeric materials and gels ultraviolet stimulation may also be employed [4, 5]. Ionic strength, pH, and solvent quality may also be used to induce shape transitions in gels [5]. Actuation stresses span the range from 10^3 Pa to 10^6 Pa and recovery strains may vary from 10% to 100% depending on the polymer employed.

Typical preparation of a SMP includes production of the material in some specified and desired permanent configuration, e.g. as a cylindrical fiber of length l_o and radius r_o. The SMP is then programmed or deformed to meet specifications of the desired temporary shape, e.g. a longer thinner cylindrical fiber of length l ($l > l_o$) and radius r ($r < r_o$). Often the deformation temperature is selected to be above the inherent transition temperature ($T_{trans}=T_g$ *or* T_m) of the polymer—the temperature which triggers entropic recovery—so that less work is needed to deform the material. If deformed at an elevated temperature the polymer is then cooled to the storage temperature, vitrifying or crystallizing the softer phase and holding or 'setting' the deformed, temporary shape. This temporary shape is maintained while the temperature is held below T_{trans}; however, upon an increase in temperature to a value greater than or equal to T_{trans} the mobile chains of the second phase entropically return to their previous configuration and the permanent shape is recovered—the fiber returns to its original length l_o and radius r_o. It would be advantageous to utilize a polymeric processing method that deforms the material to the desired temporary shape as it is processed so that no extra mechanical work input is needed. One such processing method is electrospinning. Furthermore, utilization of shape recovery is not a new idea—Shrinky Dinks©, popular toys since 1973 that contract to one-third their original size and grow nine times through their thickness upon oven heating, exclusively utilize shape memory [6]. However, neither the development of porous, shape memory materials, the characterization of their respective recovery, nor devices that exploit shape change and porosity have been addressed previous to this work. Consequently, the development of electrospun, shape memory materials, their characterization and their exploitation discussed in this chapter is the first of its kind and may transform future filter and drug delivery device design.

Electrospinning is a processing method that accelerates a polymer solution from a nozzle under action of an electric field to make fibers with diameters that range from 10 nm to 10 μm. The process exploits surface charge-repulsion, polymer viscoelasticity, surface tension, extensional viscosity, and solvent evaporation to deform and solidify material elements without capillary breakup [1, 3]. The large draw-ratio induced by the electric field and three-dimensional whipping instability significantly stretches the polymeric chains. Upon removal of solvent the intrinsic stretch is 'frozen' or locked in the fiber if the polymer utilized has a T_g or T_m which is greater than T_{amb}. The glass transition temperature of a polymer in solution depends strongly on the concentration of polymer utilized at concentrations within the dilute solution regime [7-9]. As the polymer concentration increases so too does the glass transition temperature until the maximum or bulk value is obtained. The glass transition temperature of concentrated solutions, however, is not dependent upon polymer concentration, but instead remains constant and equal to the bulk glass transition temperature. If T_g or T_m of the polymer is below T_{amb} the chains within the fiber are able to flow and relax and the strain applied during processing is lost upon fiber collection. Likewise, if the polymeric chains of the material with T_g or T_m greater than T_{amb} are allowed time to relax, the intrinsic stretch applied during processing is lost. An example of such a process is if the fibers are annealed at a temperature below but near T_{trans} or the solvent is not completely removed. Consequently, electrospinning offers a method to make non-woven mats randomly composed of stretched polymeric fibers with T_g or T_m above T_{amb} that recovers entropy and shrinks upon thermal stimulus. However, the extent of shrinkage of the non-woven mats and fibers from which the mat is composed is a priori unknown due to an incomplete understanding of the electrospinning process and an inability to control or monitor the draw down of the polymeric solution during whipping.

Development of new, responsive, polymeric electrospun fibers and systems offer potential for development of high-performance engineering thermoplastics that may be used as smart, actuating textiles [10], selective filters [11] and coatings [12-14], as artificial muscles [4, 15-17], shape-changing scaffolds, wound dressing or other biomedical devices [18-23]. Barhate and co-workers reviewed the status of nano-fibrous filteration in 2007 and indicate that prototypes have been successfully prepared for antimicrobial air filtering, catalytic filtering, ion exchange filtering among other applications; however, the key for further advancement relies upon advances in surface treatment [11]. Yoshida et al reviewed the current trend in advanced bio-coatings of utilizing biodegradable, shape memory materials to develop multi-functionalized biomaterials that can be used to control cell growth of tissues or in drug delivery systems [14]. Pawlowski and co-workers utilized electroactive polymer fibers composed of poly(vinylidene fluoride) and trifluoroethylene electrospun onto the wing frame of a micro air vehicle (mass less than 50 g) to induce wing vibration at 6.7 Hz with a 2.0 kV amplitude [16]. Samatham and co-workers used electrospun polyacrylonitrile as a type of artificial muscle. By changing the pH of the solution in which the non-woven mat was submerged, the fibers were observed to expand in basic solutions and contract in acidic solutions more quickly than commercially available larger diameter fibers [17]. There are only a handful of publications investigating electrospun, shape memory polyurethanes and the emphasis of this previous work was often to identify spinning parameters that enable production of a uniform fibrous morphology. Minimal mechanical analysis or shape memory characterization was presented, and only after applying stretch after processing and formation of the fibrous mat [10, 24-26]. The following chapter investigates the entropic recovery of electrospun, shape memory polyurethane (SMPU) mats after processing and discusses further applications for this behavior.

7.2 Materials and Experimental Methods

7.2.1 Materials

In this study we utilized a commercial, biocompatible, thermoplastic polyurethane, MM 5510 from the DiAPLEX Series provided by Mitsubishi Heavy Industries, Ltd. This polyurethane is composed of diphenylmethane-4,4-diisocynate, adipic acid, ethylene oxide, polypropylene oxide, 1,4-butanediol, and bisphenol A [27] and the glass transition temperature of the soft segment is specified by the provider as 55°C. The shape memory polyurethane (SMPU) was supplied in pellet form and used as received. Dimethyl formamide (DMF) from Sigma Aldrich was used as received to dissolve the polyurethane pellets. Nano-clay platelets, Laponite RD (Southern Clay), with diameter of ~25 nm and thickness of 1 nm were used as received in powder form.

7.2.2 Solution Preparation

Polyurethane-DMF solutions were prepared so that the final concentration of polyurethane in solution was 13, 17, 20, 24 and 27 wt%. The solutions were then roll-mixed at a moderate speed for two days prior to use to ensure that the polyurethane was completely dissolved. To disperse Laponite in the 17 wt% polyurethane-DMF mixture, Laponite was first dispersed in pure DMF at ~0.6 wt% using the solvent exchange approach [28] detailed in Chapter 3 and then added to the polyurethane-DMF mixture. Consequently, the resultant polyurethane concentration in solution was less than that desired. After thoroughly mixing the solution using a magnetic stir bar (for approximately two days) and placing the solution on a Cimarec digital hot plate stirrer, the cap was removed and some of the excess DMF was then evaporated off the mixture at 50°C while the stir bar rotated slowly at setting of 2. The mass of the remaining solution was measured intermittently until the desired polyurethane concentration of 17 wt% was obtained. Once thoroughly mixed the temperature was reduced to ambient and the solution continually stirred until the sample was removed for electrospinning.

7.2.3 Electrospinning Parameters and Mat Preparation

The solution was electrospun using the parallel plate setup described and depicted schematically in [29] is also shown below in Figure 7-1.

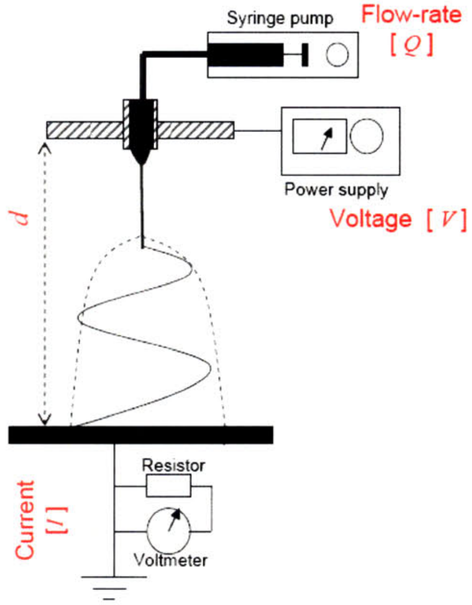

Figure 7-1: Schematic representation of the parallel-plate fiber spinner.

The spinning parameters for each of the solutions are given in Table 7-1. The protrusion of the spinneret from the upper plate was 2 cm and distance, *d*, between the capillary tip and the collector plate is given in Table 7-1. The fiber mats were collected on a grounded non-stick aluminum foil.

PU Concentration, c wt% in solution	Voltage, V kV	Flow Rate, Q mL.s^{-1}	Distance, d m	Temperature, T C	Relative Humidity %
13	20.0	1.67E-04	0.37	21	27-31
17	24.0	1.67E-04	0.37	21	24-28
17	32.7	1.82E-04	0.48	24	24
17 (4 wt% Laponite)	33.8	4.25E-05	0.43	22-24	11-16
20	28.0	1.67E-04	0.44	22	32-37
24	37.1	1.67E-04	0.44	22	25-38
27	34.3	1.67E-04	0.46	21-22	25-26

Table 7-1: Electrospinning parameters for each fibrous morphology discussed.

The voltage and flow rate applied to the solution as well as the laboratory temperature and relative humidity during spinning were all recorded; however, note the electrical current, *I*, during spinning was not monitored. Immediately after collection the sample and aluminum foil were placed in an oven for forty-eight hours at 20°C with a N_2 purge flow of 0.03 m^3 h^{-1} and then stored in zip-lock plastic bags at ambient temperature until samples were needed for characterization. Each sample mat used for characterization was a small film-like section cut from the original electrospun mat.

7.2.4 Characterization Methods

7.2.4.1 Interrogation of Solution Conductivity

The Solartron 1287A Potentiostat and 1260A Impedance/Gain-Phase Analyzer were used in combination as an impedance analyzer to measure the conductivity of the pure 17 wt% polyurethane solution and 4 wt% Laponite-filled solution. The solution was placed in an electroporation cuvette with a 0.2 cm gap (d_{gap}), surface area equal to 2.3 cm^2 (A) and was connected to the instrument via double-sided copper tape and alligator clamps. A frequency sweep was run from 10^{-1} to 10^7 Hz with an AC current of 0.1 Amps and the complex plane impedance diagram recorded. The conductivity, σ, was then calculated following the procedure detailed in [30], as shown below:

$$\sigma = \frac{d_{gap}}{A \cdot |Z|}, \tag{7.1}$$

where $|Z|$ is the closest absolute complex impedance value to the real axis when the semi-circular electrical response transitions to the monotonically increasing tail, as seen in Fig 7-3.

7.2.4.2 Interrogation of Fiber Morphology

The general morphology of the resultant mats was characterized using a JEOL JSM-6060 scanning electron microscope (SEM) operating at 10-15 kV with a spot size of 45. Prior to imaging the electro-spun mats were sputter coated with a 9-12 nm coating of gold (i.e. 30 seconds of sputter time). The average fiber diameter and standard deviation was calculated from twenty different fiber locations in one representative SEM image taken at a magnification of 2000 using the ruler tool in Adobe Photoshop CS. In situ thermal-actuated shrinkage of mats without the gold sputter coating was captured in the FEI/Philips XL30 FEG Environmental SEM by adhering two edges of a long rectangular mat specimen to a thermoelectric cooler using double-sided copper tape and increasing the temperature in an instantaneous step from 0°C to 62°C.

7.2.5.2 Interrogation of Non-Woven Mat

To actuate the material the mats were either placed on a Cimarec hot plate held at 70°C for 120 seconds or placed in a beaker of hot deionized water for twenty-four hours unless otherwise denoted and then dried on a chem-wipe for five minutes. In either case the mats were allowed to recover the intrinsic strain (or shrink) freely without any constraining load. The dimensions of the mat samples prior and after actuation were measured using calipers. The stretch recovered in each of the lateral directions was calculated as follows

$$\lambda_{\mathrm{Recovered}} = 1 - \frac{L}{L_0}, \qquad (7.2)$$

where L_0 represents the initial lateral dimension and L represents that same dimension after actuation. The average value and standard deviation reported are based on two measurements taken from four different mat samples.

The thermal transition temperatures of the fiber mats were evaluated and the presence of water absorbed within the fibers was verified using a TA Instruments Q1000 differential scanning calorimeter (DSC) with a 10°C min^{-1} ramp rate from -90°C to 250°C. The thermomechanical properties of the mats were evaluated using a TA Instruments Q800 dynamic mechanical analyzer (DMA) with a 3°C min^{-1} ramp rate from -150°C to 200°C.

The amount of water absorbed into the electrospun mats was monitored with a laboratory mass balance with a ±0.1 mg resolution. At various recorded times the mat was removed from the beaker of deionized water, wrapped in a chem-wipe for 120 seconds to wick away any excess water trapped amid pores or pinned to the surface and then the mass measured. Obviously, this technique is filled with numerous sources of error; however, the results allow an order of magnitude estimate of the mass diffusivity to be determined.

7.2.5.3 Interrogation of Pore Size

The pore size distribution of the electrospun mats was measured using Micromeritics AutoPore IV 9500 mercury porosimeter. As the pressure increased incrementally from 3.65 kPa to 68.8 MPa the mercury invaded smaller and smaller specimen pores. Pore size was determined based on evaluation of the capillary pressure given by the following equation

$$P = \frac{4\gamma \cos\theta}{D}, \qquad (7.3)$$

where P is the pressure, $\gamma = 0.48\ \mathrm{N\ m^{-1}}$ is the surface tension of mercury, $\theta = 140^{\circ}$ is the assumed contact angle between mercury and the pore wall, and D is the calculated cylindrical pore diameter following the arguments of Washburn [31, 32].

7.3 Results and Discussion

7.3.1 Fibrous Morphology

While many polymer solutions have a small envelope of spinnable concentrations [1] this commercial, shape memory polyurethane (SMPU) was found to be spinnable in DMF over a wide range of concentrations from 13 wt% to 27 wt% in solution.

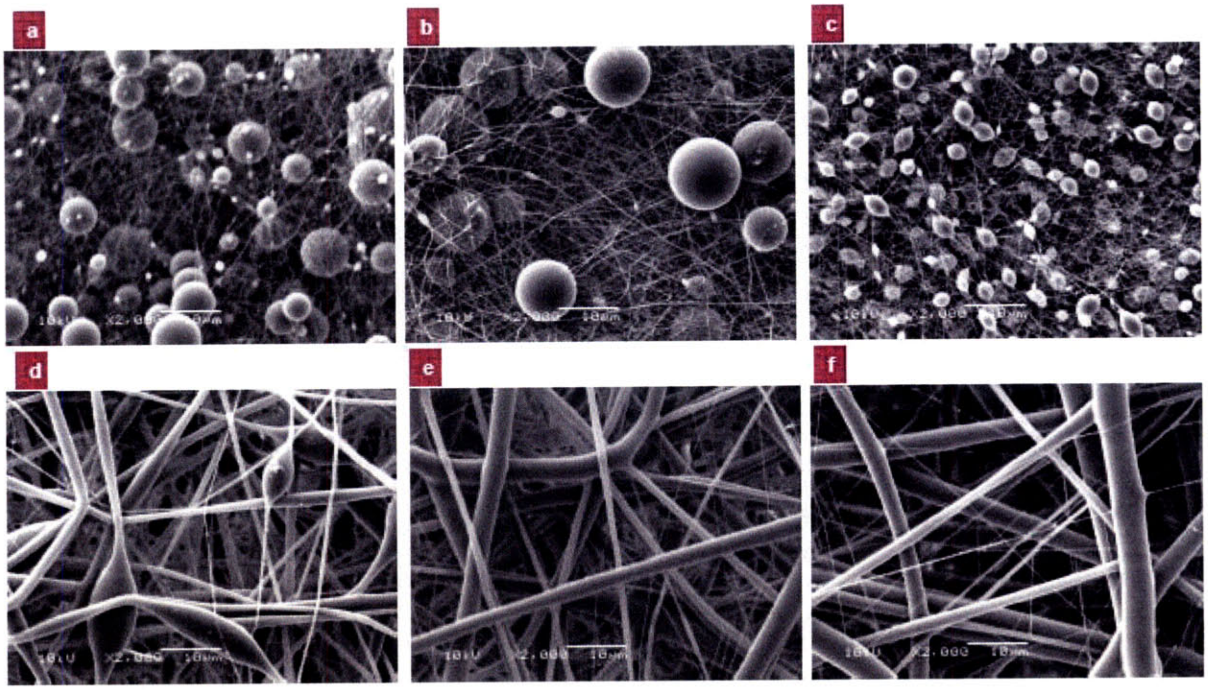

Figure 7-2: Scanning electron micrographs demonstrate the change in fibrous morphology as the concentration of polyurethane in solution increases: a) 13 wt%, b) 17 wt%; low *Q*; low *E*, c) 17 wt%; high *Q*; high *E*, d) 20 wt%, e) 24 wt%, and f) 27 wt% (scale bar is 10 µm in all images).

The resulting fibrous morphologies that correspond to the spinning parameters of Table 7-1 are displayed in Figure 7-2. As the concentration increases above 20 wt% polyurethane in solution, the fiber morphology transitions from 'beads on a string' (BOAS) to smooth continuous fibers. It is important to note that the resulting fiber diameters as well as bead diameters are polydisperse. The beads observed in the 13 and 17 wt% based mats are frequent and quite spherical in contrast to the fewer, more elongated beads observed in the mat obtained from 20 wt% solution. The resulting shape of the bead is determined by the relaxation time afforded the polymeric material comprising the beads. By utilizing a more volatile solvent, such as tetrahydrofuran (B.P. = 66°C) instead of dimethylformamide (B.P. = 153°C) or by increasing the characteristic relaxation of the polymer with nano-filler the beads become more elongated and less spherical [33]. While the beads resulting from the polyurethane-dimthylformamide solution appear smooth and spherical, the beads Tuteja et al observe in [13] when poly(methyl methacrylate) and tetrahydrofuran are electrospun appear to be oblong and wrinkled. These oddly shaped beads result when high concentrations of polymer coupled with volatile solvents are utilized in the electrospinning solution because a solid skin forms along the fiber due to quick evaporation. Meanwhile, solvent still remains within the fiber unless the material is further post-processed.

It is important to note that scanning electron micrographs shown in Figure 7-2b and 7-2c are of two separate electrospun mats both utilizing 17 wt% polyurethane in solution. However, as noted in Table 7-1, the flow rate, Q, and the magnitude of the electric field, E, given by the voltage, V, divided by the distance, d, between capillary tip and collection plate differ. The morphology exhibited in Figure 7-2b which is characterized by a polydisperse assortment of large beads, most of which measure 8-10 μm in diameter, connected by strings with an average diameter of 170 ± 70 nm, are produced when a flow rate of $Q = 1.67\text{x}10^{-4}$ mL s^{-1} and an electric field of $E = 6.52\text{x}10^{4}$ kV m^{-1} are utilized. In contrast, the resultant morphology when a higher flow rate ($Q = 1.82\text{x}10^{-4}$ mL s^{-1}) and electric field magnitude ($E = 6.81\text{x}10^{4}$ kV m^{-1}) are utilized is characterized by numerous beads measuring 2-4 μm in diameter connected by strings with an average diameter of 130 ± 30 nm.

By adding Laponite platelets at a small to moderate concentration, $\phi < \phi_P$ which does not exceed the percolation limit ($\phi_P = 6$ wt% [28]), to the 17 wt% polyurethane solution it is possible to further tailor the resulting fibrous morphology and extend the spinnable solution envelope. If the Laponite concentration exceeds the percolation limit the microstructure in the Laponite/polymer solution jams, hindering the development of solution viscoelasticity and promoting capillary break-up. Even when a small concentration of Laponite is added to the solution (4 wt% in the solid or ~0.7 wt% in solution) the conductivity increases to ~60 times that of the pure solution. Figure 7-3 depicts the complex plane impedance diagram of the two solutions. Note that the absolute magnitude of the complex impedance of the polyurethane solution is $9.8\text{x}10^{4}\,\Omega$ while that of the Laponite filled solution is $1.9\text{x}10^{3}\,\Omega$; therefore, the resultant conductivity is $8.9\text{x}10^{-7}$ S cm^{-1} and $5.5\text{x}10^{-5}$ S cm^{-1}, respectively.

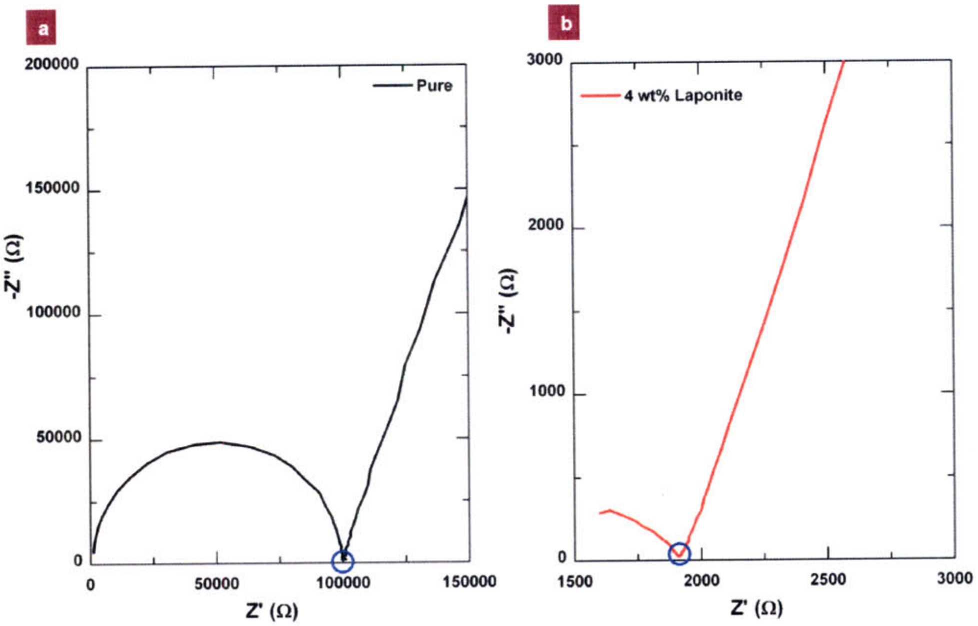

Figure 7-3: Complex plane impedance diagram of the 17 wt% polyurethane solution with (b) and without Laponite (a) from which the solution conductivity is calculated.

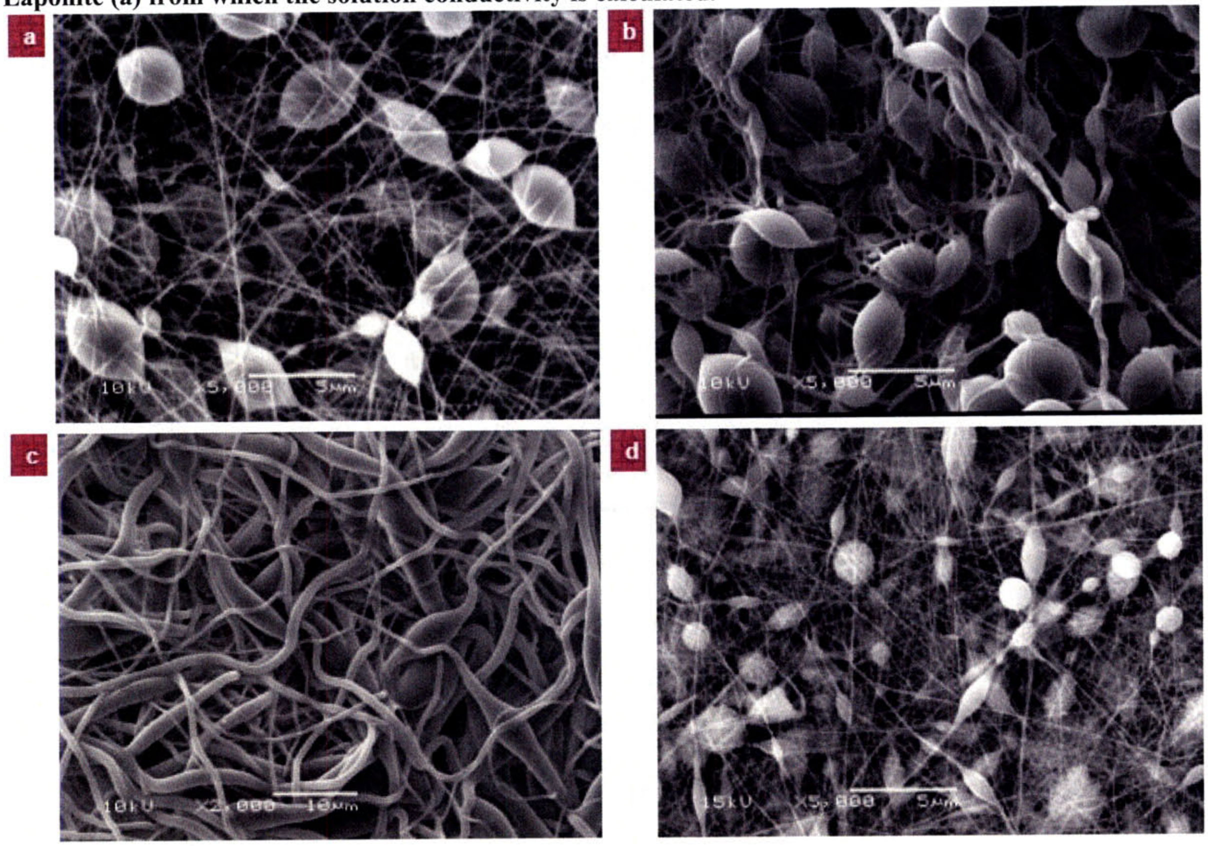

Figure 7-4: Microscopic images of the as spun, pure, non-woven mat prior to and after actuation and of a 4 wt% Laponite-filled mat: (a) pure, as spun mat, (b) pure mat after thermal actuation and shrink, (c) pure mat after aqueous actuation and shrink, and (d) 4 wt% Laponite-filled mat as spun. Note smaller magnification in image c allows greater viewing area. Despite the addition of Laponite upon actuation the strings relax and re-coil and grow in diameter while the beads remain unchanged.

The charged Laponite discs act effectively like a salt increasing the conductivity of the solution but simultaneously increasing the solution viscosity and relaxation time [34, 35]. Consequently, as shown in Figure 7-4d, the addition of enough Laponite so the final concentration in the solid is 4 wt% allows a slower flow rate and greater electric field magnitude to be applied ($Q = 4.25\text{x}10^{-5}$ mL s^{-1}; $E = 7.83\text{x}10^{4}$ kV m^{-1}). This produces smaller, elongated beads that measure less than 2 μm in diameter and are connected by finer fibers with average diameter of 120 ± 20 nm.

7.3.2 Results of Thermal and Aqueous Actuation

The ambient temperature (T_{amb}) at which the material is spun and stored is between 20-25°C. The glass transition of the soft phase or transitioning phase (T_g = 55°C) of the SMPU is greater than T_{amb}. Despite the fiber morphology, the stretch applied during electrospinning is 'frozen' in the strings or fibers. Consequently, upon thermally stimulating the non-woven mat (e.g. by placing it atop a hot plate set at 70°C) the mat shrinks in each lateral direction and the thickness of the fibers increases as shown in the movies in Appendices A-5. The extent of the change in fibrous morphology upon heating, namely the increase in fiber diameter and noticeable relaxation and coiling of the strings, is clearly observed in the micrographs presented in Figures 7-4a and 7-4b. Upon heating, the taut polymer chains relax and re-coil, attempting to recover the entropy lost during electrospinning. The elongated chains are driven to return to the coiled configuration in solution. Consequently, the average diameter of strings after thermal stimulation measure 260 ± 80 nm and are two times thicker than they were prior to stimulation.

These fibrous materials respond not only to thermal stimulus but also to aqueous stimulus [36]. Because the polyurethane utilized contains ethylene oxide, a very hydrophilic component, within its transition segment or softer phase it is possible to plasticize the segments with water and allow the stretched polymeric chains to relax and recovery entropy without increasing the temperature. Although the water is absorbed and plasticizes the ethylene oxide component of the linear block-copolymer, the T_g measured via differential scanning calorimetry does not significantly change as is shown in Figure 7-5.

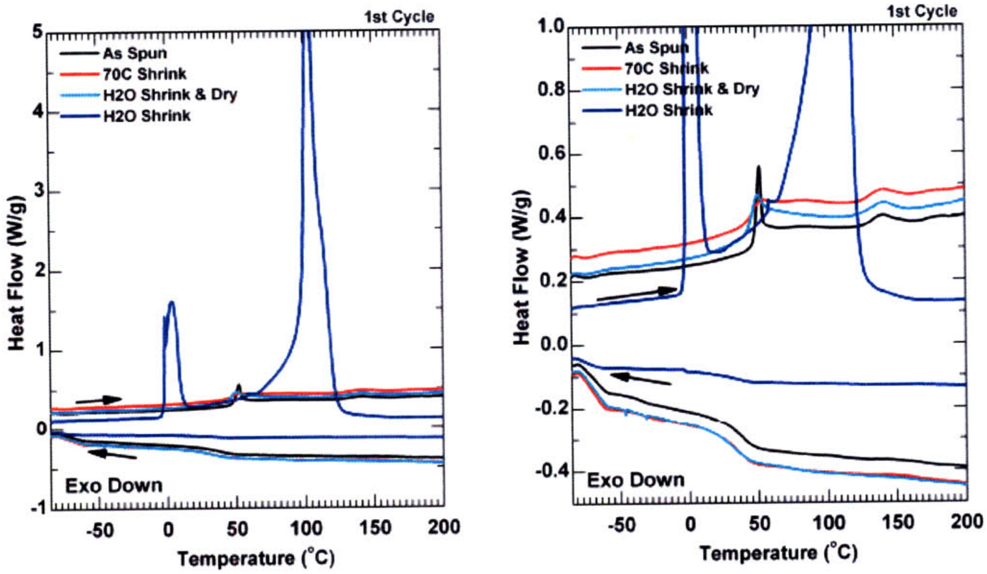

Figure 7-5: Differential scanning calorimetry of the as spun non-woven mat, the thermally actuated mat, and the water soaked mat prior to drying and after drying. Note the image on the right is a zoomed view of that on the left.

The rate of absorption of water into the fibers is highly dependent on the surface area to volume ratio of the available fibers [37]. Consequently, fibers of high aspect ratio ($\alpha = l \,/\, d$ where l is fiber length and d is fiber diameter) absorb water more quickly than mats composed of shorter or larger diameter fibers. Mats consisting of a ‘beads on a ‘ morphology may absorb less water than a mat consisting of thicker continuous fibers if the overall surface area to volume ratio of the strings and beads is less than that of the other mat composed larger diameter fibers [37]. This actuatable system is more complex than that of the thermal stimuli system because the water is absorbed first. The ‘BOAS’ electrospun mat prepared at C=17 wt% with a high electric field and high flow rate increases its mass almost fourfold in five minutes when exposed to water. However, as the mat continues to be soaked in the water bath the polymer chains relax and the mat contracts laterally and water is squeezed from the mat so that an equilibrium mass of only 1.8 times the original mass is achieved (see Figure 7-6 below). In forty-eight hours the equilibrium mass is reached and in twenty-four hours the mass is within 10% of the equilibrium value. Despite utilization of high aspect ratio nanofibers, response to aqueous stimulation is observed to be ~10^2 times slower than the response to thermal stimulation.

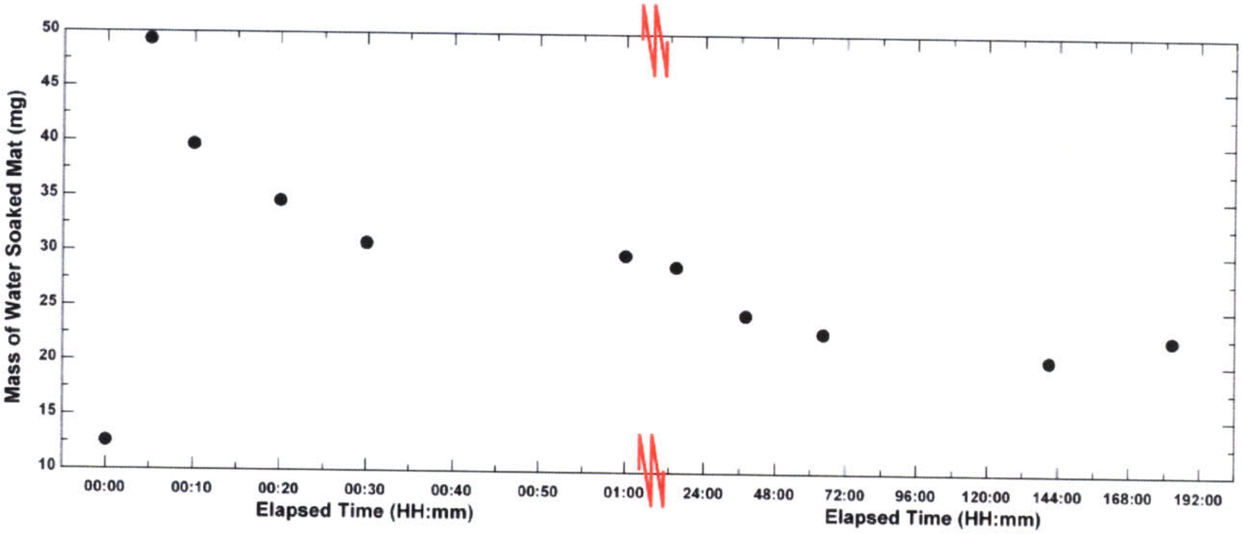

Figure 7-6: Evolution of water uptake in the electrospun mat as it is soaked in a DI H_2O bath. Notice the elapsed time scale changes after one hour.

The Lewis number (*Le*),

$$Le = \frac{\alpha}{D_c}. \tag{7.4}$$

a dimensionless number which compares the thermal diffusivity (α) of a system to the mass diffusivity (D_c), typically used to characterize fluid flows, can be approximated in the following manner. The thermal diffusivity can be estimated to be:

$$\alpha = \frac{k}{\rho c_p} \sim 5 - 7 \times 10^{-8} \, \frac{\mathrm{m}^2}{\mathrm{s}}, \tag{7.5}$$

where k is the thermal conductivity (and varies from 0.12 to 0.2 W $\mathrm{m}^{-1}\mathrm{K}^{-1}$ for this polyurethane depending on temperature [27, 38]), ρ is the density (1200 kg m^{-3} [27]), and c_p is the specific heat which is 2.0 kJ $\mathrm{kg}^{-1}\mathrm{K}^{-1}$ at 300°C and 2.7 kJ $\mathrm{kg}^{-1}\mathrm{K}^{-1}$ above the transition temperature (based on results from DSC). The mass diffusivity is not easily calculated for this fibrous polyurethane system due to the inherent heterogeneities in microphase-separated polyurethanes coupled with the fact that the diffusivity changes as the concentration of water within the fiber increases [39, 40]. However, based on the results of Mrotek et al. [40] and Dolmaire et al. [39] the mass diffusivity can be approximated as 10^{-12}-10^{-13} $\mathrm{m}^2\ \mathrm{s}^{-1}$. As a result the Lewis number is much greater than unity ($Le \sim 10^4$-10^5) and corroborates our experimental observations that the thermal response is quicker than the aqueous response. The discrepancy in the ratio of experimentally observed response times and the ratio of thermal diffusivity to mass diffusivity exists because the diffusion of water is not Fickian. There are strong interactions between the polyurethane and the water, i.e. swelling and/or plasticization, and the most noticeable polymer chain relaxation takes place after the maximum water uptake is achieved [40].

The morphological change of the beads on string morphology after aqueous stimulation and drying is dramatic as is depicted in Figure 7-4c. The average diameter of the strings increases almost sixfold to 810 ± 330 nm, at which point it becomes difficult to distinguish the location of beads. The scanning electron micrographs in Figure 7-4 indicate that the stretch applied during electrospinning is 'frozen' in the fibrous ligaments and not in the beads, because there is no observable change in bead dimension after thermal or aqueous stimulation. The polymer chains within the beads are completely relaxed.

It is apparent when comparing the morphologies depicted in the series of micrographs that as the concentration of polyurethane in solution increases the magnitude and variation of diameter of the strings or fibers also increases as. This trend is emphasized in Figure 7-7a. The extent of stretch recovered laterally within the mat correlates inversely with diameter as shown in Figure 7-7b. The greater the average diameters of the fibers that compose the mat, the smaller the average lateral shrink, irrespective of the mode of stimulation.

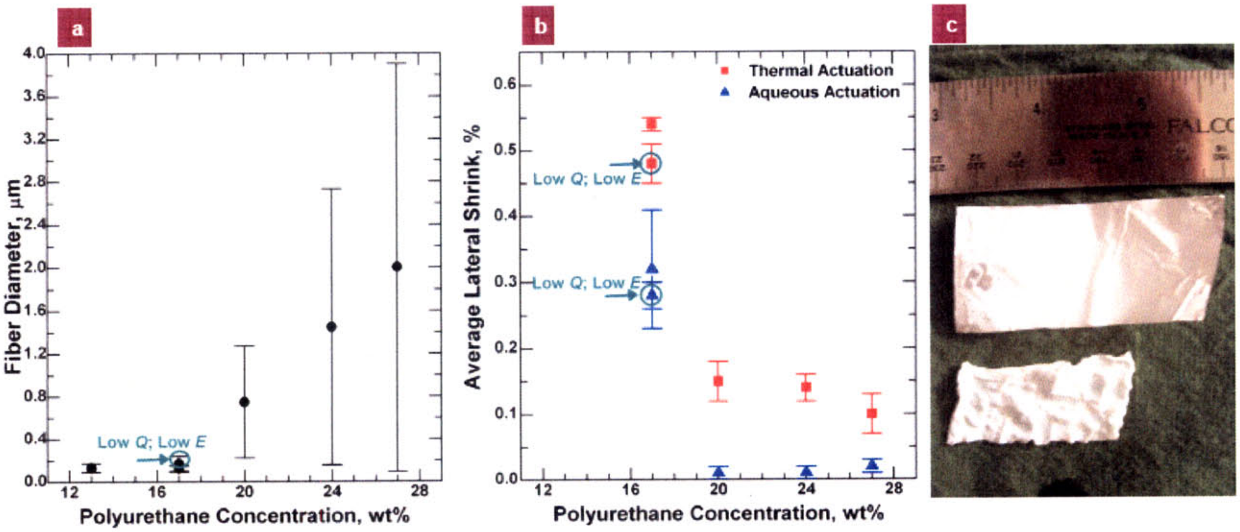

Figure 7-7: Influence of polyurethane concentration in solution on fiber diameter (a) and the extent of strain recovered after actuation (b & c). A photo of the as spun, non-woven mat prior to (c: top) and after aqueous actuation (bottom: $C = 17$ wt%; high Q; high E) visually highlights the extent of lateral shrink achieved.

The beads on a string mats produced from 17 wt% polyurethane in solution exhibit the greatest lateral shrink of ~50% when thermally actuated and ~30% when aqueously actuated. The lateral shrink recovered via aqueous actuation was always less than that recovered via thermal actuation. This difference occurs because the swelling upon exposure to water increases the fiber diameter to such an extent that the swollen fibers interfere with neighboring ones and inhibit further shrinkage. However, upon removal of all the water absorbed in the aqueously actuated samples via heating or drying (the samples are left in a case with desiccant for 48 hours) the mats shrink further and approach the shrink values obtained after thermal actuation. It is likely that the stretched ligaments in the 13 wt% based mat are stretched further; however, its recovery is not measurable because the mat is so fragile that a continuous film-like sample could not be peeled away from the collector plate and foil. All of the other mats maintain their mechanical integrity prior to, during and after shape memory actuation. The flexural storage modulus determined via dynamic mechanical analysis of one mat (*C*=17 wt%; high *E*; high *Q*) at these various stages of actuation is depicted in Figure 7-8. Note that each mat has a modulus on the order of *E*~10 MPa without accounting for the high porosity at temperatures below 30°C.

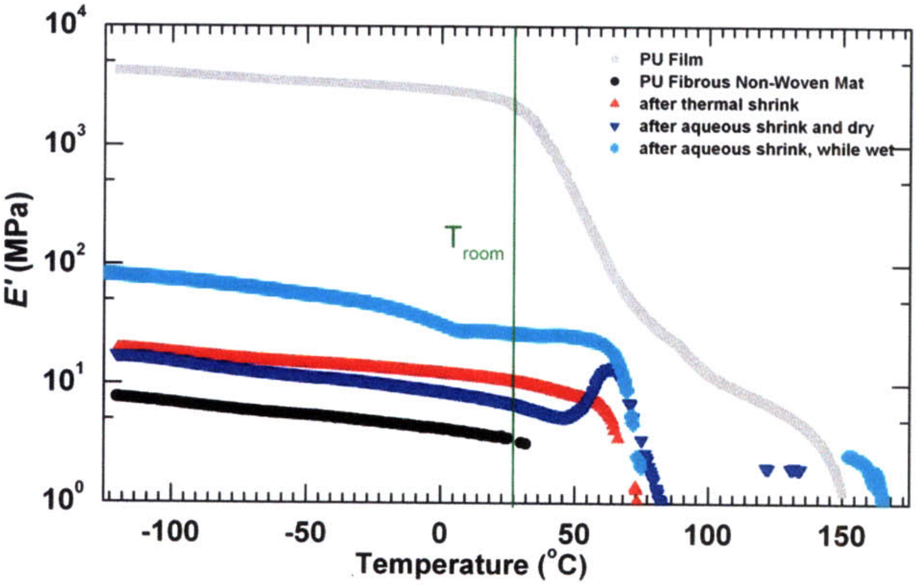

Figure 7-8: Flexural storage moduli of the BOAS electrospun mat (*C*=17 wt%; high *Q*; high *E*) at various stages of actuation. Note that the modulus values are based on the initial dimensions of the film-like samples and that it does not account for the porosity of the non-woven mat. Furthermore, the instrument does not record values during the transition region when the mat is continuing to shrink and recover entropy because an equilibrium has not been achieved.

When the temperature is close to the transition temperature the DMA, a load controlled instrument, has difficulty tracking the length of the specimen and determining the load needed to keep the specimen from buckling. This difficulty results because the instrument is trying to oscillate the specimen in tension while the mat is thermally softening and attempting to recover more entropy and shrink. Finally, the temperature becomes high enough that the material just flows as a viscoelastic liquid.

Thin fibers recover more intrinsic strain than larger diameter fibers as is confirmed by the trends portrayed in Figure 7-7. Although the 27 wt% based sample appears to contain an equal ratio of large and small diameter fibers the mat exhibits the smallest lateral shrink of ~10% after thermal stimulation. The overall mat shrink is diminished because the thicker fibers are effectively stiffer than the thin fibers and restrict the extent of strain the thin fibers may recover. From the inverse correlation of lateral shrink with fiber diameter we can infer that the strings of the BOAS fiber morphology are stretched further than the larger diameter, smooth fibers. Yet, the extent of stretch applied via electrospinning can not be quantified without a more controlled study and collection of monodisperse fibers.

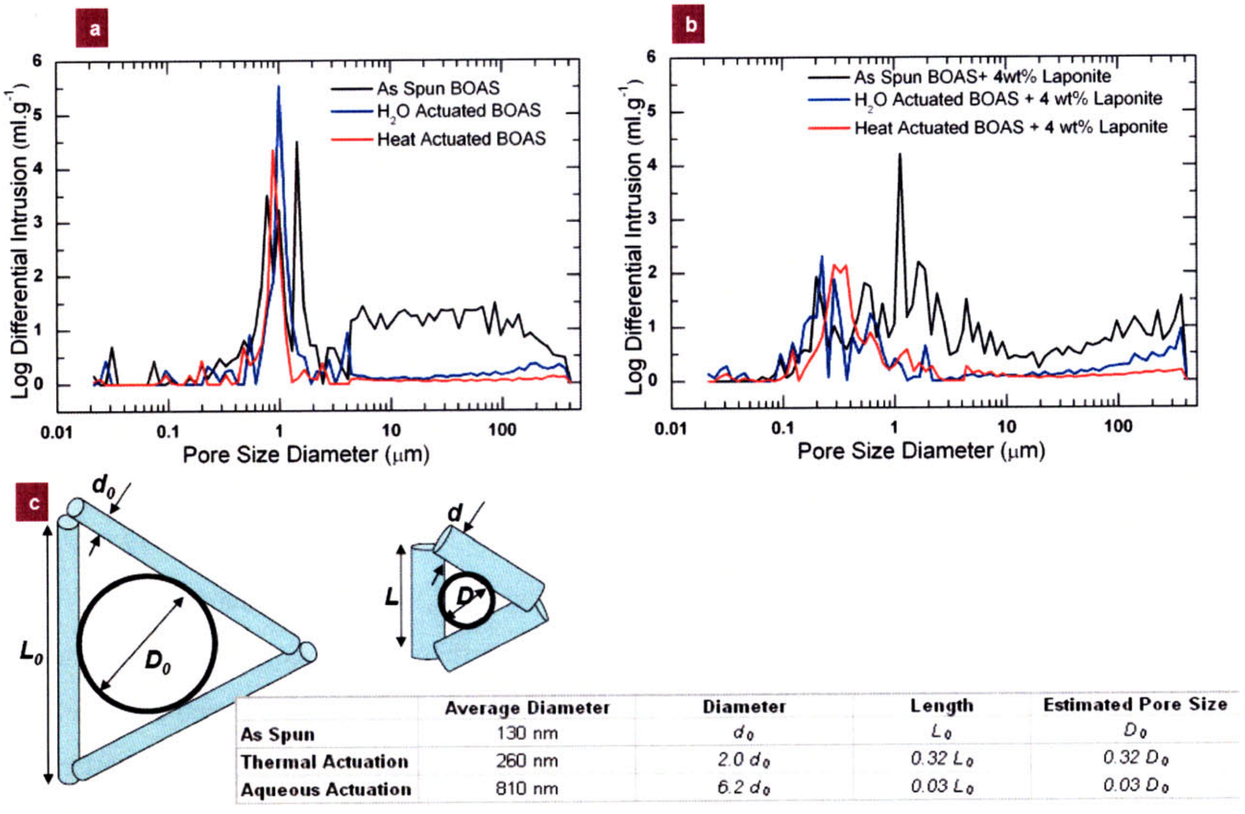

	Average Diameter	Diameter	Length	Estimated Pore Size
As Spun	130 nm	d_0	L_0	D_0
Thermal Actuation	260 nm	$2.0\ d_0$	$0.32\ L_0$	$0.32\ D_0$
Aqueous Actuation	810 nm	$6.2\ d_0$	$0.03\ L_0$	$0.03\ D_0$

Figure 7-9: Resultant change in pore size distribution within the pure (a; *C* = 17 wt%; high *Q*; high *E*) and Laponite composite (b), 'beads on a string' morphology, non-woven mats prior to and after thermal and aqueous actuation. c) Cartoon exhibiting expected pore size change, assuming affine deformation and that there are no beads.

The dramatic macroscopic change in mat shape shown in Figure 7-7c and microscopic change in fiber morphology depicted in Figure 7-4 should be accompanied by a significant reduction in pore size as shown in the cartoon in Figure 7-9c. As the results of mercury porosimetry indicate in Figures 7-8a and 7-8b, there is significant reduction in the pore size distribution after aqueous and thermal stimulation in the 17 wt% based solutions (with high *Q* and high *E* or with 4 wt% Laponite). The estimated shrink, assuming affine deformation, are not achieved. This is likely due to the presence of the beads which interfere and hinder further strain recovery. However, virtually all pores greater than the bead diameter prior to actuation disappear after stimulus. If the beads could be made smaller or the bead frequency decreased by utilization of nanoparticles, conducting salts or alteration in spinning parameters, it is possible to tailor a non-woven mat to have pores of a specific size. This technology could be useful in filtration and protective textile applications [11].

7.3.4 Evidence of Reversible Surface Energy

It is possible to exploit the change in macroscopic mat shrink and microscopic fiber topology and spacing to develop a fabric with reversible wettability [13, 41, 42]. Tuteja and coworkers[13] show that it is possible to design superoleophobic surfaces using rough, electrospun surfaces created from PMMA/FluoroPOSS blends. FluoroPOSS or 1H,1H,2H,2H-heptadecafluorodecyl polyhedral oligomeric silsesquioxane (fluorodecyl POSS) is a very low surface energy nanoparticle due to the presence and arrangement of $-CF_2$ and $-CF_3$ groups. By exploiting the ability of these mats to recover strain and shrink it is possible to develop a fabric that changes its wettability. On its own, each of these mats is wetted by water (γ_{lv} = 72.1 mN m^{-1}) and hexadecane (γ_{lv} = 27.5 mN m^{-1}) irregardless the fiber morphology. This result is not surprising since similar polyurethanes have been reported to have a solid-vapor surface energy, γ_{sv}, of approximately 40 mN m^{-1} [43] and as mentioned previously, this polyurethane absorbs water (due to the presence of ethylene oxide within the polyurethane). Consequently, a low surface energy coating was needed. A solution of a 50/50 blend of poly(methyl methacrylate) and fluorodecyl POSS in Asahiklin AK 255 was provided by A. Tuteja, W. Choi, and S. Chattre. The mats described above could be dip-coated in this solution. Note the maximum advancing contact angle on a spin-coated surface consisting of a fluorodecyl POSS/poly(methyl methacrylate) blend (44 wt% fluorodecyl POSS) is 80° [13]. After coating, the mats still were wetted by water, although not instantaneously as was observed on the untreated mats. This wetting was likely due to incomplete coverage of the fibers with the FluoroPOSS coating and the presence of large gaps between fibers. The affinity of ethylene oxide for water caused the droplet to be locally pinned to the mat and the water was absorbed by the polyurethane. However, the lower energy hexadecane was non-wetting as shown in Figure 7-10a. The mat (C=20 wt%) is rough enough and the spacing between fibers great enough so that the solid area fraction is small and a Cassie state exists [41]. Upon thermally actuating the mat the fibers grow in diameter and the pores shrink.

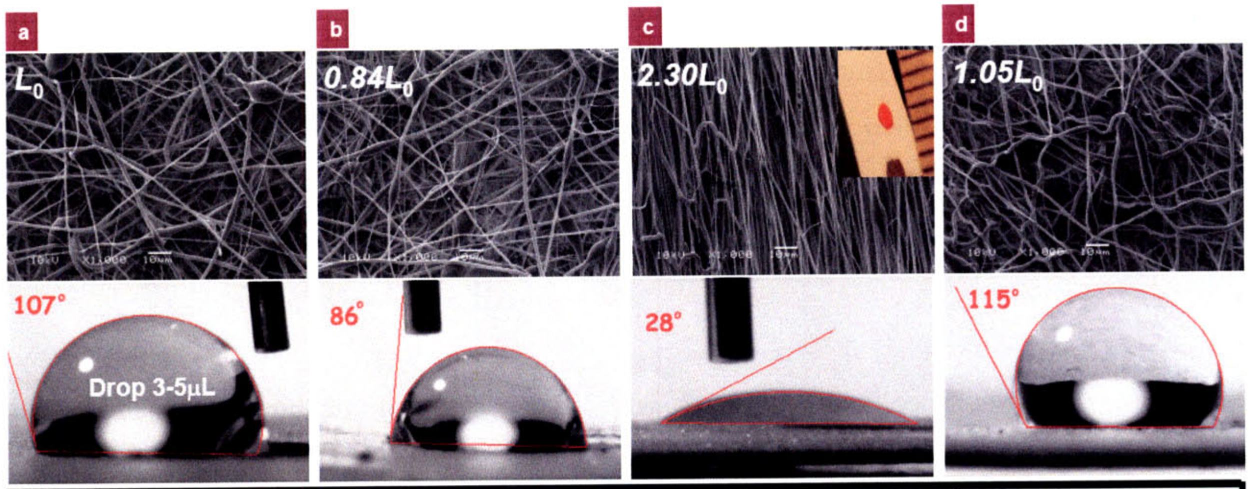

Mat Treatment	As Spun	Heat Shrunk	Heat Shrunk & Stretched	Heat Shrunk Again
Average Diameter (μm)	1.4 ± 0.4	1.5 ± 0. 4	0.97 ± 0.3	1.4 ± 0.4
Average Spacing (μm)	12 ± 4	9.6 ± 3	5.6 ± 2	14 ± 6
$\Delta\theta$ (degrees)	45	42	Fully Wetted	32

Figure 7-10: Scanning electron micrographs of the pure, non-woven, electrospun mat (C = 20 wt%) coated with a 50/50 blend of fluorinated POSS & PMMA in the relaxed, free-standing, as spun configuration (a: $L = L_0$), in the thermally actuated and shrunk state (b: $L = 0.84L_0$), the re-stretched state (c: $L = 2.30L_0$) and the again shrunk or recovered state (d: $L = 1.05L_0$) and the corresponding static contact angle of a drop of hexadecane. Note the inset in c depicts the anisotropic or elliptical wetting pattern of the hexadecane on the stretched mat. The average fiber diameter and spacing as well as the roll-off-angle, $\Delta\theta$, for each surface is reported.

Consequently, the solid area fraction grows and the spacing between fibers decreases and the hexadecane wets the surface as shown in Figure 7-10b. Upon manually stretching the mat in uniaxial tension 2.3 times its original length, the fibers become aligned in the stretch direction and closely spaced. The hexadecane then wets the mat anisotropically, leaving an elliptic residue with the long axis aligned with the direction of stretch shown in Figure 7-10c. Upon thermal actuation a second time, the mat shrinks once again, recovering 95% of its original shape.

Consequently, Figure 7-10d provides evidence that the spacing between fibers is somewhat larger than that of the relaxed, as spun configuration and the hexadecane becomes slightly more non-wetting. The contact angle hysteresis of these materials can be measured using a goniometer with a tilt stage. The roll-off-angle, $\Delta\theta$, or tilt-angle when the droplet begins to roll along the surface is equal to the difference between the advancing and receding contact angles, $\Delta\theta = \theta_a - \theta_r$ and quantifies the contact angle hysteresis of the surface [44]. The resultant contact angle hysteresis or roll-off-angles are reported in Figure 7-10. These surfaces exhibit significant hysteresis and the stretched specimen wets fully in less than 10 s making it difficult to quantify the anisotropic wetting. Ultimately, these coated, electrospun, shape memory mats demonstrate that fabrics with reversible surface energies can be achieved. With more careful control of the spinning conditions and fiber morphology and monitoring of the influence of uniaxial or biaxial stretch it may be possible to develop highly tunable, porous fabrics that could be used as actuatable filters and bandages or even as packaging, allowing the substance inside to wet when desired.

Switchable surfaces, specifically surfaces with switchable hydrophobicity and anti-fouling character are of particular interest in marine and biomedical industries: e.g. as coatings for ship hulls and organ implants or as bio-sensors for drug delivery [45-47]. Genzer has shown that by adding perfluoroalkanes at specific loacations along a stretched polydimethylsiloxane film the contact angle of water will increase from 100° to 130° when the film is released and allowed to elastically recover its original shape [47]. This is an example of mechanical switching. Switching can also be induced via an electrochemical stimulus, a change in environment i.e. thermal stimulus, or photo-stimulus as reviewed by Gras et al in [46]. This is a new research area and much work is still needed to develop switchable surfaces; specifically optimization of stimuli magnitude with resulting response is needed. Surfaces must also be tuned and the extent of their reversibility and stability quantified before devices that utilize this capability can be designed [46].

It should be noted that by adding magnetite nanoparticles to the electrospun mat it is possible to stimulate shrinkage without contact, via inductive heating. Numerous researchers have shown that by adding magnetite nanoparticles to polymers or solutions and placing the resulting composite or solution in an alternating magnetic field it is possible to heat the particles and the surrounding polymer by exploiting Néel relaxation or Brownian motion depending on the size of the particles and the viscosity of the matrix background [18, 48-50]. Néel relaxation arises from the rotation in direction of the magnetic vector of a magnetic particle with alternating external field and is the main contribution toward heating in solid polymeric systems [51]. It is possible to disperse magnetite nanoparticles and this shape memory polyurethane in a solution containing tetrahydrofuran with the aid of agitation; however, electrospinning the solution proved unsuccessful. The slow flow rate in the syringe allowed enough time for the dense magnetite particles ($\rho_{mag} = 4.8\text{-}5.1$ g cm^{-3} [49]) to precipitate to the bottom of the syringe prior to ejection. As a consequence, the resultant electrospun mat, spun in high humidity conditions, had large globules packed with magnetite particles atop a thick section of thin fibers with few magnetite particles (see Figure 7-11 below). If a rotating magnet was utilized around the syringe containing solution it may be possible to obtain electrospun, shape memory-magnetite composite mats that shrink when exposed to a third stimulus—an alternating electric field; however, time did not allow for additional experiments in such a system.

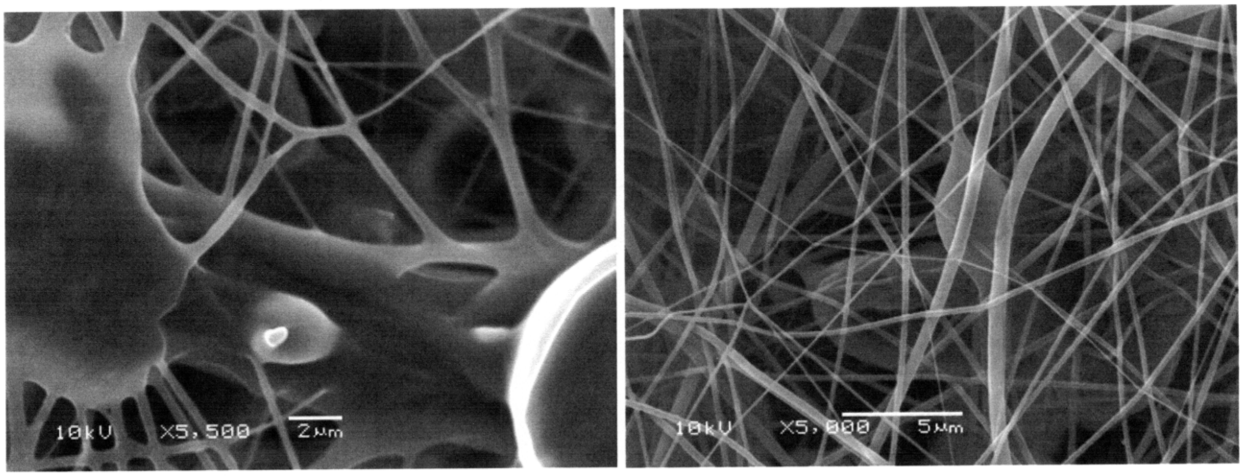

Figure 7-11: Comparison of the top and bottom side of an electrospun polyurethane mat filled with 10 wt% magnetite. The top side appears to be brown due to the presence of magnetite particles while the bottom side appears white as is typical of a pure polyurethane mat. Scanning electron micrographs show that the top side is composed of large, magnetite-filled globules while the bottom side is composed of pure polyurethane beads and thin strings.

7.4 Conclusions

By electrospinning a shape memory polymer, in this case polyurethane, it is possible to develop a porous, non-woven mat that will shrink and recover via thermal actuation the intrinsic stretch 'frozen' into the fibers during the spinning process. By adjusting the spinning parameters, the fiber morphology in the non-woven mat may be tuned. Specifically, by decreasing the polymer concentration in solution it is possible to progressively transition from mats comprised of smooth continuous fibers to fibers that resemble beads on a string. The diameter of the strings in this morphology is significantly smaller than the diameter of the continuous fibers. The intrinsic stretch ‘frozen’ in the fibers is inversely proportional to the string or fiber diameter. Consequently, a non-woven mat composed of beads on a string morphology exhibits greater shrinkage than a mat composed primarily of larger diameter, smooth fibers.

Furthermore, we have demonstrated that when the shape memory polymer is a multi-block copolymer containing a very hydrophilic component such as ethylene oxide within its transitioning segment (or softer phase) then aqueous exposure can also be used as another stimulus inducing entropic recovery. However, the response to aqueous stimulation is approximately one hundred times slower than the response to thermal actuation. We have also demonstrated that the addition of nanoparticles to the shape memory polymer allows for further tuning of fiber morphology. Irregardless of the method of actuation, we have shown that the significant entropic contraction, coupled with the beads on a string fiber morphology, provides a method to tailor the pore size distribution within the electrospun mat and offers an avenue for the production of selective filters or fabrics with reversible wettability. Ultimately, an electrospun, non-woven, fibrous mat such as the one presented here, that exhibits one-way response to multiple stimuli has significant potential in numerous applications, including drug delivery, food packaging, and filtration.

7.5 References

[1] S. V. Fridrikh, J. H. Yu, M. P. Brenner, and G. C. Rutledge, "Controlling the fiber diameter during electrospinning," *Physical Review Letters*, vol. 90, 2003.
[2] G. C. Rutledge and S. V. Fridrikh, "Formation of fibers by electrospinning," *Advanced Drug Delivery Reviews*, vol. 59, pp. 1384-1391, 2007.
[3] J. H. Yu, S. V. Fridrikh, and G. C. Rutledge, "The role of elasticity in the formation of electrospun fibers," *Polymer*, vol. 47, pp. 4789-4797, 2006.
[4] C. Liu, H. Qin, and P. T. Mather, "Review of progress in shape-memory polymers," *Journal Of Materials Chemistry*, vol. 17, pp. 1543-1558, 2007.
[5] A. Lendlein and S. Kelch, "Shape-memory polymers," *Angewandte Chemie-International Edition*, vol. 41, pp. 2034-2057, 2002.
[6] K & B Innovations, "The Magical World of Shrinky Dinks,"http://www.shrinkydinks.com, 2007: Accessed July 5th, 2008.

[7] J. D. Ferry, *Viscoelastic Properties of Polymers*, 3rd ed. New York, NY: John Wiley & Sons, Inc., 1980.

[8] J. P. Flory, *Principles of Polymer Chemistry*. Ithaca, NY: Cornell University Press, 1953.

[9] D. Huang, Y. Yang, G. Zhuang, and B. Li, "Influence of entanglements on the glass transition and structural relaxation behaviors of macromolecules: 1. Polycarbonate," *Macromolecules*, vol. 32, pp. 6675-6678, 1999.

[10] S. J. Hong, W. Yu, J. H. Youk, and Y. R. Cho, "Polyurethane smart fiber and shape memory function: experimental characterization and constitutive modelling," *Fibers And Polymers*, vol. 8, pp. 377-385, 2007.

[11] R. S. Barhate and S. Ramakrishna, "Nanofibrous filtering media: Filtration problems and solutions from tiny materials," *Journal of Membrane Science*, vol. 296, pp. 1-8, 2007.

[12] M. L. Ma, Y. Mao, M. Gupta, K. K. Gleason, and G. C. Rutledge, "Superhydrophobic fabrics produced by electrospinning and chemical vapor deposition," *Macromolecules*, vol. 38, pp. 9742-9748, 2005.

[13] A. Tuteja, W. Choi, M. L. Ma, J. M. Mabry, S. A. Mazzella, G. C. Rutledge, G. H. McKinley, and R. E. Cohen, "Designing superoleophobic surfaces," *Science*, vol. 318, pp. 1618-1622, 2007.

[14] M. Yoshida, R. Langer, A. Lendlein, and J. Lahann, "From advanced biomedical coatings to multi-functionalized biomaterials," *Polymer Reviews*, vol. 46, pp. 347-375, 2006.

[15] X. Jin and Y. L. Hsieh, "pH-responsive swelling behavior of poly(vinyl alcohol)/poly(acrylic acid) bi-component fibrous hydrogel membranes," *Polymer*, vol. 46, pp. 5149-5160, 2005.

[16] K. J. Pawlowski, H. L. Belvin, D. L. Raney, J. Su, J. S. Harrison, and E. J. Siochi, "Electrospinning of a micro-air vehicle wing skin," *Polymer*, vol. 44, pp. 1309-1314, 2003.

[17] R. Samatham, I. Park, K. J. Kim, J. Nam, N. Whisman, and J. Adams, "Electrospun nanoscale polyacrylonitrile artificial muscle," *Smart Materials & Structures*, vol. 15, pp. N152-N156, 2006.

[18] P. R. Buckley, G. H. McKinley, T. S. Wilson, W. Small, W. J. Benett, J. P. Bearinger, M. W. McElfresh, and D. J. Maitland, "Inductively heated shape memory polymer for the magnetic actuation of medical devices," *Ieee Transactions On Biomedical Engineering*, vol. 53, pp. 2075-2083, 2006.

[19] S. Chaterji, I. K. Kwon, and K. Park, "Smart polymeric gels: Redefining the limits of biomedical devices," *Progress In Polymer Science*, vol. 32, pp. 1083-1122, 2007.

[20] C. M. Yakacki, R. Shandas, C. Lanning, B. Rech, A. Eckstein, and K. Gall, "Unconstrained recovery characterization of shape-memory polymer networks for cardiovascular applications," *Biomaterials*, vol. 28, pp. 2255-2263, 2007.

[21] M. Martina and D. W. Hutmacher, "Biodegradable polymers applied in tissue engineering research: a review," *Polymer International*, vol. 56, pp. 145-157, 2007.

[22] K. Gall, C. M. Yakacki, Y. P. Liu, R. Shandas, N. Willett, and K. S. Anseth, "Thermomechanics of the shape memory effect in polymers for biomedical applications," *Journal Of Biomedical Materials Research Part A*, vol. 73A, pp. 339-348, 2005.

[23] G. Baer, T. S. Wilson, D. L. Matthews, and D. J. Maitland, "Shape-memory behavior of thermally stimulated polyurethane for medical applications," *Journal Of Applied Polymer Science*, vol. 103, pp. 3882-3892, 2007.

[24] H. T. Zhuo, J. H. Hu, S. J. Chen, and L. P. Yeung, "Preparation of polyurethane

nanofibers by electrospinning," *Journal Of Applied Polymer Science*, vol. 109, pp. 406-411, 2008.

[25] H. T. Zhuo, J. L. Hu, and S. J. Chen, "Electrospun polyurethane nanofibres having shape memory effect," *Materials Letters*, vol. 62, pp. 2078-2080, 2008.

[26] D. I. Cha, H. Y. Kim, K. H. Lee, Y. C. Jung, J. W. Cho, and B. C. Chun, "Electrospun nonwovens of shape-memory polyurethane block copolymers," *Journal Of Applied Polymer Science*, vol. 96, pp. 460-465, 2005.

[27] M. Y. Razzaq and L. Frormann, "Thermomechanical studies of aluminum nitride filled shape memory polymer composites," *Polymer Composites*, vol. 28, pp. 287-293, 2007.

[28] S. M. Liff, N. Kumar, and G. H. McKinley, "High-performance elastomeric nanocomposites via solvent-exchange processing," *Nature Materials*, vol. 6, pp. 76-83, 2007.

[29] Y. M. Shin, M. M. Hohman, M. P. Brenner, and G. C. Rutledge, "Experimental characterization of electrospinning: the electrically forced jet and instabilities," *Polymer*, vol. 42, pp. 9955-9967, 2001.

[30] J. R. MacCallum and C. A. Vincent, "Polymer Electrolyte Reviews," 1st ed. London: Elsevier Applied Science, 1987, pp. 368.

[31] E. W. Washburn, "The dynamics of capillary flow," *The Physical Review*, vol. 17, pp. 273-283, 1921.

[32] E. W. Washburn, "Note on a method of determining the distribution of pore sizes in a porous materials," *Proceedings of the National Academy of Sciences of the United States of America*, vol. 7, pp. 115-116, 1921.

[33] Knovel, "Knovel Critical Tables: Basic Physical Properties of Chemical Compounds," Knovel Corporation, 2008.

[34] V. K. Daga and N. J. Wagner, "Linear viscoelastic master curves of neat and laponite-filled poly(ethylene oxide)–water solutions," *Rheologica Acta*, vol. 45, pp. 813-824, 2006.

[35] E. Guth, "Theory of Filler Reinforcement," *Journal of Applied Physics*, vol. 16, pp. 20-25, 1945.

[36] B. Yang, W. M. Huang, C. Li, and J. H. Chor, "Effects of moisture on the glass transition temperature of polyurethane shape memory polymer filled with nano-carbon powder," *European Polymer Journal*, vol. 41, pp. 1123-1128, 2005.

[37] A. Laforgue, L. Robitaille, A. Mokrini, and A. Ajji, "Fabrication and characterization of ionic conducting nanofibers," *Macromolecular Materials And Engineering*, vol. 292, pp. 1229-1236, 2007.

[38] G. R. Lomax, "Breathable polyurethane membranes for textile and related industries," *Journal Of Materials Chemistry*, vol. 17, pp. 2775-2784, 2007.

[39] N. Dolmaire, E. Espuche, F. Méchin, and J.-P. Pascault, "Water transport properties of thermoplastic polyurethane films," *Journal of Polymer Science: Part B: Polymer Physics*, vol. 42, pp. 473-492, 2004.

[40] J. L. Mrotek, M. J. Matthewson, and C. R. Kurkjian, "Diffusion of moisture through optical fiber coatings," *Journal Of Lightwave Technology*, vol. 19, pp. 988-993, 2001.

[41] A. B. D. Cassie and S. Baxter, "Wettability of porous surfaces," *Transactions of the Faraday Society*, vol. 40, pp. 546-551, 1944.

[42] R. N. Wenzel, "Resistance of solid surfaces to wetting by water," *Industrial and Engineering Chemistry*, vol. 28, pp. 988-994, 1936.

[43] M. Lupu, D. Macocinschi, G. Ioanid, M. Butnaru, and S. Ioan, "Surface tension of poly(ester urethane)s and poly(ether urethane)s," *Polymer International*, vol. 56, pp. 389-398, 2007.

[44] G. McHale, N. J. Shirtcliffe, and M. I. Newton, "Contact-angle hysteresis on super-hydrophobic surfaces," *Langmuir*, vol. 20, pp. 10146-10149, 2004.

[45] S. Krishnan, C. J. Weinman, and C. K. Ober, "Advances in polymers for anti-biofouling surfaces," *Journal Of Materials Chemistry*, vol. 18, pp. 3405-3413, 2008.

[46] S. L. Gras, T. Mahmud, G. Rosengarten, A. Mitchell, and K. Kalantar-Zadeh, "Intelligent control of surface hydrophobicity," *Chemphyschem*, vol. 8, pp. 2036-2050, 2007.

[47] J. Genzer and K. Efimenko, "Recent developments in superhydrophobic surfaces and their relevance to marine fouling: a review," *Biofouling*, vol. 22, pp. 339-360, 2006.

[48] V. S. Kalambur, B. Han, B. E. Hammer, T. W. Shield, and J. C. Bischof, "In vitro characterization of movement, heating and visualization of magnetic nanoparticles for biomedical applications," *Nanotechnology*, vol. 16, pp. 1221-1233, 2005.

[49] R. Mohr, K. Kratz, T. Weigel, M. Lucka-Gabor, M. Moneke, and A. Lendlein, "Initiation of shape-memory effect by inductive heating of magnetic nanoparticles in thermoplastic polymers," *Proceedings Of The National Academy Of Sciences Of The United States Of America*, vol. 103, pp. 3540-3545, 2006.

[50] K. Okawa, M. Sekine, M. Maeda, M. Tada, and M. Abe, "Heating ability of magnetite nanobeads with various sizes for manetic hyperthermia at 120kHz, a noninvasive frequency," *Journal of Applied Physics*, vol. 99, pp. H102, 2006.

[51] R. E. Rosensweig, *Ferrohydro-dynamics*. Mineola, NY: Dover Publications, Inc., 1985.

8. Concluding Remarks

8.1 Summary of Accomplishments

This thesis demonstrates that the use of block polarity in conjunction with the solvent exchange approach described here offers an avenue toward the development of high performance materials that rival natural materials. While this solvent exchange dispersal technique may be applied to numerous nanoparticle-polymer systems, the extent of property enhancement depends on the time allowed for phase-segregation and preferential reinforcement. Unfortunately, the aspect ratio of the nanoparticles employed significantly limits the concentration envelope that may be utilized so that matrix polymer dissolution is achieved. Ultimately, the success of this approach hinges upon utilization of dilute solutions in conjunction with slow processing which encourages optimal property enhancement.

Using the solvent exchange technique described, it is possible to preferentially nanoreinforce the hard micro-domains of thermoplastic elastomers with smectic clay that has characteristic dimensions similar to the hard segment length. The adhesion between the clay and the hard micro-domains coupled with the formation of a percolative network not only stiffens and toughens, but increases the heat distortion temperature (HDT) of a commercial poly(ether urethane). The discotic clay platelets induce morphological ordering over a range of length scales that results in significant thermomechanical enhancement and expands high temperature applications.

The role of the nano-clay reinforcement in polyurethane, however, evolves with deformation, specifically with chain stretch and orientation. ATR-FTIR results indicate that the addition of clay does not reduce the hard segment inter-urethane hydrogen bonding and order, nor does it reduce the hydrogen bonding between the hard segment and soft segment. The long processing time utilized via slow solvent casting allows for self-assembly and complete microphase separation irregardless of Laponite concentration. Because Laponite does not influence microphase separation the equilibrium or hyperelastic response of the polyurethane matrix is unaffected by the addition of nano-clay. The preferential association of Laponite to the hard micro-domains imposes spatial restrictions and/or constraints on the hard segments. The hard micro-domain/Laponite structures act like rigid fillers around which the soft chains must stretch. Consequently, the composite develops anisotropy and the matrix undergoes irreparable damage.

These thermoplastic polyurethane nano-clay composites demonstrate strong hysteresis, time dependence, and cyclic softening. The pure and Laponite filled polyurethanes exhibit two characteristic relaxation times. The long relaxation time corresponds to the hard micro-domains and remains constant with deformation. The short relaxation time corresponds to the soft segment. As the magnitude of the applied stretch increases the soft segments stretch, align and orient and the relaxation time increases. Ultimately, nano-clay reinforces the stress response of Elasthane, but also locally damages the polyurethane matrix, especially when concentrations above the percolation threshold are utilized. Laponite does not influence the hyperelastic or equilibrium response of the material—that is matrix dependent. Instead, the nano-clay influences the non-equilibrium response—the rate sensitivity and time dependence—much like rigid particles influence the viscosity of dilute solutions.

To exploit these thermo-physical interactions, nano-clay was dispersed within commercially-available shape memory polyurethane in order to enhance the restoring or actuation stress. While adding nano-reinforcement, specifically at concentrations above the percolation threshold, can significantly enhance the modulus of the material at temperatures above the glass transition there is trade-offs. The rigid reinforcement constrains the soft, entropy recovering segments restricting the chain mobility. A small change in glass transition temperature is observed with nano-clay reinforcement, while the actuated strain recovery is delayed as the filler concentration increases. Furthermore, as the nano-clay concentration increases, irreparable damage to the polyurethane matrix upon deformation is unavoidable. Consequently, the extent of strain recovered deteriorates, particularly at concentrations above the percolation limit. So while the actuation or recovery stress can be enhanced with the addition of exfoliated nano-clay, the percolation threshold denotes the critical point, beyond which the strain recovered significantly decreases.

By electrospinning a shape memory polyurethane, it is possible to develop a porous, non-woven mat that will shrink and recover the intrinsic stretch 'frozen' in the fibers during the spinning process via thermal actuation. Aqueous actuation may also be utilized if the multi-block copolymer contains a very hydrophilic component such as ethylene oxide within its transitioning segment; however, the response time is approximately a hundred times slower. The resulting string (of a 'beads on a string' fiber morphology) or fiber diameter is inversely proportional to the intrinsic stretch 'frozen' in the fibers. Consequently, a 'beads on a string' fiber morphology exhibits greater shrinkage than a mat composed primarily of large diameter, smooth fibers. The addition of nano-clay to the shape memory polyurethane solution allows for further tuning of fiber morphology by increasing solution conductivity and relaxation time, while fluorinated coatings offer a means to tailor the resultant surface energy of the fibrous mat. This control coupled with significant entropic shrink of the porous material provides a method to tailor the pore size distribution within the electrospun mat and offers an avenue for the production of selective filters or fabrics with reversible wettability. Ultimately, an electrospun, non-woven, fibrous mat that exhibits one-way response to multiple stimuli has significant potential in numerous applications, including drug delivery, food packaging, and filtration.

8.2 Future Work

Quantifying and controlling the thermo-physical interactions between a block-copolymer with polar segments (e.g. thermoplastic polyurethane) and inorganic nanoparticles (e.g. nano-clay) are important for future nanocomposite processing strategies: the efficacy of nanoreinforcement hinges upon the close matching of characteristic length scale and the adhesion of the nanoparticles to the targeted polymer phase morphology. Exploiting block polarity in conjunction with the solvent exchange approach developed in this thesis and processing techniques, such as electro-spinning, offers an avenue toward the development of high performance, hierarchically-ordered materials that rival natural materials. Further interrogation of the thermo-physical interactions of nano-clay and polyurethane, particularly at varying temperature and high strain rate, is of interest to the various military branches since polyurethane coatings have proven to mitigate damage due to blast [1]. Characterization of other inorganic nanoparticle interactions with polyurethane is of interest and necessary for continued development of high performance, multifunctional composites.

8.2.1 Scale-Up of Time Efficient, Environmentally-Friendly, Solvent Exchange Approach

While this solvent exchange dispersal technique discussed in this thesis proved successful, and may be applied to numerous nanoparticle-polymer systems, the extent of property enhancement depends upon utilization of dilute solutions in conjunction with slow processing for optimal enhancement. Both requirements, dilute solutions and time, are expensive and prevent this solvent exchange dispersal technique from being commercially viable, despite the interest of companies that produce cable sheathing, luggage, and women's active wear and intimate apparel for preferentially nano-reinforced polymer composites. Furthermore, unless the solvent utilized is water, or another naturally occurring liquid, rather than dimethylformamide or dimethylacetamide which were utilized in this thesis, the environmental impact of the solvent must be considered—particularly when it is needed in such large quantities. Consequently, scale-up of this dispersal technique to a more time-efficient, environmentally conscious method could prove beneficial.

One such method for scale-up, includes identification and evaluation of a naturally occurring "solvent" that would disperse nanoparticles but could be mixed and remain within the polymer matrix as an "additive" after processing. Dl-α-tocopherol, otherwise known as vitamin E (a naturally occurring antioxidant), could prove to be a viable option to act as both solvent and additive. Schubert et al have shown that the addition of 5 wt% vitamin E improves the biocompatibility and biostability of poly(ether urethane urea) elastomers in *vivo* with only a small amount of plasticization as shown in Figure 8-1 [2].

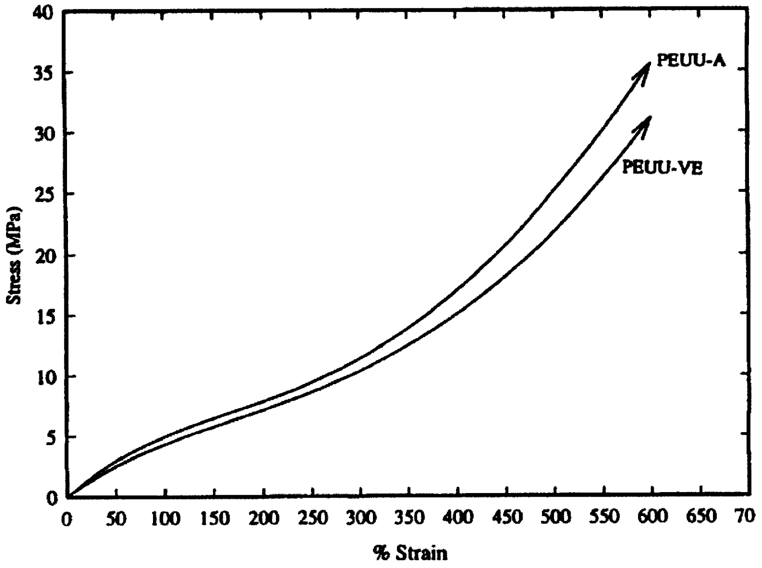

Figure 8-1: Stress-strain curves of poly(etherurethane urea) (PEUU-A) and that filled with 5 wt% vitamin E (PEUU-VE) [2].

It is possible that the slight plasticization caused by the addition of vitamin E could be negated by the inclusion of nanoreinforcement. Another difficulty that arises should vitamin E be utilized is that it is quite viscous at room temperature. Consequently, dispersal of nanoparticles like Laponite would require mixing the materials at elevated temperatures. Constant shear stress tests, when the shear stress equals 15 Pa, and constant shear rate tests, when the shear rate equals 1 s^{-1} at temperatures ramped from 25°C to 100°C at 2.5°C min^{-1} using TA Instruments AR 2000, indicate that viable mixing temperatures would be greater than 70°C, shown in Figure 8-2.

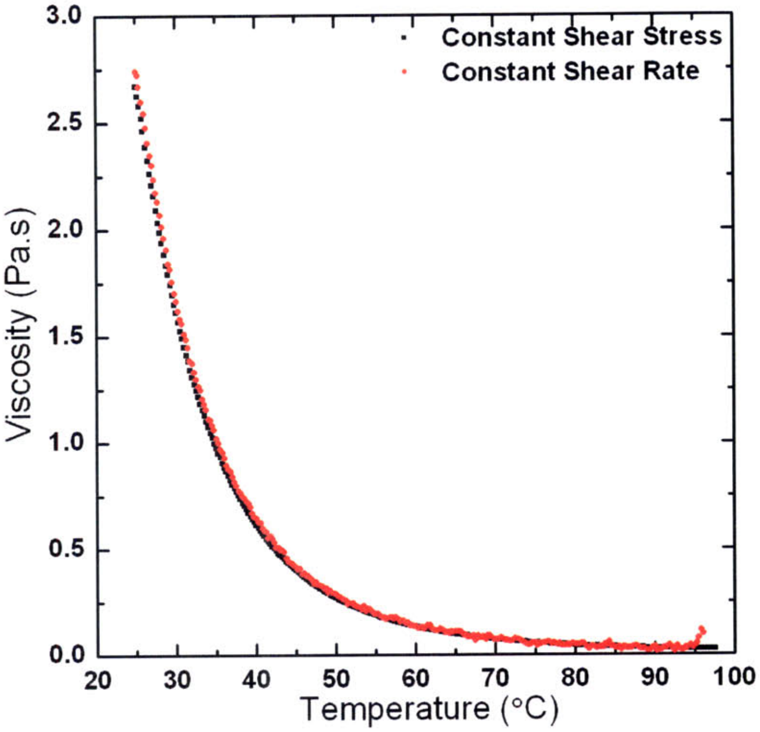

Figure 8-2: Comparison of the viscosity of Dl-α-tocopherol (Vitamin E) as a function of temperature when constant shear stress or constant shear rate is applied.

Ultimately, more research is necessary to determine whether vitamin E is a viable environmentally friendly solvent and polymeric additive and to identify other such materials.

8.2.2 Deformation Induced Orientation and Damage by Nano-Clay

This thesis makes clear that the role of the nano-clay reinforcement changes as the polyurethane composite is deformed and the polymer chains are aligned. However, it is not clear whether the platelets resist rotation and orientation or exactly how, or to what extent, the platelets induce irreparable damage. Nor are the interactions between the platelets and hard micro-domains within the strain hardening deformation region completely understood. While initial attempts at small angle x-ray scattering (SAXS) with in situ stretching proved unsuccessful because electron-density matching blurred any distinguishing features in the Laponite-filled samples, future attempts utilizing thicker specimens may allow the spacing between the Laponite platelets and hard micro-domains to be interrogated. Song et al have completed a similar study in which they found that within the elastic regime of the matrix material the *d*-spacing of the clay platelets varied in a reversible manner, increasing upon deformation but recovering to the original spacing upon removal of the imposed load [3]. Ultimately, the pairs of platelets with interspersed polymer acted as tiny nano-springs. It would be interesting to evaluate the nano-clay *d*-spacing in preferentially reinforced elastomeric polyurethanes. Quantifying the variation in the resultant platelet *d*-spacing with respect to macro-scale deformation would allow the movement, breakdown, and orientation of the jammed nano-clay network structure, as well as matrix damage, to be connected to physical mechanisms within the various deformation regimes, i.e. plastic yield, soft segment alignment, and strain-hardening. TEM images of the films stretched to these various deformation regimes would also offer visual evidence supporting the structural changes inferred through x-ray scattering and pin-point the mechanism behind irreparable matrix damage.

Interrogation of these preferentially reinforced polyurethane composites at various temperatures and high strain rates is also of particular interest to the United States military. Polyurethane coatings have proven to mitigate damage due to blast or ballistic event time and again, yet the mechanism(s) responsible for increased survivability are not entirely understood [1, 4]. In different temperature or frequency regimes, the rate sensitivities of polymers change as various molecular mobility mechanisms are stimulated. Nano-clay alters the morphology of the polyurethane and as a consequence may alter the rate-dependent mechanical deformation and failure behavior of the polyurethane.

Ultimately, understanding the correspondence between deformation and structural changes, specifically the orientation of Laponite within the nanocomposites, may help engineers design materials for specialty applications, such as ballistic protection or tear resistance in stockings. The structural changes coupled with strain rate and temperature sensitivity data can then be used to modify the constitutive model developed by Dr. Renaud Rinaldi (see Appendix A-3) to account for the addition of nano-clay and other modes of deformation interrogated and accounted. Progress in the utility of polymer composites, particularly polyurethane composites, depends upon reliable material models that are easily applied by design engineers.

8.2.3 Utility of Magnetite in Shape Memory Polyurethane Composites

Characterization of other inorganic nanoparticle interactions with polyurethane is of interest—specifically that of magnetite nanoparticles with shape memory polyurethane. Actuating biomedical devices, filters and protective coatings with switchable surface hydrophobicity are currently of great interest [5-11]. Often, however, these shape memory polymers need to be thermally stimulated in order to induce actuation. By adding magnetite nanoparticles it is possible to induce actuation without contact via inductive heating. A few researchers have shown that by adding magnetite nanoparticles to polymers or solutions and placing the resulting composite or solution in an alternating magnetic field it is possible to heat the particles and the surrounding matrix by exploiting Néel relaxation or Brownian motion (depending on the size of the particles and the viscosity of thematrix background) [7, 12-14]. While Buckley et al and Mohr et al have investigated the feasibility of actuating polyurethane via inductive heating, a systematic study evaluating the thermo-physical interaction between true, non-coated, nanoparticles and the polyurethane have not yet been evaluated and development of an efficient dispersal technique is needed [7, 13].

It is possible to disperse commercially available magnetite nanoparticles (Ocean NanoTech), measuring ~15 nm in diameter within commercial shape memory polyurethane (Mitsubishi Diaplex^{TM} Series MM 5510 PU). Ocean NanoTech provides these nanoparticles with oleic acid surface ligands dispersed in chloroform at a concentration of 5 mg ml^{-1} [15]. But the polyurethane is not soluble in chloroform. The chloroform can be exchanged with tetrahydrofuran by first adding acetone to the magnetite-chloroform solution in a ratio of 3:1. The acetone-magnetite-chloroform solution is then centrifuged at 3,000 rpm for fifteen minutes. The supernatant is then discarded and the magnetite precipitate dispersed in tetrahydrofuran at a concentration of 5 mg ml^{-1}. Then polyurethane and pure tetrahydrofuran are added to the magnetite-tetrahydrofuran solution so that 5 wt% polyurethane in solution resulted as well as a concentration of 5 wt% magnetite in solid when the polyurethane-magnetite composite was precipitated out using excess methanol. The precipitate is dried and then compression molded at 150°C. The dispersal of the magnetite nanoparticles within the compression molded films were then characterized using transmission electron microscopy after lamellae were prepared using a focused ion beam (discussed in Chapter 4). While the resultant film appears to be a homogeneous rust brown color, instead of transparent as it typically is without magnetite filler, the nanoparticle dispersal is not homogeneous. As is observed in Figure 8-3, while many of the nanoparticles are well dispersed, there are numerous small flocculates of 20-30 nanoparticles and a few huge agglomerates measuring 100-500 nm in diameter. Obviously, this dispersal is not ideal. The method for dispersal may require improvement, but at the least provides a means to prepare composites in which the thermo-physical interactions between magnetite particles and polyurethane matrix may be evaluated.

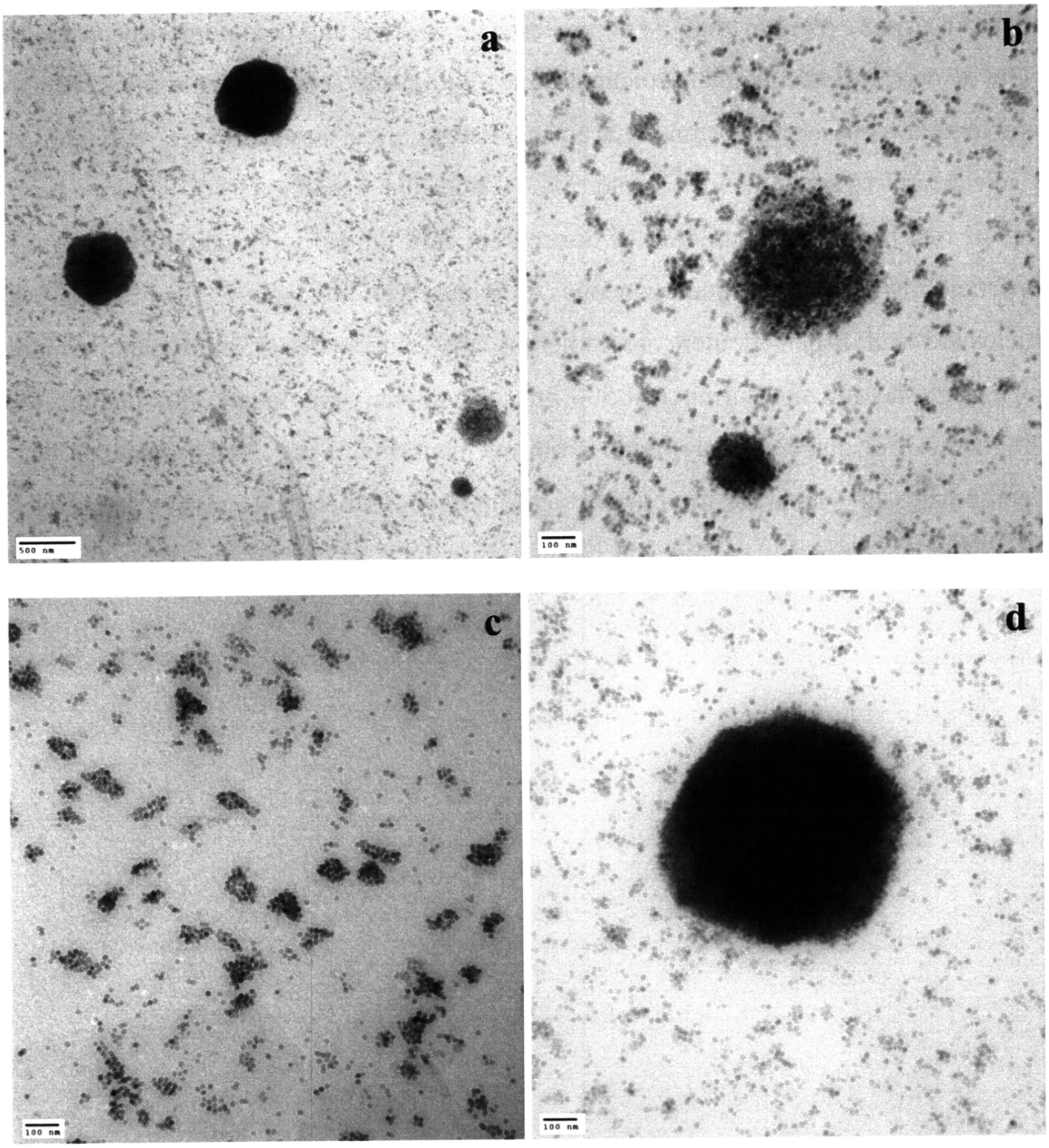

Figure 8-3: Transmission electron micrographs of magnetite nanoparticles dispersed in a commercial thermoplastic polyurethane (MM 5510) after precipitation and compression molding: scale bar 500nm in a and 100 nm in b, c, and d.

Despite the inhomogeneous magnetite dispersal, the composite films still display paramagnetic behavior. For instance, when a strong magnet is placed a couple inches above the composite film, the film jumps off the countertop and magnetically bonds to the magnet. The magnetization of the composite can be evaluated using a superconducting quantum interference device, the results of which are shown in Figure 8-4. As the applied magnetic field approaches ±1500 Oe the magnetization of the composite saturates.

However, when no magnetic field is applied there is small remnant magnetization which decays with increased temperature. This can be explained by the Néel relaxation which dominates and varies exponentially with inverse temperature[12]. Consequently, when the applied field is zero, the dipole moments of some particles remain polarized and result in a small remnant magnetization, however, as the temperature increases the remnant magnetization decreases.

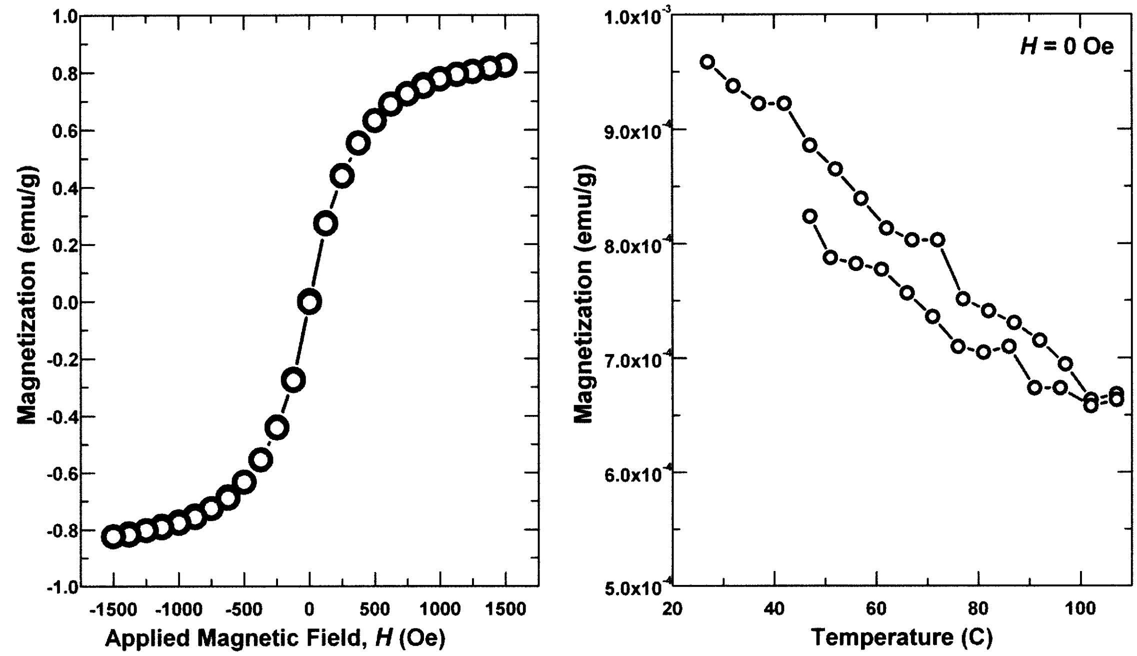

Figure 8-4: Magnetization of commercial thermoplastic polyurethane Diaplex^{TM} MM 5510 filled with 5 wt% magnetite (Fe_3O_4) as a function of applied magnetic field (left) and temperature when no magnetic field is applied (right).

Currently nanoparticle dispersal, magnetic characterization and proof of actuation via inductive heating are the extent to which most polymer-magnetite systems have been evaluated. It would be useful to understand how the inclusion of magnetite in shape memory polymers, like the polyurethane shown here, influences the response time, actuation stress, and strain recovery of the composite so that these materials can be utilized in real problems, i.e. in drug delivery or as stroke or aneurysm treatment [7].

8.3 References

[1] J. Porter, R. Dinan, M. Hammons, and K. Knox, "Polymer coatings increase blast resistance of existing and temporary structures," *AMPTIAC Quarterly*, vol. 6, pp. 47, 2003.

[2] M. A. Schubert, M. J. Wiggins, K. M. DeFife, A. Hiltner, and J. M. Anderson, "Vitamin E as an antioxidant for poly(etherurethane urea): In vivo studies," *Journal of Biomedical Materials Research*, vol. 32, pp. 493-504, 1996.

[3] M. Song and K. J. Yao, "X-ray diffraction detection of compliance in polyurethane-organoclay nanocomposites," *Materials Science And Technology*, vol. 20, pp. 989-992, 2004.

[4] J. Yi, M. C. Boyce, G. F. Lee, and E. Balizer, "Large deformation rate-dependent stress-strain behavior of polyurea and polyurethanes," *Polymer*, vol. 47, pp. 319-329, 2006.

[5] G. Baer, T. S. Wilson, D. L. Matthews, and D. J. Maitland, "Shape-memory behavior of thermally stimulated polyurethane for medical applications," *Journal Of Applied Polymer Science*, vol. 103, pp. 3882-3892, 2007.

[6] R. S. Barhate and S. Ramakrishna, "Nanofibrous filtering media: Filtration problems and solutions from tiny materials," *Journal of Membrane Science*, vol. 296, pp. 1-8, 2007.

[7] P. R. Buckley, G. H. McKinley, T. S. Wilson, W. Small, W. J. Benett, J. P. Bearinger, M. W. McElfresh, and D. J. Maitland, "Inductively heated shape memory polymer for the magnetic actuation of medical devices," *Ieee Transactions On Biomedical Engineering*, vol. 53, pp. 2075-2083, 2006.

[8] M. Yoshida, R. Langer, A. Lendlein, and J. Lahann, "From advanced biomedical coatings to multi-functionalized biomaterials," *Polymer Reviews*, vol. 46, pp. 347-375, 2006.

[9] S. Krishnan, C. J. Weinman, and C. K. Ober, "Advances in polymers for anti-biofouling surfaces," *Journal Of Materials Chemistry*, vol. 18, pp. 3405-3413, 2008.

[10] S. L. Gras, T. Mahmud, G. Rosengarten, A. Mitchell, and K. Kalantar-Zadeh, "Intelligent control of surface hydrophobicity," *Chemphyschem*, vol. 8, pp. 2036-2050, 2007.

[11] J. Genzer and K. Efimenko, "Recent developments in superhydrophobic surfaces and their relevance to marine fouling: a review," *Biofouling*, vol. 22, pp. 339-360, 2006.

[12] V. S. Kalambur, B. Han, B. E. Hammer, T. W. Shield, and J. C. Bischof, "In vitro characterization of movement, heating and visualization of magnetic nanoparticles for biomedical applications," *Nanotechnology*, vol. 16, pp. 1221-1233, 2005.

[13] R. Mohr, K. Kratz, T. Weigel, M. Lucka-Gabor, M. Moneke, and A. Lendlein, "Initiation of shape-memory effect by inductive heating of magnetic nanoparticles in thermoplastic polymers," *Proceedings Of The National Academy Of Sciences Of The United States Of America*, vol. 103, pp. 3540-3545, 2006.

[14] K. Okawa, M. Sekine, M. Maeda, M. Tada, and M. Abe, "Heating ability of magnetite nanobeads with various sizes for manetic hyperthermia at 120kHz, a noninvasive frequency," *Journal of Applied Physics*, vol. 99, pp. H102, 2006.

[15] W. W. Yu, J. C. Falkner, C. T. Yavuz, and V. L. Colvin, "Synthesis of monodisperse iron oxide nanocrystals by thermal decomposition of iron carboxylate salts," *Chemical Communications*, pp. 2306-2307, 2004.

Appendix A-1—Movie Demonstrating the Mechanical Enhancement of Elasthane at High Temperature by the Addition of Laponite.

Movie titled Appendix A-1 displays thermal creep of nanocomposite films containing 0 and 20 wt% Laponite when a constant load equal to 1.08 N is applied. The pure Elasthane deforms significantly, increasing its length by 100% at 95°C, and breaks at 120°C. Meanwhile the nanocomposite containing 20 wt% Laponite does not measurably deform at all. However, at 125°C the improvised grip holding the constant load slips off the sample.

Appendix A-2—Elasthane/Laponite Composite Moduli Measured with a Video Extensometer

The initial modulus reported in chapter 4 from the engineering stress-strain curves utilizing the Zwick Z010 mechanical tester were verified using a video extensometer. The thin-film sample was lit with a fiber optic light and videoed using a Qimaging Retiga 1300 CCD camera equipped with a 200 mm Canon f14.0 Canon lens and a Nikon 200 mm extension. A series of X's were placed along the length of the sample using a fine tip black permanent marker as shown below in Figure A-2-1 and the specimen width and thickness were measured at the vertex of each X and measured with a micrometer. The camera was placed at a distance of approximately 1 m from the specimen and images were captured every 0.5 s. The images were analyzed with a digital image correlation algorithm developed by Correlated Solutions Incorporated (CSI). The deformed image was correlated to the reference image via two distinct points of interest, i.e. two black dots, connected by a straight line. The software then output the x and y pixel position of these two distinct points. The change in longitudinal distance was used to calculate the true strain while the change in horizontal distance was used to calculate the true stress as shown below:

$$\varepsilon_{true} = \ln\left(\frac{y_2 - y_1}{y_{2,0} - y_{1,0}}\right) \tag{A-2.1}$$

and

$$\sigma_{true} = \frac{F}{(wt)} = \frac{F}{(w_0 t_o)}\left(\frac{w_0}{w}\right) = \frac{F}{(w_0 t_o)}\left(\frac{x_{2,0} - x_{1,0}}{x_2 - x_1}\right) \tag{A-2.2}$$

when changes in thickness are assumed negligible, $t \approx t_0$. This video extensometer was used because strain localization was common within these samples since the thickness of the specimen varied ±20 μm through the length due to solvent casting.

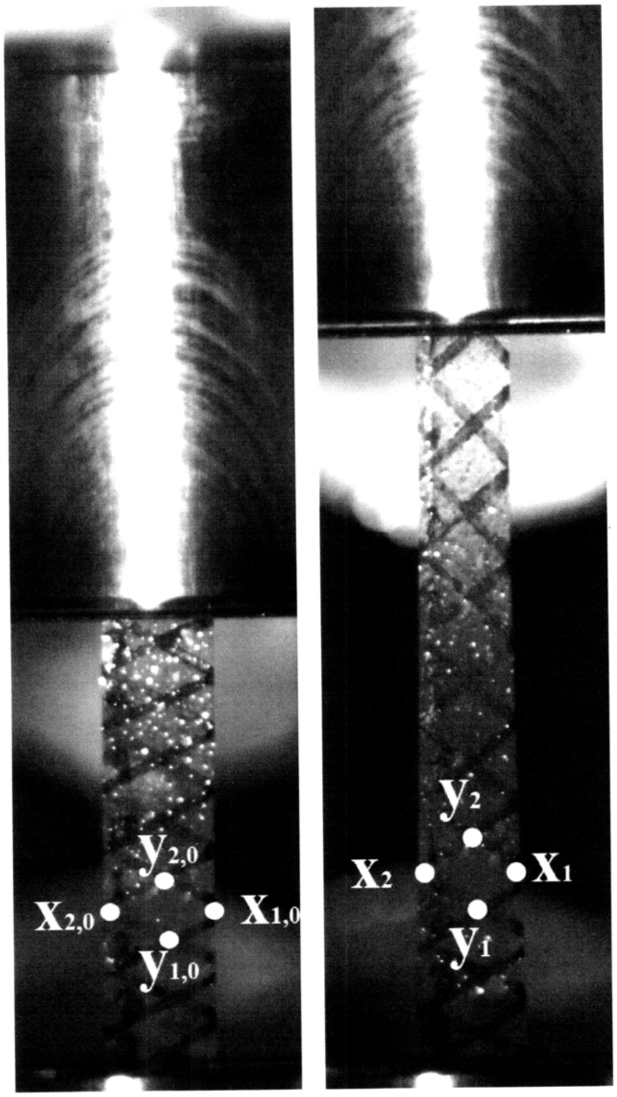

Figure A-2-1: Images of a 2 wt% Laponite-filled polyurethane film inside the Zwick Z010 as seen with the video extensometer. On the left is the un-deformed film with 45 mm gauge length. On the right is the same film after the gauge length has been extended 30%. It is important to note that 40% of the un-deformed sample is masked by the grip: recall the grip consists of a convex and flat jaw face so the upper and lower gauge length extends into the grip and is unobservable.

It is important to note that the grips used in the Zwick consisted of one flat, polyurethane jaw face placed flush against a convex, aluminum jaw face. Consequently, a portion at either end of the specimen extends between the grips and up to the line of contact that holds the specimen fixed. These grips were screw tightened and as a consequence localized deformation near the grip contact lines was common. So the deformation in the middle of the various nanocomposites was monitored.

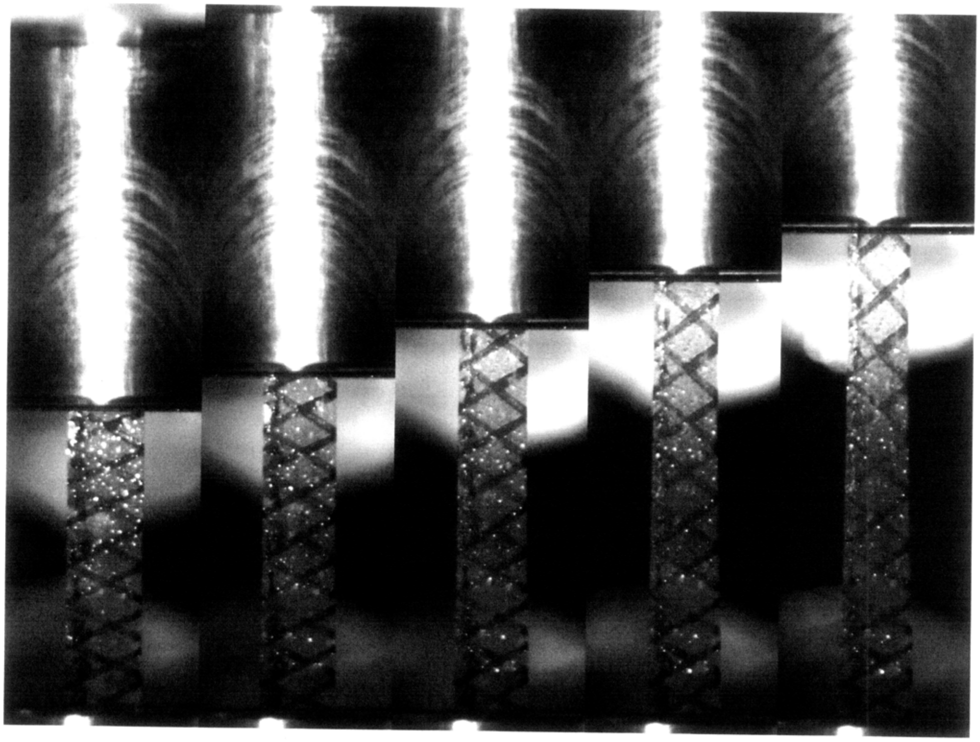

Figure A-2-2: Selection of the sequential images taken with the video extensometer as Elasthane filled with 2 wt% nano-clay is deformed using the Zwick Z010 mechanical tester at a nominal strain rate of 0.0167s^{-1}.

Figure A-2-2 depicts the deformation captured by the video extensometer typical of the nanocomposites. The results of the localized deformation captured via the video extensometer are plotted against the engineering results determined by the Zwick cross-head in Figure A-2-3. The engineering stress-strain response within the elastic regime falls within the scattered response of that calculated with the video extensometer. This behavior was true of the more highly concentrated samples as well. Consequently, the modulus measurements reported can be considered valid.

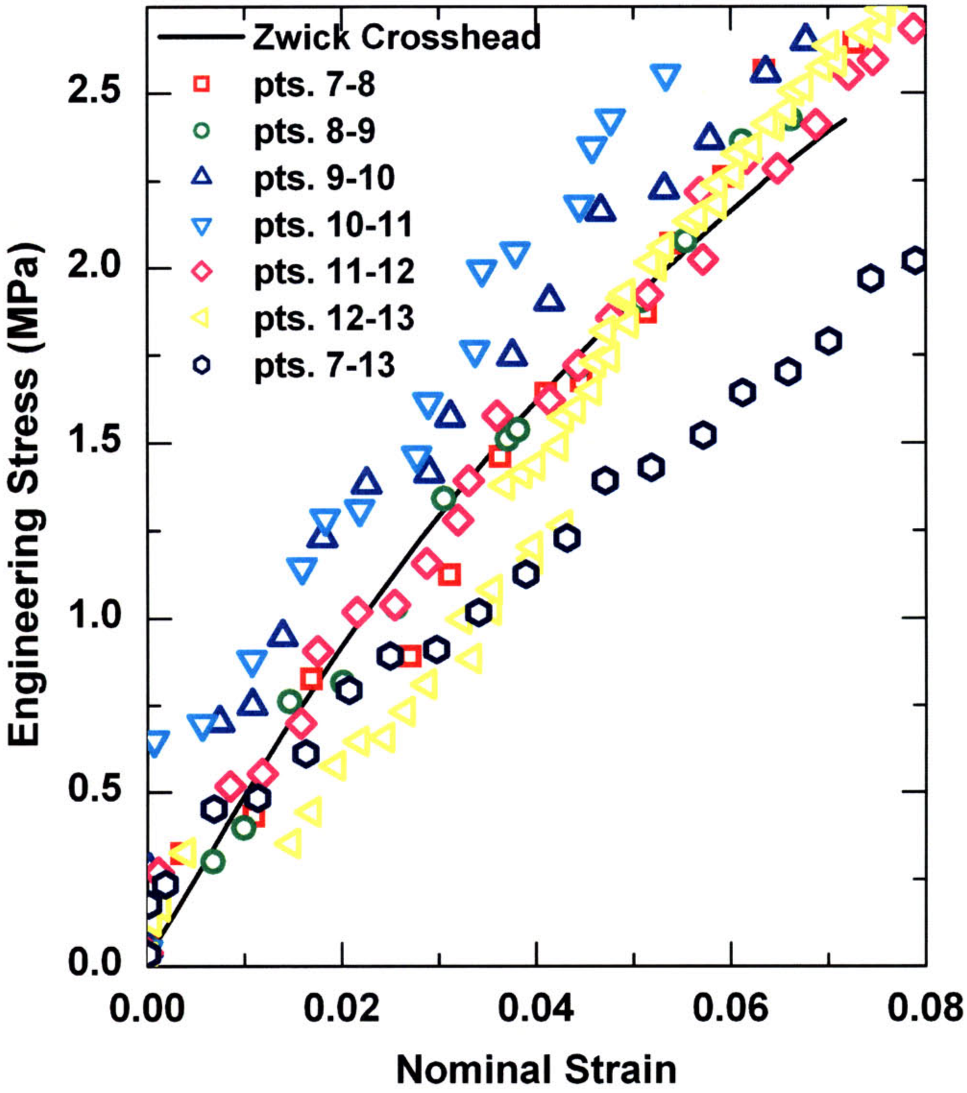

Figure A-2-3: Comparison of the engineering stress-strain response of 2 wt% nano-clay filled Elasthane calculated from the change in length reported by the Zwick mechanical tester crosshead and that measured via the video extensometer at various sections along the length of the specimen gauge length.

Appendix A-3—Discussion of Appropriate Constitutive Model

This appendix reviews the constitutive model developed by Qi and Boyce to capture the stress-strain behavior of thermoplastic polyurethanes [1]. Within this appendix the ability of the model to capture the hyperelastic equilibrium behavior of the high performance, Elasthane/Laponite nanocomposites and its inability to accurately capture the non-equilibrium response is discussed.

A-3.1 Review of Qi & Boyce Thermoplastic Polyurethane Model

Qi and Boyce developed a constitutive model that predicts the stress-strain behavior of thermoplastic polyurethanes well by coupling the mechanical behavior to the evolution of the hard and soft domain morphology of the polyurethane matrix as strain increases [1]. The model captures the nonlinear hyperelastic behavior, time-dependence, stress-softening, and hysteretic behavior by virtue of a hyperelastic spring and visco-plastic Maxwell element. This hyperelastic spring acts in parallel to the Maxwell element which consists of an elastic spring and visco-plastic dashpot that are placed in series. The one-dimensional rheological model, constitutive equations, and parameters are shown below in Figure A-3-1. The definitions of the ten model parameters are listed below.

μ: product of Boltzmann's constant, the absolute temperature, and the chain density
N: number of "rigid links" between two crosslinks and/or strong physical entanglements
v_{s0}: effective initial soft domain volume fraction
v_{ss}: effective saturation soft domain volume fraction
A: parameter characterizing the evolution of the soft domain volume fraction
E_v: elastic modulus of the linear, elastic spring in the viscoelastic-plastic Maxwell element
ν: Poisson's ratio
$\dot{\gamma}_o$: factor proportional to the visco-plastic shear strain rate
ΔG: activation energy in the limit of zero applied stress
s_o: initial athermal shear strength

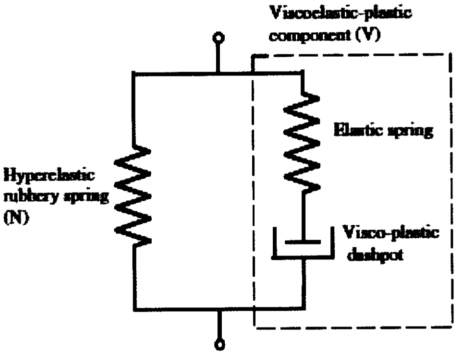

Summary of constitutive model and material parameters

$\mathbf{T} = \mathbf{T}^N + \mathbf{T}^V$	**Equilibrium stress–strain response $\mathbf{T}^N$**	**Hyperelastic rubbery spring element**	μ_r, N	**Hyperelastic "filler" effect** $\mathbf{T}^N = \frac{v_s X \mu_r}{3J} \frac{\sqrt{N}}{\Lambda_{chain}} \mathcal{L}^{-1}\left(\frac{\Lambda_{chain}}{\sqrt{N}}\right)\overline{\mathbf{B}}'$ $X = 1 + 3.5(1 - v_s) + 18(1 - v_s)^2$
			v_{s0}, v_{ss}, A	**Softening** $v_s = v_{ss} - (v_{ss} - v_{s0})\exp\left(-A\frac{\Lambda_{chain} - 1}{\Lambda^{lock}_{chain} - \Lambda_{chain}}\right)$
	Non-equilibrium rate-dependent stress–strain response $\mathbf{T}^V$	**Linear spring element**	E_v, ν	**Linear Elasticity** $\mathbf{T}^V = \frac{v_h}{\det \mathbf{F}^e}\mathbf{L}^e[\ln \mathbf{V}^e]$ $v_h = 1 - v_s$
		Viscoplastic dashpot element	$\dot{\gamma}_0$, ΔG	**Time dependence** $\dot{\gamma}^p = \dot{\gamma}_0 \exp\left[-\frac{\Delta G}{k\theta}\left\{1 - \left(\frac{\tau_V}{s}\right)\right\}\right]$
			S_0	**Softening** $s = \left(\frac{v_h}{v_{h0}}\right)s_0$

Figure A-3-1: One dimensional rheological model and material parameters summary of the Qi and Boyce thermoplastic polyurethane constitutive model as shown in [1].

Note that the soft domain volume fraction, v_s, is not constant but evolves with deformation. This is because as the polyurethane stretches, the hard domain network breaks down and the effective soft domain volume fraction increases (see Figure A-3-2). By accurately capturing the evolution of the soft domain volume fraction, the hysteresis, softening, and time-dependence of the material can be predicted. However, the effective soft segment volume fraction does not correlate to the chemically-determined composition because prior to deformation some of the soft segments are constrained by hard micro-domains and effectively increases the hard domain volume fraction. Similarly upon extensive deformation not only is the soft segment unconstrained, but the hard micro-domains are disrupted and effectively increases the soft volume fraction.

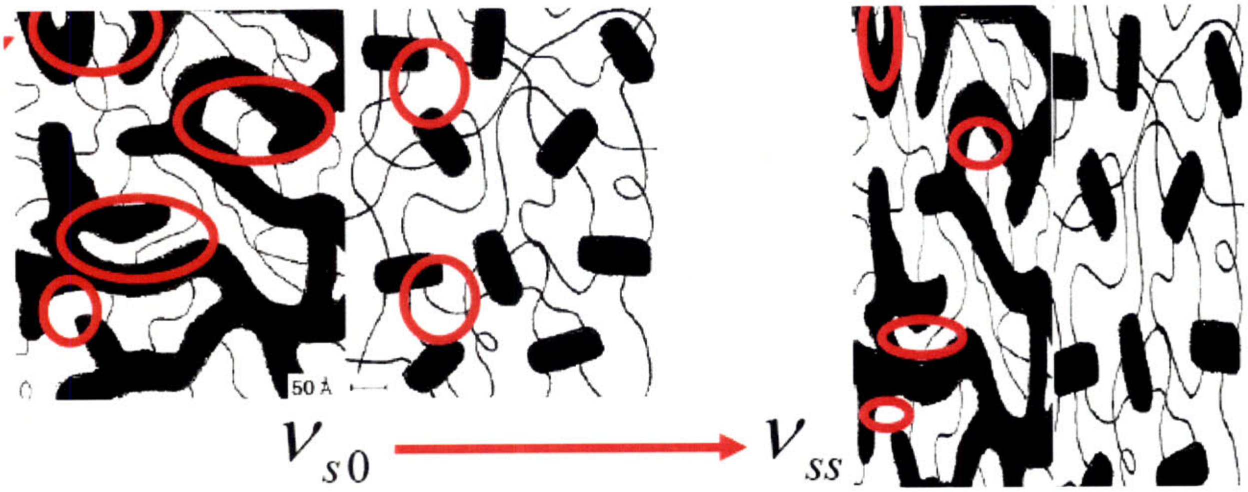

Figure A-3-2: Cartoon of soft segment evolution with matrix stretch. Red circles denote regions of soft segment constrained by hard micro-domains (black) in the polyurethane microstructure cartoon borrowed from [2]. Initially the effective soft segment volume fraction is ν_{s0} is less than the chemically-determined, soft segment volume fraction. Upon deformation the hard domains break up (at high hard segment concentration) and/or rotate and align releasing constrained soft segment. The effective soft segment volume fraction, ν_s, increases with deformation until a saturated value is achieved, ν_{ss}. This saturated value corresponds to a value larger than the chemically-determined, soft segment volume fraction due to the inclusion of damaged hard-micro-domains.

Qi and Boyce utilize this evolution to amplify the hyperelastic response and drive the evolution in the non-equilibrium response. The effective hard segment volume fraction, ν_h, is defined as

$$\nu_h = 1 - \nu_s \tag{A-3.1}$$

and the effective soft volume fraction evolves non-linearly with the maximum applied stretch according to the following equation:

$$\dot{\nu}_s = A\left(\nu_{ss} - \nu_s\right)\frac{\lambda_{chain}^{lock} - 1}{\left(\lambda_{chain}^{lock} - \Lambda_{chain}^{\max}\right)^2}\dot{\Lambda}_{chain}^{\max}, \tag{A-3.2}$$

where $\Lambda_{chain}^{\max}$ is an amplification of the equivalent maximum stretch achieved defined in [1].

A-3.1.1 Hyperelastic Rubbery Network Behavior

The hyperelastic response of the polyurethane was based on the response devised by Arruda and Boyce when an eight-chain network representative volume element (shown in Figure A-3-3) was utilized [3].

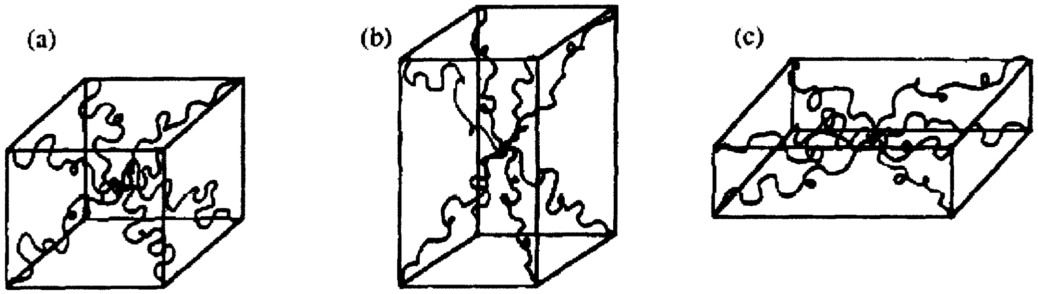

Figure A-3-3: Eight chain rubber elasticity model developed by Arruda and Boyce. The undeformed (a), uniaxially extended (b), and biaxially extended (c) configurations are displayed as shown in [3].

However, the equivalent chain stretch λ_{chain} was redefined as Λ_{chain} and the previously defined value amplified to account for the presence of obstacles, such as rigid particles, around which polymer chains must stretch. The amplified equivalent chain stretch is defined as follows

$$\Lambda_{chain} = \sqrt{X\left(\lambda_{chain}^{2} - 1\right)^{2} + 1} \tag{A-3.3}$$

where the amplification factor, X, is defined as

$$X = 1 + 3.5\left(1 - \nu_{s}\right) + 18\left(1 - \nu_{s}\right)^{2}. \tag{A-3.4}$$

It is clear that the amplification of the hyperelastic stress-response, X, is an extension of the Guth-Gold rigid particle filler model in which the hard domain volume fraction ($1-\nu_s$) is utilized as the rigid particle filler volume fraction [1, 4].

The resulting hyperelastic response can fit the equilibrium behavior (described in section 5.3.5) exhibited by pure Elasthane and the Laponite-filled nanocomposites. When the five parameters are defined as follows in Table A-3-1, the resulting response shown in Figure A-3-4 captures the equilibrium behavior of the Elasthane/Laponite nanocomposites. The addition of Laponite does not influence the equilibrium or hyperelastic response—this response is matrix driven.

N	μ_r	A	ν_{s0}	ν_{ss}
3.7	1.6 MPa	3.6	0.45	0.85

Table A-3-1: Five parameters needed to describe the hyperelastic or equilibrium response of the Elasthane/Laponite nanocomposites.

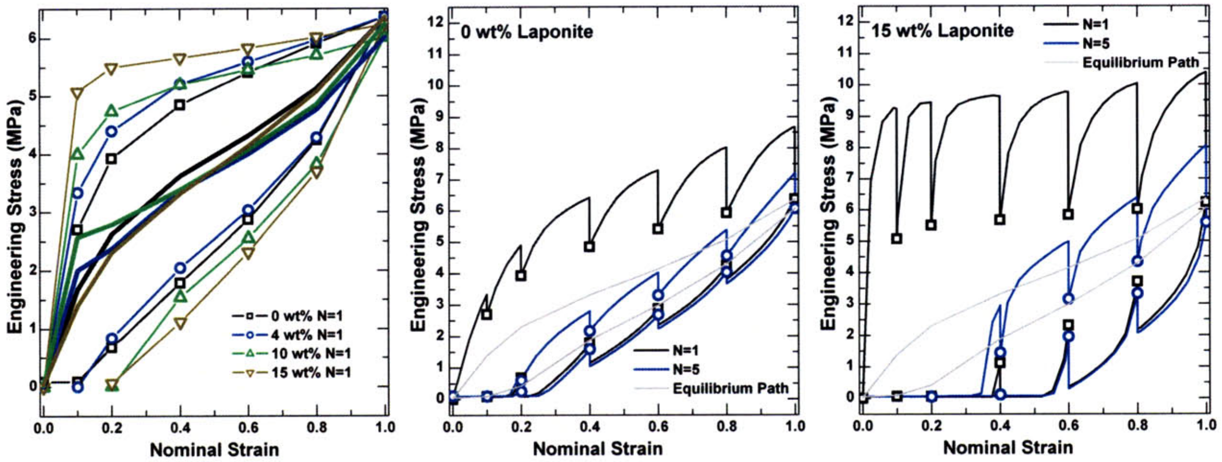

Figure A-3-4: The equilibrium or hyperelastic response of the Elasthane/Laponite nanocomposites is the same despite Laponite concentration and can be captured by the constitutive model of Qi and Boyce [1, 5]. The equilibrium paths of the 0, 4, 10 and 15 wt% Laponite filled Elasthane determined experimentally from the relaxed response are described by the solid thick lines in the left-most figure. The response is the same despite the Laponite concentration. Using the constitutive model described by Qi & Boyce this equilibrium or hyperelastic response is captured. The hyperelastic model (grey solid line) falls within the relaxed response of the pure (center) and 15 wt% Laponite-filled (right) Elasthane.

A-3.1.2 Viscoelastic-Plastic Behavior

The non-equilibrium behavior or viscoelastic-plastic behavior of this constitutive model too depends on the evolution of the soft volume fraction. The complex Maxwell element with linear spring and non-linear dashpot accounts for the rate dependence and stress relaxation of the material. The equivalent shear stress was defined as follows:

$$\bar{\tau}_V = \left[\frac{1}{2}\bar{\mathbf{T}}^{V\prime} \bullet \bar{\mathbf{T}}^{V\prime}\right]^{1/2}, \tag{A-3.5}$$

where

$$\mathbf{T}^V = \mathbf{T} - \mathbf{T}^N . \tag{A-3.6}$$

The equivalent shear stress coupled with a softening parameter, s, defined by

$$s = \left(\frac{1-\nu_s}{1-\nu_{s0}}\right) s_0 \tag{A-3.7}$$

with constant model parameters defines the visco-plastic shear strain rate, $\dot{\gamma}$:

$$\dot{\gamma} = \dot{\gamma}_0 \exp\left[-\frac{\Delta G}{k\Theta}\left\{1-\left(\frac{\bar{\tau}_V}{s}\right)\right\}\right]. \tag{A-3.8}$$

While this model exhibits two characteristic relaxation times upon relaxation, both the short and long time constant evolve with stretch or orientation. It is impossible to separate the non-equilibrium contribution of the hard segment volume fraction from the soft segment volume fraction contribution as currently prescribed. It is also not realistic to assume that the spring in the Maxwell element is linear and does not evolve too with stretch or orientation. Furthermore, the method to identify visco-plastic parameters identified by Qi and Boyce proved inadequate because the equivalent shear stress deviated from the behavior the authors observed as is shown in Figure A-3-5.

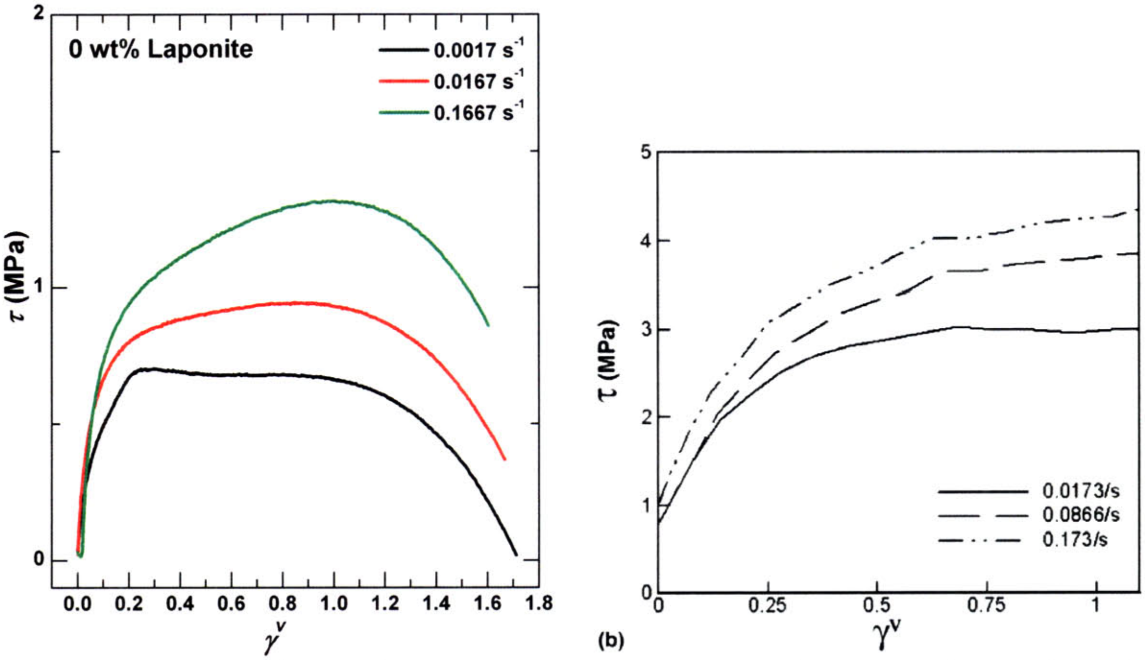

Figure A-3-5: Comparison of the equivalent shear stress versus shear strain for pure Elasthane in tension to that of the polyurethane evaluated by Qi and Boyce in compression [1].

The equivalent shear stress observed by the authors reached a plateau while the equivalent shear stress of pure Elasthane decayed with increased stretch or equivalent shear strain. This behavior, or decay, was also observed in the Laponite-filled composites. Consequently augmentation of the Qi and Boyce constitutive model is needed.

A-3.2 Necessary Augmentation of the Constitutive Model

To more accurately capture the behavior of the Elasthane/Laponite nanocomposites a constitutive model that explicitly separates the non-equilibrium stress contribution from the soft volume fraction and the hard volume fraction is needed. A more appropriate model would employ the same similar hyperelastic spring placed parallel to two Maxwell elements (see Figure 5.9). As described in Chapter 5.3.4 one Maxwell element would correspond to the soft segment, non-equilibrium stress contribution while the other element would correspond to the hard segment, non-equilibrium stress contribution. This would allow the soft segment relaxation time constant to evolve with orientation. Meanwhile, the hard micro-domain relaxation behavior could act independently and its characteristic relaxation time maintained. In both instances the stress contribution from the spring comprising the Maxwell element must decay non-linearly, following a power-law scaling that depends on Laponite concentration, aspect ratio and polydispersity. Simultaneously, the dashpots of these Maxwell elements must accurately predict the strain rate sensitivity exhibited by these nanocomposites.

Unfortunately, I was unable to develop a model to capture this behavior in my last four months at MIT. It has recently come to my attention that Dr. Renaud Rinaldi, a post-doc working for Professor Mary C. Boyce, has developed a constitutive model for polyurethanes that separates the hard and soft segment non-equilibrium contribution. It is likely that this model could easily be modified to capture the behavior exhibited by the high performance, Elasthane/Laponite nanocomposites.

A-3.3 References

[1] H. J. Qi and M. C. Boyce, "Stress-strain behavior of thermoplastic polyurethanes," *Mechanics of Materials*, vol. 37, pp. 817-839, 2005.

[2] D. J. Martin, G. F. Meijs, P. A. Gunatillake, S. P. Yozghatlian, and G. M. Renwick, "The influence of composition ratio on the morphology of biomedical polyurethanes," *Journal of Applied Polymer Science*, vol. 71, pp. 937-952, 1999.

[3] E. M. Arruda and M. C. Boyce, "A three-dimensional constitutive model for the large stretch behavior of rubber elastic materials," *Journal of the Mechanics and Physics of Solids*, vol. 41, pp. 389-412, 1993.

[4] E. Guth, "Theory of Filler Reinforcement," *Journal of Applied Physics*, vol. 16, pp. 20-25, 1945.

[5] H. J. Qi and M. C. Boyce, "Constitutive model for stretch-induced softening of the stress-stretch behavior of elastomeric materials," *Journal of the Mechanics and Physics of Solids*, vol. 52, pp. 2187-2205, 2004.

Appendix A-4—2-D WAXS Spectra Collected at Each Specimen Stretch for Pure Elasthane and that Reinforced with 8 wt% Laponite

The spectra at specimen stretches equal to 1.1, 1.6, 3.0 and 9.0 are used in the results displayed in Chapter Five. These stretches correspond to the approximate locations in the stress-strain curve given by the black, red, green and blue empty circles shown below.

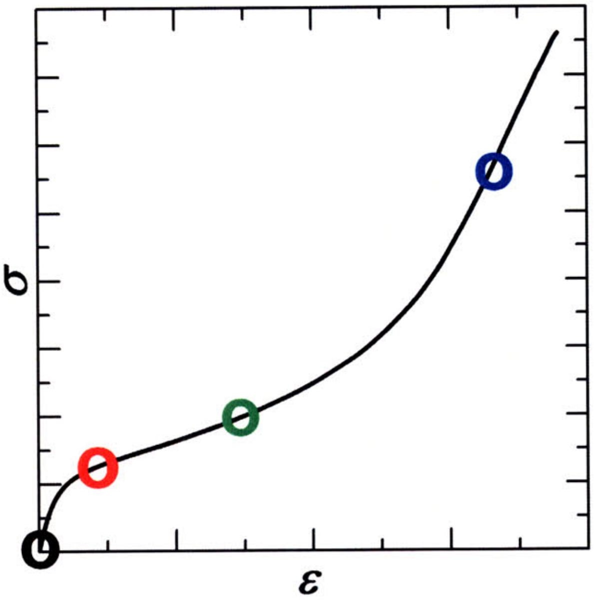

Figure A-4-1: The specimen stretches equal to 1.1, 1.6, 3.0 and 9.0 correspond to the locations shown above in the stress-strain curve due to specimen slip during testing.

All of the scatter patterns collected are shown on the fourth and fifth page of this appendix. Below find enlarged patterns for the four positions of interest for the pure and the 8 wt% Laponite-filled Elasthane composite.

Figure A-4-2: Enlarged scatter patterns at specimen stretches equal to 1.1, 1.6, 3.0, and 9.0 for pure Elasthane.

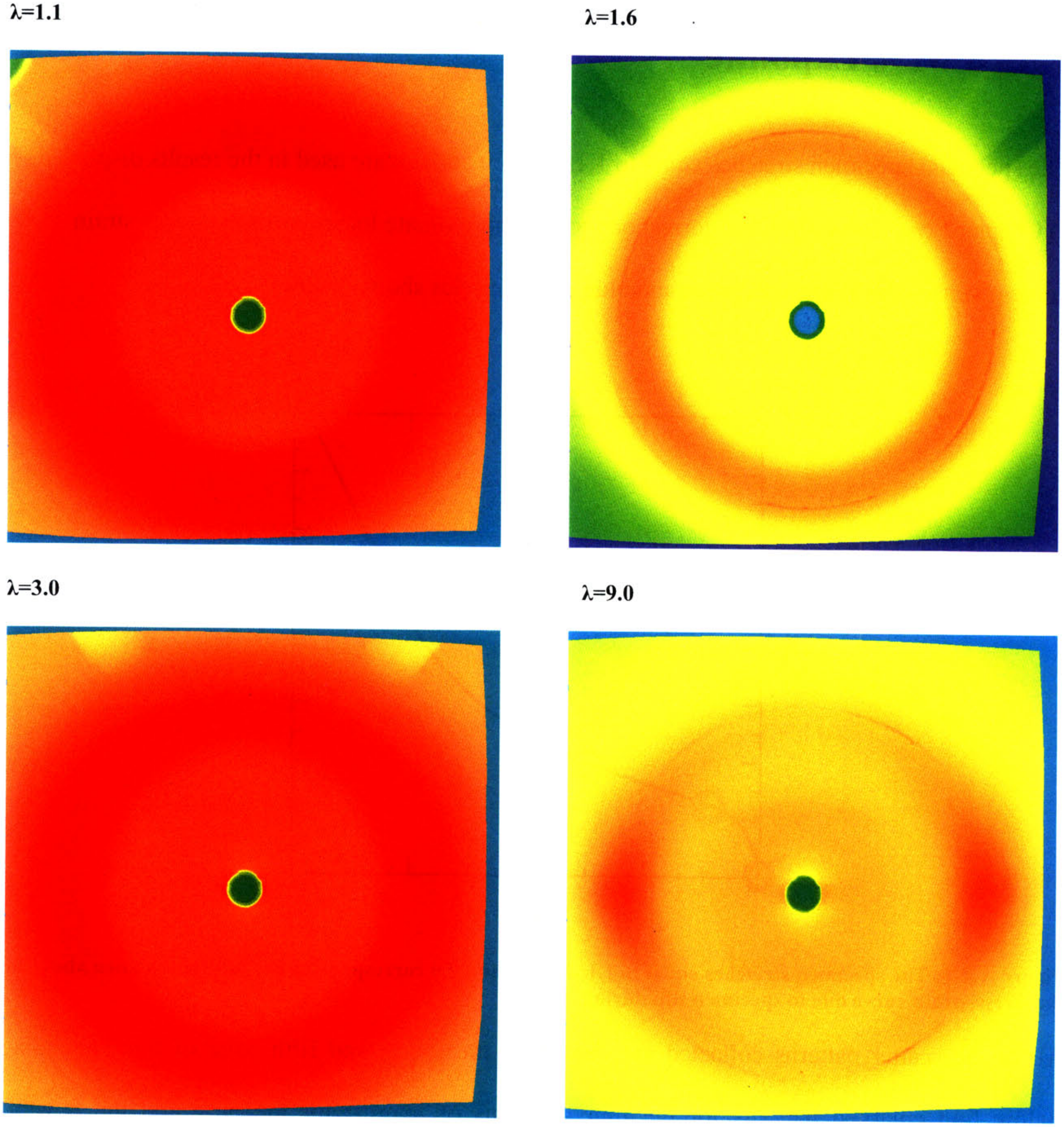
λ=1.1

λ=1.6

λ=3.0

λ=9.0

Figure A-4-3: Enlarged scatter patterns at specimen stretches equal to 1.1, 1.6, 3.0, and 9.0 for the 8 wt% Laponite-filled Elasthane nanocomposite.

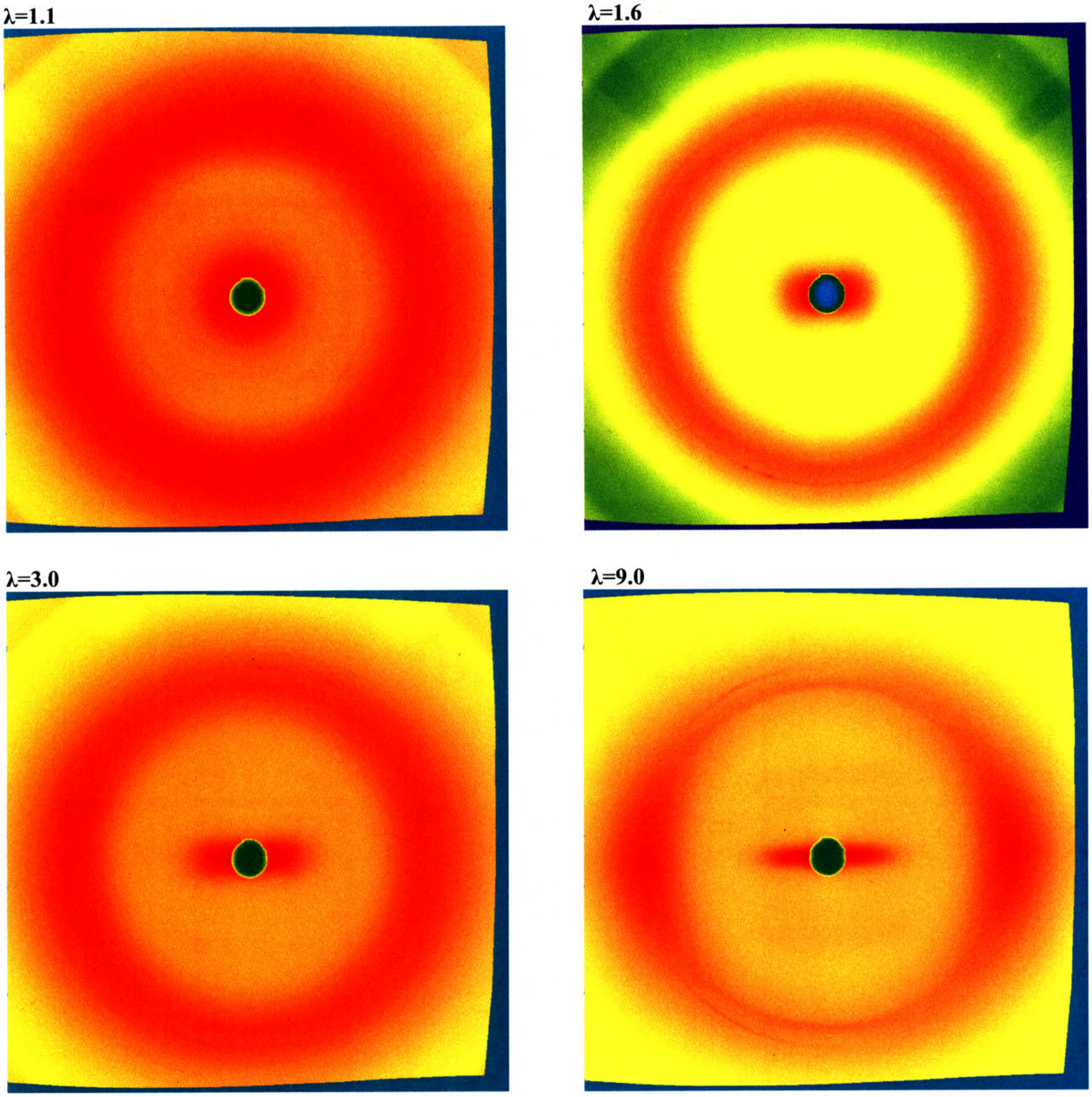
λ=1.1

λ=1.6

λ=3.0

λ=9.0

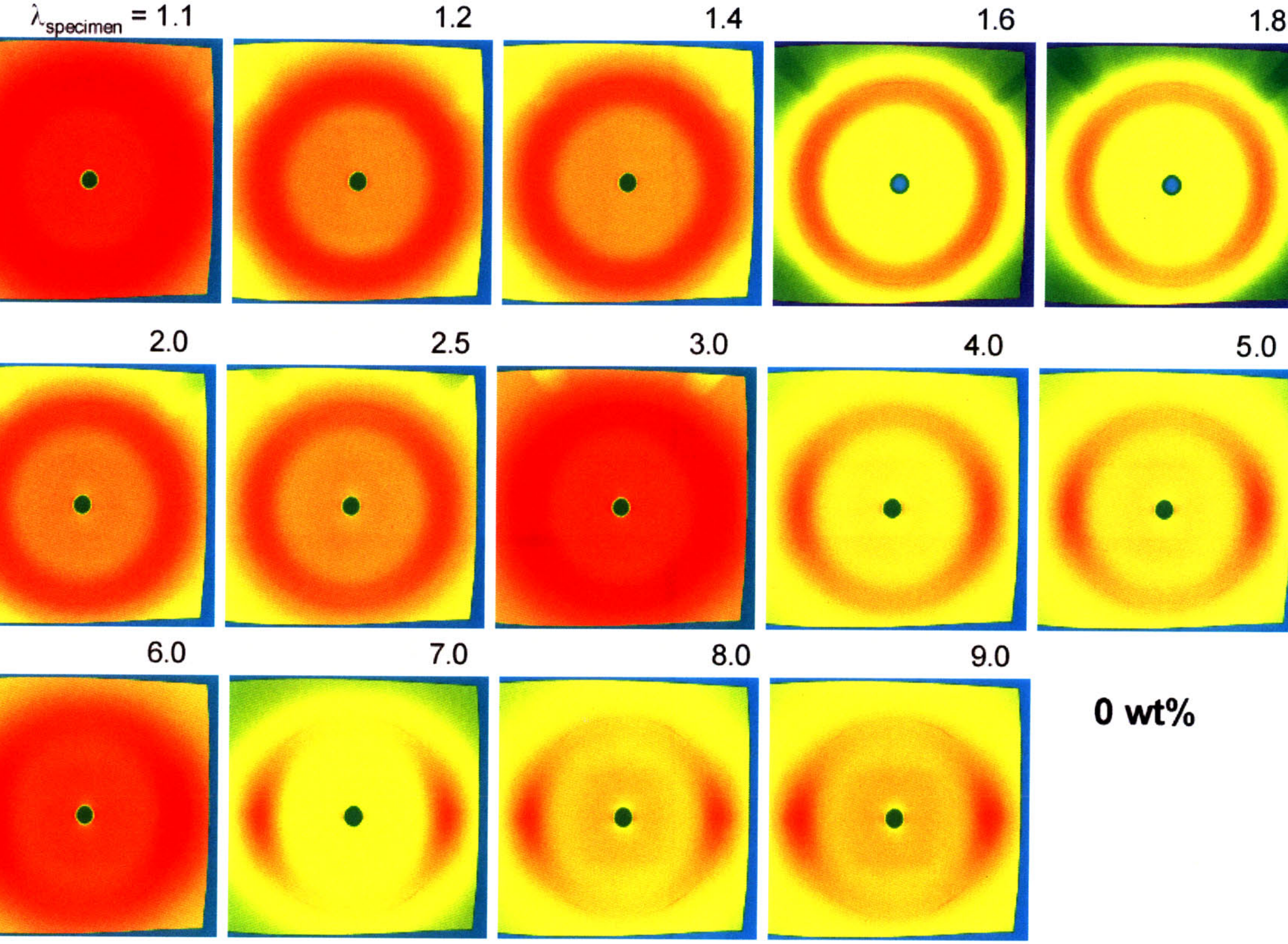

$\lambda_{specimen}$ = 1.1
1.2
1.4
1.6
1.8
2.0
2.5
3.0
4.0
5.0
6.0
7.0
8.0
9.0
0 wt%

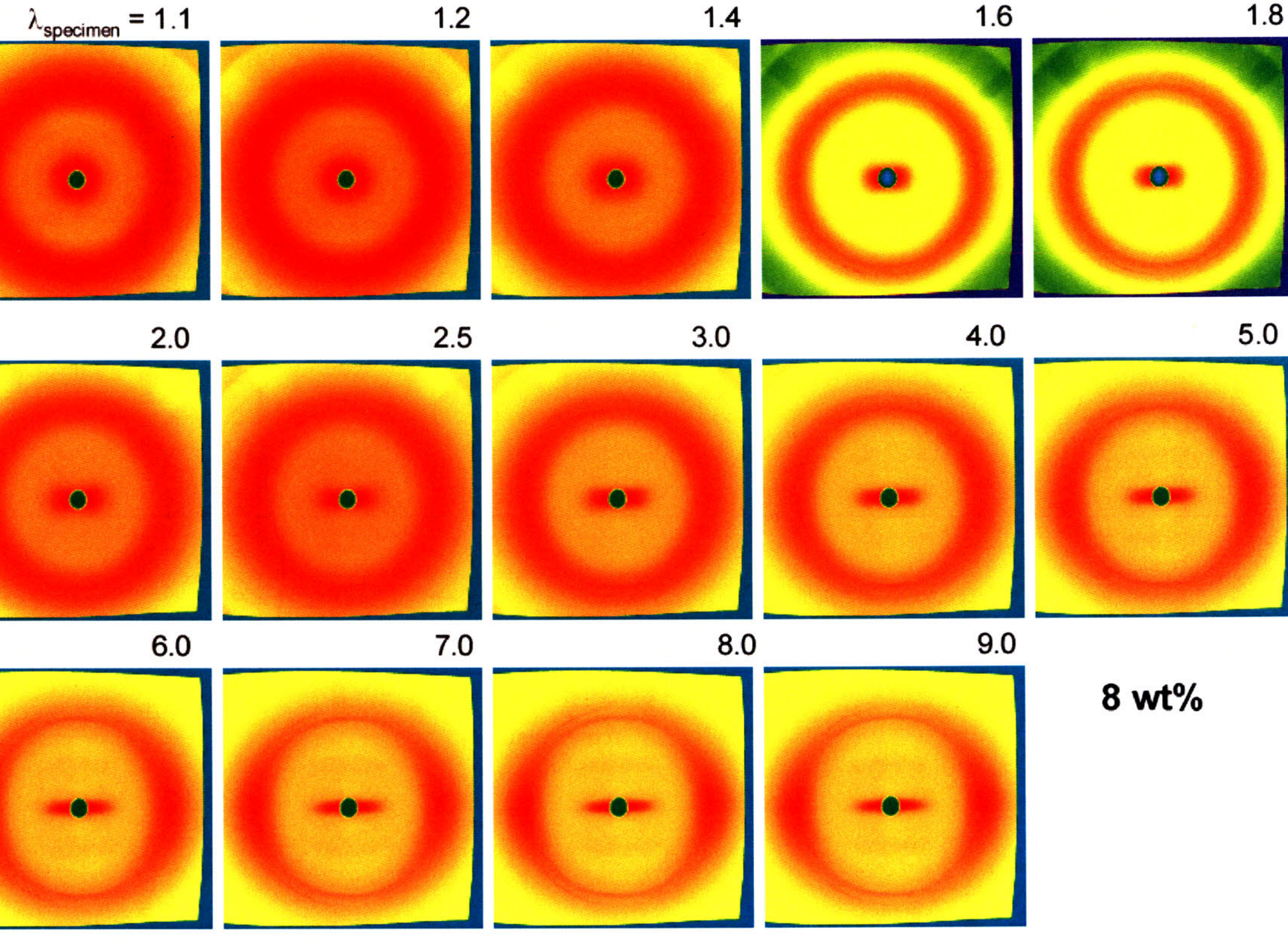
$\lambda_{specimen}$ = 1.1
1.2
1.4
1.6
1.8
2.0
2.5
3.0
4.0
5.0
6.0
7.0
8.0
9.0
8 wt%

The 1-D SAXS pattern collected on a static film of pure Elasthane and filled with 8 wt% Laponite is shown below in Figure A-4-4. The behavior of the 8 wt% filled sample is representative of the spectra exhibited by nanocomposites filled with various concentrations of Laponite. SAXS data has been expressed in terms of q, where $q = \frac{4\pi}{\lambda}\sin(\theta)$. The peaks identifiable in the pure polyurethane that correspond to the hard micro-domain size and spacing are indistinguishable in the Laponite-filled samples. Consequently, the SAXS data is not reported.

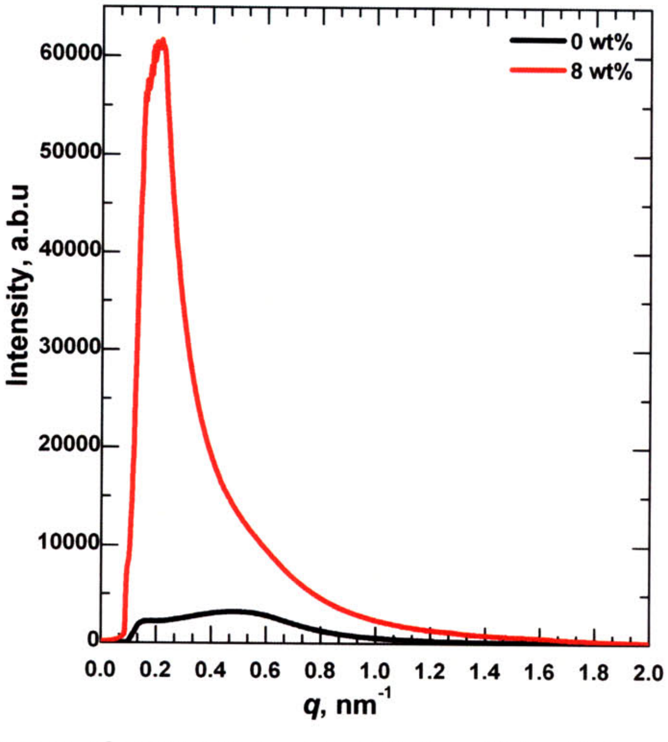

Figure A-4-4: 1-D SAXS spectra of pure Elasthane and that filled with 8 wt% Laponite. The broad peaks at q ~ 0.18 and ~0.50 are masked by the presence of Laponite due to electron-density contrast matching.

Appendix A-5—Movies of Electrospun Mat Lateral Shrink

The movie titled Appendix A-5-1 demonstrates the quick shrink of the as spun non-woven, mat (17wt% Polyurethane in solution) when it is thermally actuated by placing it on a hot plate ($T =$ 75°C; each grid edge measures 1 cm).

The movie titled Appendix A-5-2 demonstrates the micron-scale change in mat morphology observed in an environmental scanning electron microscope. The two ends of the film are held in position while the middle of the film is allowed to shrink freely—consequently, the film appears to narrow. The slow strain recovery occurs because the peltier plate can only achieve a temperature of 62°C. Notice that the BOAS morphology re-coils along the film edges where the morphology is least constrained.